Doctoral theses at NTNU, 2018:405

Thomas Sauder

Fidelity of cyber-physical empirical methods

Application to the active truncation of slender marine structures

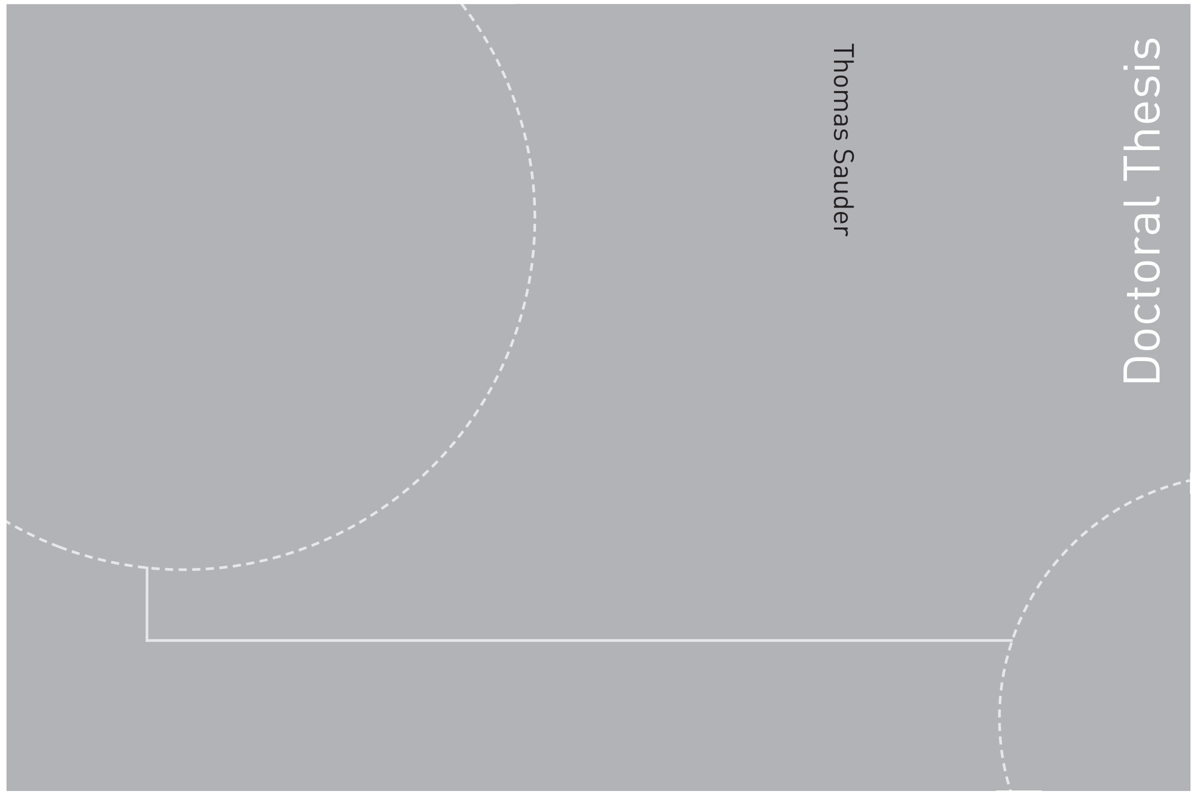

Doctoral Thesis

Thomas Sauder

Doctoral theses at NTNU, 2018:405

NTNU
Norwegian University of
Science and Technology
Faculty of Engineering
Department of MarineTechnology

ISBN 978-82-326-3600-6 (printed version)
ISBN 978-82-326-3601-3 (electronic version)
ISSN 1503-8181

NTNU
Norwegian University of
Science and Technology

NTNU

NTNU
Norwegian University of
Science and Technology

Thomas Sauder

Fidelity of cyber-physical empirical methods

Application to the active truncation of slender marine structures

Thesis for the degree of Philosophiae Doctor

Trondheim, December 2018

Norwegian University of Science and Technology
Faculty of Engineering
Department of MarineTechnology

NTNU
Norwegian University of
Science and Technology

NTNU
Norwegian University of Science and Technology

Thesis for the degree of Philosophiae Doctor

Faculty of Engineering
Department of MarineTechnology

ISBN 978-82-326-3600-6 (printed version)
ISBN 978-82-326-3601-3 (electronic version)
ISSN 1503-8181

Doctoral theses at NTNU, 2018:405

Printed by Skipnes Kommunikasjon as

à Marie

Abstract

Cyber-physical empirical methods (CPEMs) are empirical methods in which a dynamical system under study is partitioned into physical and numerical substructures. While the numerical substructures are described by validated computational models, the behaviour of the physical substructures is partly unknown. CPEMs allow to address problems in e.g. mechanical and electrical engineering that classical empirical methods alone, or models alone, cannot address in a satisfactory way. In CPEMs, the substructures are interconnected through a control system that includes sensors and actuators, having their own dynamics. The present thesis addresses how the fidelity of CPEMs, that is the degree to which they reproduce the behaviour of the system under study, is affected by the presence of this control system.

In our work, the control system is represented by a parametrized set of elementary artefacts, such as sensor calibration error, bias, noise, time delays, signal loss, and actuator dynamics. Their describing parameter is assumed to be the realization of a multidimensional random variable with a known, but arbitrary, distribution, obtained from dedicated surveys or based on experience. The proposed analysis method enables the designer of a CPEM to (1) identify the artefacts that play a significant role for the fidelity, (2) define bounds for the describing parameter ensuring high-fidelity of the CPEM, and (3) evaluate whether probabilistic robust fidelity is achieved. These analyses are generally to be performed in a high-dimensional space, and involve non-closed form models of the substructures, which are possibly expensive to evaluate. To make the problem tractable, our strategy was therefore to apply adequate surrogate modelling technique, namely Polynomial Chaos Expansions (PCE) and Polynomial Chaos-based Kriging (PCK).

The proposed method is first illustrated by a simple example involving coupled linear oscillators. It is then applied to the analysis of the active truncation of slender marine structures, a problem of direct relevance for hydrodynamic model testing of floating structures in ultra-deep water.

Preface

This thesis is submitted to the Norwegian University of Science and Technology for partial fulfillment of the requirements for the degree of philosophiae doctor. This work was supported by the Research Council of Norway through the Centres of Excellence funding scheme (project number 223254 - AMOS).

The core subject of this thesis is the fidelity of cyber-physical empirical methods (CPEM). As shown in the figure below, we developed an analysis method that builds on knowledge from the fields of empirical methods, control engineering and uncertainty quantification (UQ). The method is then applied to the active truncation problem, of relevance for marine technology, and more generally for structural dynamics.

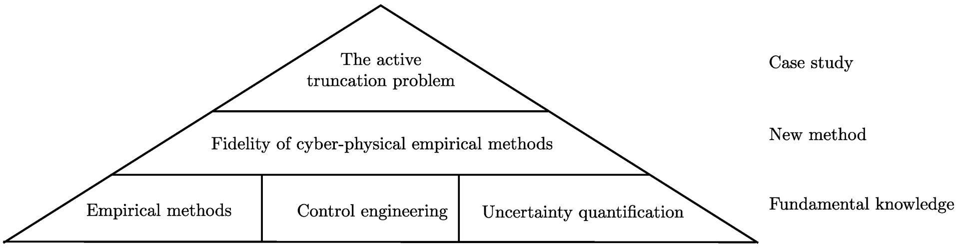

We start this thesis by introducing the subject of CPEM through examples, which cover various fields of engineering and research. Our aim was to emphasize that fidelity is a common issue to all CPEMs, regardless the field they serve. The mathematical background for the proposed fidelity analysis method is presented in Chapter 2. While the content of this chapter constitutes relatively well-known material for probabilists and statisticians, it might be new to researchers working in the field of mechanical and control engineering. We have therefore attempted to formulate this chapter in an adequate manner for researchers with this background. The fidelity analysis method, developed in Chapter 3, is applied to the active truncation problem in Chapters 4 and 5. These chapters contain discussions and results of interest for researchers in marine technology, even if they are not familiar with UQ.

As most scientific reports, this thesis is organized in a logical way, without giving an account of the chronology, the thread of the research, and the difficulties encountered on the way. The initial objective of the work was to study the active truncation of slender marine structures, and more specifically, the accuracy of such setups (at term which would later on become the *fidelity*). After several attempts to properly formulate the problem, it appeared that quite strong assumptions had to be made to address it with the classical analytical methods of mechanical and control engineering. The problem seemed indeed tractable only by simplifying excessively the control system -a common pitfall for mechanical engineers- and/or the dynamical description of slender marine structures -a common pitfall for control engineers. Such simplifications were, in our opinion, leading to weak results: how can one assess whether active truncation is "accurate", by modeling it in a coarse manner? Simulation-based methods were an alternative, as they would enable us to model the CPEM with an arbitrarily high level of details, but both sensitivity and reliability analyses would then have required a significant amount of calculations.

The solution was brought to me by a mix of serendipity and curiosity. While taking part to a workshop on CPEMs in earthquake engineering in Italy, I attended a presentation by Dr. Giuseppe Abbiati, who was proposing a method to include *uncertain* numerical substructures in CPEMs. To do so, he was applying innovative UQ techniques developed in his institute. After getting familiar with this subject, some time of maturation, and several proof-of-concepts (the coupled linear oscillator example in Chapter 3, and an unpublished analysis of a top tensioned riser), I finally managed to reformulate the active truncation problem so that these modern UQ methods could solve it. It then became clear that the method could be generalized to address any CPEM. The final part of the work consisted in consolidating the method, and applying it to active truncation. A thank-you goes therefore to Giuseppe for introducing me to fascinating novel UQ tools.

I am thankful to my supervisor, Professor Asgeir Sørensen, who gave me the freedom to explore new paths, which made this journey particularly exciting. He also helped me to make strategic decisions in the course of this study, contributing to its success. His availability, despite his obligations as the director of NTNU AMOS, has been appreciated.

My collaboration with Dr Stefano Marelli in ETH/Zurich constitutes a cornerstone for this work. Stefano has been helping me to understand the inner workings of Adaptive Kriging (AK), and provided me with a beta version of the UQLab software, which could perform offline AK with multiple sample enrichment.

I am thankful to my co-supervisor Kjell Larsen (NTNU/Equinor) for providing me with a relevant case study, and in general, stimulating problems. Thanks to Dr Karl Erik Kaasen (SINTEF Ocean) and Professor Roger Skjetne (NTNU) for constructive comments during the mid-term evaluation of my work.

My employer SINTEF Ocean (formerly MARINTEK) is acknowledged for its support to NTNU AMOS, and for allowing me to allocate time to this PhD study. The support of Øyvind Hellan and Oddvar Eide in this respect has been appreciated.

In the course of the PhD study, I also had the opportunity to perform experimental work, both in a collaboration with PhD cand. Stefan Vilsen, and with members of the NOWITECH, HYBRID KPN and LIFES50+ projects: Valentin Chabaud, Erin Bachynski, Maxime Thys, Lars Ove Saether, Øyvind Magnussen, Lene Eliassen and Fredrik Brun. Working with such highly skilled colleagues has been a source of enjoyment and self-development.

Contents

Nomenclature

$\forall$	For all
$\exists$	There exists
$\mapsto$	Maps to
$\equiv$	Identically equal to
$\lceil \alpha \rceil$	Integer ceiling, i.e. smallest integer greater than or equal to α
$\lfloor \alpha \rfloor$	Integer floor, i.e. largest integer smaller than or equal to α
$\lvert \cdot \rvert$	Cardinality of a set, determinant of a matrix
$\sim$	distributed as
$\mathrm{E}[\cdot]$	Mathematical expectation
$\mathrm{P}[\cdot]$	Probability measure
$\mathrm{Var}[\cdot]$	Variance
$x^{(i)}$	Sample of the random vector X, for $i \in \mathbb{N}^*$
c_l, c_t	Longitudinal, transverse wave velocity
c_v	Coefficient of variation, see (5.3)
C	Global damping matrix in the FE method
C_m	Added mass coefficient
C_d	Drag coefficient
d	Slender structure's diameter
D	Water depth
E	Young modulus
E_{LOO}	Leave-One-Out cross-validation error, see Definition 8
f_i	State function, for $i \in \mathbb{N}_s^*$, see Section 3.1.1
h_i	Output function, for $i \in \mathbb{N}_s^*$, see Section 3.1.1
K	Global stiffness matrix in the FE method
	Number of samples generated by Adaptive Kriging
l	Scale (hyper-)parameter of the Matérn autocorrelation function, see (2.32)
L	Slender structure's length
m	Slender structure's mass per unit length
M	Dimension of input vector, or artefact parameter
	Global mass matrix in the FE method
n_{el}	Number of elements
N	Size of the set of evaluation points, training set, experimental design
p	Total degree of multivariate polynomials, see Section 2.2.2

P_f	Probability of failure
P_m	Probability of misclassification, see (2.52)
q	Pseudo-norm index for hyperbolic truncation sets, see Section 2.2.2
s	Number of substructures, Laplace variable
S_i	First-order Sobol' index, for $i \in \mathbb{N}_M^*$, see (2.28)
S_{ij}	Second-order Sobol' index, for $i, j \in \mathbb{N}_M^*$ and $i < j$, see (2.28)
$S_{T,i}$	Total Sobol' index, for $i \in \mathbb{N}_M^*$, see Definition 11
T	Duration of excitation
	Tension in the slender structure
w	Slender structure's submerged weight per unit length

α	Tuple of integers indexing multivariate polynomials ψ_α
	Truncation ratio
α_1, α_2	Rayleigh damping coefficients
β	Tuple gathering the coefficients a_α in a PCK model
γ_0, γ	Slender structure's orientation at its top end, and at the truncation point
γ_q	Selection/comparison functions used in the fidelity calculation, see Definition 19
δ	Confidence interval
δt	Synchronization time step in a co-simulation
Δ_{ij}	Artefact (see Definition 18)
$\epsilon_{ij}, \epsilon_v, \epsilon_F$	Tolerance values used in co-simulation
ϵ_i	Error indicator in the Convergence study
ϵ_{LOO}	Normalized Leave-One-Out cross-validation error, see (3.19)
$\varepsilon_{\mathrm{adm}}$	Maximum admissible probability of failure
θ	Artefact parameter (realization)
Θ	Artefact parameter (random variable)
λ	Scaling factor in hydrodynamic model testing
μ	Mean value
ν	Shape parameter of the Matérn autocorrelation function, see (2.32)
Φ	Standard normal cumulative distribution function
φ,φ_{adm}	Fidelity, see Definition 19, Minimum admissible fidelity
ψ_α	Multivariate polynomials forming a PCE basis, see Section 2.2.1
ρ	Water density
σ	Standard deviation
τ	Exogenous excitation

$\mathcal{D}_f$	Domain of failure
$\mathcal{E}$	family of evaluation points (also denoted training set, experimental design)
$\mathcal{F}$	values of the model at the evaluation points
$\mathcal{L}$	Limit state hypersurface, see Definition 16
$\mathcal{M}$	Function representing a complex model
$\hat{\mathcal{M}}$	Surrogate of the complex model $\mathcal{M}$
$\mathcal{N}(\mu, \Sigma)$	multivariate Gaussian distribution with mean μ and covariance matrix Σ
$\mathcal{R}$	Autocorrelation function
$\mathcal{U}(a, b)$	uniform distribution with support $[a, b]$

$\mathbb{I}_{\mathcal{S}}$	Indicator function, equal to one if the argument is in $\mathcal{S}$, and to zero else.
$\mathbb{L}$	Limit state margin, see (2.55)
$\mathbb{N}^*$	Natural integers excluding 0, i.e. $\{1, 2, 3, ..., \}$
$\mathbb{N}_Q$	Natural integers less than Q, i.e. $\{0, 1, ..., Q\}$
$\mathbb{N}_Q^*$	$\mathbb{N}_Q$ excluding 0, i.e. $\{1, 2, ..., Q\}$
$\mathbb{R}_+$	Real numbers greater than or equal to zero
ANOVA	Analysis Of Variance
CDF	Cumulative Distribution Function
CPEM	Cyber-Physical Empirical Method. Plural: CPEMs.
DOF	Degree Of Freedom
FE	Finite Element
FPSO	Floating Production Storage and Offloading unit
GRP	Gaussian Random Process
LAR	Least-Angle Regression
LHS	Latin Hypercube Sampling
l.h.s/r.h.s	left-hand side, right-hand side
MCS	Monte-Carlo simulations
PDF	Probability Density Function
PCE	Polynomial Chaos Expansion
PCK	Polynomial Chaos-based Kriging
QoI	Quantity of Interest. Plural: QoIs.
RQ	Research Question
UQ	Uncertainty Quantification
VIV	Vortex Induced Vibrations

Chapter 1

Introduction

1.1 Background

The word *empirical* derives from the Ancient Greek εμπειρία (empeiría) which means *experience*. Empirical methods enable researchers to gain knowledge about some system or phenomenon *through observation*. They constitute the cornerstone of most scientific fields, as they enable us to verify hypotheses, and to build models of the reality that surrounds us. These models may take the form of mathematical formulations or algorithms embedded in computer software.

A model is said to be *validated* when it is proven that it is capable of representing reality, from the perspective of the intended use of this model. As of today, in most fields of engineering, the development of new products heavily relies on validated models, while empirical methods are usually used when no validated model is available.

1.1.1 Cyber-physical empirical methods

In this thesis, we will define cyber-physical empirical methods as follows.

Definition 1. Cyber-physical empirical methods *(CPEMs) are empirical methods in which the dynamical system under study is partitioned into physical and numerical* substructures. *The behaviour of the physical substructures is partly unknown, while the numerical substructures are described by validated computational models. The substructures interact with each other through a* control system.

CPEM therefore augment classical empirical methods with validated numerical models, to address problems that classical empirical methods alone, or models alone, can not conveniently or reliably address. This is for example the case: (**Issue 1**) *when the dynamical system under study is "ill-conditioned"*, i.e. when it contains a large span of characteristic spatial dimensions and/or time constants. In that case, the part of the system that does not fit in the laboratory, or whose dynamics is slow, can advantageously be replaced by a numerical model. (**Issue 2**) *when scaling effects should be tackled.* Scaling laws, used in classical empirical methods, aim at preserving the balance, at small scale, between two effects that are known to be of importance for the full-scale system. When other effects, disregarded by the chosen scaling law, play an important role too, so-called *scaling effects* occur, which may reduce the confidence in experimental results. A cyber-physical empirical method alleviates this issue by isolating, in the numerical substructures, the parts of the system that cause scaling issues. (**Issue 3**) *when component testing should be performed,* that is when the focus is on the performance of a specific uncertain substructure, that is interacting with the other substructures as part of a complex system. When feasible, the latter are modelled numerically, which reduces the complexity of the laboratory test campaign. As we will see in the following examples, a CPEM can address several of these issues simultaneously.

1.1.2 Examples

CPEM have been concurrently developed and applied in earthquake engineering, mechanical engineering, electrical power engineering and, to a lesser extent, in other scientific fields. In the present section, we present some key application examples that illustrate the concept and purpose of CPEM. The first example is taken from the field of earthquake engineering, a field that has played a key role in the development and practical implementation of these methods (McCrum and Williams, 2016).

Example 1. *A multi-storey building is subjected to earthquake-induced ground motions. The efficiency of damage-mitigating devices such as magnetorheological dampers, located at the ground level of the building, is to be investigated. While numerical methods do not capture adequately the highly nonlinear and hysteretic behaviour of these devices, a purely empirical method consisting in constructing and shaking the whole building until collapse, would require unrealistically large infrastructures and resources.*

Carrion (2007) solved the problem by a CPEM as follows. The dynamic response of the building was simulated with the Finite Element (FE) method, while the damage-mitigating device was modeled physically. The simulated dynamic response of the building was prescribed to the damage mitigating

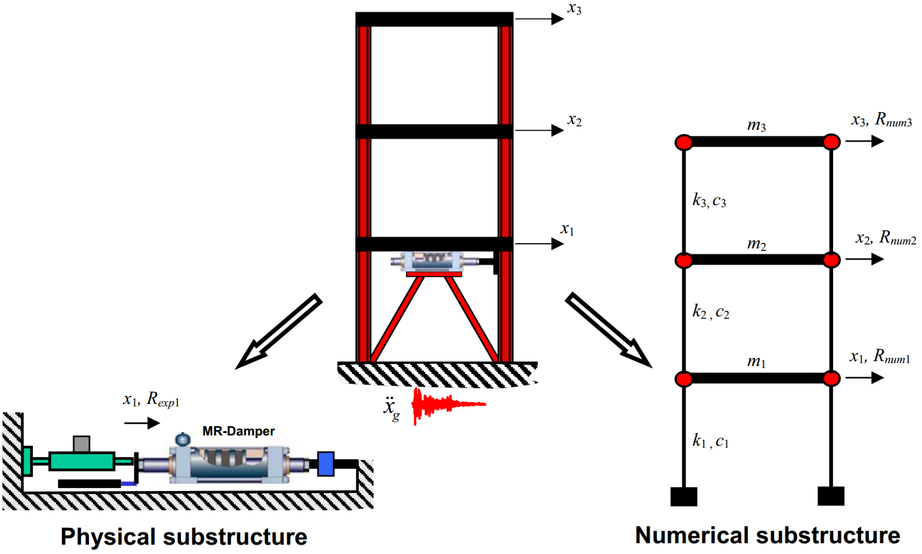

Figure 1.1: A CPEM to investigate how a magnetorheological damper mitigates the consequences of an earthquake (Carrion, 2007).

device by using large hydraulic actuators, and the resulting reaction force was fed back into the numerical model. See Figure 1.1.

The application of CPEMs to earthquake engineering was envisioned about 40 years ago by Takanashi et al. (1975), at a time in which simulation computers were not able to perform complex tasks in real-time. The first implementations of tests at a relevant seismic rate were reported in the 1990's by Nakashima et al. (1992) and Horiuchi et al. (1999). Since then, numerous developments and projects have been conducted in Japan, Europe, and in the United States (Shao and Griffith, 2013).

CPEM do also have applications in mechanical engineering, as illustrated by the following example.

Example 2. Lag dampers, *as represented in Figure 1.2a, are mechanical parts mounted between the hub of a helicopter and each of its blades. They damp the relative motion between the blade and the hub along the degree of freedom which is parallel to the ground. The dynamic properties of a lag damper have a significant effect on the vibrations of the helicopter, but are rather difficult to model numerically, due to hysteresis and complex valve dynamics. This constitutes a challenge for helicopter design.*

To alleviate this issue, the following CPEM was employed by Wallace et al. (2007) and Wagg et al. (2008). The blade, excited by forces from *steady-state flight conditions, was simulated by a modal approach, and the corresponding end vibrations (displacement at the blade root) were applied on a real lag damper as shown in Figure 1.2b. The measured reaction force was fed back into the numerical model. This test allowed to reproduce the vibratory behaviour of the whole blade/hub system, and could be used to adjust some design parameters of the lag damper.*

Beside aerospace engineering, CPEMs have been used in the automotive industry to develop engines (Filipi et al., 2006), car suspensions (Misselhorn et al., 2006), or more generally to investigate chassis dynamics and vibrations (Plummer, 2006). Thermomechanical test benches are currently under development to investigate fire-induced collapse of buildings, and thermomechanical loads on space crafts (Whyte et al., 2015) .

In both Examples 1 and 2, the numerical and physical substructures exchanged mechanical power. CPEM have also been used in power electrical engineering (Edrington et al., 2015), as exemplified in the following.

Example 3. *Fault current limiters (FCL) are devices that limit the electrical current when a fault occurs in a circuit. They feature low impedance at normal current levels and higher impedance at fault current levels. FCL operate in three-phase commercial power grids, and interact with the other power devices present on the network. Therefore, testing new FCL concepts such as the one depicted in Figure 1.3a, would require (1) rebuilding a surrounding power grid, and (2) manufacturing three prototypes, one acting on each phase of the grid.*

To simplify this setup, Naeckel et al. (2015) employed the CPEM whose principle is shown in Figures 1.3b and 1.3c. The FCL was interfaced to a simulator of the surrounding environment, including all types of devices which would be present in an actual grid environment. The voltage V_c between ① and ② in the simulated system (Figure 1.3b) was supplied as a voltage reference to a variable voltage source. The current I_{SFCL} and the voltage V_{SFCL} measured across the FCL were fed back into the simulator. To simulate the three-phase setup, variable impedance branches, whose properties are obtained from the FCL specimen, were inserted in series in the (simulated) two other phases of the system. See Figure 1.3c.

In this latter example, CPEM is typically aimed at performing component testing, i.e. at solving an issue of type 3 according to the list given in Section 1.1.1. This is somewhat the case also for Examples 1 and 2, but in those cases, the CPEM also solved an ill-conditioning issue (Issue 1), since performing such tests in a fully physical manner would have required an unrealistically large laboratory infrastructure.

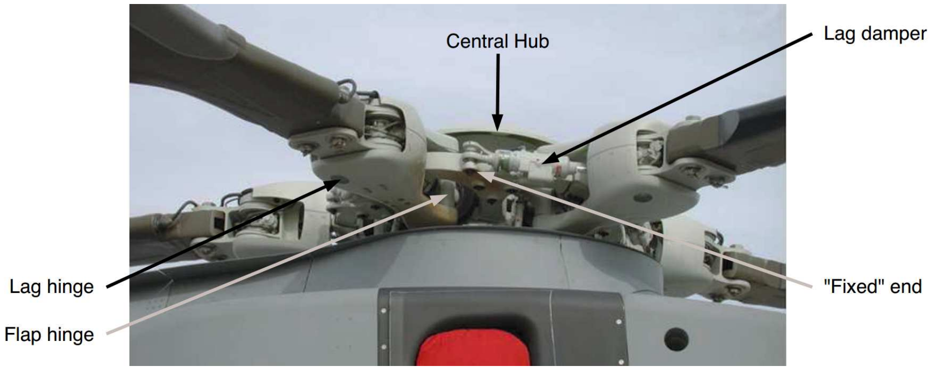

(a) Lag damper mounted between the blades and hub of a helicopter

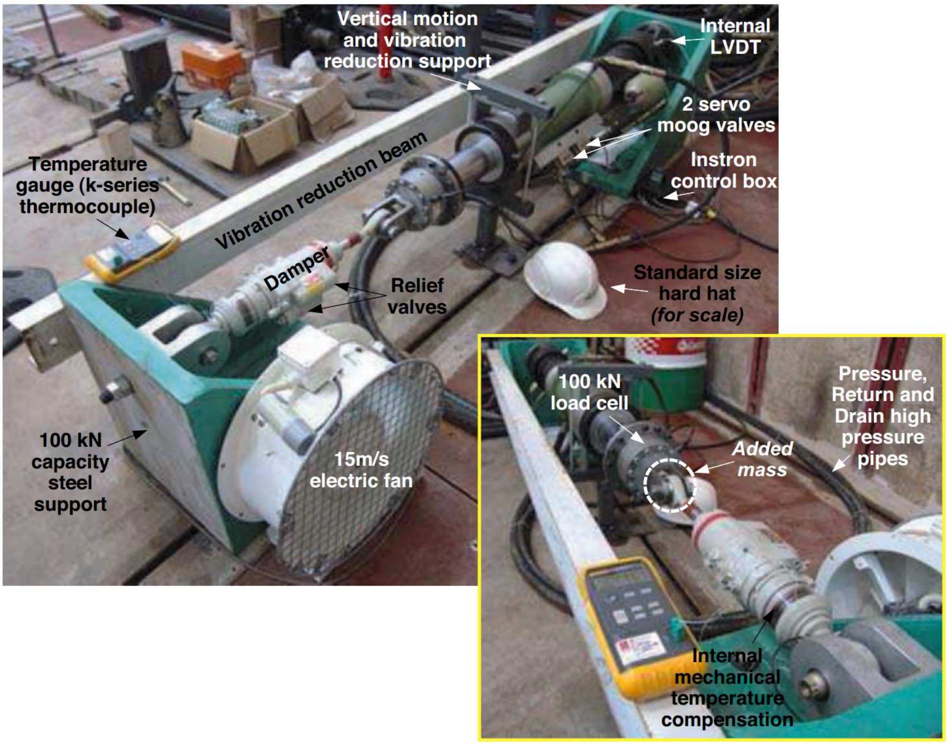

(b) Laboratory setup.

Figure 1.2: CPEM for the study of a helicopter's lag damper (Wagg et al., 2008).

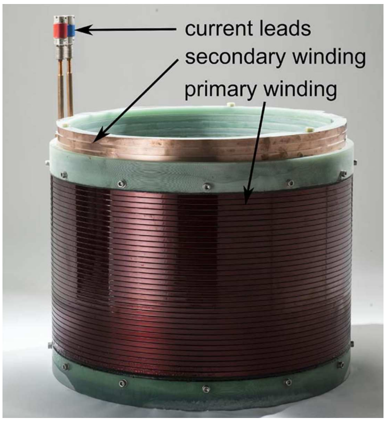

(a) Air coil superconducting fault current limiter (AC-SFCL). The primary winding (conventional conductor) is shielded by the secondary winding (superconductor), and thus conducts the nominal current with low impedance. In the event of a fault, the induced current in the secondary winding *quenches* the superconductor (it looses its superconductive property), and the sudden increase in resistance transitions the AC-SFCL to a high impedance state, which limits the fault current.

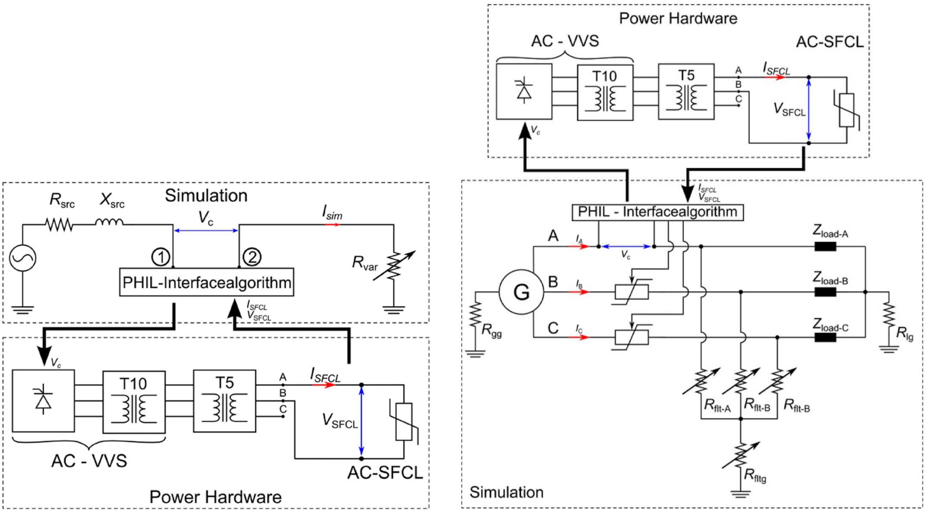

(b) One-phase setup

(c) Three-phase setup

Figure 1.3: CPEM for testing the Air Coil Superconducting Fault Current Limiter (AC-SFLC) represented in (a). Circuit diagrams for the one-phase case in (b) and for the three-phase case in (c). *PHIL* stands for Power Hardware in the Loop. *AC-VVS* represents a 5MW Alternative Current Variable Voltage Source. *T5* represents a three-phase transformer providing high currents (at a low voltage) to the AC-SFCL. All figures are from Naeckel et al. (2015).

It is also interesting to notice the very wide span of frequencies of importance in these three examples. Typical earthquake-induced ground excitation may reach some Hz, mechanical vibrations of interest for aerospace and automotive applications some tens of Hz, while the frequencies involved in power systems may reach tens of kHz. This sets stringent requirements on the computational efficiency of the *numerical* substructure. While a linear FE method could be used in Example 1, a truncated modal representation of the helicopter blade dynamics had to be used in Example 2. In Example 3, tailor-made hardware and software was used to run transient electromagnetic simulations models with a time step of 50 μs.

1.1.3 Examples of CPEM in marine technology

As of today, CPEM are not much used in marine technology. However, an important application which has been developed in the recent years is related to the study of offshore wind turbines (OWT). OWTs constitute complex dynamical systems, subjected to hydrodynamic and aerodynamic loads, and their global response is, in addition, strongly influenced by the controller regulating the generator output (Manwell et al., 2009; Goupee et al., 2014). When performing hydrodynamic model testing of an OWT, two major challenges arise. The first one is related to the poor quality of wind fields in hydrodynamic laboratories, as compared to wind tunnels (Wendt et al., 2017; Allen and Goupee, 2017). The second one is related to the incompatibility between Froude and Reynolds scaling laws[1]. Since gravity, inertia and viscous loads all have a significant effect on the response of an OWT, choosing one scaling law, and disregarding the other, leads to scaling effects and reduces the confidence in the experimental results (Issue 2).

Until recently, these two challenges have been addressed by improving wind generation capabilities in hydrodynamic laboratories, and by redesigning the rotors models with the aim to mimic full-scale aerodynamic loads (de Ridder et al., 2014; Martin et al., 2014, 2015). However, as noted by Allen and Goupee (2017), large uncertainties remain regarding the aerodynamic loads generated with such approaches.

Example 4. *Several research groups have developed CPEMs to enhance test of OWT in hydrodynamic laboratories. In such approaches, the numerical substructure consists of the rotor/nacelle assembly (RNA), so that*

---

[1] Reynolds scaling ensures a consistent balance between viscous and inertia loads at full-scale and model scale, which is important for the modeling of aerodynamic loads. Froude scaling ensures a consistent balance between gravity and inertia loads, in order to model correctly free-surface water waves, and resulting hydrodynamic loads. See e.g. (Journée and Massie, 2001, Appendix B)

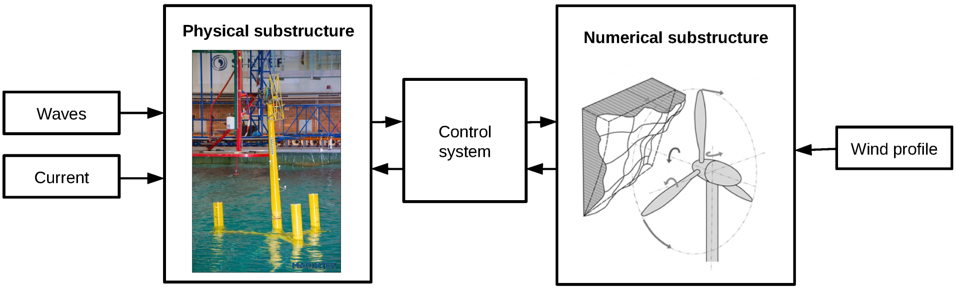

Figure 1.4: CPEM for the study of floating wind turbines. Adapted from Sauder et al. (2016).

aerodynamic loads are evaluated numerically, at full scale. The physical substructure consists of a physical model of the OWT (without RNA) installed in the hydrodynamic laboratory. See Figure 1.4. Since the wave loads are physical, Froude scaling is applied, and the (virtual) wind loads are scaled down accordingly. Azcona et al. (2014) and Oguz et al. (2018) applied these loads on the structure in real time using one or several on-board fans. Chabaud (2016) and Hall (2016) used parallel cable-driven robots (Pott and Bruckmann, 2015). This approach guarantees a consistent scaling of the problem, and a controlled (virtual) incoming wind field.

Note that CPEM have also been used to enhance wind tunnel testing of OWT (Bayati et al., 2014, 2017). In that case, the hydrodynamic loads are numerical and the aerodynamic loads physical. Zhang et al. (2016) also investigated, with a CPEM, the performance of a tuned liquid damper to mitigate tower vibrations of large wind turbines.

Another example from the field of marine technology, which will be further developed in this thesis, is related to the hydrodynamic testing of floating structures installed in ultra-deep water (Magee, 2018). Ultra-deep water refers in general to water depths greater than 1500m. When attempting to study the behaviour of such floating systems in existing hydrodynamic laboratories, Issue 1 is faced since the characteristic dimensions of importance for the problem span four orders of magnitude: the diameter of a mooring line or a riser is less than 1m, wave heights are of the order of 1-10m, the length of the floating structures is 10-100m, and the water depth is of the order of 1000-6000m. This ill-conditioning makes the choice of an adequate scaling factor difficult, and modeling such systems at a reasonably large scale in any of the existing hydrodynamic laboratories is unfeasible due to space constraints.

Example 5. *A CPEM envisioned in the late 1990's to test floating structures in ultra-deep water is called* active truncation *(ITTC, 1999). It consists in modelling physically, at a reasonably large scale, the upper part of the mooring and riser system, together with the floating production unit. The lower part of the mooring and riser system, connected to the seabed infrastructure, is simulated on a computer. See Figure 1.5. The substructures interact at the truncation point through sensors and actuators located on the floor of the hydrodynamic laboratory.*

Cao and Tahchiev (2013) and Sauder et al. (2017, 2018) investigated the feasibility of this method through simulation studies, and it has been considered as a possible testing method by the International Towing Tank Conference (ITTC, 2017) since 1999. It has however never been fully implemented in practice.

Other examples of applications of CPEM in marine technology include studies on the acoustic footprint of ships (Botelho and Christenson, 2014), verification of software and hardware components used in power management systems (Zhu et al., 2005; Yum, 2017) and in dynamic positioning systems (Sørensen, 2011).

1.1.4 A note about terminology

The terminology associated with CPEM is rather discordant across the different fields in which they are used. In earthquake engineering for instance, the term *hybrid simulations* (Nakata et al., 2014a) and *hybrid testing* (McCrum and Williams, 2016) have been coexisting for decades, reflecting two different points of view of the same method. In most cases, the chosen terminology relates to concepts and terms that were in use *before* cyber-physical approaches were introduced. In mechanical engineering, the term *real-time dynamic substructuring* is often used. It stems from the term *dynamic substructuring*, which is employed in computational mechanics when part of a complex FE model is substituted by a reduced-order version of it (De Klerk et al., 2008). In marine hydrodynamics, the terminology *real-time hybrid model testing*[2], was chosen by SINTEF Ocean to emphasize the connection to classical hydrodynamic *model testing*, and with the terms *real-time* and *model* emphasizing the fact that the involved simulations must run in Froude-scaled real-time (Sauder et al., 2016).

Some researchers have made a distinction between the above-described CPEM and the concept of *Hardware-In-the-Loop* testing (HIL) used to verify controllers in the automotive or marine industry (Wagg et al., 2008; Edrington

---

[2] abbreviated ReaTHM® testing, a registered trademark of SINTEF Ocean AS

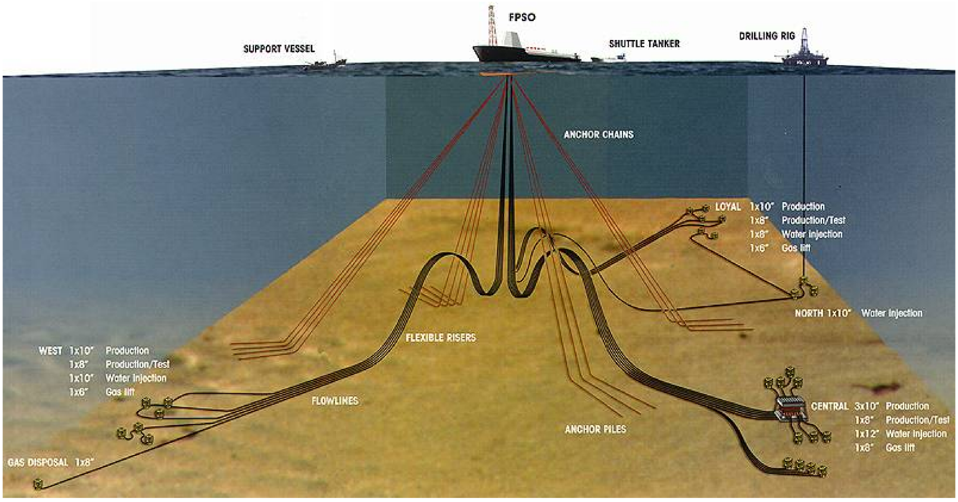

(a) A typical deep water development, including an FPSO unit, subsea equipment, and a set of slender marine structures such as mooring lines and flexible risers. From http://www.offshore-technology.com/

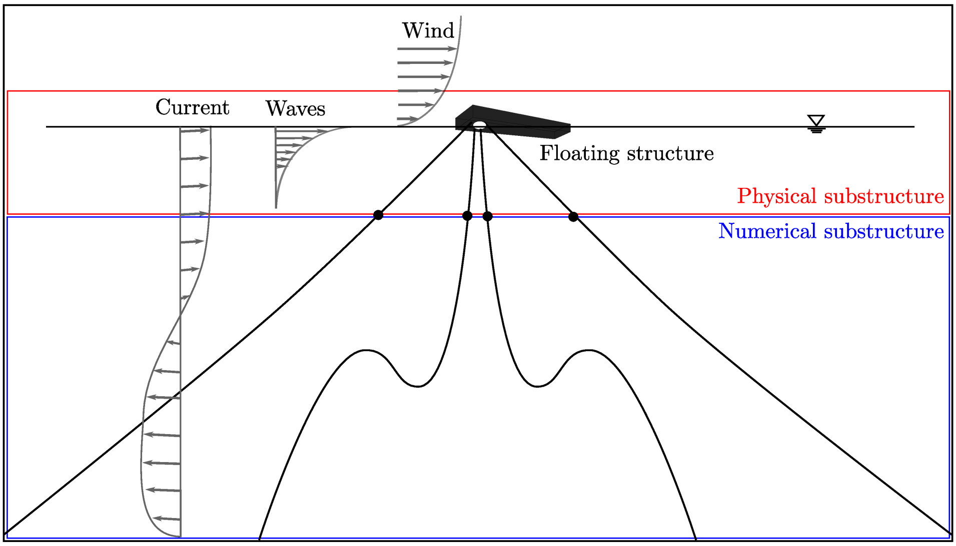

(b) Principle of active truncation

Figure 1.5: CPEM to study floating systems in ultra-deep water.

et al., 2015). They argue that the discriminating criterion between the two approaches is the amount of power exchanged between the substructures. Indeed, when using HIL to verify controllers (Sørensen, 2011; Skjetne and Egeland, 2006), only signals with low voltage and current are exchanged at the interface between the numerical and physical substructures. In Examples 1-5 outlined above, a significant amount of mechanical or electrical power must be transferred through actuators or amplifiers, which have their own dynamics. This indeed leads to specific challenges, as we will see in the next sections.

The present work will focus on the *control system* that interconnects the physical and numerical substructures. We therefore chose to use the terminology *cyber-physical* empirical methods, since it is under this denomination that the control engineering community addresses issues related to "the close interactions and feedback loop between the cyber components, such as sensing systems, and the physical components, such as varying environment and energy systems." (IEEE CPS, 2018). The results presented herein can of course be exploited in all the scientific fields using CPEM, regardless of the used terminology.

1.1.5 Definitions and important concepts

The following terms, illustrated in Figure 1.6, will be employed throughout this thesis.

Definition 2. *The* real system *is the subject of the study, whose performance under given load conditions should be documented. See Figure 1.6a.*

Definition 3. *The performances of the real system are quantified through* Quantities of Interest (QoI) *derived from the* response *of the system. See Figure 1.6a.*

Definition 4. *The set of numerical and physical substructures form the* substructural partition*. See Figure 1.6c.*

Note that in Figure 1.6c, we have assumed that the substructural partition consists of one numerical substructure and one physical substructure. However, substructural partitions may contain several specimens of each class.

Defining the substructural partition may be straightforward, given the problem at hand. In Example 4 for instance, the rotor-nacelle assembly is modeled numerically, since modeling it physically would cause scaling issues. In other cases, the choice of a substructural partition is constrained

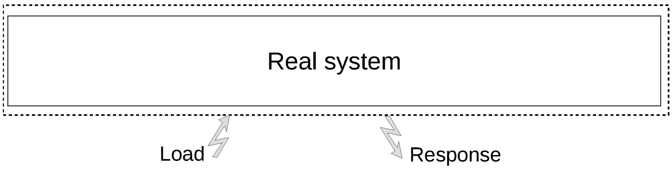

(a) Real system

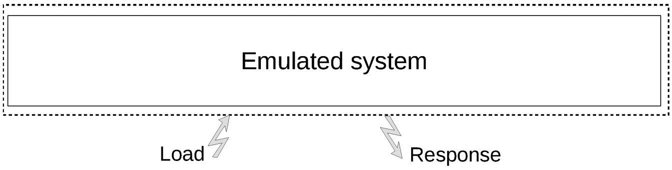

(b) Emulated system

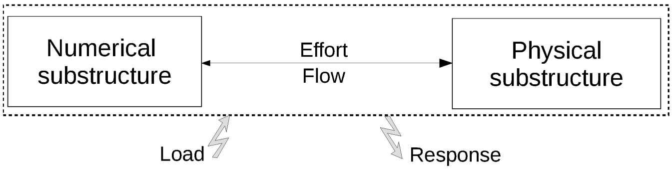

(c) Substructured system

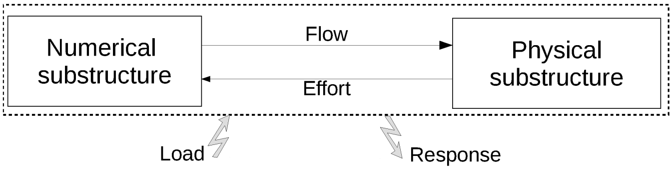

(d) Choice of a control strategy

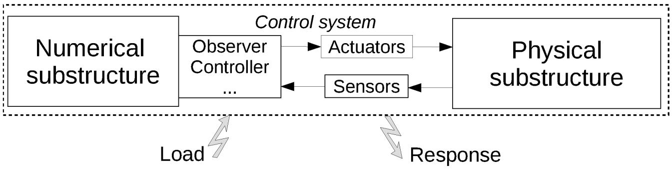

(e) Substructured system and control system.

Figure 1.6: Concepts and terminology used in the design and analysis of generic CPEM.

by the capabilities of the physical and computational infrastructures. In Example 5, the location of the truncation point is related to the available depth of ocean basin, and to the fact that the truncated part of the slender marine structures must be simulated in Froude-scaled real-time. Finally, methods have been suggested to optimally define the substructural partition when elements such as an inertia should be split between the numerical and physical substructures (Plummer, 2006; Gawthrop et al., 2009).

As illustrated in Figure 1.6c, the power, continuously exchanged between the members of the substructural partition, can be modeled as the product of a *flow* and an *effort* (Gawthrop et al., 2005). For example, in a translatory mechanical system, the flow is the linear velocity, while the effort is the force. For an electrical system, the flow is the electrical current, and the effort the voltage. The flow and the effort are said to be *dual* of each other. *Compatibility* between two substructures is achieved when the sent and received flows are equal at each instant, and similarly, *equilibrium* refers to the consistency of the efforts.

Definition 5. *The* control system *consists of hardware components (such as sensors, actuators, computers and network infrastructure) and software components (such as observers, controllers and allocation algorithms), which aim at ensuring compatibility and equilibrium between the substructures. See Figure 1.6e. Note that the control system is not part of the substructural partition.*

An important choice to be made during the control system design is *whether effort or flow will be actuated* on the physical substructure. The dual quantity must then be measured or estimated through a sensor system. In the case depicted in Figure 1.6d, the actuator is flow-controlled, and the effort is measured and used as an input to the numerical substructure. This control strategy may be dictated by stability considerations (Gawthrop et al., 2009), but also by practical issues. Off-the-shelf mechanical actuators are indeed usually delivered with well-performing *flow* controllers. In earthquake engineering the vast majority of tests use flow actuation, and only a few use effort control, see e.g. (Bousias, 2014).

1.2 Motivation

We have in the previous section, extensively described how CPEM constitute an improvement to classical empirical methods. Let us now recall that the very purpose of empirical methods is to gain knowledge about the behaviour of some system through *observation of this system.* When using a CPEM, we do not observe the *real* system (Figure 1.6a), but a substructured version of it, orchestrated by a control system (Figure 1.6e). A legitimate question is then whether the observations generated with this system, actually are representative of those we would have obtained with the real system. Only if this is the case, new knowledge about the real system can be inferred from these observations.

To support our discussion, we will define, in line with Gross (1999) and Nakata et al. (2014b), and loosely for now, the notion of *fidelity* as follows.

Definition 6. *The* fidelity *of a CPEM refers to the degree to which it reproduces the behaviour of the real system under study.*

The following statement can then be made regarding CPEMs.

High fidelity constitutes a fundamental requirement for CPEMs to be considered as valid empirical methods.

1.2.1 Loss of fidelity

Fidelity may be jeopardized by factors which are related to each component of the CPEM represented in Figure 1.6e, and which we will discuss in the following.

First of all, the *physical substructure* may differ from the corresponding part of the real system. This would typically be the case in most marine hydrodynamics experiments, such as the ones presented in Examples 4 and 5, when the physical substructure is included at reduced scale. Loss of fidelity could then occur due to model manufacturing issues (erroneous geometry, structural properties and mass distribution), or to scaling effects induced by a too low Reynolds number. How these issues affect the QoI in marine hydrodynamics has been discussed for classical experiments by Qiu et al. (2014) and Steen (2014), and the references therein.

Then, as stated in Definition 1, a requirement to the *numerical substructures* is their verification and validation (Hills et al., 2015; ASME (ed.), 2016) for the purpose of the study. (1) Fidelity loss can occur if the numerical substructure operates outside its domain of validity. For example, if a modal description of the real system is used in the numerical substructure, neglecting higher-order modes will typically cause errors if excitation occurs at a frequency range near the eigenfrequencies of the truncated modes (De Klerk et al., 2008). Similarly, when using neural networks as numerical substructures, as done by Christiansen (2014), one should ensure their input remain within the domain the network has been trained for. (2) Loss of accuracy due to an inadequate time stepping procedure may also occur.

Adequate partitioned schemes have been developed when the members of the substructural partition are tightly coupled (Bursi et al., 2013). (3) Numerical substructures that do not succeed in running in hard real-time could cause loss of fidelity due to desynchronization with the physical substructures (Vilsen et al., 2017). (4) The numerical substructure is in principle considered to be deterministic, which is beneficial when sources of randomness should be isolated in the physical substructure. In reality, there may be uncertainties in some parameters of the numerical substructure, which may have to be accounted for (Abbiati et al., 2015).

As depicted in Figure 1.6, the performance of the real system is investigated by considering its response (through the QoIs), when it is subjected to a given *loading scenario*. Fidelity may be jeopardized if the loading, acting on either the numerical or physical substructures, differs from the loading applied to the real system. In marine hydrodynamics, the quality of the laboratory infrastructure will dictate the accuracy of the (physical) wave and current loads (Qiu et al., 2014). The modeling of the loading acting on the *numerical* substructures is subjected to the validity requirements described in the previous paragraph.

In the present work, we will focus on the *control system* that interconnects the substructures. As stated in Definition 5, the control system aims at maintaining compatibility and equilibrium between the substructures. On a high level, this implies (1) a proper measurement of the flow or effort, (2) a proper transfer of this quantity to the numerical substructure, and (3) a proper actuation of the dual quantity. Loss of fidelity can then be the result of poor sensing (e.g. biases or erroneous gains in transducers), poor actuation (e.g. actuator dynamics, backlash in transfer mechanisms), communication- and processing-induced time delays, and poorly designed observers or controllers, among others.

Remark 1. *In most application of mechanical engineering, the real system under study is a stable dynamical system, in the sense that its response remains bounded when it is subjected to a bounded load. However, for reasons we will outline shortly, the stability of a corresponding CPEM is not granted. Because of the safety issues and economical losses that instability of such a setup could cause, stability has received a particular attention from researchers working with CPEM. It is, however, important to stress that* stability is not sufficient to guarantee fidelity.

1.2.2 Analysis of the control system's effect on fidelity

Following the control engineering terminology, fidelity is a *performance* indicator. The effect of the control system on fidelity can be studied by various approaches, the choice of which depends on (1) the way the control system is modeled, (2) the way the physical and numerical substructures are modelled, and (3) the choice of indicators representing the fidelity. We will detail this in the following.

Model of the control system First of all, the perturbations introduced by the control system may be of very different natures, and we will therefore use the generic term of *artefact*[3] to describe such perturbations in a generic manner. Actuator dynamics is, for example, a type of artefact that is often studied by modeling the actuator as a linear dynamical system, inducing a magnitude and phase tracking error. See for instance Jung and Benson Shing (2006); Ren et al. (2009); Gao et al. (2013); Maghareh et al. (2014); Drazin et al. (2015); Stoten (2017); Hall et al. (2017). The fidelity loss induced by incomplete actuation (the fact that some components of the effort to be actuated are simply neglected) has been studied by a simulation-based method in Bachynski et al. (2015). Noise, at the sensor or actuation level, is another type of artefact, which can be addressed for simple systems by using Stochastic Differential Equations (Øksendal, 2003). However, for industrial applications, frequency domain approaches (Ren, 2007; Ren et al., 2009) or simulations are mostly used (Mosqueda et al., 2005; Hall et al., 2017). Similarly, the effect of time delays in CPEM has been studied analytically for simple cases by Maghareh et al. (2014) and Kyrychko et al. (2006), and by simulations in other cases (Mosqueda et al., 2007b; Chabaud, 2016; Hall et al., 2017). Research performed on the security of generic cyber-physical systems (Humayed et al., 2017) has given birth to a wide range of methods to analyze the consequences of manipulating of the signals exchanged between the substructures (Pasqualetti et al., 2013; Fawzi et al., 2014). While this field of research leads to relevant methods to study some types of artefacts, security itself is in general not an issue for CPEMs, since they generally operate on closed networks, and for a very limited amount of time.

Models of the substructures When analyzing a CPEM, a distinction should in principle be made between the numerical substructures, which by definition consist of discrete-time systems, and the physical substructures which are considered in this thesis as continuous systems. From a control per-

---

[3] We will introduce a formal definition of this term in Chapter 3.

spective, these two classes of systems are treated in a radically different way, and there are ongoing efforts to develop unified frameworks to study generic cyber-physical systems (Tabuada et al., 2014). However, in the particular case of CPEM, the numerical substructures aim at representing continuous dynamical systems, and have therefore been treated as continuous systems by the majority of researchers, who could then apply the vast set of available tools to study continuous systems. Modelling the substructures as linear systems further simplifies the fidelity analysis. This, for instance, enables an investigation by frequency domain approaches of how uncertainties related to the control system propagate through the substructures (Voormeeren, 2007; Chabaud, 2016). Analysis methods have been proposed when physical substructure exhibit bounded and smooth nonlinearities (MacDiarmid and Bacic, 2007).

Fidelity indicator A final parameter dictating the choice of the fidelity analysis method is the way fidelity is quantified. In many cases, it is assumed that the main source of fidelity loss in the control system is the actuator, and it is only sought to achieve a satisfactory reference tracking at the interface. Some corresponding performance criteria are summarized in Nakata et al. (2014b). Alternative indicators have been developed which are based on the error in the transferred energy (i.e. flow *and* effort) between the substructures (Mosqueda et al., 2007a; Ahmadizadeh and Mosqueda, 2009; Maghareh et al., 2014). Instead of focusing on the interface, a radically different approach is to compare the QoI evaluated, on the one hand, from a model of the CPEM including the control system, and on the other hand, from what we refer to as the *emulated system*, defined as follows:

Definition 7. *The* emulated *system consists of a validated model or, by default, the best available* model*, that describes the behaviour of the real system. See Figure 1.6b.*

This approach, used for example by Ren (2007) and Bachynski et al. (2015), intrinsically accounts for the possibly complex interaction between the control system and the substructures, but it requires a good model of the latter. Finally, an approach in which the fidelity is formulated as an cost function penalizing error on the QoI *and* on the actuator input has been suggested by MacDiarmid et al. (2008).

1.2.3 Limitations

We will illustrate some limitations of the existing fidelity analysis methods by considering the following motivating example.

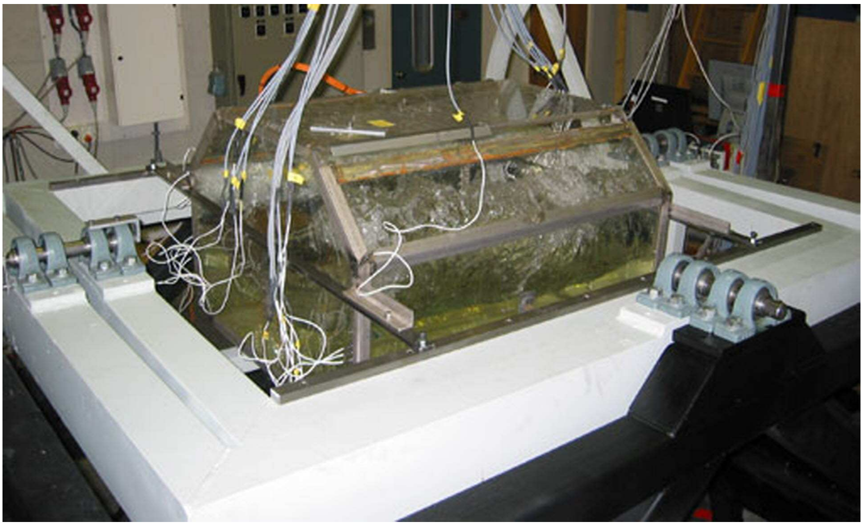

Figure 1.7: Test bench to study sloshing in a prismatic tank. The cradle prescribes ship-induced motions to the tank. Pressure gauges, connected to the visible light grey wires, measure local pressures during liquid impact on the tank walls. Courtesy of SINTEF Ocean.

When transported in ships, Liquefied Natural Gas (LNG) will slosh inside the ship's tanks, which may lead to slamming on the tank walls and possibly damage the LNG containment system (Faltinsen and Timokha, 2009). Sloshing impact is a very complex phenomenon, in which local pressures (very short duration) are strongly influenced by global motions of the fluid in the tank (much larger characteristic time scales), among other parameters. To investigate this phenomenon, a reduced-scale model of the tank is instrumented with a large amount of pressure sensors, and precalculated ship-induced motions are prescribed to the tank, see Figure 1.7. An issue with this approach is that it does not account for the fact that the global loads induced by sloshing *influence the ship motions* (Rognebakke and Faltinsen, 2003). This two-ways coupling will in turn influence the resulting impact pressures.

Example 6. *To properly account for the effect of global sloshing loads on the ship motions, the following CPEM is envisioned. The physical substructure consists of LNG tank, and the numerical substructure is the ship. The measurement of reaction forces at the tank is fed into the ship simulation, and the derived ship-induced motions of the tank are prescribed to the tank in real time, using a test bench as shown in Figure 1.7.*

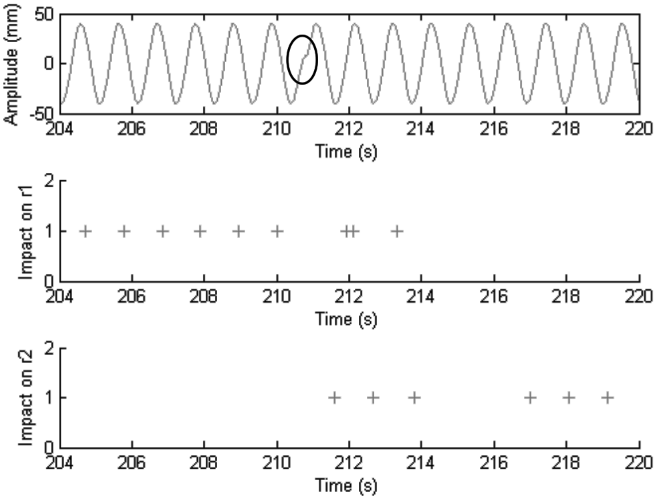

Figure 1.8: Bifurcation phenomena observed during a sloshing test. Due to the minor imperfection in the applied position (top), the occurrence of impact switches from panel `r1` on one side of the tank, to panel `r2`, on the other side of the tank (see middle and bottom plots). Figure originally published in Loysel et al. (2012).

However, results reported by Loysel et al. (2012) let us anticipate that performing such study *with high fidelity* may be delicate. In this study, a tank was undergoing (pregenerated) harmonic oscillations parallel to its largest dimension. The tank was equipped with two sets of pressure sensors, located on either side of the tank, referred to as `r1` and `r2`, respectively. The objective was to establish extreme value statistics of the impact pressure on each panel. For a given amplitude and frequency of the prescribed motions , the fluid in the tank exhibited a non-symmetric sloshing response: the fluid would almost always impact on the same panel r1, despite the symmetry of the prescribed motions. This phenomenon is described as sub-harmonic oscillations. During one repetition of the test, a one-off small variation of the motion, compared to the harmonic reference, occurred, as shown in the upper plot in Figure 1.8. It led to a switch of the impacted panel from `r1` to `r2` as shown in the lower plots in Figure 1.8. This bifurcation is explainable by the nonlinear properties of the system, and by the fact the tested condition excited mainly an unstable mode. The consequences on on the QoI (statistical properties of the pressure on `r1` and `r2`) were significant. See Loysel et al. (2012) for more details.

In that case, the control system did not involve the feedback loop envisioned in Example 6. But the described observations enables us to flag very important points regarding the fidelity assessment of this particular CPEM. (1) A nonlinear model should be used to describe the behaviour of the physical substructure (tank and sloshing fluid), in order to capture such bifurcation phenomena. (2) The fidelity should be evaluated based on the actual QoI (statistical parameters for the pressure on the tank wall), and not based on the actuator's performance, since there is in this case no continuity, in a mathematical sense, between the two quantities. (3) Investigating the effect of control system issues should not be limited to time delays and actuator frequency response performance. Other types of events, such as the unlikely glitch observed in the displacement signal actuator control, should be included, if they cannot be eliminated.

To the author's knowledge, none of the method described in Section 1.2.2 would allow us to analyze the fidelity of such a setup. Approaching the problem by combining analytical approaches such as Stochastic Differential Equations (Øksendal, 2003), Delay Differential Equations (Kyrychko and Hogan, 2010), or the Networked Control Systems theory (Hespanha et al., 2007) to address simultaneously the effect of noise, time delays, or jitter, respectively, would lead to formulations that are difficult to apply to practical industrial problems.

1.3 Outline of this thesis

In this chapter, we have introduced the notion of CPEM, and stated that they must be proven to be of sufficiently high *fidelity* in order to represent a valid alternative to purely empirical methods. In the previous section, we have outlined existing methods to analyze how the control system could affect the fidelity. We also pointed out the following limitations of these methods. (1) *Heterogeneous* types of artefacts may occur simultaneously leading to problems which become intractable by purely analytical methods. (2) Artefacts may be non-deterministic, such as sporadic signal loss (3) The artefacts may interact with substructures that exhibit a complex behaviour, which should be modeled properly.

1.3.1 Research questions

The present thesis addresses the design and analysis of CPEMs, and attempts to answer the following research questions.

RQ 1 How can the designer of a CPEM identify *artefacts that play a significant role for the fidelity*? Such information would enable the designer of the setup to focus his/her efforts on specific aspects of the control system, and leave out those of lesser importance.

RQ 2 Can *robust fidelity* of a given CPEM be proven? In other words, can the designer of a CPEM guarantee that no significant loss of fidelity would occur due to artefacts that are likely to be introduced by the control system?

RQ 3 Can *absolute bounds* be defined on these artefacts within which sufficiently high fidelity would be guaranteed? On the one hand, this would provide specifications/requirements to the control system. On the other hand, this would allow an *a posteriori* analysis of a CPEM to confirm its sufficiently high fidelity.

1.3.2 Scientific contributions

The original scientific contributions presented in this thesis are the following.

1. We provide, in Section 3.1, a unified and quantitative definition of the fidelity of a CPEM, which fits to a wide class of applications.
2. We present in Section 3.2 a method to systematically identify and rank the control system-induced artefacts that jeopardize the most the fidelity (sensitivity study). This information is of great operational relevance when designing a CPEM.
3. We also develop in Section 3.2 a framework to verify the *probabilistic robust fidelity* of cyber-physical empirical setups, and to derive *fidelity bounds*, which can be used as specifications to the control system. Our framework constitutes an improvement as compared to existing analysis methods for the following reasons. (1) The method is non-intrusive, and thus not limited to analytic models, which allows its application to the wide class of dynamical systems represented in CPEM. (2) It can handle an arbitrary *number* and *type* of artefacts, which exhibit parametric uncertainty. (3) It is based on surrogate modelling and active learning techniques to achieve computational efficiency, even for high-dimensional and high-reliability problems.
4. In the second part of the thesis, we investigate the fidelity of active truncation of slender marine structure using the developed methods (Chapter 5). We provide useful insight in the design of such setups, of interest in marine technology research.

5. Finally, at a more general level, this work establishes a bridge between the modern methods for uncertainty quantification, control engineering and marine technology. It is in particular expected that the proposed method can be applied to a much wider class of robust control problems (with parametric uncertainties) than those related to CPEM.

Some of the results reported in this thesis have been published in the following papers.

Paper 1 Sauder, T., Sørensen, A. J., and Larsen, K. (2017). Real-Time Hybrid Model Testing of a Top Tensioned Riser: A Numerical Case Study On Interface Time-Delay and Truncation Ratio. In *ASME 2017 36th International Conference on Ocean, Offshore and Arctic Engineering*, Trondheim, Norway

Paper 2 Sauder, T., Marelli, S., Larsen, K., and Sørensen, A. J. (2018). Active truncation of slender marine structures: Influence of the control system on fidelity. *Applied Ocean Research*, 74:154–169

Paper 3 Sauder, T., Marelli, S., and Sørensen, A. J. (2019). Probabilistic Robust Design of Control Systems for High-Fidelity Cyber-Physical Testing. *Automatica (accepted for publication)*

In the course of this PhD study, the author also contributed to the practical design, execution and analysis of cyber-physical experiments. These experiments constitute an important background for this thesis: they were a source of insight into practical realization of CPEMs, and nourished the developments presented here.

The first set of experiments were performed in collaboration with PhD candidate Stefan Vilsen, presently with SINTEF Ocean. The objective was to design a CPEM in which the numerical substructure was a Finite Element code, simulating the behaviour of mooring lines[4] in real-time. The physical substructure was a simple cylindrical floater, representing an oil&gas production unit, or a a fish farm. The author was responsible for the hardware and software architecture, development of several components of the control system (allocation and prediction modules, among others), and took an active part in the execution of the tests. This work was reported in the following publications.

---

[4] As opposed to Example 5, developed in this thesis, the mooring lines were not truncated, but fully replaced by their numerical counterparts.

Paper 4 Vilsen, S., Sauder, T., and Sørensen, A. J. (2017). Real-time hybrid model testing of moored floating structures using nonlinear finite element simulations. In *Dynamics of Coupled Structures*, volume 4 of *Conference Proceedings of the Society for Experimental Mechanics Series*, pages 79–92. Springer International Publishing

Paper 5 Vilsen, S., Sauder, T., Føre, M., and Sørensen, A. J. (2018). Controller analysis in real-time hybrid model testing of an offshore floating system. In *ASME 2018 37th International Conference on Offshore Mechanics and Arctic Engineering*, Madrid, Spain

Paper 6 Vilsen, S., Sauder, T., Sørensen, A. J., and Føre, M. (2019). Method for Real-Time Hybrid Model Testing of Ocean Structures: Case Study on Horizontal Mooring Systems. *Ocean Engineering (accepted for publication)*

The second set of experiments were aimed at investigating the behaviour of floating wind turbines subjected to combined wind, current and wave loads. A CPEM was used to address the Froude-Reynolds scaling conflict, as discussed in Example 4. The practical implementation of this CPEM started with the research reported in Chabaud (2016), and has then been further developed by a joint NTNU and SINTEF Ocean team. It has now reached a high level of maturity and has a significant influence on the way model testing of floating wind turbines is performed worldwide. The publications listed below have resulted from this work. The author has taken an active part in the development of this CPEM and in the execution of the tests reported in these publications.

Paper 7 Sauder, T., Chabaud, V., Thys, M., Bachynski, E. E., and Sæther, L. O. (2016). Real-time Hybrid Model Testing of a Braceless Semi-submersible Wind turbine. Part I: The Hybrid Approach. In *ASME 2016 35th International Conference on Ocean, Offshore and Arctic Engineering, No OMAE2016-54435*

Paper 8 Bachynski, E. E., Thys, M., Chabaud, V., Sauder, T., and Sæther, L. O. (2016). Real-time Hybrid Model Testing of a Braceless Semi-submersible Wind turbine. Part II: Experimental Results. In *ASME 2016 35th International Conference on Ocean, Offshore and Arctic Engineering, No OMAE2016-54437*

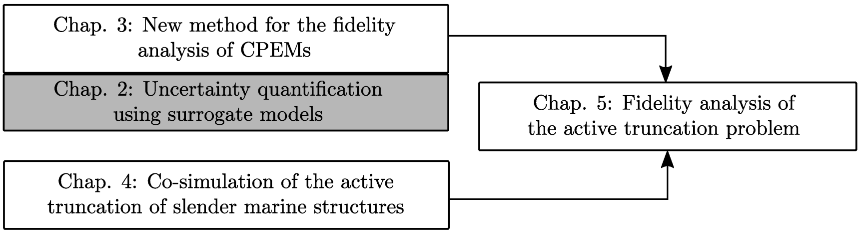

Figure 1.9: Structure of the thesis

Paper 9 Chabaud, V., Eliassen, L., Thys, M., and Sauder, T. (2018). Multiple-degree-of-freedom actuation of rotor loads in model testing of floating wind turbines using cable-driven parallel robots. *Journal of Physics: Conference Series*

Paper 10 Thys, M., Chabaud, V., Sauder, T., Eliassen, L., Sæther, L. O., and Magnussen, O. B. (2018). Real-time hybrid model testing of a semi-submersible 10 MW floating wind turbine, and advances in the test method. In *ASME 2018 1st International Offshore Wind Technical Conference*, San Fransisco

1.3.3 Limitations of the scope

We limit the scope of the present work to the study of the *control system* interconnecting the substructures of a CPEM. As outlined in Section 1.2.1, there are sources of errors and uncertainties related to the physical and numerical substructures themselves which may have a detrimental effect on the fidelity. For the purpose of the analysis, we will assume the existence of a sufficiently high-fidelity model of the physical substructures, running in engineering time.

1.3.4 Structure of the thesis

The thesis is organized as indicated in Figure 1.9. Chapter 2 provides the necessary theoretical background on selected surrogate modeling techniques, which can advantageously be used to address our research questions. Chapter 3 then describes the proposed framework for the fidelity analysis of CPEMs. In Chapters 4 and 5, this framework will be applied to the study of active truncation of slender marine structures, already evoked in Example 5. Chapter 6 will conclude on the proposed general method, and will propose some directions for further work.

Chapter 2

Uncertainty quantification using surrogate models

2.1 Introduction

This chapter presents the mathematical foundations of the tools that will be used to address our Research Questions (RQ). We first introduce, independently, the subjects of uncertainty quantification and surrogate models. We will then show, in Section 2.2, how polynomial chaos expansions can be used to conveniently perform *uncertainty propagation* and *global sensitivity analysis*, which will prove useful in addressing RQ1. Then, in Section 2.3, we will outline how *reliability analyses*, related to RQ2 and RQ3, can be conducted by combining polynomial chaos-based kriging surrogate models with active learning techniques.

Note that the present chapter is not meant to treat the subject of surrogate modeling for uncertainty quantification in an exhaustive manner, but rather to introduce the important concepts and tools which will be used in Chapter 3. Only demonstrations which contribute to the understanding of the subject will be given. For more details, the interested reader is encouraged to consult Santner et al. (2003); Sudret (2007); Saltelli (2008) and Lemaire (2009), which have been our main references, as well as more specific references which will be cited in the text.

2.1.1 Uncertainty quantification

The actual performance of engineered systems may differ from their nominal performance predicted during design, due to epistemic and aleatory uncertainties. The former refer to our lack of knowledge about some influencing phenomena while the latter is due to the natural variability of these phenomena. In automatic control, this fact has given birth to the field of robust control (Zhou et al., 1996), studying how stability and/or performance of a dynamical system can be achieved in spite of perturbations that are unknown, but generally assumed bounded. Robust control methods, such as H_∞ loop shaping or sliding mode controllers (Khalil, 2014, Chapter 10), are now routinely used in controller design to cope with such uncertainty.

The field of *uncertainty quantification* (UQ), situated at the intersection of mathematics and statistics, addresses these issues at a more general level. It aims at modeling uncertainty in a quantitative manner, studying how it propagates through functions, and providing tools to reduce it. For illustration, let us consider the following, formally defined, mapping $\mathcal{M}$ linking an M-dimensional input x to a one dimensional output y:

$$\begin{aligned} \mathcal{M}: \quad & \mathcal{D} \to \mathbb{R} \\ & x \mapsto y \end{aligned} \tag{2.1}$$

where $\mathcal{D}$ is a subset of $\mathbb{R}^M$, with $M \in \mathbb{N}^*$. Some of the sub-problems of UQ are the following.

1. *Modeling of input.* How can an uncertain input variable x be described, consistently with available *information* about x, such as known bounds, and available *data*, such as samples or measurements of x?
2. *Uncertainty propagation.* When an uncertain input x enters the deterministic function $\mathcal{M}$, y will become uncertain. How can the uncertainty on y be related to the uncertainty on x?
3. *Sensitivity analysis.* Out of the M components of the uncertain input x, which ones drive most of the uncertainty of the output y?
4. *Reliability analysis.* How likely is it that y exceeds a given maximum admissible value y_{adm}, due to the uncertainty affecting x?
5. *Inverse UQ*, or *model calibration.* Let us assume that the behaviour of the function $\mathcal{M}$ is conditioned by a set of uncertain parameters. How can these parameters be estimated, given that some observations of the input x and associated output y are available?

2.1.2 Probabilistic modeling of the inputs

In the present work we will use a *probabilistic* framework to address these questions. In a such a framework, an uncertain quantity is represented by a (possibly multidimensional) *random variable* X, and the uncertainty affecting X is described by its joint probability density function (PDF) $f_X(x)$, or equivalently, by its cumulative distribution function (CDF) $F_X(x)$, or by univariate marginal distributions and a copula, see Embrechts et al. (2003). Note that there exist other, non-probabilistic, frameworks to address uncertainty, such as interval analysis (Jaulin et al., 2001), fuzzy logic (Zadeh, 1965) and evidence theory (Shafer, 1976).

When addressing the UQ problems outlined above with a probabilistic method, a usual starting point is the probabilistic modelling of inputs, i.e. defining f_X. It might be a time consuming step but it is a key aspect for the quality of the analysis, since the input properties will in general strongly influence the results. When no *data*, but only some *information* about X is available, for example based on expert judgment, the *maximum entropy principle* (Jaynes, 1957) can be used. It states that the least biased PDF f_X describing X is the one maximizing the entropy H, defined as

$$H := -\int_{\mathcal{D}} f_X(x) \ln f_X(x) dx \tag{2.2}$$

and complying with the available information. Some of the solutions of this variational problem may seem quite intuitive.

Example 7. *If the only available information is that X* is bounded*, the solution f_X maximizing H in* (2.2) *will be the uniform distribution. If it is known that X* is unbounded, and its expected value and variance are known*, then the solution is the Gaussian distribution. If X* is positive and only its expected value is known*, the exponential distribution should be used. Additional similar results can be found in Kapur (1989).*

When *data* is available in the form of samples of X, f_X may be chosen to maximize the likelihood of the data, that is the probability of this data actually being observed. Selecting f_X on this basis only may however lead to overfitting, so criteria have been introduced that penalize the *number of parameters* involved to describe f_X. Example of such criteria are the Akaike Information Criterion, or AIC (Akaike, 1974), and the Bayesian Information Criterion, or BIC (Schwarz, 1978).

2.1.3 Surrogate models

Surrogate models, also known as metamodels or emulators, have mainly been developed to serve as a computationally cheap replacement to a function $\mathcal{M}$ that is expensive to evaluate. A surrogate model $\hat{\mathcal{M}}$ is generally *calibrated* from a discrete set of N evaluation points referred to as the *training set* or *experimental design.* We define

$$\mathcal{E} := (x^{(1)}, x^{(2)}, ..., x^{(N)})^\top \tag{2.3}$$

$$\mathcal{F} := [\mathcal{M}(x^{(1)}), \mathcal{M}(x^{(2)}), ..., \mathcal{M}(x^{(N)})]^\top \tag{2.4}$$

From $(\mathcal{E}, \mathcal{F})$, $\hat{\mathcal{M}}$ can then be used to predict the value of $\mathcal{M}(x)$ at points x not included in $\mathcal{E}$. An aspect which will be emphasized in the present chapter is that adequate surrogate models can also be used as tools to study specific *properties* of $\mathcal{M}$.

The most immediate example of surrogate model is the linear *interpolator* between the evaluation points. In that case, $\hat{\mathcal{M}}$ is exactly equal to $\mathcal{M}$ at the evaluation points. A linear *regressor* is an alternative form of surrogate model. For this one, an assumption is made regarding the global behaviour of $\mathcal{M}$ (it is linear over the whole range of evaluation points), which surpasses the requirement for $\hat{\mathcal{M}}$ to be exactly equal to $\mathcal{M}$ at the evaluation points. The *response surface methodology* by Box and Wilson (1951) was among the first surrogate model used in experimental engineering problems. It was based on second order polynomial regression. For a given number N of evaluation point, increasing further the order of polynomials in the regression generally improves the quality of the surrogate model at the evaluation points, but may cause spurious oscillations of $\hat{\mathcal{M}}$ between them (referred to as Runge effect, or overfitting). *Splines* have been developed to alleviate this issue and are now an extremely popular tool to model smooth functions (Friedman, 1991). At a higher abstraction level, *artificial neural networks* have been shown to perform adequately on very complex mappings (McCulloch and Pitts, 1943). Finally, support vector machines (Vapnik, 1995) and Kriging techniques (Cressie, 1990) have become very popular surrogate models in the last years.

The structures of the surrogate models listed above may be radically different from each other. A common point however, is that they all are *parametrized* functions, whose parameters are optimized, in some sense, so that $\hat{\mathcal{M}}$ mimics the original function $\mathcal{M}$. During this optimization process, but also when all parameters have been determined, it is necessary for the analyst to measure the error between $\hat{\mathcal{M}}$ and $\mathcal{M}$. Let us mention three methods to do so. Assume that the samples in $\mathcal{E}$ are realizations of a random variable X. The *generalization error* method uses an additional *validation* set of evaluation points to estimate empirically $\mathrm{E}[(\hat{\mathcal{M}(X)} - \mathcal{M}(X))^2]$. The main drawback of this approach is that it requires additional evaluations of $\mathcal{M}$, which may be costly. The *empirical error* method uses the *same samples* that have been used to determine the parameters in $\hat{\mathcal{M}}$ to evaluate the error. The main drawback of this approach is that it generally overestimates the quality of the surrogate model, and does not detect overfitting. The *leave-one-out (LOO) cross-validation method*, which is an unbiased empirical estimator of $\mathrm{E}[(\hat{\mathcal{M}(X)} - \mathcal{M}(X))^2]$, constitutes a good compromise between these two methods.

Definition 8. *The LOO cross validation error* E_{LOO} *is obtained as follows. A surrogate model* $\hat{\mathcal{M}}^{(\sim i)}$ *is established by using all* N *evaluation points in* $\mathcal{E}$*,* except the i^{th} one. *Then* $(\hat{\mathcal{M}}^{(\sim i)} - \mathcal{M})^2$ *is evaluated at the point* $x^{(i)}$ *which was not included. The operation is repeated for all evaluation points, and* E_{LOO} *is obtained from the following arithmetic mean.*

$$E_{LOO} := \frac{1}{N} \sum_{i=1}^{N} \left(\mathcal{M}(x^{(i)}) - \hat{\mathcal{M}}^{(\sim i)}(x^{(i)}) \right)^2 \tag{2.5}$$

The advantage of the LOO cross-validation method is that no additional evaluation of $\mathcal{M}$ are needed, and that it provides a reliable estimate of the generalization error. A drawback is that N different surrogate models should in principle be calibrated to calculate E_{LOO}. However this can be avoided for some surrogate model structures, as we will see in Section 2.2.3. The surrogate model is in general considered satisfactory when E_{LOO} is less than a few percent of the variance of $\mathcal{M}(X)$ which can be estimated from $\mathcal{F}$ (Le Gratiet et al., 2015). Note also that the concept of LOO can easily be extended to the *leave-K-out cross validation error* (Zaki and Meira, 2014, Chapter 22).

Another important question is how to select the training set $\mathcal{E}$ when there is no available knowledge about the behaviour of $\mathcal{M}$? If the surrogate model is to perform correctly in all regions of $\mathcal{D}$, a natural initial approach is to "spread" the evaluation points over the whole domain $\mathcal{D}$. This can be done for example by maximizing the distance between the N evaluation points in $\mathcal{D}$, which leads to so-called *minimax* or *maximin* distance designs (Santner et al., 2003, Section 5.3). Another approach is to minimize the *discrepancy*, which is a measure of the non-uniformity of the evaluation points over $\mathcal{D}$ (Santner et al., 2003, Section 5.4). When a probabilistic description of the input X is available, an alternative is to sample the evaluation points according to $f_X(x)$. Since there will be more evaluation points in regions of $\mathcal{D}$ where samples of X are likely to be, so one can expect $\hat{\mathcal{M}}$ to perform better in these high-probability regions of $\mathcal{D}$, at the expenses of lesser probability regions. Furthermore, and we are here reaching the topic of uncertainty propagation, once $\mathcal{M}$ has been evaluated for these samples, statistical moments of $\mathcal{M}(X)$ can be directly estimated from $\mathcal{F}$.

Monte-Carlo simulations (MCS) may be used to generate such samples of X. However, if the dimension M of $\mathcal{D}$ is large, and unless a large number N of samples are generated, the samples generated by this method tend to cluster in higher probability regions of $\mathcal{D}$, leading to surrogate models performing very poorly elsewhere. The *Latin Hypercube Sampling* (LHS) method (Stein, 1987) is a sampling method with excellent space-filling properties. More specifically, an advantage of LHS is that the generated samples tend to be spread "marginally", i.e over the range of each component of X, taken separately (Santner et al., 2003, Section 5.2). A latin *square* is a two-dimensional grid containing one (and only one) sample in each row and each column, similarly to rooks on a chess board which do not threaten each other. A latin hypercube is the generalization to larger dimensions of a latin square. In LHS, N^Mcells are generated on $\mathcal{D}$ in such a way that all cells are equiprobable. The N samples are then drawn in selected cells so that this partition of $\mathcal{D}$ forms a latin hypercube.

2.2 Polynomial chaos expansions and applications

In this section, we will first introduce the concept of polynomial chaos expansion (PCE), and show how surrogate models can be built from such expansions. We will then show that these surrogate models have interesting properties when uncertainty propagation and sensitivity analyses should be performed.

2.2.1 Orthogonal families of polynomials and PCE

Let $(\Omega, \aleph, P)$ be a probability space, and $X : \Omega \rightarrow \mathcal{D} \subset \mathbb{R}^M$ be a (possibly multidimensional) random variable. Let $L_2(\Omega, \aleph, P)$ be the space of the P-squared integrable functionals of X, in other words the space of functionals $g(X)$ with finite variance $\mathrm{Var}[g(X)]$. $L_2(\Omega, \aleph, P)$ is a Hilbert space when endowed with the following inner product

$$\langle g|h\rangle := \mathrm{E}[g(X)h(X)] = \int_{\mathcal{D}} g(x)h(x)f_X(x)dx \tag{2.6}$$

Note that the definition of this inner product depends on the input variable X. Families of orthogonal *polynomials* with respect to this inner product can be constructed by Gram-Schmidt orthogonalization of monomials of increasing order. Xiu and Karniadakis (2002) have identified the families corresponding to the most usual probability distribution functions.

Example 8. *Let X_1 be a standard Gaussian variable, i.e $X_1 \sim \mathcal{N}(0,1)$. Then two distinct members of the so-called* Hermite *family of polynomials ($\psi_0^1(x_1) = 1$, $\psi_1^1(x_1) = x_1$, $\psi_2^1(x_1) = x_1^2 - 1$, ...) are orthogonal with respect* *to X_1. Indeed, for this family of polynomials, when setting*

$$f_{X_1}(x_1) = \frac{1}{\sqrt{2\pi}} e^{-\frac{x_1^2}{2}} \tag{2.7}$$

in (2.6)*, then $\forall i, j \in \mathbb{N}^*, i \neq j \Rightarrow \left\langle \psi_i^1 | \psi_j^1 \right\rangle = 0$.*

Example 9. *Consider another random variable denoted X_2, uniformly distributed on $[-1, 1]$, i.e $X_2 \sim \mathcal{U}(-1, 1)$. Then two distinct members of the* Legendre *family ($\psi_0^2(x_2) = 1$, $\psi_1^2(x_2) = x_2$, $\psi_2^2(x_2) = 3/2x_2^2 - 1$, ...) are orthogonal with respect to X_2.*

Consider now a multidimensional random variable X with M *independent* components. The joint PDF f_X of X is then the product of the marginal distributions f_{X_i}, for $i \in \mathbb{N}_M^*$. Then, a family of *multivariate* polynomials $(\psi_\alpha)_{\alpha \in \mathbb{N}^M}$ orthogonal with respect to X can be constructed from the tensor product of M *univariate* polynomials $(\psi_{\alpha_i}^i(X_i))_{i \in \mathbb{N}_M^*}$

Example 10. *Let $M = 2$. We assume that $X \in \mathbb{R}^2$ is composed of the two independent random variables X_1 and X_2 from the previous examples. Then the member of the family of bivariate polynomials orthogonal with respect to X that is indexed by $\alpha = (2, 3)$ is*

$$\psi_{(2,3)}(x_1, x_2) = \psi_2^1(x_1)\psi_3^2(x_2) = (x_1^2 - 1)(5/2x_2^3 - 3/2x_2). \tag{2.8}$$

The first factor is the Hermite polynomial of order 2, and the second factor the Legendre polynomial of order 3. Orthogonality yields from the fact that the integral in (2.6) *can be split in two integrals since $f_X = f_{X_1} f_{X_2}$ due to independence. Then $\forall \alpha, \beta \in \mathbb{N}^2$, $\langle \psi_\alpha | \psi_\beta \rangle = \left\langle \psi_{\alpha_1}^1 | \psi_{\beta_1}^1 \right\rangle \left\langle \psi_{\alpha_2}^2 | \psi_{\beta_2}^2 \right\rangle$, which vanishes if $\alpha \neq \beta$.*

The first member of the family ψ_0 is generally chosen as the constant polynomial identically equal to 1, and the following terms are normalized, so that

$$\forall \alpha, \beta \in \mathbb{N}^M, \langle \psi_\alpha | \psi_\beta \rangle = \delta_{\alpha\beta} \tag{2.9}$$

where $\delta_{\alpha\beta}$ is the Kronecker delta. The family $(\psi_\alpha)_{\alpha \in \mathbb{N}^M}$ forms then an orthonormal *basis* of $L_2(\Omega, \aleph, P)$. This leads to the following definition of the polynomial chaos expansion.

Definition 9. *For $\mathcal{M} \in L_2(\Omega, \aleph, P)$, the polynomial chaos expansion (PCE) of $\mathcal{M}$ is*

$$\mathcal{M} = \sum_{\alpha \in \mathbb{N}^M} a_\alpha \psi_\alpha \tag{2.10}$$

where $(\psi_\alpha)_{\alpha \in \mathbb{N}^M}$ is the family of orthonormal polynomials with respect to the input variable X, and $(a_\alpha)_{\alpha \in \mathbb{N}^M}$ a family of real coefficients.

2.2.2 Truncated PCE as a surrogate model

A surrogate model of $\mathcal{M}$ can then be constructed by truncating the series (2.10). Letting $\mathcal{A}$ be a *finite* subset of $\mathbb{N}^M$, we define $\hat{\mathcal{M}}$ as

$$\hat{\mathcal{M}} := \sum_{\alpha \in \mathcal{A}} a_\alpha \psi_\alpha \tag{2.11}$$

As shown by Cameron and Martin (1947), $\hat{\mathcal{M}}$ will converge in the L_2 sense towards $\mathcal{M}$, i.e. $\mathrm{Var}[\mathcal{M} - \hat{\mathcal{M}}] \to 0$ when the cardinality of $\mathcal{A}$ goes to infinity. The rate of convergence of the a_α coefficients is related to the smoothness properties of $\mathcal{M}$, and is exponential for C^∞ functions.

An immediate question is how to select $\mathcal{A}$. Various criteria have been suggested to do so. Defining the *total degree* as the sum of the components of α, one possibility is to keep all polynomials with total degree less than a given $p \in \mathbb{N}^*$, as illustrated in the upper row of Figure 2.1 for $M = 2$. One drawback of this choice, is that the cardinality $|\mathcal{A}| = (M+p)!/(M!p!)$ grows fast with both M and p. Indeed, as discussed by Blatman and Sudret (2010), the number of evaluations of $\mathcal{M}$ that is needed to identify the $(a_\alpha)_{\alpha \in \mathcal{A}}$ is usually 2-3 times $|\mathcal{A}|$. If the model $\mathcal{M}$ is expensive to evaluate, identification is in practice unfeasible for large values of M and p. Furthermore, for large values of p, this truncation set $\mathcal{A}$ includes interaction terms between high-order univariate polynomials in the input variables. Even if theoretically possible, this type of interaction is rarely seen in practice, which has been formalized in the *sparsity of effect* principle (Montgomery, 2013, Chapter 6).

The following *hyperbolic* truncation sets were introduced by Blatman and Sudret (2011) to address this issue.

$$\forall p \in \mathbb{N}^*, \forall q \in (0,1], \mathcal{A}_q^{M,p} := \{\alpha \in \mathbb{N}^M | \left(\sum_{i=1}^{M} \alpha_i^q \right)^{1/q} \leq p\} \tag{2.12}$$

The case $q = 1$ corresponds to the previously mentioned set in which the total degree is required to be less than p. As shown in Figure 2.1, decreasing values of q, typically to $q = 0.5$, produces *sparser* truncation sets, and favors low-order interaction between the components of X. The cardinality of $\mathcal{A}_q^{M,p}$ as a function of M, p, and q has been studied in details in Blatman and Sudret (2011). However for large M, even when hyperbolic truncation sets are used, it is seen in practice that only a small subset of the identified coefficients a_α have a significant value, the remaining ones being negligible in comparison. How could $\mathcal{A}$ be further optimized to include only the member of $\mathcal{A}_q^{M,p}$ associated with the most significant a_α?

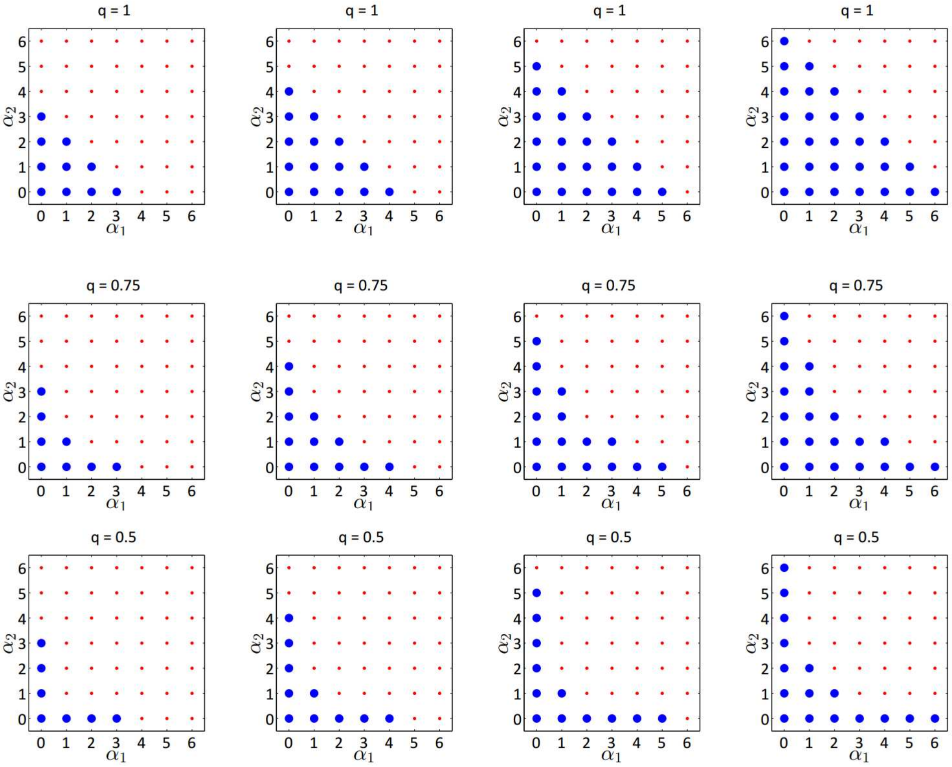

Figure 2.1: Illustration of hyperbolic truncation sets $\mathcal{A}_q^{M,p}$ for $M = 2$. The x-axis corresponds to the degree of the polynomials in X_1, and the y-axis to the degree of the polynomials in X_2. The included terms are represented in blue for various pseudo-norm parameters $q \in \{1(\text{top}), 0.75, 0.5(\text{bottom})\}$, and total degree $p \in \{3(\text{left}), 4, 5, 6(\text{right})\}$. From Sudret and Marelli (2017).

Iterative methods, based on the *least angle regression* (LAR) method, have been proven to be effective at producing such *sparse* sets (Blatman and Sudret, 2011). They start from a hyperbolic truncation set $\mathcal{A}$, obtained using predefined values for q and p, and proceed as follows. First, the member $\psi_{\alpha^{\mathrm{I}}}$ of $\mathcal{A}$ which is the most correlated with $\mathcal{M}$ is identified. This is done by evaluating empirically $\langle \mathcal{M}|\psi_\alpha\rangle$ for all $\alpha \in \mathcal{A}$, that is by using the available set of f_X-distributed evaluation points in $\mathcal{E}$. Then, the largest possible step $\lambda^{\mathrm{I}}\psi_{\alpha^{\mathrm{I}}}$, with $\lambda^{\mathrm{I}} \in \mathbb{R}$, is taken in the direction of $\psi_{\alpha^{\mathrm{I}}}$, until some other member of $\mathcal{A}$, say $\psi_{\alpha^{\mathrm{II}}}$ has as much correlation with the current residual $\mathcal{M} - \lambda^{\mathrm{I}}\psi_{\alpha^{\mathrm{I}}}$ as $\psi_{\alpha^{\mathrm{I}}}$. Then, a step is taken along $\psi_{\alpha^{\mathrm{I}}} + \psi_{\alpha^{\mathrm{II}}}$, that is an *equiangular* direction between $\psi_{\alpha^{\mathrm{I}}}$ and $\psi_{\alpha^{\mathrm{II}}}$. The step length $\lambda^{\mathrm{II}} \in \mathbb{R}$ is increased, which will reduce the correlation of the residual $\mathcal{M} - \left[\lambda^{\mathrm{I}}\psi_{\alpha^{\mathrm{I}}} + \lambda^{\mathrm{II}}(\psi_{\alpha^{\mathrm{II}}} + \psi_{\alpha^{\mathrm{II}}})\right]$ with both $\psi_{\alpha^{\mathrm{I}}}$ and $\psi_{\alpha^{\mathrm{II}}}$. When the residual becomes as correlated to a third member of $\mathcal{A}$, denoted $\psi_{\alpha^{\mathrm{III}}}$, as to $\psi_{\alpha^{\mathrm{I}}}$ and $\psi_{\alpha^{\mathrm{II}}}$, the *descent direction* is changed to become equiangular between $\psi_{\alpha^{\mathrm{I}}}$, $\psi_{\alpha^{\mathrm{II}}}$, and $\psi_{\alpha^{\mathrm{III}}}$. This until a fourth member of $\mathcal{A}$ reaches a high enough correlation with the residual, and so on. The iterations may for example be stopped when the set of selected polynomials has reached a given size, or when the E_{LOO} (2.18) associated with generated surrogate model is sufficiently low. A refined version of this algorithm, where an optimal value of the total degree p is sought, is presented in Blatman and Sudret (2011).

2.2.3 Determination of the a_α coefficients

Once the sparse polynomial basis (ψ_α) has been constructed, and a truncation set $\mathcal{A}$ has been chosen, the coefficients (a_α) must be found to obtain the surrogate model (2.11). Two classes of methods are available for this purpose. *Projection* methods build on the fact that

$$\forall \alpha \in \mathcal{A}, a_\alpha = \langle \mathcal{M}|\psi_\alpha\rangle = \mathrm{E}[\mathcal{M}(X)\psi_\alpha(X)] = \int_{\mathcal{D}} \mathcal{M}(x)\psi_\alpha(x)f_X(x)dx \tag{2.13}$$

The coefficient a_α can then be determined by sampling X with LHS or MCS and evaluating $\mathrm{E}[\mathcal{M}(X)\psi_\alpha(X)]$. Alternatively, the integral on the right hand side can be evaluated by quadrature, meaning that the integrand should be evaluated at values of x given by quadrature rules. Another class of approach, denoted *regression* methods, have however been found to be generally more efficient (Le Gratiet et al., 2015). They consist in minimizing the mean square of the residual $\epsilon(X)$ defined as

$$\epsilon(X) := \mathcal{M}(X) - \hat{\mathcal{M}}(X) = \mathcal{M}(X) - \sum_{\alpha\in\mathcal{A}} a_\alpha\psi_\alpha(X) \tag{2.14}$$

Note that the two approaches are equivalent, see proof in Section A.2. In practice, given the family $\mathcal{E}$ of N samples of X obtained e.g. by LHS, the following discretized version of (2.14) is minimized:

$$a^* = \underset{a \in \mathbb{R}^{|\mathcal{A}|}}{\arg\min} \frac{1}{N} \sum_{i=1}^{N} \left(\mathcal{M}(x^{(i)}) - \sum_{\alpha \in \mathcal{A}} a_\alpha \psi_\alpha(x^{(i)}) \right)^2 \tag{2.15}$$

This is an ordinary least square problem whose solution is given by[1]

$$a^* = (F^\top F)^{-1} F^\top \mathcal{F} \tag{2.16}$$

where F is the *information matrix* defined by

$$\forall i \in \mathbb{N}^*_N, \forall j \in \mathbb{N}^*_{|\mathcal{A}|}, F_{ij} = \psi_j(x^{(i)}) \tag{2.17}$$

and $\mathcal{F}$ has been defined in (2.4).

To verify that the obtained surrogate model $\hat{\mathcal{M}}$ represents well $\mathcal{M}$, the LOO cross-validation error (see Definition 8) can be used. If the LOO error is deemed too large, several polynomials could be added to the set $\mathcal{A}$, or the number of samples N could be increased.

Note that owing to the linearity of (2.16), there exists an explicit expression of the LOO error that does not require establishing N separate PCE models, but uses the one established from *all* N samples. Denoting d_i the i^{th} diagonal term of the matrix $F(F^\top F)^{-1} F^\top$, Saporta (2006) showed that

$$E_{LOO} = \frac{1}{N} \sum_{i=1}^{N} \left(\frac{\mathcal{M}(x^{(i)}) - \hat{\mathcal{M}}(x^{(i)})}{1 - d_i} \right)^2 \tag{2.18}$$

We will in the following show how he obtained PCE-based surrogate model can conveniently be used for UQ purposes.

2.2.4 Uncertainty propagation

Once the surrogate model $\hat{\mathcal{M}}$ in (2.11) is established, it is straightforward to obtain an estimate of the *expected value* of $\mathcal{M}(X)$. Indeed $\mathrm{E}[\hat{\mathcal{M}}(X)] = \mathrm{E}[\hat{\mathcal{M}}(X)\psi_0(X)]$ since $\psi_0 \equiv 1$. Then, then replacing $\hat{\mathcal{M}}$ by its expansion (2.11), and using the fact that ψ_0 is orthogonal to all ψ_α with $\alpha \neq 0$, we find that

$$\mathrm{E}[\hat{\mathcal{M}}(X)] = a_0 \tag{2.19}$$

---

[1] Note that we have for simplicity identified a_α, indexed by the M-tuple $\alpha \in \mathcal{A}$, with a $|\mathcal{A}|$-dimensional vector a. The same abuse of notation is made for ψ_α in the following equations.

The variance of $\mathcal{M}(X)$ can be estimated from $\mathrm{Var}[\hat{\mathcal{M}}]$. Noticing that

$$\hat{\mathcal{M}}(X) - \mathrm{E}[\hat{\mathcal{M}}(X)] = \sum_{\alpha \in \mathcal{A} \setminus \{0\}} a_\alpha \psi_\alpha(X) \tag{2.20}$$

and using the orthogonality of the (ψ_α) yields:

$$\mathrm{Var}[\hat{\mathcal{M}}(X)] = \mathrm{E}[(\hat{\mathcal{M}}(X) - \mathrm{E}[\hat{\mathcal{M}}(X)])^2] = \sum_{\alpha \in \mathcal{A} \setminus \{0\}} a_\alpha^2 \tag{2.21}$$

We see from (2.19) and (2.21) that the two first statistical moments of a PCE-based surrogate model are given by very simple expressions. Analytical expressions of higher-order moments exist for some types of polynomials (Savin and Faverjon, 2017), but in general, the skewness and kurtosis must be estimated numerically from the following expressions:

$$\mathrm{E}[(\hat{\mathcal{M}}(X) - \mathrm{E}[\hat{\mathcal{M}}(X)])^3] = \sum_{(\alpha,\beta,\gamma) \in (\mathcal{A} \setminus \{0\})^3} a_\alpha a_\beta a_\gamma \mathrm{E}[\psi_\alpha \psi_\beta \psi_\gamma] \tag{2.22}$$

$$\mathrm{E}[(\hat{\mathcal{M}}(X) - \mathrm{E}[\hat{\mathcal{M}}(X)])^4] = \sum_{(\alpha,\beta,\gamma,\delta) \in (\mathcal{A} \setminus \{0\})^4} a_\alpha a_\beta a_\gamma a_\delta \mathrm{E}[\psi_\alpha \psi_\beta \psi_\gamma \psi_\delta] \tag{2.23}$$

One may wonder about the consequences of selecting Hermite polynomials (ψ_α) to build the surrogate model, when X is not normally distributed. In that case, one must expect to achieve sub-optimal convergence of the spectral coefficients a_α with respect to the number of terms in the PCE. If a consistent basis is chosen, it has been shown by Blatman and Sudret (2010), among others, that for a given confidence interval, the present approach enables to estimate the statistical moments of $\mathcal{M}(X)$ using up to two orders of magnitude less evaluations of $\mathcal{M}$ than if crude MCS were used.

2.2.5 Global sensitivity analysis

The objective of a sensitivity analysis is to determine which component of the vector x has the most influence on $\mathcal{M}$. *Local* sensitivity analyses examine the impact of input parameters' variations around a *working point* x^*, by considering the value of the gradient and possibly the Hessian of $\mathcal{M}$ at x^* (when such quantities are defined). Local sensitivity analyses are particularly relevant when $\mathcal{M}$ is a linear, or weakly nonlinear, function, since the results obtained at x^* also reflect the sensitivity of $\mathcal{M}$ to its input elsewhere in $\mathcal{D}$.

Example 11. *Let $\mathcal{M}(x_1, x_2) = x_1^3 + x_2$ defined for $\mathcal{D} = \{x \in \mathbb{R}^2, ||x||_\infty \leq \rho\}$ and $\rho \in \mathbb{R}_+^*$. Computing the gradient of $\mathcal{M}$ at $x^* = 0$*

$$\nabla \mathcal{M}|_{x^*=0} = \left(\frac{\partial \mathcal{M}}{\partial x_1}, \frac{\partial \mathcal{M}}{\partial x_2} \right)^\top_{x^*=0} = (0,1)^\top \tag{2.24}$$

puts in evidence the sensitivity of $\mathcal{M}$ to x_2. When ρ is small, this is representative of the global behaviour of $\mathcal{M}$ since the function is weakly nonlinear over $\mathcal{D}$. For large values of ρ, $\mathcal{M}$ will clearly be more sensitive to variations x_1 than to x_2 in most regions of $\mathcal{D}$, so the results obtained locally for $x^* = 0$ are not representative of the global behaviour of $\mathcal{M}$.

This example shows that for nonlinear functions, sensitivity properties of $\mathcal{M}$ may be radically different in different regions of $\mathcal{D}$. This rules out local sensitivity analysis for nonlinear functions, especially when there are uncertainties regarding the value of x.

Assuming that X is a random vector with independent components, the *global* sensitivity of $\mathcal{M}(X)$ can be studied by *Analysis of Variance* (ANOVA), i.e. by determining how much of the variance of $\mathcal{M}(X)$ can be attributed to each component of X. Indeed, if fixing some component of X to their "true" value significantly reduces the variance of $\mathcal{M}(X)$, then it can be concluded that the sensitivity to this component is large. If, on the contrary, a component is left free to vary over its whole range of uncertainty without causing large variations of the variance of $\mathcal{M}(X)$, then this component has no global influence on $\mathcal{M}$ and could be fixed.

More particularly, we will make use of *Sobol' indices*, which are introduced through the following theorems.

Theorem 1. *If $\mathcal{M} : \mathcal{D} \to \mathbb{R}$ is integrable on $\mathcal{D}$, then $\mathcal{M}$ has a unique so-called* Sobol' decomposition

$$\begin{aligned}\mathcal{M}(x_1, ..., x_M) = \mathcal{M}_0 + \sum_{i=1}^{M} \mathcal{M}_i(x_i) + \sum_{1 \leq i < j \leq M} \mathcal{M}_{i,j}(x_i, x_j) \\ + ... + \mathcal{M}_{1,2,...,M}(x_1, x_2, ..., x_M)\end{aligned} \tag{2.25}$$

where $\mathcal{M}_0$ is constant, and for any $s \in \mathbb{N}_M^*$ and $k \in \mathbb{N}_s^*$, the integral of any $\mathcal{M}_{i_1,...,i_s}(x_{i_1}, ..., x_{i_s}) f_{X_k}(x_k)$ over the domain of variable x_k is zero.

Proof. See Sobol (1993). □

Theorem 2. *The variance V of $\mathcal{M}(X)$ can be decomposed as*

$$V = \sum_{i=1}^{M} V_i + \sum_{1 \leq i < j \leq M} V_{i,j} + ... + V_{1,2,...,M} \tag{2.26}$$

where each term is the variance of the corresponding term in Sobol' decomposition (2.25)*.*

Proof. First, one should note that the summands in (2.25) are orthogonal in pairs in the sense that: $\forall (i_1, ..., i_s) \neq (j_1, ..., j_t)$,

$$\int_{\mathcal{D}} \mathcal{M}_{i_1,..,i_s}(x_{i_1}, ..., x_{i_s}) \mathcal{M}_{j_1,...,j_t}(x_{j_1}, ..., x_{j_t}) f_X(x) dx = 0 \tag{2.27}$$

This comes first from the fact that $f_X(x)$ can be written as $\prod_{i \in \mathbb{N}^*_M} f_{X_i}(x_i)$ due to independence. Then, assuming without loss of generality that $s \leq t$, at least one of the indices $i_1, ..., i_s$, say i_k, is not repeated in $j_1, ..., j_t$. Then, the integral with respect to x_k can be separated from the integral over the other variables in (2.27). By property of the Sobol' decomposition (2.25), the integral of $\mathcal{M}_{i_1,...,i_s}(i_1, ..., i_s) f_{X_k}(x_k)$ over the variable x_k is zero, which causes the integral in (2.27) to vanish, and shows the orthogonality of the summands in the Sobol' decomposition.

The expected value of $\mathcal{M}(X)$ is obviously $\mathcal{M}_0$. Taking the variance of both sides of (2.25), the cross terms appearing when computing $\mathrm{E}[(\mathcal{M}(X) - \mathcal{M}_0)^2]$ will vanish due to the orthogonality relationship (2.27), which proves (2.26). □

Definition 10. *The* Sobol' indices *or* sensitivity indices *are defined as the terms appearing when dividing* (2.26) *by V (Sobol', 2001). They satisfy*

$$\sum_{i=1}^{M} S_i + \sum_{1 \leq i < j \leq M} S_{ij} + ... + S_{1,2,...,M} = 1 \tag{2.28}$$

The S_i are called *first-order* Sobol' indices[2], S_{ij} *second order* Sobol' indices, and so on. S_i measures the proportion of the variance of $\mathcal{M}(X)$ that is due to X_i only, and S_{ij} describes the proportion of the variance of $\mathcal{M}(X)$ that is due to X_i and X_j, but cannot solely be explained by

---

[2] An equivalent definition of the first-order Sobol' index, which is based on the *conditional expectation* $\mathrm{E}[\mathcal{M}(X)|X_i]$, is

$$S_i := \frac{\mathrm{Var}[\mathrm{E}[\mathcal{M}(X)|X_i]]}{\mathrm{Var}[\mathcal{M}(X)]} \tag{2.29}$$

As illustrated in (Saltelli, 2008, pages 21-23), it leads to an intuitive representation of the meaning of S_i. Indeed, when samples of X and $\mathcal{M}(X)$ are available, $\mathrm{E}[\mathcal{M}(X)|X_i]$ can be computed by partitioning the X_i domain into slices, and averaging the values of $\mathcal{M}(X)$ *given* x_i within each slice. If these average values vary much across the x_i domain, i.e. if $\mathrm{Var}[\mathrm{E}[\mathcal{M}(X)|X_i]]$ is large, then $\mathcal{M}$ is sensitive to the input x_i. Note that definition (2.29) can be extended to Sobol' indices of arbitrary order by using conditional expectations covering several input variables.

individual variations of X_i or X_j. So the fact that $S_i = 0$ is a necessary, but not sufficient, criterion to conclude on the insensitivity of $\mathcal{M}$ to the i^{th} component of its input. Indeed, this component could play a significant role *in interaction with another component*, which would be visible by examining the higher-order Sobol' indices.

Definition 11. *The* total Sobol' index S_{T_i} *is defined as the sum of all Sobol' indices in* (2.28) *involving the parameter* i*.*

S_{T_i} quantifies the total effect of an input parameter, either alone, or in combination with others. $S_{T_i} = 0$ is then a necessary and sufficient condition to conclude that X_i is non-influential. Furthermore, by ranking the $S_{T,i}$, the components of X having the greatest impact on the variations of $\mathcal{M}$ can be identified. Also, by comparing each $S_{T,i}$ to S_i, it is possible to evaluate whether X_i influences $\mathcal{M}$ alone (in the case $S_i \approx S_{T,i}$), or jointly with other components of X.

When they were introduced, the Sobol' indices were computed from equations such as (2.29) using Monte-Carlo simulation (Homma and Saltelli, 1996). This proved to be quite time consuming, and higher-order Sobol indices were rarely accessible in practice. Recently, Sudret (2008) put in evidence the analytical connection between the coefficients a_α of a PCE surrogate model in (2.11) and the Sobol' indices. This was done by noticing the similarity of the orthogonality conditions (2.6) and (2.27). In other words, once the a_α were identified, the Sobol' indices could be obtained at practically no cost. This finding, combined with the methods outlined in Section 2.2.2 to efficiently identify sparse polynomial bases have now made PCE an intermediate of choice for global sensitivity analyses.

2.3 Gaussian process modeling and applications

In this section, another type of surrogate model will be presented, which builds upon the assumption that $\mathcal{M}$ is the realization of a Gaussian process $\hat{\mathcal{M}}(x, \omega)$ defined over $\mathcal{D} \times \Omega$. This assumption enables us to estimate quantitatively how uncertain $\hat{\mathcal{M}}$ is at each location of $\mathcal{D}$. This information can then be exploited to sequentially improve $\hat{\mathcal{M}}$ in strategic regions of $\mathcal{D}$, which will prove interesting in reliability analyses (task 4 in Section 2.1.1).

2.3.1 Gaussian processes and autocorrelation functions

We refer the reader to Appendix A.1 for the definition of Gaussian random vectors. Gaussian random processes can be considered as extensions, to continuous sets, such as $\mathcal{D}$, of Gaussian random vectors, whose components are indexed by the discrete and finite set $\mathbb{N}_k^*$, with $k \in \mathbb{N}^*$.

Definition 12. *A collection of random variables $Z_x(\omega)$ indexed by $x \in \mathcal{D}$ is a* Gaussian Random Process (GRP) *if $\forall k \in \mathbb{N}^*, \forall (x_1, x_2, ..., x_k) \in \mathcal{D}^k$, the random vector $(Z_{x_1}(\omega), Z_{x_2}(\omega), ..., Z_{x_k}(\omega))^\top$ is multivariate normally distributed.*

The functions $x \mapsto Z_x(\omega)$ obtained for a given $\omega \in \Omega$ are denoted *sample paths*. The covariance of Z between two fixed points x and x' is given by the autocovariance function $\mathcal{C}_Z(x, x')$:

$$\mathcal{C}_Z(x, x') := \mathrm{cov}(Z_x, Z_{x'}) = E[(Z_x - \mu_x)(Z_{x'} - \mu_{x'})] \tag{2.30}$$

For so called *weakly stationary* processes (and *a fortiori* for *stationary* processes), the mean $\mu_x = \mu$ does not vary with x, and the autocovariance function $\mathcal{C}_Z(x, x')$ only depends on the gap $h = x - x'$. This implies that the variance σ_Z^2 of the process is constant and equal to $\mathcal{C}_Z(x, x)$. In that case, the autocorrelation function $\mathcal{R}_Z$, defined as

$$\mathcal{R}_Z(x, h) := \mathcal{C}_Z(x, x + h)/\sigma_Z^2 \tag{2.31}$$

is also independent of x, which can then omitted. Obviously, $\mathcal{R}(h = 0) = 1$. Other properties of $h \mapsto \mathcal{R}(h)$ for a stationary GRP, such as symmetry, definite positiveness, continuity, asymptotic values are discussed in Santner et al. (2003), Section 2.3.3.

The smoothness of the sample paths (i.e. the $x \mapsto Z_x(\omega)$ functions) of a stationary GRP is strongly related to the shape and smoothness of the corresponding autocorrelation function. The Matérn correlation function provides a flexible and unified way of describing the autocorrelation of various classes of processes.

Definition 13. *The general Matérn correlation function is defined by:*

$$\mathcal{R}_Z(h, l) := 2^{1-\nu}\Gamma^{-1}(\nu)\left(2\nu h'^2\right)^{\nu/2} K_\nu\left(\sqrt{2\nu h'^2}\right) \text{ with } h'^2 = \sum_{i=1}^{M}\left(\frac{|h_i|}{l_i}\right)^2 \tag{2.32}$$

where Γ is the Gamma function, K_ν is the modified Bessel function of the second kind, $l \in (\mathbb{R}_+)^M$ contains scale parameters describing the amount of correlation between neighbours for each component x_i and x_i' (we recall that $h = x - x'$), and $\nu \in \mathbb{R}_+^*$ is a shape parameter related to the continuity properties of the sample paths $x \mapsto Z(x, \omega)$.

Plots of this function for various values of ν and l are presented on the left hand side of Figure 2.2. By setting $\nu = 1/2$, the Matérn correlation function can be specialized into the exponential autocorrelation function

$$\mathcal{R}_Z(h, l) = e^{-h'} \text{ with } h'^2 = \sum_{i=1}^{M} \left(\frac{|h_i|}{l_i} \right)^2 \tag{2.33}$$

which leads to continuous, but non differentiable sample paths [3], as shown in Figure 2.2a. Letting $\nu \to \infty$, we obtain the squared exponential autocorrelation function

$$\mathcal{R}_Z(h, l) = e^{-h'^2} \text{ with } h'^2 = \sum_{i=1}^{M} \left(\frac{|h_i|}{l_i} \right)^2 \tag{2.34}$$

which leads to smooth ($\mathcal{C}_\infty$) sample paths, see Figure 2.2b. For other values of $\nu > 0$, the sample paths drawn from a GRP with Matérn correlation function are continuously differentiable up to order $\lfloor \nu \rfloor$. In the next chapters, we will use $\nu = 5/2$, leading to the following simplified expression:

$$\mathcal{R}_Z(h, l) = \left(1 + 5h' + 5/3h'^2\right) e^{-\sqrt{5}h'} \text{ with } h'^2 = \sum_{i=1}^{M} \left(\frac{|h_i|}{l_i} \right)^2 \tag{2.35}$$

Additional examples of autocorrelation functions, together with associated sample paths, can be found in Santner et al. (2003), Section 2.3.4.

2.3.2 Kriging

As in the previous section, we consider that x is a realization of a multidimensional random variable X with independent components. We also assume that N samples of X have been generated using space-filling method such as LHS, and gathered in $\mathcal{E}$. The corresponding outputs of the $\mathcal{M}$ function are gathered in $\mathcal{F}$. We will now show how a surrogate model of $\mathcal{M}$ can be created *by assuming that $\mathcal{M}(x)$ is the sample path of a GRP* with the following form.

Definition 14. *$\mathcal{M}(x)$ is the realization of the underlying GRP*

$$\hat{\mathcal{M}}(x, \omega) := \sum_{\alpha \in \mathcal{A}} a_\alpha \psi_\alpha(x) + \sigma^2 Z(x, \omega, l) \tag{2.36}$$

---

[3] This assertion and all corresponding ones below are valid *almost surely*, that is except on a subset of Ω with zero probability

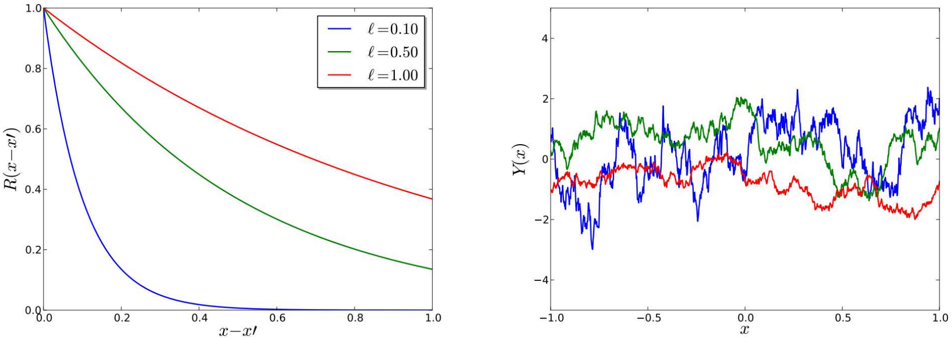

(a) Exponential autocorrelation function ($\nu = 1/2$) leading to continuous but non-differentiable ($\mathcal{C}_0$) sample paths. Effect of varying the scale parameter l.

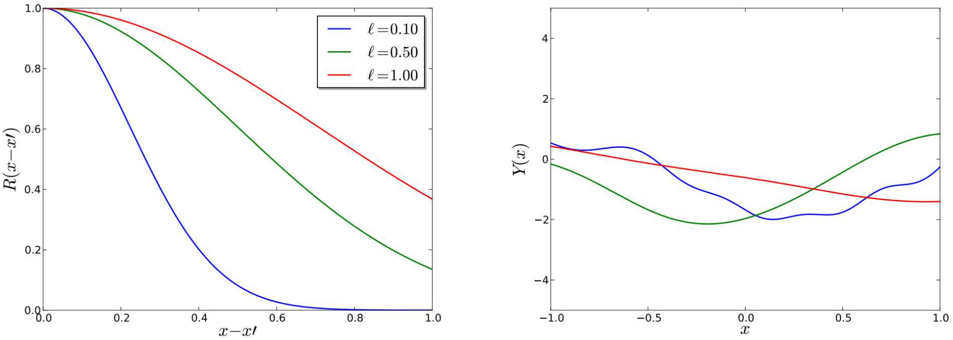

(b) Squared exponential autocorrelation function ($\nu \to \infty$) leading to smooth ($\mathcal{C}_\infty$) sample paths. Effect of varying the scale parameter l.

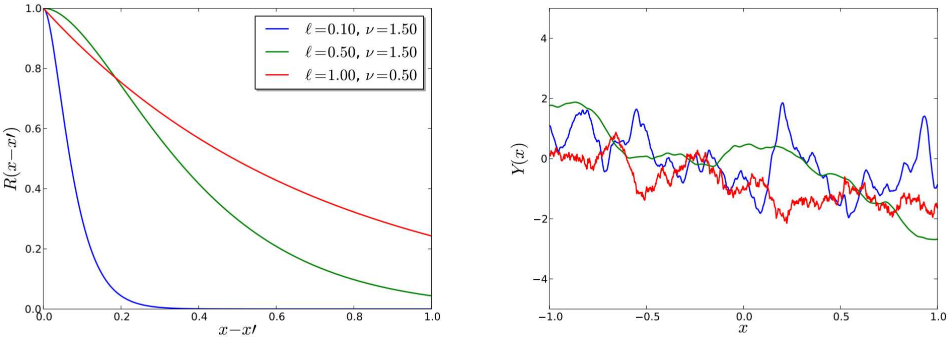

(c) Effect of the shape parameter ν and scale parameter l on the sample paths.

Figure 2.2: Matérn autocorrelation function in dimension $M = 1$ with various shape parameters ν and scale parameters l (l.h.s.), and corresponding sample paths $x \mapsto Y(x, \omega)$ (r.h.s.). From Dubourg (2011).

where $\mathcal{A}$ *is a finite subset of* $\mathbb{N}^M$, $(a_\alpha)_{\alpha\in\mathcal{A}}$ *are real numbers,* $(\psi_\alpha)_{\alpha\in\mathcal{A}}$ *form a finite set of orthonormal polynomials with respect to* X, $Z(x,\omega)$ *is a zero mean and unit-variance stationary GRP and* $\sigma \in \mathbb{R}^+$. Z *is assumed to be described by the general Matérn correlation function* $\mathcal{R}_Z$, *with parameters* ν *and* l.*The GRP in* (2.36) *is denoted Polynomial-Chaos Kriging (PCK) model Schöbi et al. (2016).*

The first term of this model (denoted the *trend*) aims at describing the *global* variations of $\mathcal{M}$ over $\mathcal{D}$. Here, the trend has the same structure as the PCE developed in the previous section, and the polynomials ψ_α are in general selected using similar methods, such as the LAR algorithm described in Section 2.2.2. The selected ψ_α are weighted by the coefficients a_α, gathered in a $|\mathcal{A}|$-tuple which we denote β. Note however, for a given set of evaluation points $(\mathcal{E},\mathcal{F})$, the a_α coefficients in the PCK model are not equal to those which would have been obtained when identifying a PCE model with (2.15). This is due to the presence of the second term in the PCK (2.36), a zero mean and stationary Gaussian process with variance σ^2, that accounts for local variations of $\mathcal{M}$.

The structure of (2.36) is a particular case of *universal kriging* (Santner et al., 2003, Section 3.3). The advantages of PCK over *ordinary* kriging (in which the regressors ψ_α are limited to one constant) and over PCE, in which no GRP is involved have been demonstrated by Schöbi et al. (2015). More specifically, it was shown that the LOO error associated with a PCK surrogate model tend to be lower for small $\mathcal{E}$ sets, i.e. satisfactory surrogate models could be obtained with fewer samples .

Definition 14 provides a framework for surrogating $\mathcal{M}(x)$, but also for estimating how uncertain the value of $\mathcal{M}(x)$ is at a point $x \notin \mathcal{E}$, given the fact that some information has been gathered at neighbouring points. Indeed, assuming that the values of a_α (gathered in the vector β), σ, and l, involved in (2.36) are known, then

Theorem 3. *the most probable value of* $\mathcal{M}(x)$ *at any point in* $\mathcal{D}$ *is*

$$\mu_{\hat{\mathcal{M}}(x)} := f(x)^\top \beta + r(x)^\top R^{-1}(\mathcal{F} - F\beta) \tag{2.37}$$

with an uncertainty

$$\sigma^2_{\hat{\mathcal{M}}(x)} := \sigma^2(1 - r(x)^\top R^{-1} r(x)^\top) \tag{2.38}$$

where

- $f(x) \in \mathbb{R}^{|\mathcal{A}|\times 1}$ *contains the* $\psi_\alpha(x)$ *polynomials evaluated at* x,
- $F \in \mathbb{R}^{|\mathcal{A}|\times N}$ *is the information matrix defined in* (2.17), *containing, in each column the* $\psi_\alpha(x)$ *polynomials evaluated at* $x^{(i)}$,

- *$r(x) \in \mathbb{R}^{N\times 1}$ is the cross-correlation vector defined by*

$$\forall i \in \mathbb{N}_N, r_i(x) := \mathcal{R}_Z(x - x^{(i)}, l) \tag{2.39}$$

- *and $R \in \mathbb{R}^{N\times N}$ is the correlation matrix defined by*

$$\forall i, j \in \mathbb{N}^*_N, R_{ij} := \mathcal{R}_Z(x^{(i)} - x^{(j)}, l) \tag{2.40}$$

Proof. According to Definition 12, a GRP is a collection of random variables, any finite number of which have a joint Gaussian distribution. Based on Definition 14, $(\mathcal{M}(x), \mathcal{F}^\top)^\top$ is then the realization of a random vector $V \in \mathbb{R}^{N+1}$ distributed as:

$$V \sim \mathcal{N}\left(\begin{bmatrix} f(x)^\top \beta \\ F\beta \end{bmatrix}, \sigma^2 \begin{bmatrix} 1 & r(x)^\top \\ r(x) & R \end{bmatrix}\right) \tag{2.41}$$

According to Theorem 3.2.1 in Santner et al. (2003), the estimator of $\mathcal{M}(x)$ with minimum mean-squared prediction error is $\mathrm{E}[V_1 | [V_2, ..., V_{N+1}]^\top]$. As derived in (Eaton, 2007, page 117), this conditional expectation is a Gaussian random variable, whose mean $\mu_{\hat{\mathcal{M}}(x)}$, and thus most probable value, is equal to the right hand side of (2.37). Its variance is given by (2.38). □

Remark 2. *It is important to make the distinction between the randomness of X and the randomness introduced through ω in Definition 14. While the former is a reality of our UQ problem, the latter provides a* tool to model the epistemic uncertainty *on $\mathcal{M}(x)$ at locations where it has not been evaluated, and leads to the result stated in Theorem 3.*

Theorem 3 shows how $\mathcal{M}$ can be estimated once the parameters in (2.36) are known. These parameters are determined based on the available data $(\mathcal{E}, \mathcal{F})$ as follows. In a first step, the sparse set of polynomials $(\psi_\alpha)_{\alpha\in\mathcal{A}}$ in the trend is determined using the LAR method (see Section 2.2.2). Then,

Theorem 4. *the optimal parameters β and σ^2 can be estimated by:*

$$\hat{\beta} = \left(F^\top R^{-1} F\right)^{-1} F R^{-1} \mathcal{F} \tag{2.42}$$

$$\hat{\sigma}^2 = \frac{1}{N}(\mathcal{F} - F\beta)^T R^{-1} (\mathcal{F} - F\beta) \tag{2.43}$$

Proof. Let us first assume that the correlation function $\mathcal{R}$ in (2.32) is known. The optimal coefficients $\hat{\beta}$ and $\hat{\sigma}^2$ in (2.36) are those which lead to a process $\hat{\mathcal{M}}$ whose most likely realization is $\mathcal{M}(x)$. Since by construction, $\hat{\mathcal{M}}$ is a

Gaussian process, the optimal coefficients $\hat{\beta}$ and $\hat{\sigma}^2$ in (2.36) are those which maximize the likelihood, or log-likelihood of $\mathcal{F}$, expressed as

$$\log L(\mathcal{F}|\beta, \sigma^2) = -\frac{N}{2}\log 2\pi\sigma^2 - \frac{1}{2}\log|R| - \frac{1}{2\sigma^2}(\mathcal{F} - F\beta)^\top R^{-1}(\mathcal{F} - F\beta) \tag{2.44}$$

The values of β and σ^2 maximizing this expression necessarily satisfy the first-order optimality conditions $\nabla_\beta(\log L) = 0$ and $\nabla_{\sigma^2}(\log L) = 0$. Since R is symmetric, they read

$$F^T R^{-1}(\mathcal{F} - F\beta) = 0 \tag{2.45}$$

$$-\frac{N}{2}\frac{1}{\sigma^2} + \frac{1}{2\sigma^4}(\mathcal{F} - F\beta)^\top R^{-1}(\mathcal{F} - F\beta) = 0 \tag{2.46}$$

which leads to (2.42) and (2.43). □ □

Finally, the hyperparameter l in $\mathcal{R}$ is determined as the one minimizing the E_{LOO} (2.18). In the present work, we used a genetic optimization algorithm (Goldberg, 1989) to determine l.

We have in this section presented PCK surrogate models. In the next section, we will introduce the class of UQ problems called *reliability* problems, before showing, in Section 2.3.4, how such problems can efficiently be solved by using the PCK model.

2.3.3 Reliability analysis

The field of reliability engineering is concerned with the *failure* of systems, and on quantifying the probability of occurrence of such failures. Note that the engineered systems under study can be mechanical systems (Lemaire, 2009) or control systems (Calafiore et al., 2011), among others. Assuming that $y = \mathcal{M}(x)$ measures the performance of the system, failure can be defined as $\mathcal{M}(x) \leq y_{\mathrm{adm}}$, where y_{adm} defines a minimum admissible performance. Given that uncertainties exist on x, a *reliability analysis* will aim at estimating the probability $P_f := \mathrm{P}[\mathcal{M}(X) \leq y_{\mathrm{adm}}]$ of the system to fail.

Definition 15. *The* domain of failure $\mathcal{D}_f \subset \mathbb{R}^M$ *is defined by*

$$\mathcal{D}_f := \{x \in \mathcal{D} | \mathcal{M}(x) \leq y_{adm}\} \tag{2.47}$$

Definition 16. *The* limit state surface $\mathcal{L} \subset \mathbb{R}^M$ *is defined by*

$$\mathcal{L} := \{x \in \mathcal{D} | \mathcal{M}(x) = y_{adm}\} \tag{2.48}$$

Failures are, in general, *rare events*, meaning that the probability $P_f = P[X \in \mathcal{D}_f]$ will be small. This causes practical challenges when attempting to estimate P_f. Indeed, consider for example a naive MCS-based approach to estimate P_f, that would consist in drawing N samples of X, calculating $\mathcal{M}(x^{(i)})$ for each of them, and comparing the result to y_{adm}. P_f could then be estimated by

$$\hat{P}_f = \frac{1}{N} \sum_{i \in \mathbb{N}_N^*} \mathbb{I}_{\mathcal{D}_f}(x^{(i)}) \tag{2.49}$$

where $\mathbb{I}$ is the indicator function. In that case, $\mathbb{I}_{\mathcal{D}_f}(x^{(i)})$ follows a binomial distribution, and estimating P_f with a confidence interval of δ, requires performing at least

$$N \geq (1 - P_f)(\delta^2 P_f)^{-1} \tag{2.50}$$

simulations. For instance, if $\delta = 5\%$ and $P_f = 10^{-3}$, N should be of the order of magnitude of 10^5, which is practically unfeasible when $\mathcal{M}$ is computationally expensive. See also Chernoff (1952) for bounds not depending directly on P_f.

Optimized methods have therefore been developed to perform reliability analyses. The first-order and second-order reliability methods (FORM and SORM, respectively) are *approximation methods* that have been developed in the 1970's and are still very much used in structural engineering (Lemaire, 2009, Chapter 7). Both methods work in a suitable probabilistic space, and first identify a *most probable point of failure* x^* by performing simulations of $\mathcal{M}$. Then they approximate $\mathcal{L}$ by either the tangent hyperplane at x^* (for FORM), or by the tangent second-order hypersurface at x^* (for SORM). P_f can then be estimated from analytical formulas. An advantage of such approximation methods is that they require few evaluations of $\mathcal{M}$, mainly associated with the search for x^*. It is clear that these methods perform well if D_f is a connected set (or else the approximation of $\mathcal{D}_f$ at x^* will not be representative of the whole domain of failure) and if the shape of $\mathcal{L}$ can reasonably well be represented by a first- or second-order hypersurface.

These approximation methods can be completed by so-called *simulation methods*. For example, once x^* has been identified, a distribution $g_X(x)$ could be defined that generates samples that are located *near* x^* with high probability. Then, by noting that

$$P_f = \int_{\mathcal{D}} \mathbb{I}_{\mathcal{D}_f}(x) f_X(x) dx = \int_{\mathcal{D}} \mathbb{I}_{\mathcal{D}_f}(x) \frac{f_X(x)}{g_X(x)} g_X(x) dx \tag{2.51}$$

P_f could be estimated from $\mathrm{E}[\mathbb{I}_{\mathcal{D}_f}(X) \frac{f_X(X)}{g_X(X)}]$ using g_X-distributed samples. This method called *importance sampling* can estimate P_f with significantly less samples than the naive MCS approach (2.50) (Melchers, 1990). *Subset simulation* is another strategy that consists in solving a sequence of *nested* reliability problems, each of them featuring probabilities of failures significantly larger than P_f. These simulation based methods lead to precise estimates of P_f, are clearly more efficient than naive MCS (2.50), but may still require a large number of evaluations of $\mathcal{M}$ (Echard et al., 2013).

In the following, we will present results from recent research, in which a PCK surrogate model, such as presented in Section 2.3.2, is refined with active learning techniques to identify $\mathcal{D}_f$ and estimate P_f. The resulting reliability analysis method has been shown to be extremely efficient when high dimensions M and low values of P_f are involved.

2.3.4 Adaptive Kriging for reliability analysis

The heuristics behind Adaptive Kriging (AK) is the following. Assuming that a good surrogate model $\hat{\mathcal{M}}$ of $\mathcal{M}$ is available, the reliability problem could in principle be solved with the naive MCS approach, using $\hat{\mathcal{M}}$ and an arbitrarily *large* auxiliary set of samples $\mathcal{S}$ of X (typically $|\mathcal{S}| > 10^6$). $\hat{\mathcal{M}}(x)$ could be (cheaply) computed for each sample, and P_f could be evaluated from (2.49). This strategy requires that $\hat{\mathcal{M}}$ at least captures the distinction between failure and success, i.e. that $\hat{\mathcal{M}}$ models accurately $\mathcal{M}$ near $\mathcal{L}$. However, as mentioned in Section 2.1.3, the initial calibration of a surrogate model is usually done from a limited set of samples, generated from space-filling sampling methods such as LHS. In that case, there is a large probability that none of these samples falls into $\mathcal{D}_f$, which means that $\hat{\mathcal{M}}$ is not likely to capture $\mathcal{L}$ correctly.

To address this issue, adaptive methods were developed, in which the set of evaluation points $\mathcal{E}$ is sequentially *enriched* in locations of $\mathcal{D}$ which might be near $\mathcal{L}$. The adaptive strategy that we will consider here makes use of a PCK model, and has been suggested by Schöbi et al. (2016). For each sample x in the auxiliary set $\mathcal{S}$, the *probability of misclassification* $P_m(x)$ is evaluated, that is the probability that the PCK model predicts that x is in $\mathcal{D}_f$ while it is actually not, or vice versa. This corresponds to the two following distinct cases. Case 1: the PCK model predicts failure, that is $\mu_{\hat{\mathcal{M}}}(x) < y_{\mathrm{adm}}$, while the system is safe, that is $\mathcal{M}(x) > y_{\mathrm{adm}}$. The probability of such an event can be evaluated from our assumption that $\mathcal{M}$ behaves as GRP, and is thus normally distributed at x. Denoting Φ be the standard normal cumulative distribution function,

$$\text{If } \mu_{\hat{\mathcal{M}}}(x) \leq y_{\mathrm{adm}}, P_m(x) := P[\mathcal{M}(X) > y_{\mathrm{adm}}] = 1 - \Phi\left(\frac{y_{\mathrm{adm}} - \mu_{\hat{\mathcal{M}}}(x)}{\sigma_{\hat{\mathcal{M}}}(x)}\right)$$

Case 2: the PCK model does not predicts failure, that is $\mu_{\hat{\mathcal{M}}}(x) > y_{\mathrm{adm}}$, while $\mathcal{M}(x) \leq y_{\mathrm{adm}}$. This corresponds to a probability

$$\text{If } \mu_{\hat{\mathcal{M}}}(x) > y_{\mathrm{adm}}, P_m(x) := P[\mathcal{M}(X) \leq y_{\mathrm{adm}}] = \Phi\left(\frac{y_{\mathrm{adm}} - \mu_{\hat{\mathcal{M}}}(x)}{\sigma_{\hat{\mathcal{M}}}(x)}\right)$$

Combining these two cases, the probability of misclassification can then be written, in a compact manner, as

$$P_m(x) := \Phi\left(-\frac{|\mu_{\hat{\mathcal{M}}}(x) - y_{\mathrm{adm}}|}{\sigma_{\hat{\mathcal{M}}}(x)}\right) \tag{2.52}$$

The value of P_m is largest (1) when $\mu_{\hat{\mathcal{M}}}(x)$ is close to y_{adm}, meaning that x is close to the $\mathcal{L}$ estimated from the PCK, and/or (2) when the uncertainty on the value of $\mathcal{M}$ is large, meaning that the proximity to $\mathcal{L}$ is uncertain. Based on this information, $\mathcal{E}$ is enriched with the auxiliary sample x^{new} in $\mathcal{S}$ that features the largest P_m. For this reason, P_m is referred to as a *learning function*. Then $\mathcal{M}(x^{\mathrm{new}})$ is evaluated and added to $\mathcal{F}$, and the enriched sets $\mathcal{E}$ and $\mathcal{F}$ are used, as described in Section 2.3.2, to define a new PCK model (2.36), which sequentially will be refined near $\mathcal{L}$.

When several model evaluations can be performed *in parallel*, several new promising samples (and not only the one with the largest P_m) can advantageously be selected at each enrichment step. To do so, an δ-confidence bound about the estimated $\mathcal{L}$ is first derived by identifying an "upper bound" of the failure domain $\mathcal{D}_f$:

$$\mathcal{D}_f^+ := \{x \in \mathcal{D} | \mu_{\hat{\mathcal{M}}}(x) - k\sigma_{\hat{\mathcal{M}}}(x) \leq y_{\mathrm{adm}}\} \tag{2.53}$$

and a lower bound for $\mathcal{D}_f$:

$$\mathcal{D}_f^- := \{x \in \mathcal{D} | \mu_{\hat{\mathcal{M}}}(x) + k\sigma_{\hat{\mathcal{M}}}(x) \leq y_{\mathrm{adm}}\} \tag{2.54}$$

where $k = \Phi^{-1}(1-\delta/2)$ [4]. The limit state margin (Dubourg, 2011) is defined as the relative complement of the lower bound in the upper bound.

Definition 17. *The limit state margin is the set*

$$\mathbb{L} := \mathcal{D}_f^+ \setminus \mathcal{D}_f^- \tag{2.55}$$

The domain $\mathbb{L}$ contains locations where $\mathcal{M}$ is probably close to y_{adm}, and where new relevant samples should be found to refine the PCK model. Assuming that we wish to enrich $\mathcal{E}$ with K samples, and more than K samples

---

[4] If $\delta = 5\%$, then $k \approx 1.96$.

in $\mathcal{S}$ have fallen into the limit state margin, one can identify K *clusters* of points in $\mathbb{L}$ with high P_m values. Samples which are "representative" of each cluster are then selected using a K-means clustering algorithm (Zaki and Meira, 2014, Chapter 13). The K samples $[x^{\mathrm{new},1}, ..., x^{\mathrm{new},\mathrm{K}}]$ are added to $\mathcal{E}$, $\mathcal{M}$ is evaluated for each of them, and the enriched sets $\mathcal{E}$ and $\mathcal{F}$ are used to refine the PCK model. This process is illustrated by an example in Appendix 2.3.4.

The enriched sets $\mathcal{E}$ and $\mathcal{F}$ are then used to define a new, refined, PCK model as described in Section 2.3.2. The locations of $\mathcal{D}_f$, and the associated estimate P_f become, step by step, more exact. Various *stopping criteria* have been suggested, to decide when to end this enrichment process, and some have been compared by Schöbi et al. (2016). Here, the uncertainty on the estimated P_f is quantified by comparing the probabilities of failure estimated from $\mathcal{D}_f^+$ and $\mathcal{D}_f^-$, respectively. If the difference between them is less than 5% of P_f (evaluated from the estimated $\mathcal{D}_f$), we consider that convergence is achieved. Convergence towards the true value of P_f when $N \to \infty$ is guaranteed by the fact that (1) the learning function (2.52) weights uncertain areas of $\mathcal{D}$, and thus eventually explores the whole space $\mathcal{D}$, and (2) the resulting PCK (2.36) will interpolate exactly $\mathcal{M}(x)$ since it is an universal approximation function. Note, however, that no formal proof of i*optimal* convergence, as compared to other established methods, is available for this algorithm. Adaptive Kriging has however been shown to be more computationally efficient than other established methods, such as e.g. importance sampling[5] (Echard et al., 2011). It is also more precise than the FORM/SORM methods (Schöbi et al., 2016), as it tackles non-connected, and arbitrarily shaped failure regions $\mathcal{D}_f$.

The following example, borrowed from Schöbi et al. (2016), illustrates both single and multiple sample enrichment with the Adaptive Kriging method. Similar examples will be provided in the next sections.

Example 12. *We define the function* $\mathcal{M}(x) := 20-(x_1-x_2)^2-8(x_1+x_2-4)^3$ *on* $\mathcal{D} = [-5, 5]^2$. *Failure occurs when* $\mathcal{M}(x) \leq 0$. *Consider Figure 2.3. In (a),* X *has first been sampled using a space-filling sampling method. Some of the samples (represented by circles) are found to lead to unacceptable values of* $\mathcal{M}(x) \leq 0$, *and others (represented by pluses) lead to acceptable values. The exact (and a priori unknown)* $\mathcal{L}$ *is represented with a thin line, while its PCK-estimated counterpart, that is the set* $\{x \in \mathcal{D} | \hat{\mu}_{\hat{\mathcal{M}}}(x) = y_{adm}\}$ *is represented by a thick line. In (b), the lower bound of* $\mathcal{D}_f$, $\mathcal{D}_f^-$ *is represented in red, and in (c),* $\mathcal{D}_f^+$ *is represented in green. The resulting limit state margin*

---

[5] It has also been *combined with* importance sampling, as shown in Echard et al. (2013)

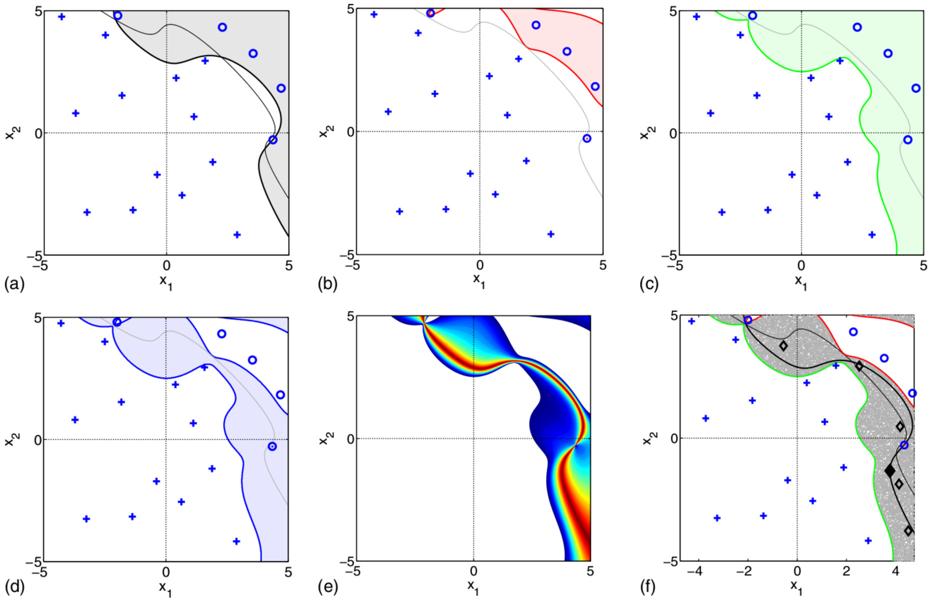

Figure 2.3: Design enrichment procedure for $M = 2$. See the main text for explanations. From Schöbi et al. (2016).

$\mathbb{L}$ is represented in (d). A color map of the probability of misclassification $P_m(x)$ within the limit state margin is represented in (e). In (f), the black diamond is the sample in $\mathcal{S}$ with the largest P_m, while the five other diamonds have been selected using multiple points enrichment. Note that multiple point enrichment refines the PCK on larger portions of $\mathcal{D}$ near $\mathcal{L}$, even if none of the selected point is the one featuring the largest $P_m(x)$.

2.4 Summary

We have in this chapter introduced two types of surrogate models, namely PCE and PCK surrogate models. We have also shown how each of them could assist us in solving uncertainty quantification problems listed in Section 2.1.1, such as uncertainty propagation, sensitivity analysis, and reliability analysis, when complex functions $\mathcal{M}$ were involved.

As a complement to the present chapter, the interested reader could consult Le Gratiet et al. (2015) which shows how Kriging surrogate models (such as the one introduced in Section 2.3.2) could also be used for sensitivity analysis, and Owen et al. (2015) which presents a general comparison between PCE and Kriging surrogate models.

Chapter 3

New method for the fidelity analysis of CPEMs

In this chapter, we first define a framework which enables us to formalize the Research Questions (RQ) stated in Section 1.3.1. Then, in Section 3.2.1, by combining this framework with the tools presented in Chapter 2, we present a method to address the RQ. Finally, in Section 3.3, we apply the presented method to a simple CPEM, namely a coupled linear oscillator, with one oscillator being physical and the other one numerical. The proposed method, together with case studies, has been partially presented in Sauder et al. (2018) and Sauder et al. (2019).

3.1 Reformulation of the problem

3.1.1 Modeling of cyber-physical empirical setups

Let s denote the total number of substructures. We consider a substructural partition[1], as represented on the left hand side of Figure 3.1 for $s = 3$. Given a duration $T > 0$, let $\tau(t) = (\tau_1(t), ..., \tau_s(t))$ represent an exogenous excitation, with support $[0, T]$, acting on the substructural partition. A generic way of modelling the emulated system after substructuring, which is suitable for most existing applications of CPEMs, is the following interconnected system:

$$\forall i \in \mathbb{N}_s^*, \quad \dot{x}_i = f_i(x_i, u_{ij}, \tau_i) \tag{3.1}$$

$$y_i = h_i(x_i) \tag{3.2}$$

---

[1] The terms used in this section, such as substructural partition, emulated system, etc... have been defined in Chapter 1.

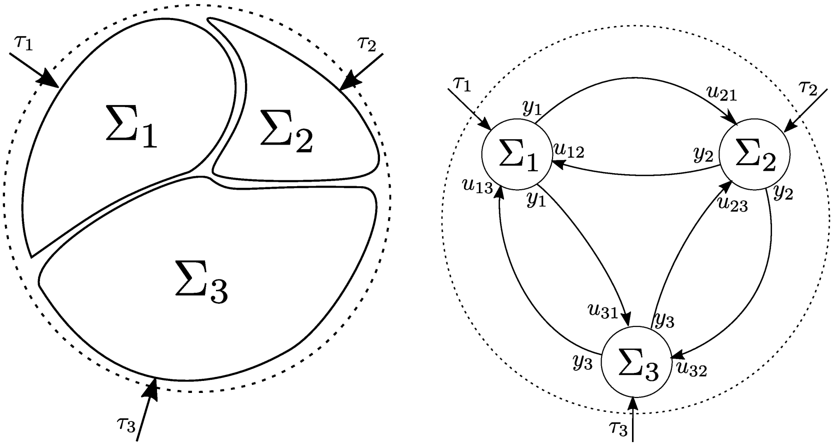

Figure 3.1: Conceptual representation (l.h.s) and block diagram (r.h.s.) of the *emulated* system, substructured with $s = 3$. Note that, for clarity, the outputs $(y_i)_{i \in \{1,2,3\}}$ are doubled in the block diagram.

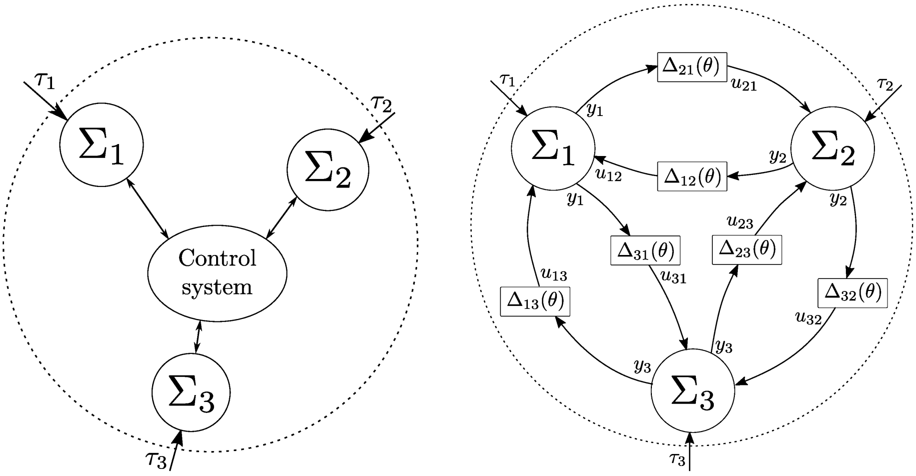

Figure 3.2: Conceptual representation (l.h.s) and block diagram (r.h.s.) of the *CPEM*, including the control system, with $s = 3$. Note that, for clarity, the outputs $(y_i)_{i \in \{1,2,3\}}$ are doubled in the block diagram.

and

$$\forall i \in \mathbb{N}_s^*, \forall j \in \mathbb{N}_s^* \setminus \{i\}, u_{ij} \equiv y_j \tag{3.3}$$

where x_i is the internal state of substructure Σ_i, y_i its output, and u_{ij} is the input to Σ_i originating from Σ_j. A block diagram of this interconnected system is presented on the right hand side of Figure 3.1. The y_i and u_{ij} are related to the power continuously exchanged between the substructures. If y_i represents a *flow*, such as a velocity or an electrical current, then $\forall j \neq i, u_{ij}$ represent *efforts*, such as a force or a voltage, and vice versa. The behaviour of the (ideal) substructured system, described by equations (3.1)-(3.3), is identical to the behaviour of the *emulated system*, but does not account for the effect of the control system.

Definition 18. *An* artefact Δ_{ij} *is a parametrized function describing the effect the control system on the connection between the output of substructure* Σ_j *and the input of* Σ_i.

Artefacts are not necessarily first principles-based models of the components of the control system, but model the consequences, on the exchanged signals, of including these components in the substructural partition. In other words, two components of the control system of different natures, such as a communication link or an actuator, could in a first approximation, be modelled by the same artefact, such as a time delay.

An artefact Δ_{ij} consists in general of a combination of *elementary* artefacts of various natures (heterogeneous), which simultaneously affect the signal. The effect of selected elementary artefacts on a reference signal is shown in Figure 3.3a, and more examples of elementary artefacts, together with their possible sources, are given in Table 3.1. The properties of each elementary artefact are described by one or several parameters denoted θ_i with support $\mathcal{D}_i \subset \mathbb{R}$, and described in the third column of Table 3.1.

Example 13. *The* signal loss *elementary artefact is parametrized by a probability of occurrence* $\theta_1 \in [0, 1)$ *and an inverse duration parameter* $\theta_2 > 0$. *When it occurs, the duration* d *of the signal loss is distributed as* $f_D(d) = \theta_2 e^{-\theta_2 d}$, *with both mean and standard deviation equal to* $1/\theta_2$

The artefact Δ_{ij} presented in Figure 3.3b consists of five elementary artefacts, and is parametrized by six values: the scaling factor, bias value, noise variance, duration of the delay, probability of occurrence of the signal loss, and inverse duration parameter of the signal loss. The effect of such a "composite" artefact on an input signal is illustrated in Figure 3.3c. Note that in the present work, there has not been made any attempt to achieve the *unicity* of the decomposition of an artefact into elementary artefacts.

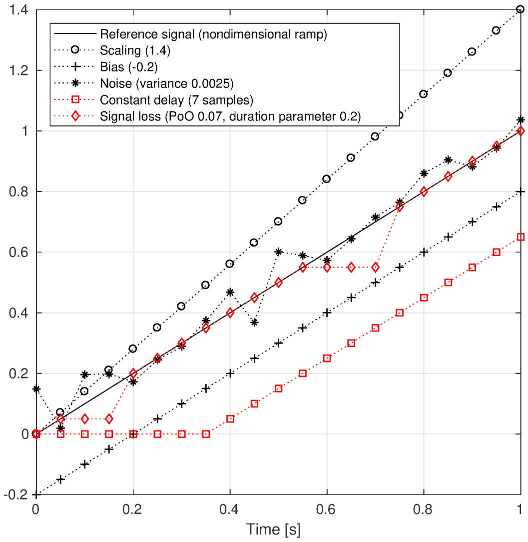

(a) Effect of elementary artefacts on a reference signal. The parameter(s) of each elementary artefact is/are given in parenthesis. See Table 3.1 for a description of these parameters.

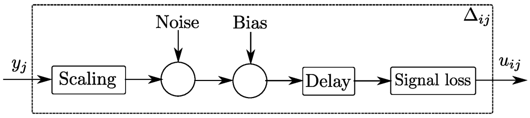

(b) Synthesis of an artefact Δ_{ij} from the elementary artefacts above.

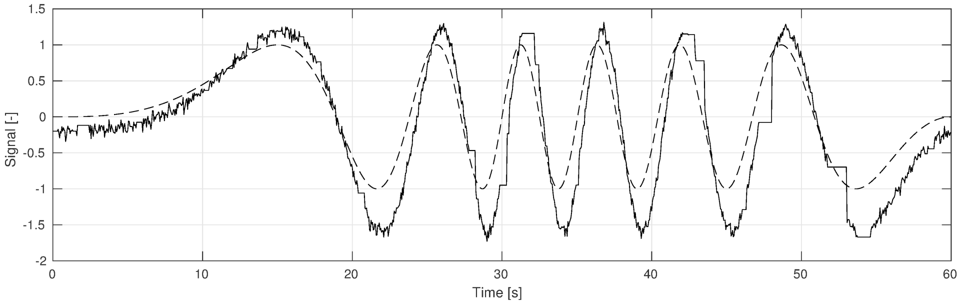

(c) Effect of Δ_{ij} on a reference signal represented by a dashed line.

Figure 3.3: Construction of an artefact from elementary artefacts, and effect on a reference signal.

Table 3.1: Examples of elementary artefacts, their possible sources, and the corresponding describing parameters (component of θ).

Elementary artefact	Example of sources	Describing parameter(s)
Gain	calibration error actuator limitations	scaling factor
Bias	zero measurement	bias value
Noise	measurement noise	noise variance
Constant time delay	computational time communication time	duration
Signal loss	unfinished iteration process faulty position measurement	probability of occurrence inverse duration parameter
Quantization	analog to digital conversion	resolution
Zero-order hold	sampling	sampling period
Saturation	actuator limitations	saturation threshold
1^{st}-order dyn. sys.	actuator dynamics	time constant
2^{nd}-order dynamical system	transfer system dynamics (spring, cables, ...)	natural frequency damping ratio
dynamic bias	sensor drift	first-order Markov process rate

The ideal interconnection represented in Figure 3.1 can now be modified, to model the effect of the control system on the signals. This is done as shown on the right hand side of Figure 3.2. Equations (3.1) and (3.2) remain valid, but the relationship (3.3) between the output of substructure j and the input to substructure i originating from substructure j becomes: $\forall i \in \mathbb{N}_s^*, \forall j \in \mathbb{N}_s^* \setminus \{i\}, \forall t > 0$,

$$u_{ij}(t) = \Delta_{ij} \left(\left(y_j(t') \right)_{t' \in [0,t]}, \theta \right) \tag{3.4}$$

where $\theta \in \mathcal{D} \subset \mathbb{R}^M$ gathers *all* the θ_i parameters describing the elementary artefacts in *all* Δ_{ij}. In other words, if the artefact Δ_{ij} presented in Figure 3.3b was affecting all interconnections in Figure 3.2, then θ would be of dimension $M = 36$ (6 artefacts × 6 parameters per artefact).

Remark 3. *As discussed in 1.2.2, owing to the presence of* numerical *substructures among the Σ_i, modeling the such an interconnection would in principle imply the use of digital or hybrid control theory, see e.g. Tabuada et al. (2014); Goebel et al. (2012). In the particular case of CPEM, however, the "cyber" parts of the system (the numerical substructures) represent continuous dynamical systems. Assuming that adequate time-stepping algorithms are employed, see e.g. Bursi et al. (2013), we can make abstraction of their digital nature. Note, however, that some aspects related to the digital nature of the hardware, such as quantization, sampling, and zero-order hold, can be approached by the present method, by modeling them as artefacts.*

3.1.2 Fidelity

According to Definition 6, the concept of fidelity translates the capacity of the setup represented in Figure 3.2 to "resemble" the one represented in Figure 3.1. This resemblance can be measured by the fact that some quantities of interest (QoI) remain undisturbed in spite of the artefacts introduced by the control system. Based on the model established in Section 3.1.1, we now introduce a quantitative definition of the fidelity of a CPEM.

For $i \in \mathbb{N}_s^*$, let $\bar{x}_i$ denote the state of Σ_i when $\forall j \neq i, u_{ij} \equiv y_j$. In that case, no artefact is present, and the CPEM behaves exactly as the emulated system. For a given $Q \in \mathbb{N}^*$, let then $(\gamma_q)_{q \in \mathbb{N}_Q^*}$, be a family of cost functions satisfying

$$\forall q \in \mathbb{N}_Q^*, (\forall i \in \mathbb{N}_s, x_i|_\theta \to \bar{x}_i) \Rightarrow (\gamma_q \to 0) \tag{3.5}$$

Definition 19. *The* fidelity φ *is defined as*

$$\begin{aligned}\varphi :& \mathcal{D} \to \mathbb{R} \\ \theta \mapsto& -\frac{1}{2} \log \sum_{q \in \mathbb{N}_Q^*} \gamma_q^2(\{x_i|_\theta(t), \bar{x}_i(t)\}_{i \in \mathbb{N}_s^*, t \in [0,T]})\end{aligned} \tag{3.6}$$

The rationale behind the proposed definition is the following.

1. Each γ_q function compares selected QoI derived from the states $(x_1, x_2, ..., x_s)|_\theta$ with the corresponding QoI derived from $(\bar{x}_1, \bar{x}_2, ..., \bar{x}_s)$. If all states x_i converge towards $\bar{x}_i$, then all γ_q tend to zero, and $\varphi \to \infty$. Fidelity quantifies therefore the capability of the CPEM to generate QoIs that are similar to the real system, when subjected to same excitation.
2. The reciprocal is however not true: high fidelity can be achieved even if some states x_i which are *not* of interest, i.e. not included in the calculation of any γ_q, differ from $\bar{x}_i$. This is a major difference with the concept of *resilient* cyber-physical systems (Fawzi et al., 2014). A high fidelity value does not imply a correct estimation of the complete state $(x_i)_{i \in \mathbb{N}_s^*}$ in presence of artefacts, but rather a correct estimation of selected state-derived quantities.
3. If the cyber-physical system becomes unstable because of the introduced artefacts, some γ_q may blow up in some domains of $\mathcal{D}$. On the other hand, when studying *high-fidelity* setups, we may be interested in emphasizing the difference between small values of the γ_q. The logarithm in (3.6) is introduced for this reason.
4. A sum of the squares, rather a *maximum* function, is used in (3.6) to combine the cost functions γ_q, which preserves the smoothness

properties of the functions $\theta \mapsto \gamma_q(\theta)$. Using a *maximum* function instead would have compromised the differentiability of φ even if the γ_q were smooth functions. This choice will prove convenient when analyzing the problem.

Definition 19 is rather general, and must be adapted to the specific problem at hand. More specifically, the exogenous excitation τ, and the functions γ_q that *select* and *compare* the QoI, should be carefully defined.

The excitation $\tau(t)$ must reflect the loads that the empirical setup will eventually be subjected to. It may for instance include impulsive loads, ramps, frequency sweeps, pink noise, or combine several of the above. If nonlinear effects are significant, several excitation levels should be included.

The selection of the QoI through the γ_q functions must be connected to the very *purpose* of the tests, and may not necessarily be related to the outputs y_i that play an active role in the interconnection. To illustrate this, let us consider again Example 5 in Chapter 1. The overall objective of active truncation was for the truncated line to replicate the behaviour of a non-truncated line, *in interaction with the floater*. In this setting, the behaviour of the truncation point (physical location of the interconnection) is of no interest, as opposed to the other extremity of the physical substructure (connected to the floater) whose behaviour is of high interest.

QoI may also be of different natures. They can be time series or more generally fields, such as in Drazin et al. (2015). They can also be *derived* quantities, such as statistical moments, parameters of extreme value distributions, or transfer functions. The QoI should obviously be selected carefully, and in accordance with the purpose of the tests, since the fidelity, calculated from the extrema of a signal for instance, will convey a very different type of information from the fidelity calculated from the full time series.

To be meaningful, a fidelity value should always be related to a given CPEM, and stated together with the excitation τ and the selection/cost functions γ_q that have been used to compute it.

3.1.3 Reformulation of the Research Questions.

The concepts introduced in the previous sections enabled us to define, in a quantitative manner, the fidelity φ of a CPEM. Our objective is to investigate how the control system, modelled by the artefacts $\Delta_{ij}(\theta)$, may deteriorate the fidelity. Even if CPEM are developed in a controlled laboratory environment, some uncertainty is entailed to the artefacts: sensor noise variance, or the interconnection delays between the substructures, remain for example uncertain at the design stage, may vary during the execution of the experiment, and can only be quantified accurately when the experiment has finished. However, the *amount of uncertainty* on these quantities can be estimated from expert judgment or dedicated surveys, as discussed in 2.1.2, and therefore modeled within a probabilistic framework.

Assumption 1. *The artefact parameter θ is the realization of a multidimensional random variable Θ with a known, but* arbitrary*, distribution f_Θ.*

The RQ outlined in Section 1.3.1 can now be reformulated as follows. **(RQ1)** *Sensitivity*: which component of Θ does influence the most $\varphi(\Theta)$? **(RQ2)** *Probabilistic robust fidelity*: given a minimum admissible fidelity $\varphi_{\mathrm{adm}} \in \mathbb{R}$, and given a maximum acceptable probability of failure $\varepsilon_{\mathrm{adm}} \in (0, 1)$, does $P[\varphi < \varphi_{\mathrm{adm}}] \leq \varepsilon_{\mathrm{adm}}$ hold? **(RQ3)** *Fidelity bounds*: what is the set of artefact parameters θ which leads to $\varphi(\theta) > \varphi_{\mathrm{adm}}$?

Formulated in this way, RQ2 and RQ3 can be seen as variations of a class of problems referred to as *probabilistic robust analysis of control systems*, an account of which has been given by Calafiore et al. (2011). Probabilistic robustness has been shown to have great advantages, in terms of conservatism and complexity, when compared to the classical *worst-case* robustness[2]. See for instance Tempo et al. (2013), Chapter 5, and the case study in Chen et al. (2005).

The main drawback of probabilistic approaches is that estimating the probability in RQ2 implies the evaluation of a multidimensional integral over $\mathcal{D}$. This is challenging in high-dimensions M and when non-analytic models are involved, which is a typical situation encountered when dealing with CPEMs. Indeed, (1) the Σ_i representing *numerical* substructures may typically consist in complex computer programs, see Examples 1-5. Furthermore, (2) for the purpose of the analysis, the Σ_i representing the *physical* substructures, in which the most challenging physics generally takes place, must be modeled in a rather realistic way. In practice, this means that the f_i and h_i functions are often *black box* functions, for which no analytical or even closed-form expressions exist.

To address such problems, so-called *randomized algorithms* have been developed (Tempo et al., 2013), which rely on *sampling* the performance function, here $\varphi(\theta)$. The required number of samples is however large for highly reliable CPEM (Alamo et al., 2015). This becomes an issue when the f_i functions are costly to evaluate. As discussed in Chapter 1, a "classical" approach would be to simplify the Σ_i, but this would be detrimental for the fidelity analysis, since some important information about the substructures

---

[2] in which bounds only, and no probabilistic information regarding Θ is available.

could be lost. The analysis method proposed in the next section aims at avoiding such a compromise.

3.2 Proposed fidelity analysis method

The reformulation of the RQ in the previous section, combined with the theoretical background introduced in Chapter 2, yields a natural approach to address our RQ, which will be outlined in the following. Let us first define, consistently with Definitions 15 and 16, the following sets.

Definition 20. *The* domain of failure *of a CPEM is the set* $\mathcal{D}_f \subset \mathcal{D}$ *defined by:*

$$\mathcal{D}_f := \{\theta \in \mathcal{D} | \varphi(\theta) \leq \varphi_{adm}\} \tag{3.7}$$

Definition 21. *The* limit state surface $\mathcal{L} \subset \mathcal{D}$ *is defined by*

$$\mathcal{L} := \{\theta \in \mathcal{D} | \varphi(\theta) = \varphi_{adm}\} \tag{3.8}$$

We notice that addressing RQ2 and RQ3 is equivalent to identifying $\mathcal{D}_f$. Indeed, identifying $\mathcal{D}_f$ answers immediately RQ3 since the θ leading to sufficiently high fidelity are found in $\mathcal{D} \setminus \mathcal{D}_f$. Then, letting $\mathbb{I}_{\mathcal{D}_f}(\theta)$ be the indicator function for $\mathcal{D}_f$, the probability of failure of a CPEM, involved in RQ2, can be evaluated from

$$P_f := \int_{\mathcal{D}_f} f_\Theta(\theta) d\theta = \int_{\mathcal{D}} \mathbb{I}_{\mathcal{D}_f}(\theta) f_\Theta(\theta) d\theta \tag{3.9}$$

3.2.1 Solution outline

As noted in Section 3.1.3, the functions f_i describing the substructure dynamics, and hence involved in the calculation of φ, may be non-analytical or so-called *black boxes.* A sampling-based approach must therefore be employed to address our RQ. The solution we propose is presented as a flow chart in Figure 3.4, and described in the following.

Step 1 First, N samples of Θ in $\mathcal{D}$ are generated using a *space-filling* sampling method.

$$\mathcal{E} := (\theta^{(1)}, \theta^{(2)}, ..., \theta^{(N)})^\top \tag{3.10}$$

For each sample θ, the interconnected system including artefacts (represented in Figure 3.2), when subjected to τ, is *co-simulated*[3]. The fidelity $\varphi(\theta)$ is

---

[3] This term will be defined and details about these co-simulations will be given in Section 3.2.2.

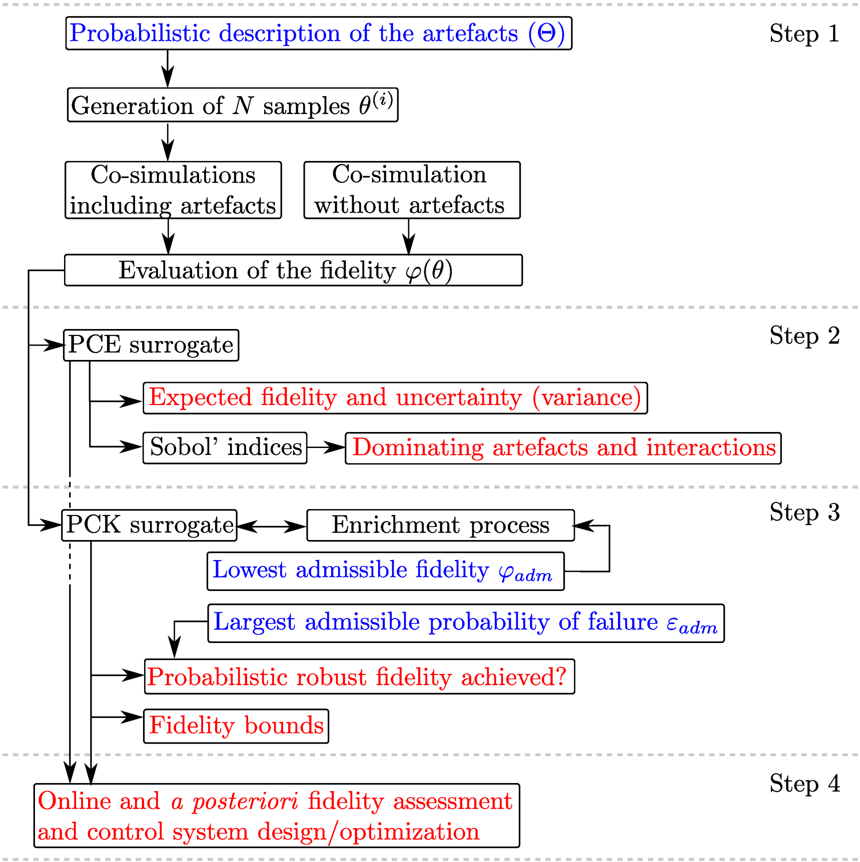

Figure 3.4: Overview of the analysis method. Inputs are represented in blue and outputs in red.

obtained for each $\theta^{(i)}$ by comparing the result of this co-simulation to the one *without* artefacts (Figure 3.1) using (3.6). We let

$$\mathcal{F} := [\varphi(\theta^{(1)}), \varphi(\theta^{(2)}), ..., \varphi(\theta^{(N)})]^\top \tag{3.11}$$

Step 2 By using $\mathcal{E}$ and $\mathcal{F}$, a PCE-based surrogate model of φ is constructed as outlined in Section 2.2. The expected fidelity $\mathrm{E}[\varphi]$ and the associated uncertainty $\mathrm{Var}[\varphi]$ can be estimated from this surrogate model (Section 2.2.4). The sensitivity of φ to the components of Θ can be expressed through the Sobol' indices derived from the PCE (Section 2.2.5), which answers RQ1.

Step 3 We stated that RQ2 and RQ3 can be solved through the identification of $\mathcal{D}_f$. However, at the present stage, the information available on φ is insufficient for this purpose. Indeed, as discussed in 2.3.4, $\mathcal{E}$ was so far aimed at *filling* the space $\mathcal{D}$, and not at resolving $\mathcal{L}$. If $\mathrm{E}[\varphi]$ is well above φ_{adm} and $\mathrm{Var}[\varphi]$ is small, it may happen that none of the samples in $\mathcal{E}$ yields too low fidelity.

By using the Adaptive Kriging technique discussed in 2.3.4, additional relevant samples of Θ can iteratively be generated to enrich $\mathcal{E}$ and resolve the boundaries of $\mathcal{D}_f$. The resulting PCK surrogate model, whose accuracy near $\mathcal{L}$ step-by-step increases, can be interrogated to find out if a given θ is in $\mathcal{D}_f$ or not (answer to RQ3). Furthermore, MCS, using a large number of auxiliary samples can be performed, with the PCK model, to calculate P_f. This allows to verify probabilistic robustness of the setup, and answer (RQ2).

Step 4 The PCE and PCK surrogate models established in Steps 2 and 3, respectively, can be used to perform *online*, or *a posteriori*, fidelity assessment of a test based on measured or estimated values of θ. The PCK model will be correct in sign when θ is near the boundary of $\mathcal{D}_f$, and adequate if we wish to know whether sufficient fidelity has been achieved. The PCE model can be used when θ takes higher probability values to document the achieved fidelity value.

Furthermore, using the defined surrogate models, an optimal control system design can be found as the one minimizing some cost function $c(\theta)$, maximizing the fidelity, and with a hard constraint on the minimum fidelity:

$$\underset{\theta\in\mathcal{D}}{\text{minimize}}\ w_1 c(\theta) - w_2 \hat{\varphi}_{\mathrm{PCE}}(\theta) \text{ subject to } \hat{\varphi}_{\mathrm{PCK}}(\theta) - \varphi_{\mathrm{adm}} \geq 0 \tag{3.12}$$

where w_1 and w_2 being positive weights. In the next section, we will provide some more details regarding the computer implementation of this method.

It will then be applied on a simple example, with additional explanations and details, in Section 3.3.

3.2.2 Co-simulation and fidelity calculation

In Steps 1 and 3, $\varphi(\theta)$ must be evaluated for given samples $\theta^{(i)}$ of Θ. This is done by using equation (3.6), which involves the time-histories of the states $\bar{x}_i$ and $x_i|_\theta$. These latter are found by *co-simulating* the substructured emulated system, described by (3.1)-(3.3), and the substructured system *subjected to the artefacts* parametrized by θ, which is described by (3.1), (3.2), and (3.4).

Definition 22. *Co-simulation is a simulation technique in which the computations associated with different substructures Σ_i are performed independently from each other, and the exchange of data between the substructures is restricted to discrete synchronization points*[4].

Algorithm 1 presents the iterative co-simulation procedure that has been developed to generate the time histories of $\bar{x}_i$ and $x_i|_\theta$. In this algorithm, after the initialization phase on lines 1-3, the co-simulation is performed for the time interval $[0, T]$on lines 4-21. The synchronization between the substructures is carried out in the `while` loop located on lines 8-19. The algorithm can be used for the co-simulation of a system with or without artefacts, by selecting either line 14 or line 15, respectively.

A *synchronization time step δt* is introduced at line 4. It is the duration between two time instants, at which dynamic equilibrium between the substructures shall be fulfilled when co-simulating the emulated system. Dynamic equilibrium is checked via a *convergence criterion*, stated on Line 8, that involves the exchanged signals $u_{ij}(t + \delta t)$, between two successive iterations indexed by $k - 1$ and k. In more precise terms, it is checked that the values of all these quantities differ, in infinite norm, by less than a set of pre-defined thresholds ϵ_{ij}, between two iterations. Note that the time integration performed *within each substructure* (Line 10) may require smaller internal time steps than δt, and may be steered by an adaptive step size algorithm.

When artefacts are present (i.e. line 14 is used instead of line 15), they prevent equilibrium between the substructures Σ_i to be fulfilled . Indeed, the flow and effort the substructures "perceive" from each other are modified by

---

[4] This definition is adapted from (Skjong, 2017, Definition 2.2). See also Sadjina et al. (2017) for a good introduction to co-simulation, in particular when applied to marine systems.

Algorithm 1 Pseudo-code for co-simulation

```
$\forall i \in \mathbb{N}_s^*$, initialize the $x_i(t=0)$
$\forall i \in \mathbb{N}_s^*$, evaluate $y_i(0)$ from (3.2)
$\forall i \in \mathbb{N}_s^*, \forall j \in \mathbb{N}_s^* \setminus \{i\}$, $u_{ij}(0) \leftarrow y_j(0)$
for $t \in \{0, \delta t, ..., T - \delta t\}$ do
    $u_{ij}^{(-1)}(t + \delta t) \leftarrow \infty$
    $u_{ij}^{(0)}(t + \delta t) \leftarrow u_{ij}(t)$
    $k \leftarrow 0$
    while $\exists i \in \mathbb{N}_s^*, j \in \mathbb{N}_s^* \setminus \{i\}, \|u_{ij}^{(k)}(t + \delta t) - u_{ij}^{(k-1)}(t + \delta t)\|_\infty \geq \epsilon_{ij}$ do
        for $i \in \mathbb{N}_s^*$ do
            Perform time-integration of $\Sigma_i$ from $t$ to $t + \delta t$ according to (3.1)
            (note: $\forall j \in \mathbb{N}_s^* \setminus \{i\}$, $u_{ij}$ varying linearly from $u_{ij}(t)$ to $u_{ij}^{(k)}(t + \delta t)$)
            Evaluate $y_i(t + \delta t)$ from (3.2)
            for $j \in \mathbb{N}_s^* \setminus \{i\}$ do
                Evaluate $u_{ji}^{(k)}(t + \delta t)$ from $\{y_i(t'); t \in [0, t + \delta t]\}$ and (3.4)
                or when co-simulating the emulated system: $u_{ji}^{(k)}(t + \delta t) \leftarrow y_i(t + \delta t)$
            end for
        end for
        $k \leftarrow k + 1$
    end while
    $u_{ij}(t + \delta t) \leftarrow u_{ij}^{(k)}(t + \delta t)$
end for
```

the artefacts. In that case, Algorithm 1 ensures consistency of all exchanged signals, accounting for the substructures' dynamics *and* the presence of artefacts.

While dynamic equilibrium should in principle be fulfilled in a *continuous* and *exact* manner, the equilibrium achieved in a co-simulation is neither exact, as it depends on $\epsilon_{ij} > 0$, nor continuous as it is only ensured every $\delta t > 0$. The result $(\bar{x}_i(t))_{i \in \mathbb{N}_s^*, t \in [0,T]}$ of a co-simulation of the emulated system will therefore differ from the result $(x_i^*(t))_{i \in \mathbb{N}_s^*, t \in [0,T]}$ that would have been obtained if dynamic equilibrium was fulfilled in an exact and continuous way. As classically done in computational physics, a *convergence study* must therefore be carried out, to define adequate values of δt and ϵ_{ij}, and possibly other parameters involved in the Σ_i, that yield "small enough" errors between $(\bar{x}_i)$ and (x_i^*).[5] The magnitude of this admissible error depends on the objective of the co-simulation. In our method, the co-simulation result is going to be used in a fidelity calculation (3.6), that is a comparison of $(x_i|_\theta)$ with $(\bar{x}_i)$ using the squared γ_q functions. So, for $(\bar{x}_i)$ to adequately represent (x_i^*) in this context, $(\bar{x}_i)$ should be is much closer

---

[5] The indexing ${}_{i \in \mathbb{N}_s^*, t \in [0,T]}$ is omitted for clarity.

to (x_i^*) than to any of the $(x_i|_\theta)$. This can be formulated as

$$\forall q \in Q, \theta \in \mathcal{D}, \gamma_q(\bar{x}_i, x_i^*)^2 \ll \gamma_q(x_i|_\theta, \bar{x}_i)^2 \tag{3.13}$$

In practice, it means that studying higher fidelity setups, for which all $\gamma_q(x_i|_\theta, \bar{x}_i)$ are small, will set more stringent requirements on the accuracy of the co-simulation. In that case, small values for δt and ϵ_{ij} will be needed, which in turn increases the required computational budget. This will be investigated in detail in the case study presented in Chapter 4.

Remark 4. *If in accordance with the criterion* (3.13)*, the synchronization time step δt in Algorithm 1 should be chosen equal to the minimum loop time of the control system orchestrating the CPEM. This simplifies the modeling and implementation of artefacts changing at this rate or at lower ones, such as noise and zero-order hold artefacts.*

Let us finally stress that the *duration of the co-simulation T* should be large enough, when elementary artefacts that involve randomness are included. This is in order to ensure that the result of a co-simulation is statistically representative of the given value of θ. Indeed, let us consider the signal loss artefact (see Table 3.1 and Example 13). If its probability of occurrence is small compared to $\delta t/T$, signal loss occurs seldom in $[0, T]$. If in addition, it has an inverse duration parameter small compared to $1/T$, signal loss would last (in average) for a sensible portion of $[0, T]$. In that case, $(x_i|_\theta)$ would not be representative of θ, since another realization of *this* artefact (same θ, but signal loss occurring for instance at a different time instant) would lead to a significantly different response.

3.2.3 PCE and PCK: implementation and parameters

In the present work, the surrogate models have been established as outlined in Section 3.2.1 by using the UQLab software, developed at the *Chair of Risk, Safety & Uncertainty Quantification*, at ETH Zürich (Marelli and Sudret, 2014). UQLab is developed in the Matlab programming language, and implements state-of-the-art UQ methods, but also results of recent research such as the APCK-MCS method presented in 2.3.4, which has been used here. The reader is referred to Marelli and Sudret (2017) for the documentation of UQLab related to PCE, to Marelli et al. (2017a) for sensitivity analysis, to Schöbi et al. (2017) for PCK, and to Marelli et al. (2017b) for rare events estimation, and Adaptive Kriging in particular.

When defining the PCE surrogate model (Step 2), the LAR method described in Section 2.2.2 was used. The truncation set used at the initiation of the LAR method is the hyperbolic truncation set given by (2.12), where $q = 0.75$. The second row of Figure 2.1 illustrates which polynomials are retained in this truncation set in the case $M = 2$.

```
MetaOpts.Method = 'LARS';
MetaOpts.TruncOptions.qNorm = 0.75;
```

The analysis in Step 3 that involves PCK and AK-MCS is performed as described in Section 2.3.4. The PCK model is based on the Matérn correlation function with $\nu = 5/2$, see (2.35), which assumes that $\theta \mapsto \varphi(\theta)$ is twice continuously differentiable. The hyperparameter l in the correlation function is found by global optimization, using a genetic algorithm with 20 stall generations (Goldberg, 1989). The corresponding configuration options in UQLab read:

```
ROpts.Method = 'AKMCS';
ROpts.AKMCS.MetaModel = 'PCK';
ROpts.AKMCS.PCK.Kriging.Corr.Type = 'ellipsoidal';
ROpts.AKMCS.PCK.Kriging.Corr.Family = 'matern-5_2';
ROpts.AKMCS.PCK.Kriging.Optim.Method = 'ga';
ROpts.AKMCS.PCK.Kriging.Optim.GA.nStall = 20;
```

As explained in Section 2.3.4, once the PCK surrogate model of φ is established, MCS is performed using a large set $\mathcal{S}$ of auxiliary samples of Θ, in order to estimate P_f, see (2.50). The confidence interval on P_f depends on the cardinality $|\mathcal{S}|$, and for low values of P_f and tight confidence intervals, the required $|\mathcal{S}|$ may become very large.

```
ROpts.Simulation.MaxSampleSize = 1e6;
```

In UQLab, MCS is performed by calling the PCK once in a vectorized way. This may require too much memory for large $|\mathcal{S}|$. To alleviate this issue, it is possible to split the call to the PCK into several calls or "chunks" of given maximum sample size, which are then treated sequentially.

As discussed in Section 2.3.4, an enrichment step of Adaptive Kriging can generate $K > 1$ new interesting samples of Θ at which φ should be evaluated. These samples are chosen by using a learning function based on the probability of misclassification (2.52). The new co-simulations, and fidelity calculations, to be performed are independent of each other, and have therefore been parallelized. The number of new samples that should be generated during the enrichment depends on the available hardware and on the dimensionality of the problem. In the case studies which we will report in Chapter 5, we explore a twelve-dimensional space, and we found beneficial to add a "maximum" number of new samples at each step. This amount was set to 16, which was the maximum number of processes that could be run simultaneously on one node of the cluster we had access to.

```
ROpts.AKMCS.LearningFunction = 'U';
ROpts.AKMCS.NEnrich = 16;
```

The analysis stopped when the uncertainty on the estimated probability of failure is deemed small enough. It is quantified by comparing the probabilities estimated from $\mathcal{D}_f^+$ and $\mathcal{D}_f^+$ defined in (2.53) and (2.54), respectively. If the difference between them is less than 1% of P_f estimated from the mean of the PCK, convergence is considered to be achieved. The corresponding configuration command reads:

```
ROpts.AKMCS.Convergence = 'stopPf';
ROpts.Simulation.Alpha = 1e-2;
```

3.3 Example: coupled linear oscillators

The method presented in the previous section will now be illustrated with a simple example.

3.3.1 Description of the problem

The system under study is the coupled linear oscillators represented in Figure 3.5. Each oscillator, denoted Σ_i, consists of a mass m_i, a damper c_i and a spring k_i. The left hand side (l.h.s.) of Σ_1 is fixed, while its right hand side (r.h.s.) is free to oscillate, and subjected to the force applied by the l.h.s. of Σ_2. The r.h.s. of Σ_2 is subjected to a unit step force $\tau_2(t)$, and we wish to investigate the velocity response of the application point of τ_2 during $T = 100$ s. The undamped eigenfrequencies of this system are

$$\omega_\pm^2 = \frac{\omega_1^2 + \omega_2^2 + \chi^2}{2}\left(1 \pm \sqrt{1 - \frac{4\omega_1^2\omega_2^2}{(\omega_1^2 + \omega_2^2 + \chi^2)^2}}\right) \tag{3.14}$$

where $\omega_1 = \sqrt{k_1/m_1}$, $\omega_2 = \sqrt{k_2/m_2}$ and $\chi = \sqrt{k_2/m_1}$. Setting $m_1 = m_2 = m = 1$kg and $k_1 = k_2 = k = 1$N/m leads to

$$\omega_\pm^2 = \frac{3k}{2m}\left(1 \pm \sqrt{\frac{5}{9}}\right) \tag{3.15}$$

Inserting numbers, $\omega_+ = 1.62$ rad/s and $\omega_- = 0.62$ rad/s. The damping coefficients c_1 and c_2 are both set to 1% of $2\sqrt{km}$, leading to a lightly damped system.

For the sake of the example, let us assume that the behaviour of this system is to be investigated by a CPEM. The coupled oscillator is partitioned into $s = 2$ substructures, where Σ_1 is the numerical substructure and Σ_2 the physical substructure. The force measured on the l.h.s. of Σ_2 is input to the computer code representing Σ_1 as a force acting on the r.h.s. of Σ_1. The computed velocity response of Σ_1 is then actuated on the l.h.s. of Σ_2.

The effect of the control system, including the force sensor, the velocity actuator, and other intermediate components, is modeled by the following set of artefacts. The force measurement is affected by a calibration error, i.e. a constant gain α_s, and a data processing-induced time delay τ_s. Similar artefacts affect the velocity actuation (parametrized by α_a and τ_a), representing a first approximation of the actuator dynamics (amplitude mismatch and lag). The artefact parameters are gathered in

$$\theta := (\alpha_s, \tau_s, \alpha_a, \tau_a)^\top \tag{3.16}$$

which is assumed to be the realization of random vector Θ with independent components. α_s and α_a are both assumed to be normally distributed, with unit mean and a standard deviation of 0.5%. The delays τ_s and τ_a are assumed to be uniformly distributed between 0 and 20ms.

The objective is to study the influence of these artefacts on the QoI for the problem, namely the velocity V_2 of mass m_2. Since $Q = 1$, the fidelity (3.6) can simply be written as

$$\varphi(\theta) := -\frac{1}{2}\log\gamma_1^2 \text{ where } \gamma_1^2(\theta) := \frac{\int_0^T [V_2|_\theta(t) - \bar{V}_2(t)]^2 dt}{\int_0^T \bar{V}_2(t)^2 dt} \tag{3.17}$$

In Figure 3.6, different realizations of Θ, leading to different velocity time series, and different fidelity values are compared. This illustrates how artefacts influence the QoI, and how this translates to a loss of fidelity.

Remark 5. *It is worth noting that, due to the nature of the present set of artefacts, some properties of this CPEM can be established from classical frequency domain analysis. The transfer function, in the Laplace domain, between τ_2 and the QoI V_2 indeed reads*

$$H(s) = \frac{s\,[P_1(s) + \alpha e^{-\tau s}(k_2 + c_2 s)]}{P_1(s)P_2(s) + \alpha e^{-\tau s}(k_2 + c_2 s)m_2 s^2} \tag{3.18}$$

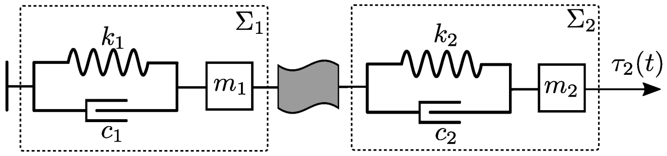

(a) Representation of the coupled linear oscillator. The grey flag-shaped block corresponds the interface where the sensor and actuator are introduced.

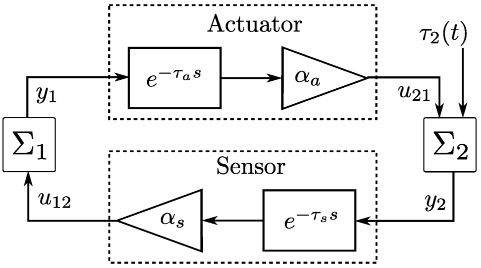

(b) Block diagram of the CPEM. Σ_1 is the numerical substructure and Σ_2 the physical substructure. The control system parametrized by $\theta = (\alpha_s, \tau_s, \alpha_a, \tau_a)^\top$

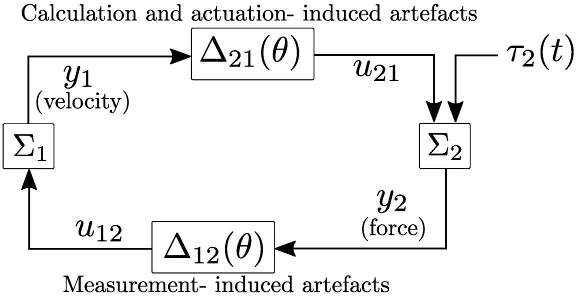

(c) Equivalent block diagram, with notations consistent with the formulation presented in Section 3.1.1, including the artefacts $\Delta_{12}(\theta)$ and $\Delta_{21}(\theta)$

Figure 3.5: CPEM for the study of coupled linear oscillators

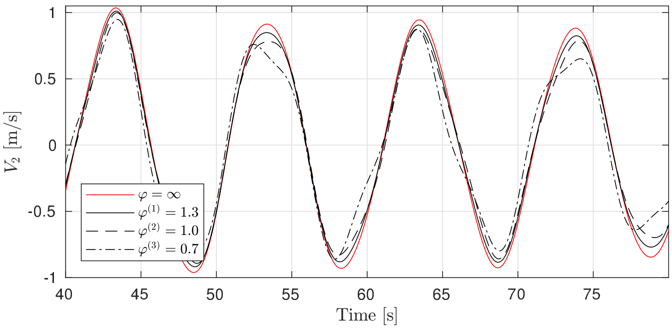

Figure 3.6: Time series of the QoI, in the absence and presence of artefacts (red and black curves, respectively). For the latter case, three different samples of Θ, leading to three values of φ are shown: $\theta^{(1)} = (1.007, 4.23, 0.993, 6.75)^\top$ (solid line), $\theta^{(2)} = (1.004, 10.33, 0.998, 12.31)^\top$ (dashed line), and $\theta^{(3)} = (0.990, 18.53, 0.993, 17.17)^\top$ (dash-dot line).

where $P_i(s) = m_i s^2 + c_i s + k_i$, $\alpha = \alpha_s \alpha_a$ *and* $\tau = \tau_s + \tau_a$. *Equation* (3.18) *indicates that* α_s *and* α_a *(resp.* τ_s *and* τ_a*) play symmetric roles, and that it is the* total *scaling factor* α *and the* total *delay* τ *that are of importance for this system.*

3.3.2 Expected fidelity, uncertainty and sensitivity

In Step 1, an initial set $\mathcal{E}$ containing N=100 samples of Θ is generated using LHS. The corresponding co-simulations are performed as described in Section 3.2.2. Since the linear oscillators are extremely fast to simulate, no convergence study on δt, ϵ_{12} and ϵ_{21} was performed. Their value were rather set to "conservative" values ensuring the accuracy of numerical integration, namely $\delta t = 1$ms (three orders of magnitude less than the lowest eigenperiod of the system), and $\epsilon_{12}[N]$ and $\epsilon_{21}[m/s]$ set to 2.22×10^{-15}, that is one order of magnitude above machine precision. For each of the N co-simulations, the value of φ is evaluated and stored in $\mathcal{F}$. In Figure 3.7, φ is plotted as a function of the components of the samples $\theta^{(i)}$. As expected, the general trend is that the fidelity decreases when τ_s and τ_a increase, and when α_s and α_a deviate from unity.

In Step 2, the two sets $\mathcal{E}$ and $\mathcal{F}$ are then used to establish the PCE surrogate model $\hat{\varphi}$, using the method outlined in Section 2.2. Since the artefact parameters are uniformly and normally distributed, Legendre and Hermite polynomials are used to build a (ψ_α) basis satisfying (2.9). This corresponds exactly to the bases used in Examples 8 and 9. The obtained PCE

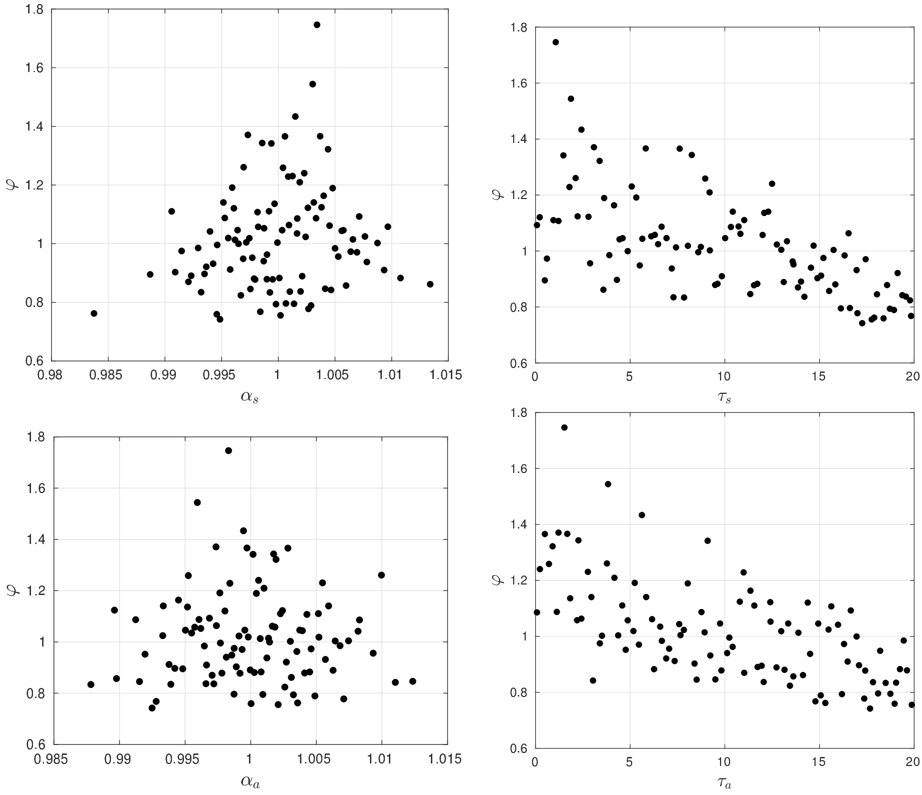

Figure 3.7: φ as a function of each component of $\theta^{(i)}$ for $N = 100$ samples of Θ. We recall that $\theta = (\alpha_s, \tau_s, \alpha_a, \tau_a)$.

surrogate model $\hat{\varphi}$ contains $|\mathcal{A}| = 27$ terms, and its associated normalized leave-one-out cross-validation error

$$\varepsilon_{\mathrm{LOO}} := \frac{E_{\mathrm{LOO}}}{\sqrt{\mathrm{Var}[\varphi(\Theta)]}} \tag{3.19}$$

is about 10%. From (2.19) and (2.21), we obtain directly that the expected value of the fidelity for this setup is $\mathrm{E}[\varphi(\Theta)] \approx 1.03$, and its standard deviation $(\mathrm{Var}[\varphi(\Theta)])^{1/2} \approx 0.18$. In other words, the dashed curve in Figure 3.6 represents an average situation, while the two other black curves represent "good" and "bad" cases with much lower probability of occurrence.

To identify which artefacts have the greatest impact on the fidelity, Sobol' indices are evaluated as described in Section 2.2.5. They are presented in the lower part of Figure 3.8 (consider only the bars corresponding to $N = 100$, in a first stage). As expected for this kind of system, notoriously sensitive to time delays, the parameters τ_s and τ_a (i.e. θ_1 and θ_3), feature the largest total Sobol' indices (shown in the background), and hence influence the most the variance of φ. The outcome of this analysis is that the designer should aim at minimizing τ_s and τ_a first, and that they are equally important to the fidelity. The scaling artefacts, parametrized by α_s and α_a, play a secondary, but non-negligible, role in influencing the variance of φ. The symmetrical structure between τ_s and τ_a (and α_s and α_a, respectively) observed in (3.18) is also visible from the Sobol' indices. Finally, the fact that first-order and total Sobol' indices differ (and this, for all four parameters θ_i) indicates some non-additive interaction between the parameters, which is consistent with (3.18). This answers our research question RQ1 for this simple setup.

Note that we have used $N = 100$ samples in $\mathcal{E}$ and $\mathcal{F}$ to reach this conclusion. For this value, the value of E_{LOO} for our surrogate model was above the values recommended by Le Gratiet et al. (2015). To investigate the effect of a rather large E_{LOO} on our conclusion, sets $\mathcal{E}$ of various sizes N were generated by successive LHS enrichment, see Figure 3.9, and the global sensitivity analysis was run for each of them. Figure 3.8 shows how the choice of N influences E_{LOO}, our estimates of the moments, and the Sobol' indices. For $N \geq 100$, E_{LOO} is indeed reduced, but the resulting variations of $\mathrm{E}[\varphi(\Theta)]$ and $\mathrm{Var}[\varphi(\Theta)]$ are less than 1%, and the conclusions of the sensitivity analyses are similar. For $N = 50$, E_{LOO} has a similar value as for $N = 100$, satisfactory estimates of $\mathrm{E}[\varphi(\Theta)]$ and $\mathrm{Var}[\varphi(\Theta)]$ are obtained, but the estimated Sobol' indices may lead to an erroneous conclusion regarding the relative importance of θ_2 and θ_4. It is therefore good practice to not only rely on E_{LOO}, but also study the statistical convergence of the statistical moments and Sobol' indices in our study.

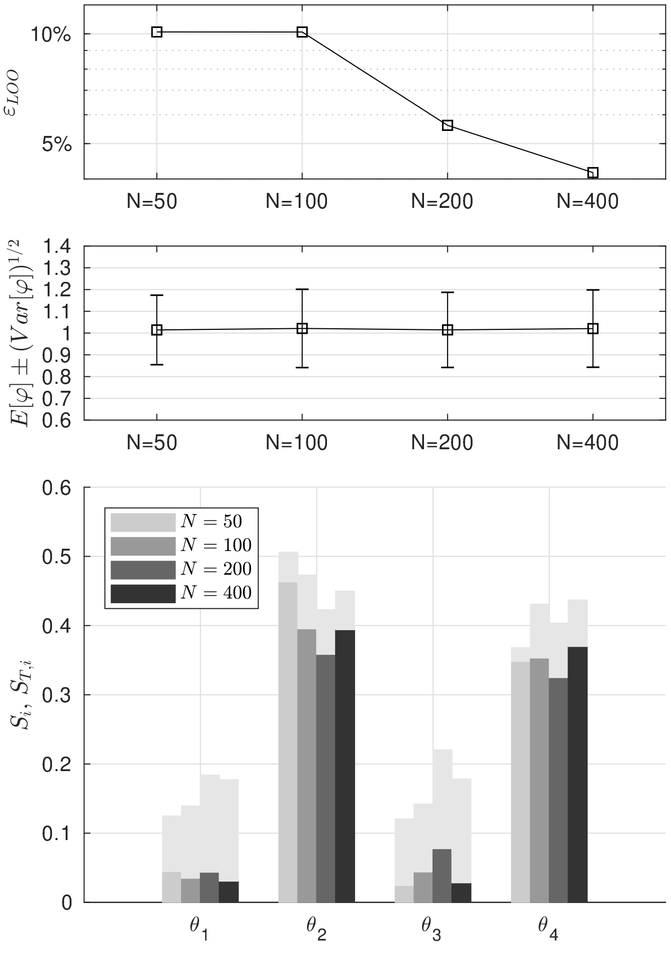

Figure 3.8: Upper Figure: normalized leave-one out cross-validation error of the PCE surrogate model. Middle figure: estimated mean value and standard deviation of $\varphi(\Theta)$. Lower Figure: first-order Sobol' indices and total Sobol indices (in the background) of φ. We recall that $\theta = (\alpha_s, \tau_s, \alpha_a, \tau_a)^\top$. The statistical moments and Sobol' indices are estimated from sets $\mathcal{E}$ and $\mathcal{F}$ of four sizes $N \in \{50, 100, 200, 400\}$.

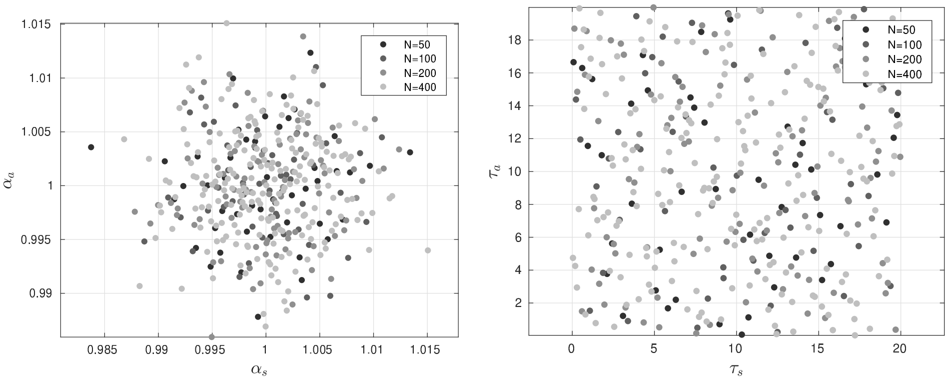

Figure 3.9: Samples of Θ obtained by LHS and successive enrichment. Left: scatter diagram representing the first and third components of θ. Right: scatter diagram representing the second and fourth component of θ

3.3.3 Probabilistic robust fidelity

As a design choice, we request the cyber-physical setup to guarantee a fidelity of *at least* $\varphi_{\mathrm{adm}} = 0.7$, which corresponds to the worst case in Figure 3.6. In Step 3, we will now check that this criterion is met with sufficiently high probability (RQ2), and establish the resulting constraints on the components of θ (RQ3).

We use a PCK surrogate model $\mathcal{K}$, describing φ near the locations of the four dimensional space where $\varphi(\theta) = \varphi_{\mathrm{adm}}$. The initial set $\mathcal{E}$, which contains $N = 100$ samples of Θ at this stage, is used to initialize the PCK model, as outlined in Section 2.3. It is then enriched with new samples as described in Section 2.3.4, and illustrated in Figure 3.10. The set of samples added step-by-step by this process are represented by square markers in the (α, τ) plane in Figure 3.11. The following remarks are in order when considering this Figure.

1. The fact that failure clearly occurs in well-defined regions *of the* $\alpha - \tau$ *plane* is consistent with the knowledge we have from (3.18): the individual values of τ_s and τ_a (resp. α_s and α_a) are irrelevant for this system, it is their sum (resp. product) that matters. Note however that in general such knowledge is not available, and that such structures are not easily identifiable, especially when dealing with high-dimensional Θ.
2. As expected, we also see that loss of fidelity occurs when τ becomes large and when α deviates (i.e. increases *or decreases*) by more than 1% from unity. In contrast, by inspection of (3.18), it can be established

that the dynamical system becomes *unstable* for $\tau \geq 40$ ms when α is equal to 1, and that the stability margin may be increased only by *decreasing* α, when τ=40ms. This illustrates the fact that, while stability is in general necessary to ensure high fidelity of a cyber-physical empirical setup, it is clearly not a *sufficient* condition.

3. Finally, while most of the samples generated by the enrichment algorithm are located near the boundaries of $\mathcal{D}_f$ (which is the objective), some of them seem inadequately located in regions with high fidelity. The reason is that these samples typically feature an unlikely large value of α_s, combined with an unlikely small value of α_a (or vice-versa). Even if $\alpha = \alpha_s \alpha_a$ is close to unity, such a combination falls in an unexplored region of the four-dimensional space $\mathcal{D}$, leading to a large value of the uncertainty (2.38), and therefore P_m in (2.52). The corresponding sample is therefore selected by the AK algorithm. This is commonly referred to as sample space *exploration.*

The evolution of the estimated probability of failure P_f during the enrichment process is shown in Figure 3.12. We recall that P_f is calculated from (3.9) by performing Monte-Carlo simulations (MCS) using the PCK model, which is updated at each step. The confidence intervals represented in Figure 3.12 can be made as small as desired by increasing the number of auxiliary samples involved in this MCS. Significant variations of P_f are observed initially and until the 40th step. They occur when the enrichment process "discovers" a sample that refines the PCK model at a location where it is close to φ_{adm}. This changes the estimated location of $\mathcal{D}_f$, which in turn causes large variations of P_f. Smaller variations in the estimated P_f are also due to statistical noise, since P_f is evaluated by MCS, which can lead to different estimates, even for a given PCK model. In the present case, convergence is achieved after ca 80 iterations, and it is found that $P[\varphi < 0.7] \simeq 1.6 \times 10^{-3}$. This probability should be compared with a target ε_{adm}, set by the designer. Robust fidelity is achieved if $P_f < \varepsilon_{\text{adm}}$.

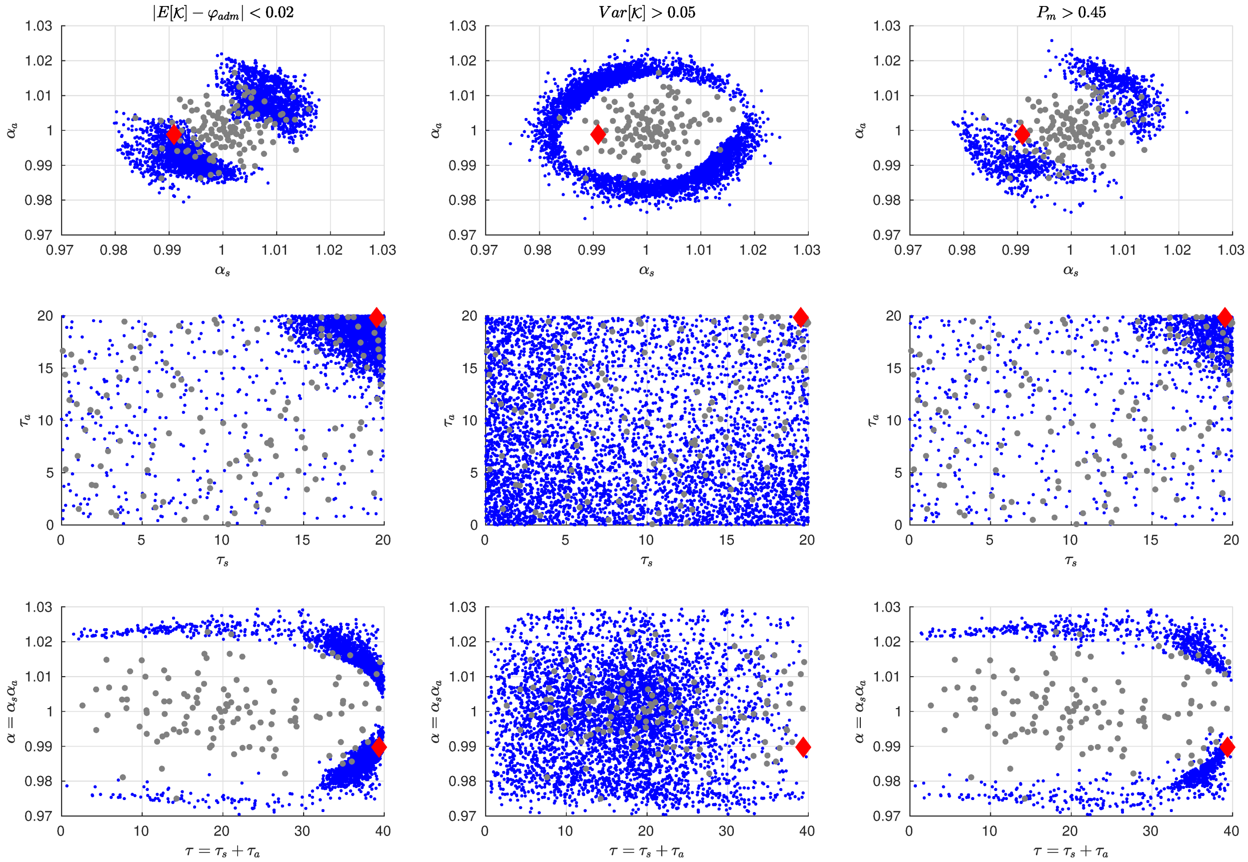

Figure 3.10: Illustration of the enrichment procedure. In all plots, the grey points correspond to the initial space-filling set $\mathcal{E}$. In the first column, the blue points correspond to all auxiliary samples for which $\mathrm{E}[\mathcal{K}]$ is close to φ_{adm} (projection in the (α_s, α_a)-plane on top, and in the (τ_s, τ_a)-plane on the middle line, and on the (α, τ)-plane on the bottom line). The second column shows the regions of large uncertainty $\mathrm{Var}[\mathcal{K}]$, and the third column to resulting high values of the learning function P_m. The red diamond marker represents θ^{new}.

3.4 Conclusion

We have in this chapter proposed a method to address the RQ formulated in Section 1.3.1. We first defined a generic model for CPEM as an interconnection between the substructures. This interconnection is subject to random and heterogeneous artefacts, such as measurement noise and actuator dynamics, which prevent the dynamic equilibrium between the substructures to be fulfilled. We then introduced a definition of the fidelity (3.6) that quantifies the detrimental effect of the artefacts on the quantities of interest (QoI) for the experiments. We finally described how the fidelity could be computed by co-simulating the ideal system (without artefact) on the one hand, and the system subjected to the artefacts on the other hand.

Based on this problem formulation, and by using the uncertainty quantification tools presented in Chapter 2, we showed how to assess the robust fidelity of a CPEM. The proposed method enables us to conclude whether the substructural partition and the control system at hand are suitable to study of the dynamical system at hand (RQ2). A bi-product of this analysis are fidelity bounds, yielding requirements on the control system connecting the substructures (RQ3). These latter are obtained by interrogating the PCK surrogate model established during the analysis. Finally, by using another type of surrogate model (PCE), the influence of each artefact on the fidelity could be quantified, which is of great operational relevance during the design of a CPEM (RQ1).

For illustration purposes, the method was applied to a simple CPEM, aimed at studying the behaviour of coupled oscillators. In the two next chapters, we will show how the proposed method can be used to address a more complex problem of industrial relevance, namely the active truncation of slender marine structures.

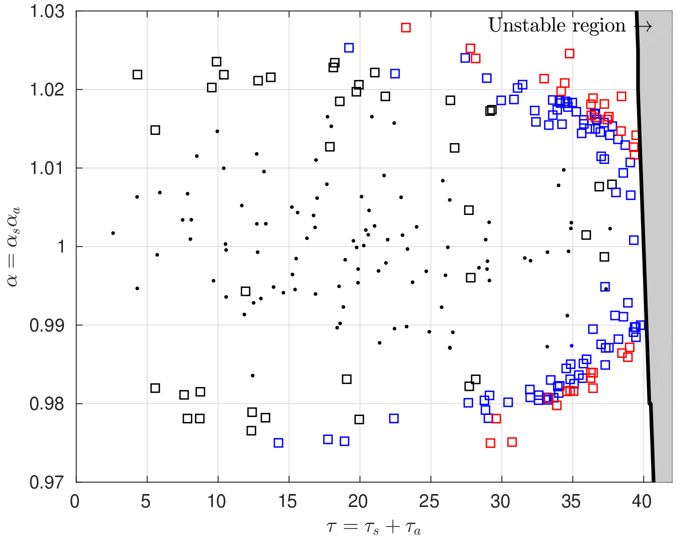

Figure 3.11: Samples of $\theta = (\alpha_s, \tau_s, \alpha_a, \tau_a)^\top$, represented in the α-τ plane. Dots represent samples from the initial experimental design (100 samples), while squares correspond to the enrichment process (160 samples). Black markers corresponds to $\varphi(\theta) > 0.75$, blue markers to $\varphi(\theta) \in (0.70, 0.75]$ and red markers correspond to $\varphi(\theta) \leq 0.70$.

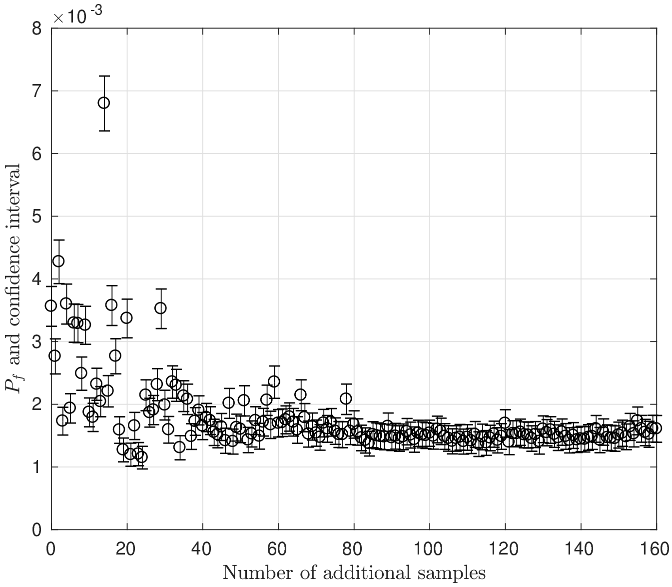

Figure 3.12: Evolution of the estimated probability of failure during the enrichment process.

Chapter 4

Co-simulation of the active truncation of slender marine structures

In the previous chapter, we presented a method to analyze the fidelity of generic CPEM. In the next two chapters, we will apply this method to the study of the active truncation of slender marine structures, already mentioned in Example 5.

A slender marine structure can be defined as a structure whose length is several orders of magnitude larger than its characteristic cross-sectional dimension, and which is used in the marine industry. Slender structures usually combine a soft transverse stiffness with a strong axial stiffness, coupled through the curvature of the structure (Papazoglou and Mavrakos, 1990). They operate in water and are therefore subjected to drag loads, possibly vortex-induced vibrations, and contact with the sea-bed, which pose specific modeling and analysis issues. Examples of slender marine structures are mooring lines, risers, umbilicals, the tethers of a tension leg platform, or hawsers used in towing or trawling.

In Section 4.1, we will introduce in detail the background for the active truncation of such structures. In Section 4.2, we will show how co-simulations of substructured slender marine structures can be performed. Finally, in Section 4.3, we will investigate how some given types of artefacts affect the behaviour of a substructured polyester mooring line. The content of this section will serve as background to Chapter 5, in which a complete fidelity analysis of an active truncation setup will be performed. Parts of this chapter have been published earlier in Sauder et al. (2017) and Sauder et al. (2018).

4.1 The active truncation problem

4.1.1 Hydrodynamic model testing in ultra-deep water

Floating oil&gas production units are generally designed based on functional requirements which are specific to the targeted hydrocarbon field. Examples of such requirements are the reservoir type, the required on-board processing and storage capabilities, and the surrounding environment. During the design phase, hydrodynamic model testing of these structures is usually performed to validate the numerical models used by the designer, to study of specific complex physical phenomena, and to eventually perform a final verification of the design (Magee, 2018). During such verification tests, the floating structure is modelled at reduced scale, as depicted in Figure 4.1, and exposed to the wave, wind and current conditions it may experience during its design life, see e.g. DNV GL (2015). It is then verified that the motions of the platform, and the loads in the mooring and riser systems are acceptable under these environmental conditions. The test campaign is in general also a final risk mitigation campaign, during which unexpected events such as green water on deck, wave impact (see Figure 4.2), could be detected.

When subjected to irregular waves, the motions of moored floating systems in the horizontal plane generally contain a wave-frequency (WF) component, with periods ranging from 5 to 20s, and a low-frequency (LF) component. Both components play an important role for the extreme excursions of the floater and the extreme tensions in the mooring lines. The LF motions may feature large amplitudes and a narrow banded spectrum, and can be described, in a first approximation, by a forced linear oscillator whose damping term includes wave drift damping, viscous damping on the floater, and damping induced by the mooring and riser system[1]. The latter is mainly induced by transverse drag loads along the mooring lines when their upper end undergoes horizontal motions. Which of these three damping components contributes most to the LF damping depends on the water depth, the sea state and on the floating system at hand, but mooring-induced damping plays in general an important role (Huse, 1986; Webster, 1995). The static and dynamic properties of the mooring system must therefore be properly

---

[1] In this oscillator, the mass term consists of the mass of the floater and the asymptotic value of its added mass for low frequencies, and the stiffness is due to the mooring system. The external excitation is due to second-order (in terms of wave amplitude) hydrodynamic loads on the floater. Second-order wave loads are in practice predicted by perturbation methods, despite the fact that the amplitude of LF motions is very large compared to the wave amplitude. This inconsistency gives birth to an additional damping load denoted wave drift damping (Molin, 2002)

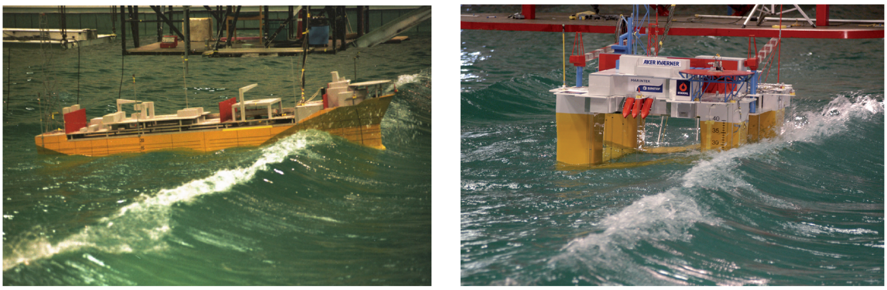

(a) FPSO platform (b) Semi-submersible platform

Figure 4.1: Hydrodynamic model testing of oil and gas production platforms. Courtesy of SINTEF Ocean.

accounted for when performing model tests of a floating production unit.

Modeling accurately the mooring system may, however, be challenging. Exploitation of natural resources is taking place at steadily increasing water depths. The company Shell set a new record in September 2016, when their disconnectable FPSO started to exploit the Stones field (Gulf of Mexico) in 2900m water depth (Bowers, 2016). Deep-sea mining of minerals, such as copper, gold, silver, zinc, nickel, cobalt and manganese, seems to become a reality, with fields under development in 1600 water depths (The Maritime Executive, 2018), and long-term prospects down to 6000m (Sharma, 2017; Takaya et al., 2018) Let us assume that such floating systems, together with their mooring and riser systems, should be tested in a hydrodynamic laboratory at a scale[2] $\lambda < 1$. Denoting D the water depth, an estimate of the radius of the mooring system footprint is $1.0D$-$1.7D$ for a taut mooring systems generally used in deepwater developments, and $1.5D$-$2.5D$ for a catenary mooring system (ITTC, 2017; Chakrabarti, 2005; Argyros, 2011), see Figure 4.3. Testing a structure in 3000 m at a scale $\lambda = 1/60$ would require a laboratory with a diameter of at least 100 m and a water depth of 50m. In other words, it is unfeasible in any of the existing ocean basins.

This challenge has extensively been discussed by Stansberg et al. (2002). While existing laboratory infrastructure may not have the spatial extent required to accommodate ultra-deep water systems, outdoor testing and ultra-small scale testing do not guarantee the accurate modelling of the

---

[2] The reader not familiar with scaling laws used in hydrodynamic testing may consult Journée and Massie (2001), Appendix B, and Newman (1977), Chapter 2. Hydrodynamic model testing of offshore structures must, in general, be performed at a scale less than 1/30, due to wave-maker capacity and other practical issues, but no less than 1/100 for accuracy reasons (Steen, 2014).

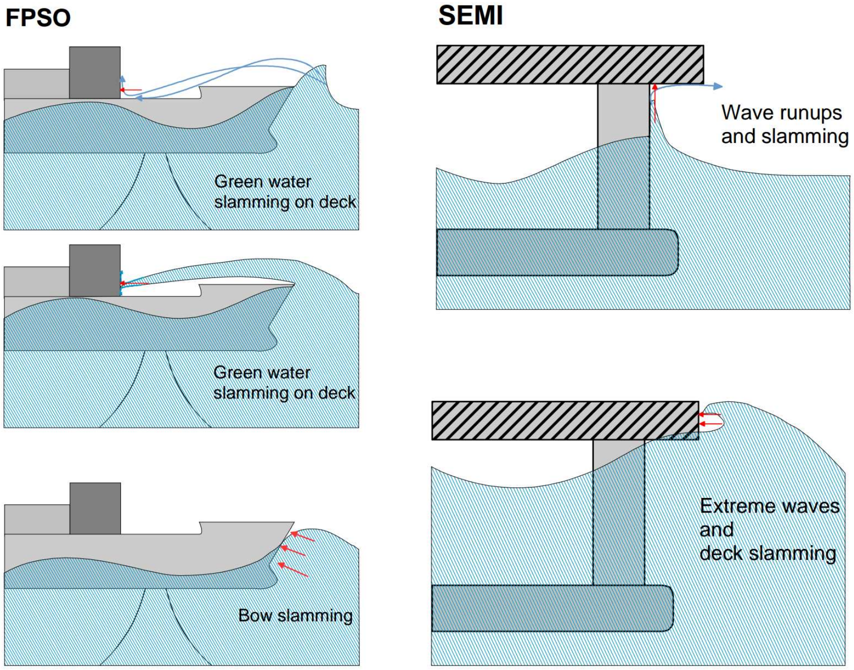

Figure 4.2: Example of complex hydrodynamic phenomena at the free-surface for FPSO and semi-submersibles. From Muthanna (2014)

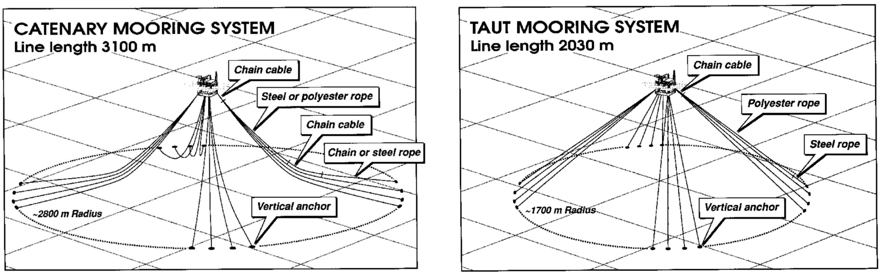

Figure 4.3: Sketch of catenary and taut mooring systems in 1200m water depth ITTC (1999).

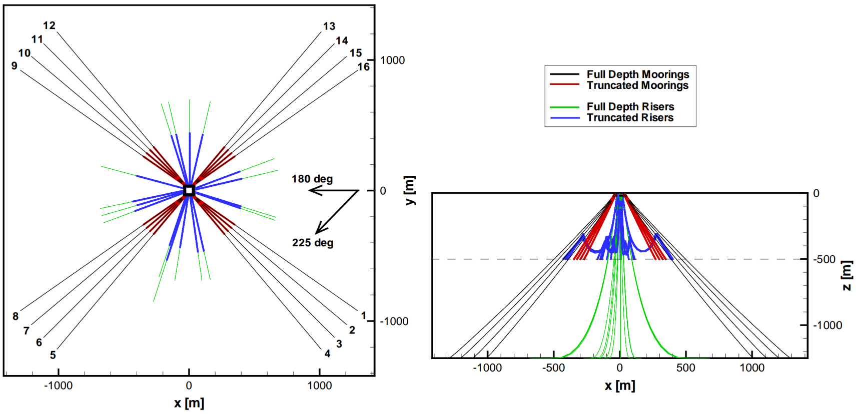

Figure 4.4: Passive truncation of a mooring/riser system. The full-depth system includes 16 identical taut mooring lines (in grey) and 17 risers in J-configuration (in green). The truncated version of these slender marine structures are plotted in blue and red, respectively. From Kendon et al. (2008)

floating system and a controlled environmental loading.

4.1.2 Passive truncation

The state-of-the-art approach to address this problem is denoted *passive truncation*, and it is founded on the fact that (1) most of the complex hydrodynamic phenomena, such as wave-current interaction, wave impact, and important viscous effects, occur near the free-surface, and (2) the dynamic behaviour of slender marine structures is well-described by validated numerical codes such as RIFLEX (Aksnes et al., 2015). Note that these considerations leave aside the notoriously difficult problem of vortex induced vibrations (VIV). The verification of a typical floating production platform (with mooring and risers) using passive truncation consists of the following four-step procedure.

Step 1. A *truncated* version of the mooring and riser system is designed as shown in Figure 4.4. The objective is to achieve *static* similarity between the truncated and full-depth systems. The design of the truncated system is very dependent on the type of system under study. The process involves in general an architectural design phase during which the truncation point, a first estimate of line properties, and the use of clump weights or blocking springs are decided upon. The parameters of the truncated system are then refined by solving an optimization problem (Fylling and Stansberg, 2005; Molins et al., 2015; Felix-Gonzalez and Mercier, 2016), whose objective function is a measure of the difference between the static characteristic of the full-depth and truncated systems. The constraints of the optimization problem are typically related to the manufacturability and strength of the truncated system. The yield strength of coil springs should, for instance, not be exceeded.

Step 2. Hydrodynamic model testing is performed with this statically-equivalent truncated system, which leads to similar (but not identical) floater motions as if it was the full-depth system. It is important to emphasize that the *dynamic* tension in the mooring and riser lines measured during these model tests, cannot be used directly for design verification: indeed, inertial loads and transverse drag loads on the truncated slender marine structures are in general significantly less than on the full-depth system, which causes discrepancies on the dynamic tension, especially in harsh sea-states (Kim et al., 2005).

Step 3. A numerical model *of the truncated setup* is established using a state-of-the-art analysis program, such as SIMA (SINTEF Ocean, 2015). The hydrodynamic model of the floating system is calibrated in order to match model test results (Baarholm et al., 2006). This involves the identification of second-order wave loads and damping on the floater, wave-current interaction parameters, and viscous damping coefficients, among others.

Step 4. When satisfactory agreement with model tests is achieved, the numerical results are "extrapolated". In other words, the truncated mooring/riser system is replaced by the full-depth system in the numerical model, and simulations are run in relevant environmental conditions to obtain dynamic line tensions, extreme excursions of the floater, which are used to verify the design. As of today, this verification method is considered as reliable and is the common practice (ITTC, 2005). However, its main weakness lies in the execution time of this four-step process, and also to possible challenges related to numerical model identification (Kendon et al., 2008).

In the last years, researchers have therefore attempted to create truncated setups exhibiting a correct *dynamic* behaviour. Starting from a statically-equivalent system, Ferreira et al. (2016) suggested to achieve dynamic equivalence by jointly varying the diameter and mass of the segments, while keeping the submerged weight constant, and the static properties of the system unchanged. Based on a numerical case study, they concluded that the truncated setup was able to replicate the dynamic line tensions in sea-states *with comparable strength* to the ones used in the calibration. When quite different sea-states were investigated, motions of the floater could however deviate significantly. No detailed results were reported regarding dynamic line tensions in these sea-states. Using a similar approach, Wei et al. (2017) presented a step-wise, systematic and efficient way of solving the optimization problem mentioned in the previous paragraph. However, dynamic equivalence was only verified for quite mild sea-states, very close in terms of strength to the ones used in the optimization process. This approach also requires a number of nonlinear time domain simulations to be performed prior to the test.

Following a radically different approach, Argyros (2011) studied the drag-induced decay of transverse vibrations of taut polyester mooring lines, subjected to top motions. Based on this, he defined a truncation length as the minimum length below which drag-induced damping and added mass would have an insignificant effect on the transverse motions of the line. To model the lower, truncated, part of the line, he suggested to use a nonlinear (polynomial) spring at the truncation point, as well as a dashpot acting transversely to the line. An additional axial force, calibrated from numerical simulations at full-depth, may be added when studying extreme sea states. However, while the method seems very adequate for the truncation of a large class of taut polyester mooring systems in deep water, it cannot be applied directly to other classes of slender marine structures, such as steel catenary risers depicted in green in Figure 4.4. Also, even though the boundary conditions at the truncation point seem quite simple (polynomial stiffness, transverse damping, and additional axial force), they may be difficult to achieve in practice with simple ”passive” components, such as springs or dashpots.

4.1.3 Active truncation: introduction and case study

The verification of floating systems in ultra-deep water in general, and the truncation of slender marine structures in particular, are ill-conditioned problems. They are multi-scale problems in time, since several hours (in full-scale time) of exposure to irregular waves are required to obtain reliable statistical information about extreme mooring line tensions and floater excursions, while wave impact events and snatch loads in the mooring system, also of interest, last less than one second. They are also multi-scale problems in space. Indeed the characteristic dimensions involved, i.e. the cross-sectional dimension of the mooring lines, the characteristic size of the platform, the wave height and length, and the water depth, span four orders of magnitude.

We argued in Section 1.1.1 that CPEM could be an adequate tool to address such ill-conditioned problems. In the late 1990’s, some researchers have indeed suggested to use *active truncation* to study deep water floating systems. The truncated part of the slender marine structures would become a numerical substructure, and would then be simulated using a FE method (Watts, 1999; Buchner et al., 1999). The connection between the physical and numerical substructures happens through a set of sensors and actuators, located at the truncation point, in other words on the floor of the hydrodynamic laboratory. In that setting, spatial ill-conditioning is solved, and *dynamic* similarity between the full-depth and truncated setup is achieved intrinsically.

Active truncation of slender marine structures has however never been realized, most probably due to practical challenges. Indeed, Froude scaling sets quite stringent requirements on the performance of both the numerical substructure and the control system. When Froude scaling is applied with a factor $\lambda < 1$, time runs $\lambda^{-\frac{1}{2}}$ faster than full-scale real-time, velocities are $\lambda^{-\frac{1}{2}}$ times larger, and forces are λ^{-3} times smaller. As an example, if model testing was to be performed at a scale of $\lambda = 1/64$, the numerical substructure would have to run 8 times faster than full-scale real time, tension variations of 200 kN would correspond to variations as small as 0.76 N at model scale, and these should be applied with velocities 8 times larger than at full-scale. Note that in addition to be *efficient* from a computational speed point of view, the model used in the numerical substructure should of course be *validated* for the CPEM to be meaningful, as discussed in Chapter 1. For practical reasons, it should also be *robust*, in the sense that it should not lead to numerical instabilities or excessive jitter.

Main requirements for numerical substructures used in active truncation: validity, computational efficiency and robustness

Even if active truncation has never been applied to the verification of complete moored floating systems, CPEM have been developed to address other issues involving slender marine structures: VIV have for instance been studied by Hover et al. (1997, 1998) and Smogeli et al. (2003), and more recently, the installation of a steel catenary risers (SCR) was studied by Ye et al. (2014).

Our objective is now to study active truncation in details, by applying the fidelity analysis method for generic CPEM, presented in Chapter 3. This will be done through the following case study. We will consider a taut polyester mooring line, as depicted on the right hand side of Figure 4.3. Note that there are generally chain segments at the top and bottom ends of the mooring line[3] which are not considered here for simplicity. The property

---

[3] For more details, see the interesting study on impedance mismatch at the connection

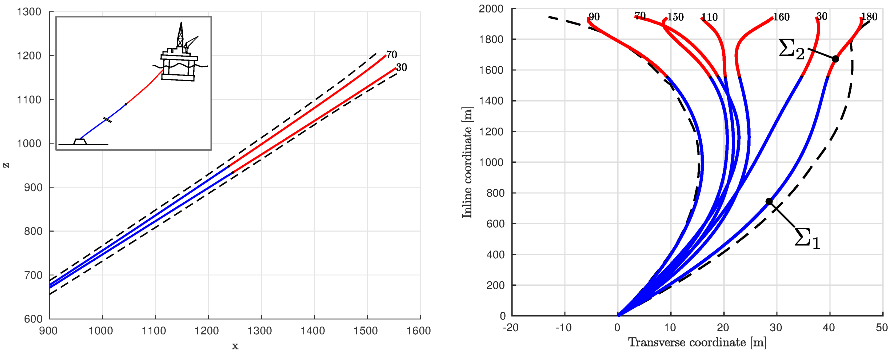

Figure 4.5: Top left: overview of active truncation with the physical substructure Σ_2 in red and the numerical substructure Σ_1 in blue. Left: snapshots of the upper part of the polyester line at $t = 30s$ and $t = 70s$, when subjected to the characteristic excitation τ. Right: snapshots of the full line in a "local" coordinate system (rotated by $\gamma_0 = 50^o$). The dashed lines correspond to the envelope of the line's displacement during the analysis.

Table 4.1: Properties of the polyester mooring line used in the case study. Tangential added mass and drag forces are neglected. *: MBL stands for Minimum Breaking Load, and is taken equal to 18.64MN (Bridon, 2013)

Parameter and symbol	Unit	Value	Comment
Length L	m	1934	
Diameter d	mm	264	cross-sectional area of $A = 5.47 \times 10^{-2}$ m^2
Mass per unit length m	kg/m	44.7	
Young modulus E	GPa	8.513	so that $EA = 25 \times \text{MBL}^*$
Submerged weight per unit length w	N/m	93.2	
Rayleigh damping coefficient α_2	s	$4.77.10^{-2}$	damping ratio [0.30% 5.73%] for modes 1-10
Top tension module T_0	kN	2500	
Top tension angle γ_0	^{o}	50	with respect to vertical
Normal added mass coefficient C_m	-	1.0	
Normal drag coefficient C_d	-	1.6	selected according to DNV GL (2014)
Axial stiffness	kN/m	241.0	equal to EA/L
Longitudinal wave velocity c_l	m/s	3328	given by $\sqrt{EA/m}$
Transverse wave velocity c_t	m/s	157.5	approximated by $\sqrt{T_0/(m+\rho C_m A)}$

of the mooring line are given in Table 4.1. Without loss of generality, we assume that the problem is two dimensional, and we define a direct x-z coordinate system, whose z axis is vertical and pointing upwards. The water depth is D=1200 m and water density ρ=1025 kg/m^3. Active truncation is to be performed as shown in Figure 1.5b and at the top left of Figure 4.5. We set the scale to $\lambda = 1/60$, the truncation ratio to α=0.8, so the required water depth in the laboratory is $(1-\alpha)\lambda D = 4m$. Σ_1 is the numerical substructure, representing the lower portion of the mooring line, and the physical substructure Σ_2 represents the upper portion of the line.

The fidelity of active truncation will be evaluated by studying the response of this slender marine structure to an external excitation $\tau(t)$, with a duration T. This load is meant to be representative, in terms of amplitude, frequency content and direction, of a severe load that can be encountered during the testing of a floating system. The *dynamic* part of this load represents wave loads transferred from the floater to the slender structure, and is therefore applied to the top of the line. It has two components. The first *low-frequency* component mainly acts axially, has an amplitude of 1MN, and a frequency content sweeping [0, 0.02] Hz. It mimics the effect of second-order difference-frequency wave loads. The superimposed *wave-frequency* component has an amplitude of 250kN, and a frequency content sweeping [0,0.2] Hz, and a direction with constant rate of change. Time series of the described top load can be seen in Figure 4.10. This dynamic load comes in addition to the *static* top tension applied to the slender structure (see Table 4.1), and to the drag load associated to a shear current, whose velocity varies linearly throughout the water column for 0m/s at the seabed to 0.5m/s at the free surface.

We will now focus on the definition of the fidelity indicator φ for the active truncation problem. As mentioned earlier, hydrodynamic model test campaigns focus generally on the behaviour of the floater, and on extreme tensions in the slender marine structures. They do not consider their local deflection or curvature. The objective is therefore to make the *interaction* between the truncated slender marine structure, the (physical) floater and the (numerical) sea bottom reflect the corresponding interactions in a fully physical setup.

Based on this reasoning, two fidelity indicators are suggested as outlined in Section 3.1.2. Let $V_{x,top}$ and $V_{z,top}$ be the components of the top velocity of the slender structure when it is subjected to $\tau(t)$, and $F_{x,bottom}$ and $F_{z,bottom}$ the components of the force vector at its lower end. These four values are

---

between polyester rope and chain, and its consequences on dynamic tension in Argyros (2011) calculated as outlined in Section 3.2.2 by co-simulation of the substructured system, subjected to artefacts described by a parameter θ that will be defined later on. Letting $\bar{V}_{top}$ and $\bar{F}_{bottom}$ be their ideal counterparts, obtained by simulation of the emulated system without artefacts, the first indicator can be written, consistently with (3.6)

$$\varphi_1(\theta) := -\frac{1}{2}\log_{10}\left(\gamma^2_{\mathrm{Vx}}(\theta) + \gamma^2_{\mathrm{Vz}}(\theta)\right) \tag{4.1}$$

where

$$\gamma^2_{\mathrm{Vx}}(\theta) := \frac{\int_0^T \left(V_{x,top}(t|\theta) - \bar{V}_{x,top}(t)\right)^2 dt}{\int_0^T \bar{V}_{x,top}(t)^2 dt} \tag{4.2}$$

$$\gamma^2_{\mathrm{Vz}}(\theta) := \frac{\int_0^T \left(V_{z,top}(t|\theta) - \bar{V}_{z,top}(t)\right)^2 dt}{\int_0^T \bar{V}_{z,top}(t)^2 dt} \tag{4.3}$$

φ_1 quantifies how well the top end of the structure responds to the prescribed external load τ, and thus how well the substructured system manages to replicate the mechanical impedance of the slender structure (Argyros, 2011; Fahy and Gardonio, 2007). φ_1 is therefore important when motions of the floater are investigated.

The second fidelity indicator is defined by

$$\varphi_2(\theta) := -\frac{1}{2}\log_{10}\left(\gamma^2_{\mathrm{Fx}}(\theta) + \gamma^2_{\mathrm{Fz}}(\theta)\right) \tag{4.4}$$

where

$$\gamma^2_{\mathrm{Fx}}(\theta) := \frac{\int_0^T \left(F_{x,bottom}(t|\theta) - \bar{F}_{x,bottom}(t)\right)^2 dt}{\int_0^T \bar{F}_{x,bottom}(t)^2 dt} \tag{4.5}$$

$$\gamma^2_{\mathrm{Fz}}(\theta) := \frac{\int_0^T \left(F_{z,bottom}(t|\theta) - \bar{F}_{z,bottom}(t)\right)^2 dt}{\int_0^T \bar{F}_{z,bottom}(t)^2 dt} \tag{4.6}$$

φ_2 quantifies how well the external load is transferred to the sea bottom, and is then more relevant when the focus is on the loads at the anchors (or blow-out preventer, if considering a drilling riser). If both aspects are important, φ_1 and φ_2 could easily be combined into a single indicator.

4.2 Co-simulation of an active truncation setup

To analyze the fidelity of active truncation, we must be capable of performing co-simulation of this CPEM, using a validated model of the substructures. The emulated system must indeed be representative of the real system, for the fidelity assessment of the CPEM to be meaningful. In the following section, we will review possible models for slender marine structures, and select the adequate one for our case study.

4.2.1 Numerical modeling of slender marine structures

In the general context of verification of ultra-deep water floating systems, active truncation must potentially be applied to a wide class of slender marine structures. Examples of such structures are catenary mooring systems (generally composed of chain and steel wire), taut mooring systems (based on fiber rope), steel catenary risers, flexible risers, top-tensioned risers, tendons of a TLP, etc... The requirements to a numerical model that could perform a global[4] analysis of *all* these structures are quite extensive. It should be a time domain, dynamic, three-dimensional model, accounting for nonlinearities due to large geometrical deformations. It should model the axial/bending/torsional stiffness, and possibly the nonlinear material properties of the slender structures. It should handle concentrated loads (from clump weights or buoys) and distributed loads (as current loads), as well as contact with the sea floor. The employed numerical integration methods should be adequate for stiff problems, to handle snatch loads for instance.

The standard approach to model slender marine structures is to use the nonlinear Finite Element (FE) method (Cook, 2002), implemented in commercial codes such as OrcaFlex, Deeplines, Flexcom and RIFLEX (Zhan, 2010). The FE method can satisfy all requirements listed in the first paragraph, and it has been validated for an increasing number of marine applications over the years. However, since the nonlinear FE method relies on Newton-Raphson iterations to account for large deformation of the slender structures, it is not a natural candidate for CPEM due to a possible lack of robustness. There is indeed no theoretical guarantee that the simulation of one time-step can be executed in a fixed time interval. Such a "jitter" phenomenon was observed by Vilsen et al. (2017).

Some classes of slender marine structures, operating in certain conditions, may, however, be described by simpler models. Such particular cases may be identified by dimensional analyses, see e.g. (Webster, 1995). Some adaptations in the structural formulation have been suggested by Johansen (2007) and Rustad (2007), among others, to enhance efficiency and robustness. Another possibility to ensure efficiency is to step away from a first

---

[4] as opposed to a *local*, or *cross-sectional*, analysis, which removes a level of abstraction and includes a detailed model of the cross-section of the slender marine structure. See e.g. Fergestad and Løtveit (2015).

principles-based resolution of the problem, and use *semi-empirical models*, such as proposed by Mainçon (2011) and Thorsen (2016) to model VIV in time domain. Using surrogate models *of FE models* is another possibility. Christiansen (2014) suggested for example to use Artificial Neural Networks (ANN), calibrated with RIFLEX simulations, to efficiently carry out fatigue analyses. When used in their domain of validity, ANN lead to accurate results, at a fraction of the computational cost used by the corresponding FEM analysis. They also feature a constant and predictable computational time, and are therefore suitable for real-time applications. However, the validity of ANN is jeopardized when they are used on a set of data for which they have not been trained for, as shown for VIV induced forces by Mainçon (2011).

As a conclusion, there is as of today no method to describe the dynamics of *generic* slender marine structures, that fully satisfies the validity, efficiency and robustness requirements set by active truncation. However, such tools can be found for *some classes* of slender marine structures, as the polyester mooring line we consider in our case study.

4.2.2 A class for the simulation of polyester mooring lines

When included in a deep water mooring system, taut mooring lines provide restoring mainly through axial deformations. The catenary restoring effect is not significant, since the weight in water of polyester lines is rather small, compared to steel wire or chain. Bending-induced loads do neither play a significant role in the deep water configuration, since the curvature in such lines structure is small. Neglecting VIV, the transverse deformations of polyester lines are mainly induced by current, and by the top motions of the floater. These latter are damped out by drag loads when propagating downwards in the water column (Argyros, 2011). Dynamic deformations are in general sufficiently small, so that geometric nonlinearities can be neglected in the dynamic analysis. A challenge related to such fiber ropes is the nonlinearity and rate-dependency of the relationship between the axial force they are subject to, and the resulting elongation (DNV GL, 2017, Section 2.10). There is no mature model to fully describe this phenomenon yet, but it seems reasonable to assume linear material properties when performing a dynamic analysis *about a working point.*

Provided that (nonlinear) drag loads are included, the linear FE method is therefore adequate to describe polyester mooring line dynamics. Since bending stiffness plays an insignificant role in ultra-deep water systems, a linear *bar* FE model can be used to address our case study. For practical reasons which will be clear in the next section, we set the boundary condition

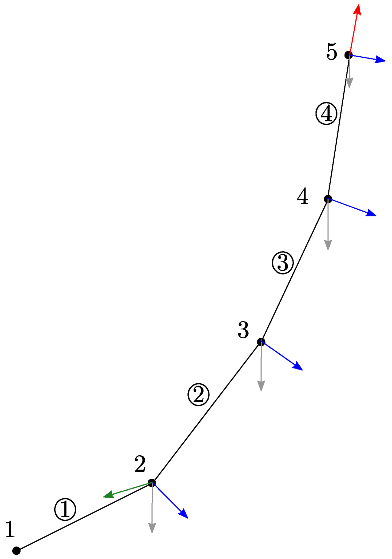

Figure 4.6: Finite element model of a fixed-free slender marine structure, with $n_{el} = 4$. Nodal forces are weight forces (in grey), current forces (in blue), external top force (in red), and nodal force induced by the prescribed displacement (in green). Node numbering and element numbering (circled numbers) are indicated.

of the structure to *fixed-free*, which means that the velocity of lower end of the structure, and the force on the upper end, are prescribed, and their dual left free. Figure 4.6 presents the convention used for the numbering of elements and nodes, and illustrates the involved load components on the structure.

Inertia, added-mass and effective weight loads are calculated in a similar way as described in Rustad et al. (2008), Section 2.3. This will not be detailed again here. Since forces must be input as nodal quantities, drag loads are computed on the semi-element adjacent to each node, using the relative velocity at this node. The stiffness matrix has both an elastic and a geometric component. Since the geometric component strongly depends on the configuration of the structure, the *static* equilibrium of the polyester mooring line is found using Newton-Raphson iterations.

The dynamic time-domain analysis is however linear, in the sense that it uses the mass matrix M and the stiffness matrix K, determined by the static analysis. Nonlinearities due to drag loads are modelled exactly. The structural damping matrix is of the form $C = \alpha_1 M + \alpha_2 K$ (Rayleigh damping) where α_1 is chosen to be null. In that case, the damping ratio associated to a vibration mode with circular frequency ω_i is $\omega_i \alpha_2/2$, with α_2 as indicated in Table 4.1. The time integration is performed with MATLAB®'s `ode45` function (Shampine and Reichelt, 1997) featuring an adaptive step size. Our model is implemented as a class named `fixedFreeCableSegment`.

To verify our implementation, the eigenvalues and associated modeshapes computed from `fixedFreeCableStructure` are compared to known analytical solutions. We consider the polyester line properties are given in Table 4.1, but work first under the assumptions of vertical top tension, infinite axial stiffness and zero submerged weight. When it comes to transverse vibrations, the eigenfrequencies $\omega_{t,i}$ of the line and the associated modeshapes $\phi_{t,i}$ are given by:

$$\forall i \in \mathbb{N}^*, \omega_{t,i} = \frac{(2i-1)\pi}{2L} c_t \text{ and } \phi_{t,i}(z) = (-1)^{i+1} \sin\left(\frac{(2i-1)\pi z}{2L}\right) \tag{4.7}$$

For finite stiffness, longitudinal vibrations occur, and a similar expression describes the corresponding eigenfrequencies $\omega_{l,i}$ and associated modeshapes $\phi_{l,i}$:

$$\forall i \in \mathbb{N}^*, \omega_{l,i} = \frac{(2i-1)\pi}{2L} c_l \text{ and } \phi_{l,i}(z) = (-1)^{i+1} \sin\left(\frac{(2i-1)\pi z}{2L}\right) \tag{4.8}$$

The expression and values of the longitudinal and transverse wave velocities c_l and c_t are given in Table 4.1. Note that the ϕ_i have been normalized so that $\phi_i(L) = 1$. The six first modeshapes obtained from the analytical solution (4.7) are represented with solid lines in Figure 4.7, and the values of the 15 first eigenperiods are tabulated in the second column of Table 4.2, page 103.

These analytical eigenmodes are compared to those obtained for a `fixedFreeCableSegment` object with n_{el}=500 elements, whose axial stiffness has been increased by one order of magnitude (to mimic the infinite stiffness assumption used in the analytical model), and whose submerged weight has been set to zero. The eigenmodes of a `fixedFreeCableSegment` object are obtained numerically from the eigenvalue analysis of $M^{-1}K$ after then nonlinear static analysis. The corresponding eigenperiods are tabulated in the third column of Table 4.2, page 103, and the difference with the analytical solution is found to be insignificant. When n_{el} is decreased to 80 elements (fourth column of Table 4.2), the error is less than 1% for the 13 first modes, and the first modeshapes, compared in Figure 4.7a, also show excellent agreement. For higher modes, with eigenperiods less than 1.80 s, the model with n_{el}=80 becomes too coarse to model transverse vibrations, with less than 12 elements per wavelength $4L/(2i-1)$, and the estimated eigenperiods become erroneous. So provided that n_{el} is chosen adequately, the dynamic system modelled by `fixedFreeCableSegment` can be considered as verified against the corresponding analytical solution.

In reality, several physical effects will make the eigenmodes of a polyester line deviate from the ideal solution (4.7).

- First, the elasticity of the polyester influences the dynamics of long lines. This is shown in the fifth column of Table 4.2, in which eigenperiods are evaluated from a vertical `fixedFreeCableSegment`, now featuring its nominal stiffness. The first eigenperiod for axial vibrations is $2\pi/\omega_{l,1} = 2.41$ s. While the elasticity of the line does not influence significantly the ten first transverse modes (less than 0.5% deviation on the eigenperiod), it must be accounted for when higher frequencies are to be modelled.
- The submerged weight of the slender structure causes (static) tension variations throughout the water column, which also affects the eigenmodes. See e.g. Eq. (61-62) in Vandiver and Li (2005). By considering the sixth column of Table 4.2, it is seen that this effect has an impact on all modes of our structure, including the the lower modes, making the corresponding eigenperiods deviate by 2 to 3% from the zero-weight case.
- Then, since such a polyester line is in general installed in an oblique way, it will exhibit a small static lateral deflection (of the order of 1%

of the structure's length in the present case), due to its submerged weight. As shown in the sixth column of Table 4.2, this change of static configuration has some effect on all eigenmodes.

- Finally, the oblique line is subjected to oceanic current. Considering a shear current whose velocity varies linearly throughout the water column for 0 m/s at the seabed to 0.5 m/s at the free surface. It is found to have an insignificant additional effect on the eigenmodes (last column in Table 4.2). Note however that current has an important effect on the drag-induced damping of transverse motions.

As a conclusion, the `fixedFreeCableSegment` class developed in this Section is suitable to simulate structures with minimal changes of configuration (typically when lateral deflections do not exceed a few percent of the structure's length), such as the deep water taut mooring line in our case study. Note that it could also be used to simulate top tensioned risers or TLP tendons, as long as they remain taut. If slack occurs, the bending stiffness should be modeled (Howell, 1992; Triantafyllou and Howell, 1994), and beam elements should be used instead of bar elements.

4.2.3 Co-simulation: implementation and convergence study

In the following, we will show how the active truncation setup can be co-simulated by coupling two `fixedFreeCableSegment` objects. The numerical substructure Σ_1 (in blue) and the physical substructure Σ_2 (in red), are *each* modelled by a `fixedFreeCableStructure` object denoted `n` and `p`, respectively. The top velocity V_{top} in (4.1) will hence be evaluated from `p`, and the bottom force F_{bottom} in (4.4) from `n`. Focusing now on the truncation point, the selected boundary conditions in `fixedFreeCableSegment` are such that the bottom velocity of `p` and the top force acting on `n` can be prescribed. Their dual values, that is the bottom force on `p`, and the top velocity of `n`, must be evaluated by time integration. The dynamic equilibrium and kinematic compatibility at the truncation point is satisfied by the iterative procedure described in Algorithm 2, which is a specialized version of Algorithm 1 for $s = 2$ and when no artefacts are included. Modifications of this algorithm to accommodate artefacts will be discussed in the following section.

Parameters of this algorithm, such as δt, ϵ_f and ϵ_v (these latter were denoted ϵ_{12} and ϵ_{21} in the general case) have been discussed in Section 3.2.2. As also emphasized in that section, a convergence study must be performed to select the value of these parameters, together with the number of elements n_{el}.

To do so, we consider the truncated taut polyester mooring line, exposed

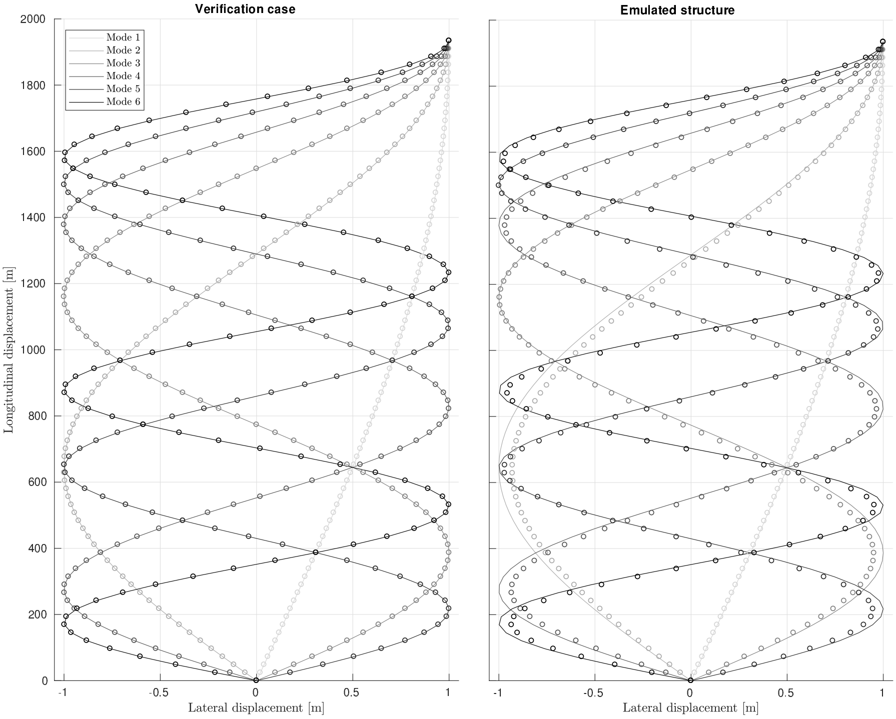

(a) Verification case: ideal cable.

(b) Additional physical effects

Figure 4.7: Modeshapes corresponding to the six first eigenmodes of the fixed-free cable structure. The corresponding eigenperiods can be found in Table 4.2, page 103. In both figures, the analytical solutions for an ideal (weightless and infinitely stiff) cable are plotted with solid lines, and numerical results using the `fixedFreeCableSegment` class with 80 elements are plotted with circle markers.In (a) `fixedFreeCableSegment` models an ideal cable. In (b) the class models a line with nominal weight in water, stiffness, and under inclined top force and current loads. The resulting modeshapes are compared to those of an ideal cable.

Algorithm 2 Co-simulation of two coupled `fixedFreeCableSegment` objects, denoted `n` and `p`.

```
for $t \in \{0, \delta t, ..., T - \delta t\}$ do
    v ←top velocity of n at time instant $t$
    v_next ← $\infty$
    f ←bottom force of p at time instant $t$
    f_next ← $\infty$
    while true do
        Perform time-integration of p from $t$ to $t + \delta t$ with varying external excitation and
        bottom velocity varying linearly to v
        f_next ←bottom force of p at $t + \delta t$
        Perform time-integration of n from $t$ to $t + \delta t$ with varying external excitation and
        top force varying linearly to f_next
        v_next ←top velocity of n at $t + \delta t$
        if $||$v_next − v$||_\infty > \epsilon_v$ OR $||$f_next − f$||_\infty > \epsilon_f$ then: v ← v_next ; f ← f_next
        else: Jump to next synchronization time step
        end if
    end while
end for
```

to the current and wave-induced loads described in Section 4.1.3. The response of the substructured system (we recall that at this stage, no artefact is introduced) is evaluated by the co-simulation procedure described in Algorithm 2. Each of the four parameters is varied, keeping the other ones constant and equal to the following nominal values: n_{el}=80 elements, δt=10 ms, ϵ_v=10^{-6} m/s and ϵ_f=0.1 N. Based on the discussion in Section 3.2.2, criteria for the convergence study ϵ_1 and ϵ_2 are selected based on the fidelity indicators (4.1) and (4.4).

$$\epsilon_1 := \left(\frac{\int_0^T \left(V_{x,top}(t) - V^{\infty}_{x,top}(t)\right)^2 dt}{\int_0^T V^{\infty}_{x,top}(t)^2 dt} + \frac{\int_0^T \left(V_{z,top}(t) - V^{\infty}_{z,top}(t)\right)^2 dt}{\int_0^T V^{\infty}_{z,top}(t)^2 dt} \right)^{1/2} \tag{4.9}$$

$$\epsilon_2 := \left(\frac{\int_0^T \left(F_{x,bottom}(t) - F^{\infty}_{x,bottom}(t)\right)^2 dt}{\int_0^T F^{\infty}_{x,bottom}(t)^2 dt} + \frac{\int_0^T \left(F_{z,bottom}(t) - F^{\infty}_{z,bottom}(t)\right)^2 dt}{\int_0^T F^{\infty}_{z,bottom}(t)^2 dt} \right)^{1/2} \tag{4.10}$$

where the $^{\infty}$ superscript refers to the time series obtained with the finest mesh, smallest synchronization time step or tolerance value, depending on which parameter is varied. Figure 4.8a to 4.8d show the variations of ϵ_1 and ϵ_2 as a function of each parameter, and Figure 4.8e shows the effect of the parameters on the computational time.

As expected, ϵ_1 and ϵ_2 decrease when refining the mesh (Figure 4.8a), while the computational time increases proportionally to n_{el}^2 (Figure 4.8e). As seen in Section 3.3, the present study requires a possibly large number of

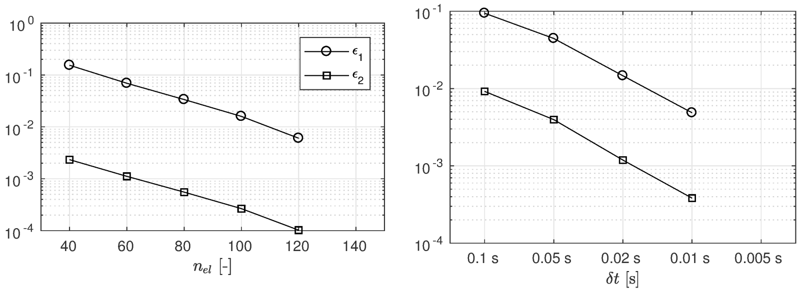

(a) Number of elements

(b) Time step

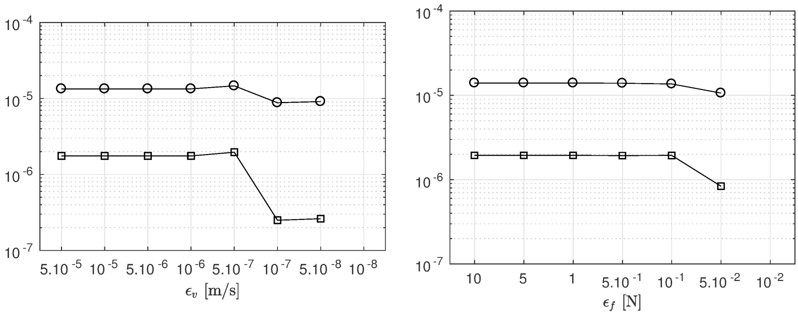

(c) Tolerance criterion - compatibility

(d) Tolerance criterion - equilibrium

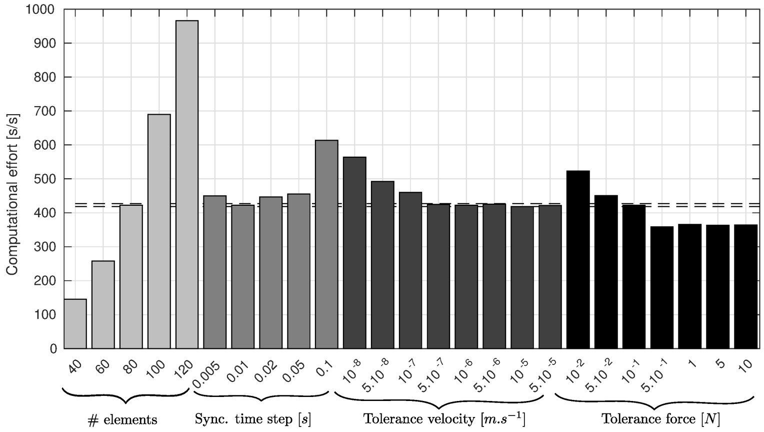

(e) Computational time: number of seconds required per simulated second. The dashed lines correspond to the mean value ± one standard deviation of the duration of the simulation using the nominal set of parameters.

Figure 4.8: Convergence study. Effect of varying the number of elements, the synchronization time step and synchronization tolerances on the error indicators ϵ_1 and ϵ_2 (four top figures), and on the computational time (lower figure).

co-simulations, so n_{el}=80 is selected, which keeps computational costs to an acceptable level.

Convergence is also clearly observed when the synchronization time step is reduced (Figure 4.8b). It can be observed (Figure 4.8e) that the computational time is minimum for δt=10 ms, and increases significantly when δt=100ms. Indeed, even if reducing total number of synchronizations (calls to Algorithm 2) during the given simulation time, increasing δt leads to a larger required number of iterations (lines 6-14 in Algorithm 2) at each synchronization step. On the other hand, it can be observed that the computational time is larger for δt=5ms than for δt=10ms. In that case, even if very few iterations are required to achieve compatibility and equilibrium, the total computational burden increases due to some expensive operations (such as writing data), which are performed at the end of each synchronization step.

As expected when considering line 11 in Algorithm 2, for a given ϵ_f, decreasing ϵ_v will only have an influence on the outcome of the co-simulation (and thus on ϵ_1 and ϵ_2) if it is ϵ_v, and not ϵ_f, that forces the iteration process to continue. Indeed, when ϵ_v is chosen to be very large, the dynamic equilibrium condition will be the limiting constraint, and the value of ϵ_f will thus steer the number of iterations. When ϵ_v is decreased and reaches a certain threshold, which depends on the mechanical impedance of the structure, it may be either the equilibrium or the compatibility condition that steers the number of iterations, at a given synchronization step. Finally, decreasing further ϵ_v will yield a more accurate compatibility condition, which decreases the error, and increases the number of iterations and the computational time. This shift is clearly happening for ϵ_v=10^{-7} m/s in Figure 4.8c. It should however be noted, that within the range of investigated ϵ_v and ϵ_f, the errors ϵ_1 and ϵ_2 are extremely small. The selected values are n_{el}=80 elements, δt=10 ms, ϵ_v=10^{-6} m/s and ϵ_f=0.1 N.

We have, in this section, shown how to co-simulate the *emulated* system. Performing the fidelity analysis described in Section 3.1.2 requires now also artefacts to be introduced in the coupling between the substructures, which will be the object of the next section.

4.3 Effect of deterministic artefacts

4.3.1 The `artefact` class

An `artefact` class was developed, which enables us to apply a gain (multiplicative error), bias (additive error), white noise, delay, zero-order hold and signal loss to a signal, as presented in Figure 3.3. The class has a `signalIn` method to get an input, a `signalOut` method to retrieve an output, and in the particular case when no artefact should affect the signal, it works simply as a First-In-First-Out (FIFO) queue. When artefacts are present, the input is modified before being returned. As an example, in Figure 3.3, successive calls to `signalOut` were made on `artefact` objects with different properties, which received identical samples of the reference signal via the `signalIn` method.

To study active truncation, two `artefacts` objects are needed, one acting on the measured force, obtained from the physical substructure Σ_2, and the other one acting on the imposed velocity, obtained from the numerical substructure Σ_1. Because they act on signals which are obtained from sensors, or used as reference to actuators, the corresponding `artefact` objects will be denoted `aS` and `aA`, respectively. In this setting, performing a co-simulation that includes the effect of these artefacts requires only minor modifications to Algorithm 2. (1) At line 8, `f_next` should be input to `aS.signalIn`, and the output of `aS.signalOut` should be used instead of `f_next` in line 9. (2) Similarly, `v_next` should be passed through `aA` after line 10 before being used. (3) At line 11, the convergence criterion should be evaluated on the values *affected by the artefacts.* The state of each `artefact`, which conditions how the artefact will modify a future entering signal, must be modified several times during the iterations. Implementing artefacts as classes is convenient, since they can easily be saved in a given state, copied or deleted.

4.3.2 Example: effect of signal loss in active truncation

We will now illustrate how the `artefact` and `fixedFreeCableSegment` classes can be used in Algorithm 2, to co-simulate the active truncation setup, including the effect of artefacts. As an example, we will consider a co-simulation in which *signal loss* affects both the measured force and the applied velocity. Signal loss may for example be due to sensor and communication issues, or to unfinished calculations in the numerical substructure, such as reported in Vilsen et al. (2017). As presented in Example 13, signal loss is parametrized by a probability of occurrence θ_1, and an inverse duration parameter θ_2. When signal loss occurs, the signal is "frozen" to the last measured force, or the last commanded velocity, for a period of time, which is random, see Example 13. The probability distribution of this duration is exponential, with rate parameters θ_2. This means that *longer* and *more variable* signal losses are expected for smaller values of θ_2. In the present case, θ_1 is set to 1%, and θ_2 to 0.1, on both sensor and actuator side. So in this case, the artefacts are parametrized by $M = 4$ components, and

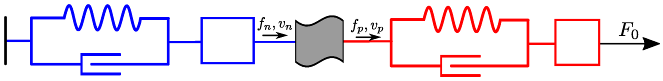

Figure 4.9: Stylized version of the active truncation problem, used to illustrate the effect of signal loss on the response of the substructures. The red linear oscillator represents the physical substructure, and the blue one represents the numerical substructure. The flag-shaped box represents the truncation point, where signal loss occurs. F_0 represents the top excitation. f and v represent the force and velocity at the truncation point, respectively: f_n and v_n are seen from the numerical substructure, and f_p and v_p from the physical substructure.

$\theta = (1\%, 0.1, 1\%, 0.1)^\top$.

The results of the co-simulation are presented in Figure 4.10, page 104, and described in the following. The dynamic excitation at the top node (first row) is identical for the emulated structure (black) and the physical substructure (red). This disturbance travels along the physical substructure (`p`), and reaches the truncation point where a force is measured (second row, red line). This force is possibly subjected to signal loss (`aS`) before being transferred, as a top force, to the numerical substructure (second row, blue line). The numerical substructure (`n`) responds to this top force (third row, blue line), and this response, which may also be affected by some signal loss (`aA`), is used to command the bottom velocity of the physical substructure (third row, red line). The effect of these signal losses on the QoIs, which are the top velocity and the bottom force, are shown (in red and blue) in the fourth and fifth rows, respectively. The fidelity is evaluated by comparing these signals to the ones obtained with the emulated structure (black lines). By applying (4.1) and (4.4), it is found that $\varphi_1 = 1.30$ and $\varphi_2 = 1.99$ for this case.

The right column in Figure 4.10 shows a selected time window during which signal losses happen on the measured force and on the applied velocity. On the second row, we can for instance observe that the signal of the force sensor freezes for about half a second shortly after $t = 174$ s, since the red and blue lines differ from each other. On the third row, it can be seen that the velocity command signal freezes twice, first at $t = 176$ s for half a second, then for about 300ms.

An important remark is that the substructure *which the signal comes from* has no direct information about the occurrence of a signal loss, but is anyway affected indirectly by the feedback it receives from the other substructure. Let us illustrate this by constructing a stylized version of our setup, represented in Figure 4.9. We assume that signal loss occurs *on the force measurement only*, and that the velocity actuation is perfect, that is $v_p = v_n$ at all times, while $f_n \neq f_p$ when signal loss occurs. Starting from static equilibrium, when F_0 increases, all other variables f_p, f_n, v_p and v_n will increase. If signal loss occurs in the force measurement, f_n keeps a constant value (instead of increasing), and v_n will eventually decrease due to the stiffness and damping of the numerical substructure. Since v_n directly steers the actuator command, v_p will decrease immediately, causing the stretching of the physical substructure, and an in increase in f_p. When the signal on the force senors is recovered, f_n will jump to to the (larger) f_p value, causing a sudden increase of v_n, and thus v_p. This simplified example describes well the mechanism causing the significant variations of the velocity of the truncation point (on the physical substructure side) observed in Figure 4.10 for $t \in [174, 176]$ s. This perturbation propagates according to the dynamics of the slender structure, to the top and bottom ends of the line, and is clearly observed both on the top velocity and bottom force time series. It will thus affect both φ_1 and φ_2.

4.4 Conclusion

We have in this section presented how active truncation could alleviate existing issues related to the hydrodynamic testing of ultra-deep water systems. We developed the necessary co-simulation tools needed to compute the fidelity of this CPEM. With the last example, we illustrated the possibly complex interaction mechanisms resulting from e.g. signal losses at the truncation point. In the next chapter, we will extend this analysis, and investigate the effect of a larger set of *random* and *heterogeneous* artefacts, occurring simultaneously, on the fidelity. We will, to this end, apply the framework developed in Chapter 3.

Table 4.2: Eigenperiods in seconds corresponding to the 15 first modes of a 1934m long cable subjected to a top tension of 2.5MN. In italic: deviation in percents between the analytical solution (transverse vibrations of a weightless and infinitely stiff string) and various numerical solutions computed with the `fixedFreeCableSegment` class. Note that in the four last columns, mode 11 computed with `fixedFreeCableSegment` corresponds to the first axial resonance mode. For these columns, the eigenperiods of modes 12-15 are therefore compared to those of modes 11-14 from the analytical solution.

	Analytical solution	Numerical solution using the `fixedFreeCableSegment` class											
Axial stiffness	Infinite	Nominal×10		Nominal×10		Nominal		Nominal		Nominal		Nominal	
Weight in water	Weightless	Weightless		Weightless		Weightless		Nominal		Nominal		Nominal	
Top force direction	-	Vertical		Vertical		Vertical		Vertical		Nominal		Nominal	
Current	-	None		None		None		None		None		Nominal	
Number of elements	-	500		80		80		80		80		80	
			%		*%*		*%*		*%*		*%*		*%*
Mode 1	49.15	49.15	*0.00*	49.15	*0.00*	49.39	*0.48*	50.68	*3.12*	50.17	*2.08*	50.17	*2.07*
Mode 2	16.38	16.38	*0.00*	16.38	*-0.01*	16.46	*0.47*	16.78	*2.42*	16.66	*1.71*	16.66	*1.71*
Mode 3	9.83	9.83	*0.00*	9.83	*-0.04*	9.87	*0.44*	10.06	*2.33*	9.99	*1.62*	9.99	*1.62*
Mode 4	7.02	7.02	*0.00*	7.02	*-0.08*	7.05	*0.41*	7.18	*2.28*	7.13	*1.57*	7.13	*1.57*
Mode 5	5.46	5.46	*0.00*	5.45	*-0.13*	5.48	*0.35*	5.58	*2.22*	5.54	*1.51*	5.54	*1.51*
Mode 6	4.47	4.47	*0.00*	4.46	*-0.19*	4.48	*0.29*	4.56	*2.15*	4.53	*1.45*	4.53	*1.44*
Mode 7	3.78	3.78	*-0.01*	3.77	*-0.27*	3.79	*0.21*	3.86	*2.07*	3.83	*1.37*	3.83	*1.36*
Mode 8	3.28	3.28	*-0.01*	3.26	*-0.36*	3.28	*0.12*	3.34	*1.98*	3.32	*1.27*	3.32	*1.27*
Mode 9	2.89	2.89	*-0.01*	2.88	*-0.46*	2.89	*0.02*	2.95	*1.87*	2.92	*1.17*	2.92	*1.16*
Mode 10	2.59	2.59	*-0.01*	2.57	*-0.58*	2.58	*-0.10*	2.63	*1.76*	2.61	*1.05*	2.61	*1.05*
Mode 11	2.34	2.34	*-0.02*	2.32	*-0.70*	2.41	-	2.41	-	2.41	-	2.41	-
Mode 12	2.14	2.14	*-0.02*	2.12	*-0.84*	2.34	*-0.25*	2.38	*1.78*	2.36	*1.01*	2.36	*1.00*
Mode 13	1.97	1.97	*-0.02*	1.95	*-0.99*	2.13	*-0.40*	2.17	*1.61*	2.15	*0.85*	2.15	*0.84*
Mode 14	1.82	1.82	*-0.03*	1.80	*-1.16*	1.96	*-0.56*	1.99	*1.43*	1.98	*0.67*	1.98	*0.67*
Mode 15	1.69	1.69	*-0.03*	1.67	*-1.34*	1.81	*-0.73*	1.84	*1.24*	1.83	*0.49*	1.83	*0.49*

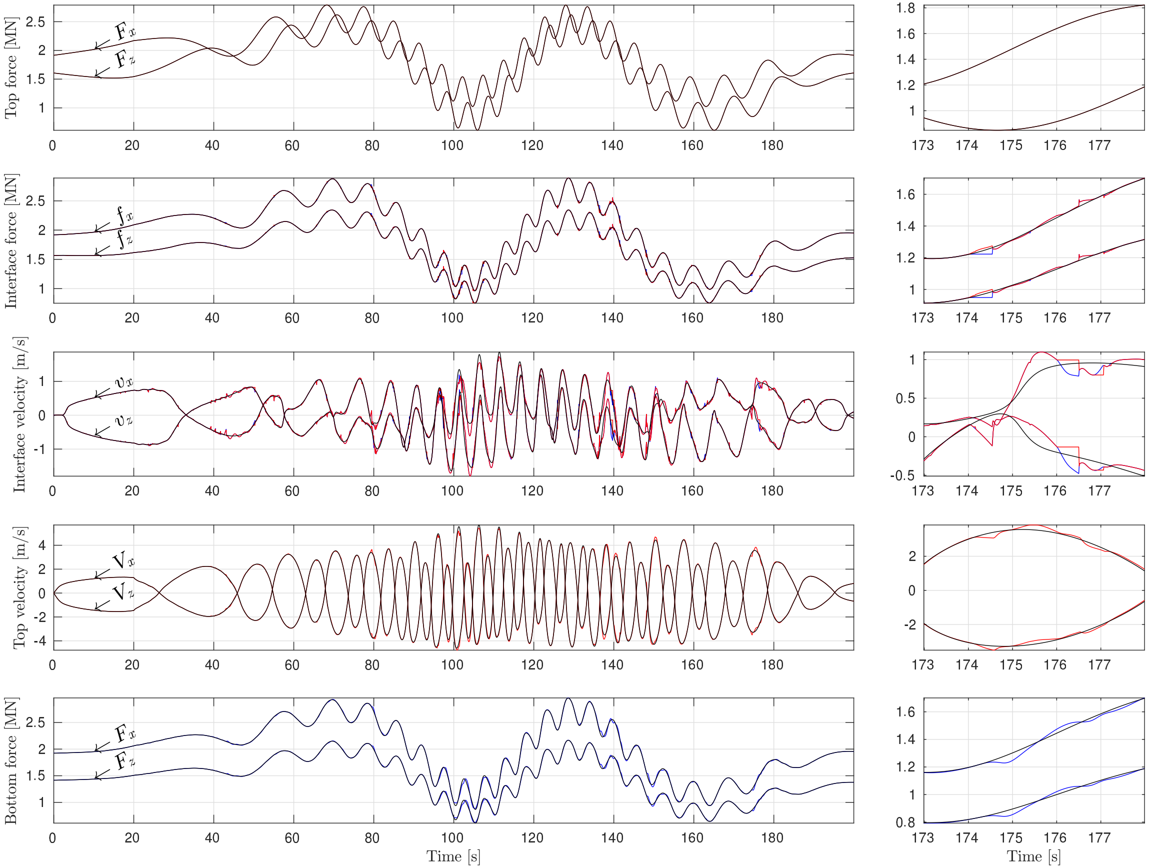

Figure 4.10: Active truncation setup subjected to the characteristic load τ. The red curves are obtained from the physical substructure p, and the blue curves from the numerical substructure n. The black curves represent the emulated system. Signal loss occurs at the force sensors level (as visible on the second row) and at the velocity actuation level (third row). The right column is a zoom on the time series at a location of interest.

Chapter 5

Fidelity analysis of the active truncation problem

In this chapter, we will investigate the fidelity of the active truncation setup defined in Chapter 4. This study will provide useful information for the design of active truncation, but also illustrate the capabilities of the generic fidelity analysis method developed in Chapter 3 when multiple, heterogeneous and random artefacts are involved. The numerical tools described in Chapter 4, i.e. the `artefact` and `fixedFreeCableSegment` classes will be used. Parts of this chapter have been published in Sauder et al. (2018) and Sauder et al. (2019).

5.1 Nominal analysis with $\alpha = 0.8$

We consider the polyester mooring line introduced in Section 4.1.3, and whose properties are given in Table 4.1. We still have $D = 1200$ m, α =0.8, and $\lambda = 1/60$. The bottom of the hydrodynamic laboratory, where sensors and actuators are installed, is located at a water depth of $(1 - \alpha)D\lambda = 4$ m. The force components f_x and f_z, originating from the physical part of the line at the truncation point, are measured by two independent force sensors. An actuator prescribes the velocity (v_x, v_z) of the truncation point. The mooring line is subjected to the current- and wave-induced loads introduced in Section 4.1.3. The fidelity indicators based on top velocity (φ_1) and bottom force (φ_2), defined in (4.1) and (4.4) are considered. In the following, φ may designate either φ_1 or φ_2, for conciseness.

As shown in Figure 5.1, ten individual artefacts, described by $M = 12$ parameters, are assumed to affect the setup. Each component of the force measurement is assumed to be contaminated by calibration error (gain),

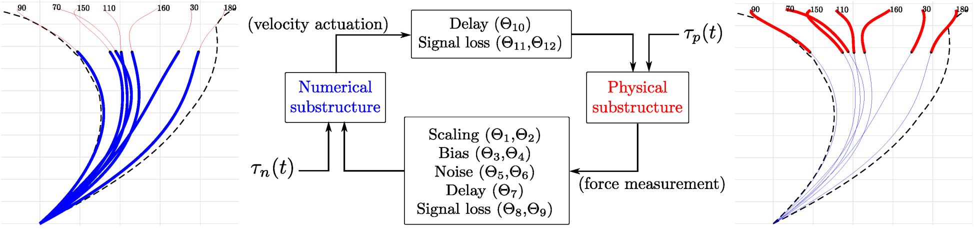

Figure 5.1: Structure of the system, modelled artefacts, and their describing parameters Θ_i. τ_n represents the current loads acting on the numerical substructure (in blue), and τ_p represents the current loads and varying wave loads acting on the physical substructure (in red).

bias, and noise. In the acquisition process, the force signals can be delayed, or lost, before entering the numerical substructure. A signal loss artefact, affecting the output of the numerical substructure, models the fact that nonlinear iterations in the numerical substructure may not complete on time (see discussion in Section 4.2.1). An additional delay on the actuation side models computation and communication processes. It is assumed that some delay-compensation techniques have been applied (Carrion, 2007; Vilsen et al., 2017), so that only values of the *residual* delay are considered here.

The artefacts and their probabilistic description are summarized in Table 5.1. Estimates of upper bounds, lower bounds, mean values, or standard deviations of the θ_i parameters were obtained from the experimental work reported in Vilsen et al. (2017), and the maximum entropy principle was used to define $f_\Theta(\theta)$ (see Section 2.1.2). Note that the core method would apply also if other artefacts were selected, or if Θ was described by another arbitrary distribution.

5.1.1 Uncertainty propagation

Following the steps in Section 3.2.1, the first objective is to estimate the expected fidelity $\mathrm{E}[\varphi(\Theta)]$ of the active truncation setup when it is affected by the present set of artefacts, and the associated uncertainty $\mathrm{Var}[\varphi(\Theta)]$, due to the uncertainties on Θ.

The first step to do so is to establish a PCE surrogate model of φ, denoted $\hat{\varphi}$, whose structure enables us to estimate efficiently $\mathrm{E}[\varphi(\Theta)]$ and $\mathrm{Var}[\varphi(\Theta)]$, as discussed in Sections 2.2.4 and 3.2.1. To determine $\hat{\varphi}$, $\varphi(\theta)$ must be evaluated for a space-filling set $\mathcal{E}$ containing samples of Θ. This set, of cardinality N, is generated with LHS as described in Section 2.1.3. For the purpose of our analysis, we have here generated an expanding sequence of

Table 5.1: Description of the artefacts affecting the setup, including their probabilistic description. Here λ=1/60 and δt=10 ms, and the values are given in full-scale.

Type of artefact	Affected signal	Describing parameter(s)	Unit	Probabilistic description
Calibration error	f_x	Θ_1 (gain)	-	$\mathcal{N}(1, 0.015)$
Calibration error	f_z	Θ_2 (gain)	-	$\mathcal{N}(1, 0.015)$
Bias	f_x	Θ_3 (bias value)	N	$\mathcal{N}(0, 0.05\lambda^{-3})$
Bias	f_z	Θ_4 (bias value)	N	$\mathcal{N}(0, 0.05\lambda^{-3})$
Noise	f_x	Θ_5 (noise variance)	N^2	$\mathcal{U}((0.025\lambda^{-3})^2, (0.05\lambda^{-3})^2)$
Noise	f_z	Θ_6 (noise variance)	N^2	$\mathcal{U}((0.025\lambda^{-3})^2, (0.05\lambda^{-3})^2)$
Delay	f_x,f_z	Θ_7 (duration)	s	$\mathcal{U}(0, 5\delta t)$
Signal loss	f_x,f_z	Θ_8 (probability of occurrence) Θ_9 (duration parameter)	- s^{-1}	$\mathcal{U}(1\%, 10\%)$ $\mathcal{U}(0.1, 0.5)$
Delay	v_x,v_z	Θ_{10} (duration)	s	$\mathcal{U}(0, 5\delta t)$
Signal loss	v_x,v_z	Θ_{11} (probability of occurrence) Θ_{12} (duration parameter)	- s^{-1}	$\mathcal{U}(1\%, 10\%)$ $\mathcal{U}(0.1, 0.5)$

five sets $(\mathcal{E}_i)_{i \in \mathbb{N}_5^*}$ of cardinality N equal to $32 \times 2^{i-1}$. This was done by using *nested LHS* (Blatman and Sudret, 2010), which sequentially add samples to $\mathcal{E}$, while ensuring that the updated set $\mathcal{E}$ still is a latin hypercube containing samples distributed according to $f_\Theta(\theta)$.

$\varphi(\theta)$ is evaluated by co-simulation, as explained in Section 4.2.3, for each sample in $\mathcal{E}_5$. Note that these 512 co-simulations are independent of each other and can therefore be performed in parallel. In Figure 5.2, the markers shows a scatter diagram of φ_1, plotted against each component of θ. The corresponding figure for φ_2 is reported in Appendix (Figure B.1). The distributions of φ_1 and φ_2, estimated from each $\mathcal{E}_i$ are shown in Figure 5.3.

Based on the initial set $\mathcal{E}$, the PCE model $\hat{\varphi}$ is established as described in Section 2.2.2. Since Θ is member of a twelve dimensional space, the polynomial basis $\mathcal{A}$ obtained with a hyperbolic truncation set and $q = 0.75$ has a cardinality of 1481. We recall that the required cardinality of $\mathcal{E}$ to identify a PCE is usually N = 2-3 $\times|\mathcal{A}|$, which is rather large with the present $\mathcal{A}$. The size of the basis is dramatically reduced, down to $|\mathcal{A}|$ =58 terms, by applying the LAR method detailed in Section 2.2.2. The PCE can then, in principle, be identified from a set $\mathcal{E}$ containing not more than a few hundred of samples. The accuracy, in terms of ε_{LOO}, of the PCEs obtained from each $\mathcal{E}_i$ is presented as a function of N on the top of Figure 5.5. It will be commented on later on.

The values of E$[\varphi(\Theta)]$ and Var$[\varphi(\Theta)]$ are evaluated from (2.19) and (2.21), and presented for various values of N in the middle of Figure 5.5. For $N = 128$, they are within 1% of the values obtained with the largest set

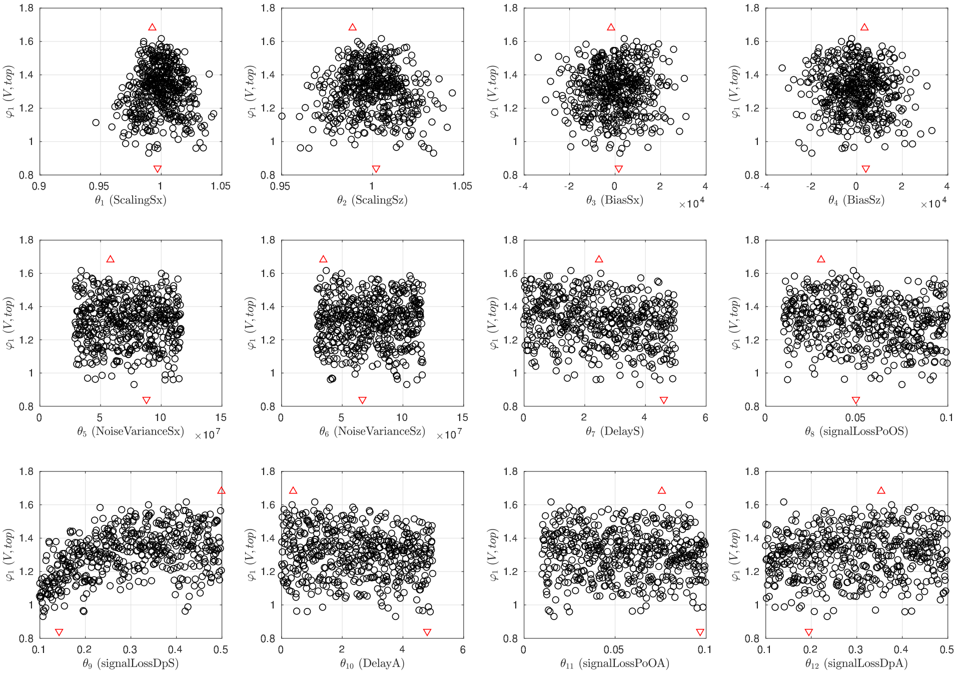

Figure 5.2: Scatter diagrams showing the value of φ_1 (fidelity indicator based on the top velocity of the line), as a function of the twelve parameters describing the artefacts. The dots correspond to N =512 samples of Θ obtained by Latin Hypercube Sampling (set denoted $\mathcal{E}_5$ in the text). The samples leading to the highest and lowest fidelity are represented by red triangles.

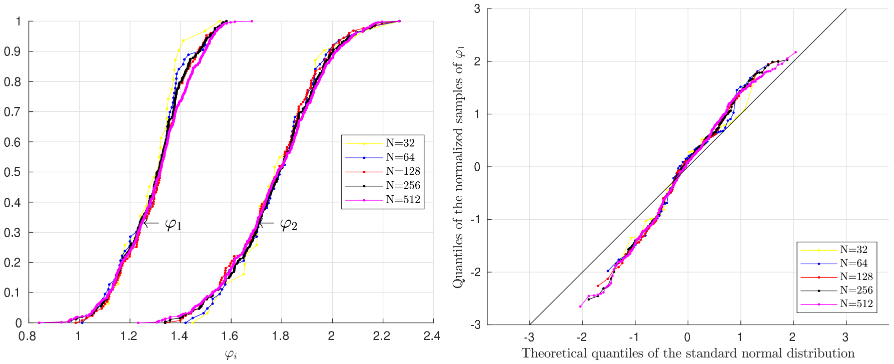

Figure 5.3: Cumulative distribution functions of φ_1 and φ_2 obtained from sets $\mathcal{E}$ of different sizes (l.h.s.), and quantile-quantile plot comparing the distribution of φ_1 to a normal distribution (r.h.s., Figure B.3 shows the corresponding plot for φ_2).

$\mathcal{E}$, and equal to:

$$E[\hat{\varphi}_1(\Theta)] = 1.32 \text{ and } \mathrm{Var}[\hat{\varphi}_1(\Theta)] = 0.13^2 \tag{5.1}$$

$$E[\hat{\varphi}_2(\Theta)] = 1.77 \text{ and } \mathrm{Var}[\hat{\varphi}_2(\Theta)] = 0.17^2 \tag{5.2}$$

The coefficient of variation of φ, defined as

$$c_v[\varphi[\Theta]] := \frac{\sqrt{\mathrm{Var}[\varphi(\Theta)]}}{\mathrm{E}[\varphi(\Theta)]} \tag{5.3}$$

quantifies the uncertainty on the fidelity relative to its mean value, and is approximately equal to 10% for both φ_1 and φ_2.

For illustration, Figure 5.4 shows the realization of Θ leading to the *median* value of φ_1, for which φ_1=1.33 and φ_2=1.62. Seen in light of (5.1) and (5.2), this realization corresponds to an *average fidelity* if the behaviour of the top of the line of interest, and to a *quite poor fidelity* if the objective was to reproduce the bottom force correctly.

Note that this uncertainty propagation analysis does not, by itself, assess whether the expected fidelity of the active truncation setup at hand is *sufficiently* high. The value of the minimum admissible fidelity depends on the intended use of the empirical data, and is to be assessed by the designer of the active truncation setup. Lower fidelity values might be tolerated in early-stage conceptual studies of floating systems, for instance, while high-fidelity would be required for final verification tests, or for the validation of numerical methods.

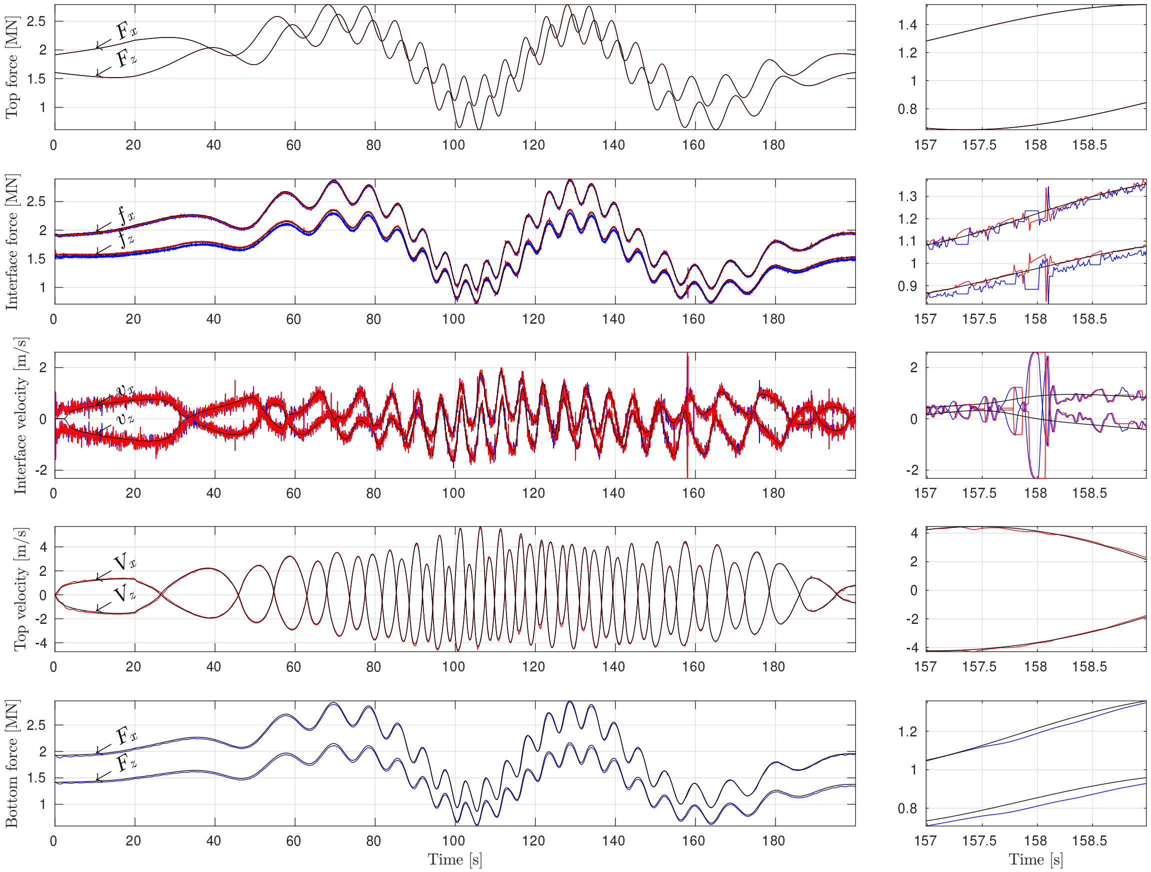

Figure 5.4: Co-simulation of active truncation with a set of the artefacts leading to the *median* value of φ_1. For this realization, the measurement of f_x (resp. f_z) is affected by a -0.3% (resp. -3%) calibration error, a -0.012 N (resp. 0.28 N) bias, and noise with a standard deviation of 0.040 N (resp. 0.037N), in model scale. The force measurement is delayed by 2.6ms, and has a probability of signal loss of 7.5%, with a duration parameter of 0.47, which corresponds to frequent and short periods of signal loss. On the actuation side, the delay is 1.3ms, and the probability of occurrence and duration parameter of signal loss are 6.8 % and 0.17, respectively. The resulting fidelity indicators are φ_1=1.33 and φ_2=1.62.

5.1.2 Sensitivity analysis

As discussed in Sections 2.2.5 and 3.2.1, the sensitivity analysis aims at identifying the artefacts contributing the most to the uncertainty on the fidelity, evaluated in (5.1) and (5.2). This provides a rational course of action to reduce this uncertainty, but also to improve the expected fidelity if it is deemed too low.

In low-dimension (i.e. small M) cases, and particularly when the number of samples in $\mathcal{E}$ is large, visual inspection of scatter diagrams such as Figure 5.2, enables one to determine directly which artefact component(s) affects the most the fidelity. This inspection-based method becomes however less reliable in high dimensions, such as in the present case with $M = 12$. As introduced in Section 3.1.2, Sobol' sensitivity indices can instead be used, and derived directly from $\hat{\varphi}$. Before looking at the Sobol' indices, let us recall that the *absolute* values of the total Sobol' indices $S_{T,i}$ are of secondary importance: the $S_{T,i}$ should be *compared to each other* to identify the most influencing artefacts' parameters. Furthermore, $S_{T,i}$ can be compared to the first order Sobol' index S_i, to understand whether the artefact parameter Θ_i influences the variance of $\varphi(\Theta)$ alone, or in an interaction with another parameter Θ_j, or several others.

With these interpretation keys in mind, let us consider the bottom plots in Figure 5.5, showing the $S_{T,i}$ and S_i, estimated for various sizes N of $\mathcal{E}$. It is seen that for the present problem, reliable insight into the main mechanisms of sensitivity can be obtained for N=128. If N=256, finer conclusions can be made regarding the sensitivity to less important parameters, which do not change when N=512. Note that the recommended maximum values for ε_{LOO} in Le Gratiet et al. (2015) seem rather conservative for the present situation, since good convergence of the statistical moments and meaningful sensitivity information are obtained, in spite of an ε_{LOO} exceeding 0.1.

Let us first outline the main conclusions that can be drawn from the total Sobol' indices $S_{T,i}$, represented by grey bars in Figure B.6b (consider for example N=256). The fidelity indicator based on the *top velocity* response, φ_1, is very sensitive to θ_9 (the duration of the signal loss on the force signal) and to the calibration errors of the f_x and f_z measurement (θ_1 and θ_2). φ_1 is much less sensitive to the other θ_i, and clearly insensitive to noise (described by θ_5 and θ_6). Focusing now on the *bottom force*, we see that φ_2 is mostly sensitive to θ_1, then θ_2 (calibration errors), and then to a much less extent to the biases θ_3 and θ_4, which have both comparable total Sobol' indices. φ_2 is slightly sensitive to θ_9, the duration parameter for signal loss on the force measurement, and insensitive to the other θ_i parameters.

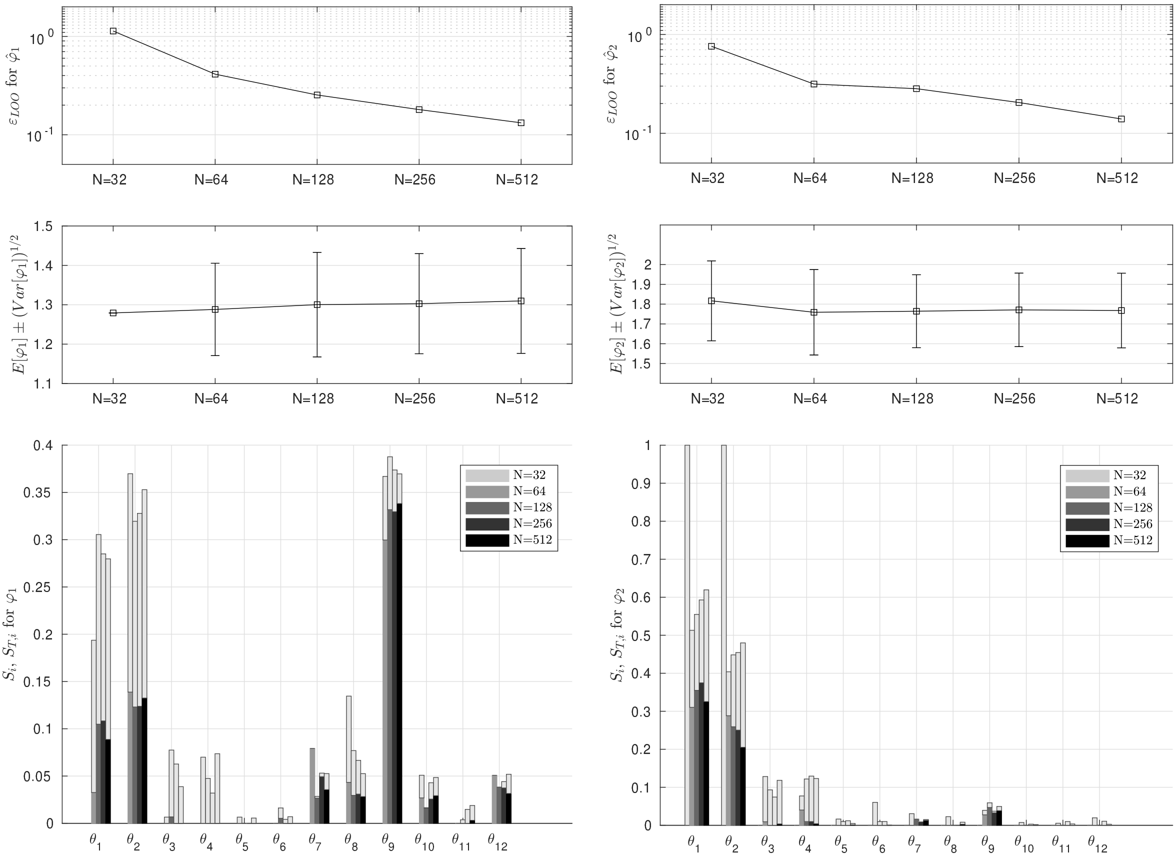

(a) Results for φ_1

(b) Results for φ_2

Figure 5.5: Upper plot: normalized Leave-One-Out cross-validation error for the PCE metamodel of φ_i. Middle plot: expected value and variance of φ_i estimated from initial empirical designs of five different sizes. Lower plot: first-order Sobol' indices of φ_i estimated from these initial experimental designs. The corresponding *total* Sobol' index of each θ_i is plotted in grey in the background.

5.1.3 Physical interpretation

We will now relate these results, obtained by a systematic and data-driven approach, to their physical causes.

It is clear from Figure 5.4 that the noise affecting force measurements (parametrized by θ_5 and θ_6) induces a significant velocity response at the truncation point. This response is however filtered mechanically by drag and, to a less extent, structural damping, before reaching the top and bottom of the mooring line. Therefore noise does not significantly affect the fidelity indicators φ_1 and φ_2. The fact that the $S_{T,i}$ associated to this artefact are negligible, means that the corresponding parameters θ_5 and θ_6 (noise variances) could have been set to deterministic values (here, zero), without affecting the variance of φ.

The force sensors feeds the numerical substructure, while the actuator controls the bottom part of the physical substructure, whose response *directly* enters in the definition (4.1) of φ_1. A natural question, when looking at Figure 5.5a, is then why the top velocity (or φ_1) is more sensitive to signal loss, when it acts on the force sensor (duration parameter θ_9) rather than when it acts on the velocity actuation (parameter θ_{12}). The reason is the following. When signal loss on the velocity command happens, the velocity of the truncation point keeps a *constant* value. On the other hand, signal loss on the force sensor may cause *large variations* of the truncation point's velocity, due to the interaction with the numerical substructure that was commented in detail in Section 4.3.2 and seen in Figure 4.10. Both the *amplitude* of these perturbations and their *duration* increase when the signal loss characteristic duration increases, which enhances their propagation to the top of the mooring line.

The fact that φ_2 is more sensitive to θ_1 (calibration error for f_x measurement) than to its counterpart θ_2 (acting on f_z) can be explained as follows. Transverse motions of the mooring line are subjected to drag damping forces, while axial motions are only damped by structural damping, which means that, with the present choice of α_2 and the present frequency range of motions, transverse motions will be subjected to a significantly higher level of damping than axial motions. Consequently, an axial dynamic force error will be less damped than its transverse counterpart. Since the mooring line forms an angle of $\gamma = 39.2\ ^o$ with respect to the x-axis at the truncation point, the axial forces have an x-component larger than their $z-$ component, and a calibration error on f_x (parametrized by θ_1) will play a greater role for φ_2 than a calibration error on f_z (parametrized by θ_2).

Also, as explained earlier, Total Sobol' indices and first-order indices differ when there is a non-additive interaction between two (or more) θ_i in φ.

The nature of this interaction can be determined by considering higher-order Sobol' indices (not shown here). Note that in principle, a finer PCE model (with lower $\varepsilon_{\mathrm{LOO}}$) would be needed to obtain accurate estimates of the higher-order Sobol' indices, so we will only comment on the trends observed with the PCEs at hand. We found for example that the interaction between θ_1 and θ_2 explains $\approx 20\%$ of the variance of φ_1, and $\approx 15\%$ of the variance of φ_2. This is due to the fact that if θ_1 and θ_2 differ significantly from each other, the amplitude, but also the *direction* of the force at the truncation point will be affected[1]. Since the stiffness and damping properties of the line are strongly anisotropic, as explained earlier, this change in direction will have a significant effect on the fidelity.

From Figure 5.5, we then see that biases have a sensible influence on φ_1 and φ_2 (total Sobol indices), and that this influence is due to interactions ($S_5 \ll S_{T,5}$ and $S_6 \ll S_{T,6}$ in both cases). Here, the mechanisms in play are slightly different for φ_1 and φ_2.

- By again studying higher-order Sobol indices, it can be shown that the interaction between θ_1 and θ_3 (resp. θ_2 and θ_4) explain $\approx 10\%$ of the variance of φ_2. This interaction is induced by the *pretension* at the truncation point, denoted T_0^*. Indeed, for example, when a scaling error θ_1 affects f_x only, it is equivalent to a bias of $(\theta_1 - 1)T_0^* \cos\gamma$ being added to θ_3, and transferred to the anchor point. Coupling terms between θ_1 and θ_3 will therefore be generated in the Sobol' decomposition (2.25) of φ_2, due to the square and logarithm in (4.4).
- Biases should, in principle have little influence on φ_1, since constant force will simply lead to a constant offset, and not change the (linear) dynamical properties of our substructures. However, about $\approx 10\%$ of the variance of φ_1 is due to one-to-one interactions between θ_1, θ_2, θ_3, and θ_4. This is due to the following effect. In the horizontal direction, for $t < 0$, the component of the pretension is $T_0^* \cos\gamma$ at the truncation point. For $t \geq 0$, it suddenly changes to $\theta_3 + (\theta_1 - 1)T_0^* \cos\gamma$, when artefacts are applied to the force signal. This impulsive load causes a transient response, visible in Figure 5.4, which has a minor, but sensible, influence on φ_1.

We have, in this section, shown how the results of the systematic sensitivity study performed in Section 5.1.2 leads to the identification of the the most

---

[1] Let $f_p = (f_{x,p}, f_{z,p})$ be the actual force at the truncation point, and f_n the force measured and sent to the numerical substructure. Let us assume that only the gains errors are present, and denote $p = \theta_1\theta_2$ and $q = \theta_2/\theta_1$. Then the distortion in the module and direction of the force, due to the measurement errors, are given by $||f_n||^2 = p\left(\frac{1}{q} f_{x,p}^2 + q f_{x,p}^2\right)$ and $\angle f_n = \arctan q \frac{f_{z,p}}{f_{x,p}}$

critical artefacts for this problem, and enables one to gain insight in the complex coupling between the control system and the mooring line dynamics.

5.1.4 Reliability analysis

While the two previous sections addressed RQ1, the present section will exemplify how probabilistic robust fidelity of the active truncation setup can be assessed (RQ2), and how the fidelity bounds of the considered setup could be established (RQ3). In this section, we will assume that the interaction of the top of the line with the floater is of interest, and consider only the fidelity indicator φ_1.

As a design choice, we set the minimum admissible fidelity for this setup to $\varphi_{\mathrm{adm}} = 0.8$, which we want to achieve with a probability of at least $1 - \varepsilon_{\mathrm{adm}} = 0.999$. In other words, we will consider that probabilistic robust fidelity is achieved if

$$P_f := P[\varphi_1 < 0.8] < 10^{-3} \tag{5.4}$$

By considering Figure 5.2, we see that none of the samples of Θ in the largest initial set $\mathcal{E}_5$ leads to a fidelity less than φ_{adm}. However this set had a cardinality of N =512, which is too low to confidently assess whether (3.3.3) holds. Furthermore, by considering the quantile-quantile plot in Figure 5.3, it can be observed that the distribution of φ_1 has heavy tails. Extrapolating the empirical distribution to lower quantile values is therefore hazardous.

The Adaptive Kriging method presented in Sections 3.2.1 and 2.3.4 is applied to address this problem. Additional samples of Θ are generated, as presented in Example 12 and in Section 3.3.3. The two key differences with the analysis performed on the coupled linear oscillators, is that the algorithm now explores a space of dimension $M = 12$, and that $K = 16$ new samples of θ are added at each step of the enrichment process. The co-simulations and evaluations of φ for the batch of 16 new samples are performed in parallel.

Starting from $\mathcal{E}_4$, which contains 256 samples of Θ all leading to a fidelity greater than φ_{adm}, the first enrichment step is taken. In this step, the PCK surrogate model established from $\mathcal{E}_4$ is used to evaluate where the probability of misclassification P_m is large, i.e. where φ_1 could have dropped close to φ_{adm} and/or is highly uncertain. As illustrated in Figure 5.6, the regions of $\mathcal{D}$ associated with a large P_m are detected where the ratio θ_2/θ_1 deviates significantly from unity, where θ_8 is small, and, to some extent where θ_7 and θ_{10} are simultaneously large. In physical terms, this corresponds to a distortion of the measured force angle, to long periods of signal loss of the force sensor (both have a significant influence on the fidelity as commented in Section 5.1.2), and to significant delays in the loop, which may yield an unstable, and thus low-fidelity, system. We note that since the new samples are chosen by a clustering algorithm, they are nicely spread over the limit state margin (2.55).

The evolution of the estimated probability of failure P_f during the enrichment process is shown in Figure 5.8 (consider $\alpha = 0.8$ only, in a first stage). From the initial sample set (256 samples), P_f is estimated to $2.5 \times 10^{-2} > \varepsilon_{\text{adm}}$, but after about 60 enrichment steps in which the accuracy of the PCK model near $\mathcal{L}$ is improved, P_f stabilizes at $3.6 \times 10^{-4} < \varepsilon_{\text{adm}}$. Small oscillations are still visible in the 20 last steps, which are induced by the randomness of the *auxiliary* sample sets used in the computation of (3.9). The amplitude of these oscillations can be decreased by increasing the cardinality of this auxiliary set. This is, however, necessary only if P_f is close to ε_{adm}, and if these oscillations were preventing us to conclude on the robust fidelity of this setup.

Note that even if the problem is twelve-dimensional, the total number of required enrichment steps remained of the order of 10^2.

5.2 Some variations of the problem

In the previous section, we studied the fidelity of an active truncation setup with $\alpha = 0.8$. In this section we will present two variations of this problem. The first variation aims at illustrating the consequence of using a *local* performance indicator (this term will be defined in the next section). The second variation aims at investigating the effect of truncating the mooring line at a deeper location.

5.2.1 Distinction between fidelity and local performance

Considering exactly the same truncation setup and set of artefacts as in the previous section, we now introduce another indicator denoted φ_3, which quantifies the mechanical power mismatch between the numerical and physical substructures at the truncation point. This indicator is defined as

$$\varphi_3 := -\frac{1}{2}\log_{10}\gamma^2_{\Delta P} \tag{5.5}$$

where

$$\gamma^2_{\Delta P} := \frac{\int_0^T (f_n \cdot v_n - f_p \cdot v_p)^2 dt}{\int_0^T (f_p \cdot v_p)^2 dt} \tag{5.6}$$

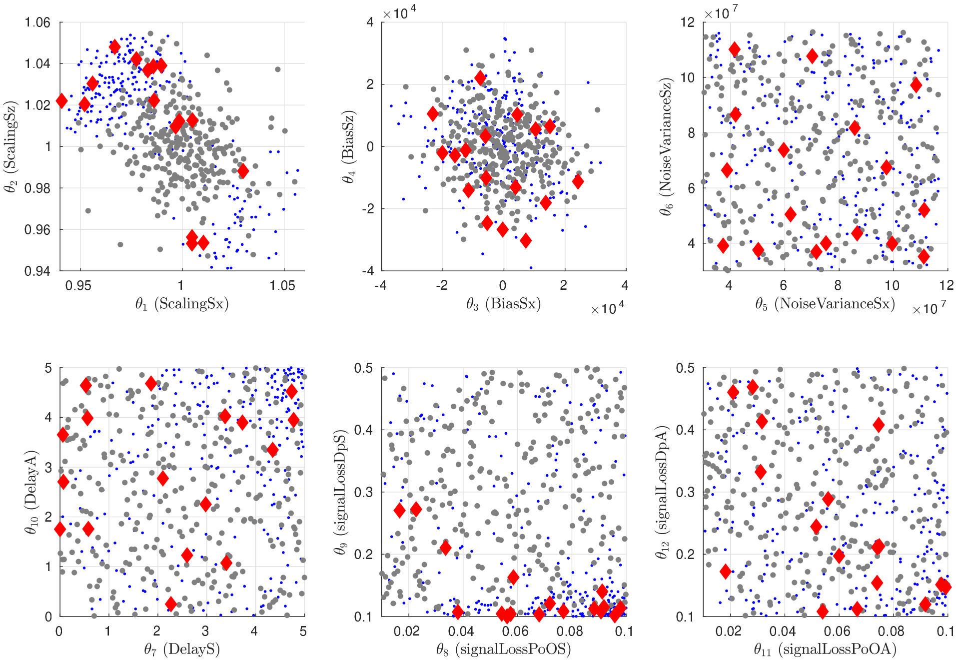

Figure 5.6: Illustration of the first enrichment step. The grey dots represent the samples in the initial set $\mathcal{E}$. The blue dots corresponds to areas of the twelve dimensional space with large probability of misclassification ($P_m > 0.45$). The red diamonds represent the K =16 samples selected by the clustering algorithm, at this step.

and where f and v denote the force and velocity vectors, respectively, and Σ_n and Σ_p, the numerical and physical substructures, respectively. In other words, considering the plots on the second and third rows of Figure 5.4, φ_3 quantifies the mismatch between the power obtained from the red curves and the blue curves. This type of indicator has been used in the analysis of several CPEM, as discussed in Section 1.2.2.

We qualify this performance indicator as "local", since it penalizes a loss of compatibility and equilibrium *at the truncation point*, without considering the behaviour of other parts of the substructures. It is quite different from φ_1 and φ_2, in the sense that it is not based on a quantity of direct interest for the test, and does neither use the emulated system as a reference. The indicator φ_3 is therefore not a *fidelity* indicator, according to Definition 19.

However, φ_3 is based on a similar comparison structure (normalized time integration of the squared error) as the one used in φ_1 and φ_2, which makes the comparison between these three indicators meaningful and interesting. Using the same set $\mathcal{E}_5$ as in the previous section, and the same PCE-based approach, the following observations are made.

- The two first moments of φ_3 can be estimated to

$$E[\hat{\varphi}_3(\Theta)] = 1.01 \text{ and } \mathrm{Var}[\hat{\varphi}_3(\Theta)] = 0.18^2 \tag{5.7}$$

  By comparing $E[\hat{\varphi}_3(\Theta)]$ to $E[\hat{\varphi}_1(\Theta)]$ and $E[\hat{\varphi}_2(\Theta)]$ given in (5.1) and (5.2) for the same set of artefacts, it is seen that the error on the transfer of power between the substructures can be significantly larger[2] than the resulting errors on the quantities of interest. Furthermore, the coefficient of variation for φ_3 is 17%, while it was close to 10% for φ_1 and φ_2, meaning that the local indicator is in comparison more sensitive to the the given set of artefacts than the fidelity indicators.
- The Sobol' indices for φ_3 are shown in Figure B.5 for sets $\mathcal{E}_i$ of various sizes, and compared to the Sobol'indices for φ_1 and φ_2 in Figure 5.7. The conclusions drawn from this sensitivity analysis are radically different from the ones obtained for φ_1 and φ_2. Indeed, while calibration errors and signal loss on the force sensors were found to be the most influencing parameters for φ_1 and φ_2, they have an insignificant effect on φ_3. Besides, φ_3 is mostly affected by the artefacts acting the velocity actuation (time delay and signal loss), which played a very minor role for φ_1 and φ_2. We will come back to this in the next section.
- The probability of this indicator to drop below $\varphi_{\text{adm}} = 0.8$ can be directly estimated by considering the distribution of φ_3, without need

---

[2] We remind the reader about the logarithm in the definition of the φ_i

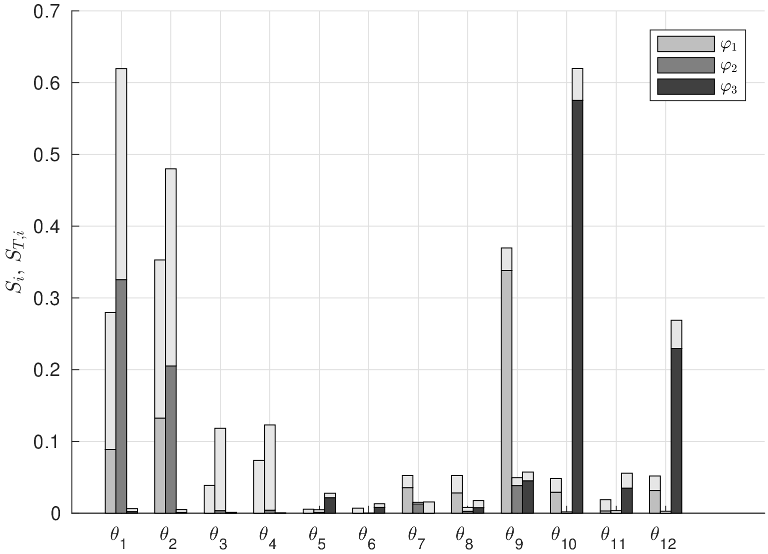

Figure 5.7: Comparison of the outcomes of the sensitivity analyses for the fidelity indicators φ_1 and φ_2, and the local performance indicator φ_3

for Adaptive Kriging, due to the generally lower values taken by φ_3. This probability is found to be about 10%, which is significantly larger than ε_{adm}.

From this analysis, we can conclude that designing the control system based on the local indicator φ_3 would have led to an over-conservative (or possibly unfeasible) design for given performance targets. Furthermore, based on the conclusions of the sensitivity analysis, the designer would have attempted to minimize the artefacts present on the velocity actuation side, which have been shown to be of marginal importance for the fidelity.

5.2.2 Influence of the truncation ratio

As a second variation of the problem presented in Section 5.1, we investigate the consequence of decreasing the truncation ratio α from 0.8 to 0.5 and 0.2. In that case, the required water depth in the hydrodynamic laboratory $(1-\alpha)\lambda D$ increases from 4 m to 10 m and 16 m, respectively. The control system, and the artefacts used to describe it, remain the same as above.

Let us first describe the dynamical behaviour of the truncation point at these water depths. For the mooring line considered here, the amplitude of the transverse wave-frequency vibrations of the structure decreases approximately exponentially with the depth[3]. For $\alpha = 0.8$, the standard deviation of this amplitude at the truncation point is about 10% of its counterpart at the top of the line. For $\alpha = 0.5$ the ratio is about 2%. When α decreases, the motions of the truncation point become mainly axial. Since the largest excitation frequency in τ is twice lower than the first axial eigenfrequency of the mooring line, the lower portions of the line will undergo *quasi-static* stretching, whose amplitude goes to zero when $\alpha \to 0$, since the line is fixed to the seabed. The *tension* in the line is very much influenced by the drag and transverse line dynamics at the top of the line, but when the transverse velocity become negligible (say for $\alpha < 0.5$), the dynamic part of the tension becomes approximately uniform along the line. Note that the static part of the tension decreases slightly due to the weight in water of the polyester.

The expected fidelity for $\alpha \in \{0.8, 0.5, 0.2\}$ and coefficient of variations due to the randomness of the artefacts are summarized in Table 5.2. The two fidelity indicators φ_1 and φ_2 are considered, as well as the local performance indicator φ_3. The sensitivity indices of the φ_i are compared in Figure 5.9 for three values of α. The following comments can be made.

Table 5.2: Comparison of the statistical moments of $\varphi_i(\Theta)$ for three truncation ratios.

	$\mathrm{E}[\hat{\varphi}_i(\Theta)]$			$\sqrt{\mathrm{Var}[\hat{\varphi}_i(\Theta)]}$			$c_v[\hat{\varphi}_i(\Theta)]$		
α	0.8	0.5	0.2	0.8	0.5	0.2	0.8	0.5	0.2
φ_1	1.32	1.43	1.68	0.13	0.13	0.12	10.2%	8.9%	7.3%
φ_2	1.77	1.74	1.72	0.17	0.18	0.18	10.7%	10.1%	10.4%
φ_3	1.01	0.86	0.5	0.18	0.18	0.18	17.4%	20.7%	36.0%

Influence of α on φ_1 We find that the expected fidelity increases significantly when α decreases. Since the variance of the fidelity remains approximately constant, the coefficient of variation of φ_1 decreases.

From Figure 5.9, calibration errors, which were important when $\alpha = 0.8$, have less influence when α decreases. Indeed, as discussed in Section 5.1.3, combinations of θ_1 and θ_2 lead to both a change of amplitude and direction of the measured force. For low α, errors in the amplitude of the quasi-static axial

---

[3] For our lightweight polyester mooring line with $C_d = 1.6$, the drag loads per unit length are much greater than inertia loads, which translates into a β parameter, defined in equation (2.25) in Argyros (2011), much larger than 1. This case is analyzed in Appendix A in the same reference.

stretching will lead to decreasing errors in the deflection of the truncation point since the stiffness of the numerical substructure is proportional to α^{-1}. And if the (axial) force is distorted, the resulting lateral vibrations at the truncation point will be absorbed by drag loads before reaching the top of the line, and influencing the QoI (the top velocity).

On the other hand, the sensitivity to the signal loss of the force sensors increases significantly when α decreases. The mechanisms giving rise to large spurious forces and velocities due to force signal loss have been discussed in Section 4.3.2 for $\alpha = 0.8$. How the location of the truncation point influences these mechanisms? The axial stiffness of the physical substructure is proportional to $(1-\alpha)^{-1}$, so when α decreases, larger force and velocity perturbations, with a higher-frequency content, will be generated at the truncation point. The characteristic duration of signal loss is much shorter than the first axial resonance frequency of the structure, which means that these spurious forces are of impulsive nature, and will excite all axial modes of the structure. However, the damping ratios associated with the second and third axial modes are 17% and 29%, respectively, so mainly the first axial mode (with a damping ratio of 6%) of the slender structure will exhibit a significant response. In other words, the perturbations induced by signal loss increase when α decreases, but their influence on the QoI decreases. This balance explains why, in Figure 5.9, the importance of the force signal loss artefact is larger for $\alpha = 0.5$ than for $\alpha = 0.2$ or 0.8.

The estimated P_f drops from 3.6×10^{-4}, for $\alpha = 0.8$, to about 8.7×10^{-5} and 4.8×10^{-5} for $\alpha = 0.5$ and 0.2, respectively, meaning that the probabilistic robustness of the setup increases when α decreases. Figure 5.8 shows the convergence plots of P_f, defined in 5.4 for the three truncation ratios. Again, small oscillations of P_f are still visible in the last steps, which could be attenuated by increasing the cardinality of this auxiliary set. This is, however, not necessary here, since $P_f \ll \varepsilon_{\text{adm}}$. Note also that all AK-MCS analyses have been initiated with 256 samples of $\varphi_1(\Theta)$. Since the expected fidelity was increasing for $\alpha \in \{0.5, 0.2\}$, less than 16 of the 10^6 auxiliary samples at which the PCK is evaluated fell into the limit state margin at the first enrichment step. The K-means algorithm could then not be applied. A work-around was to temporarily increase φ_{adm} to 0.9 (for $\alpha = 0.5$) or 1.0 (for $\alpha = 0.2$) during the first enrichment steps. This allowed to refine the PCK in low fidelity regions, before switching φ_{adm} back to 0.8 for the rest of the analysis. Since the values of P_f are not available for these first enrichment steps, they are missing from Figure 5.8.

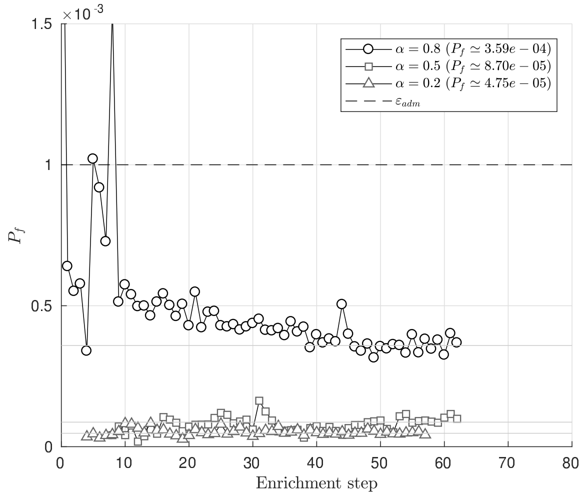

Figure 5.8: Evolution of the estimated probability of failure as a function of the number of enrichment steps for two different truncation ratios. The reasons for the missing values of P_f for the first enrichment steps for $\alpha = 0.5$ and 0.2 are detailed in the text.

Influence of α on φ_2 The influence of α on the expected fidelity is much less pronounced for φ_2 than for φ_1. The coefficient of variation is approximately independent of α. As indicated earlier, the line undergoes mainly quasi-static stretching at the truncation point for $\alpha < 0.8$, meaning that the forces will be the nearly the same for all three truncation ratios.

It is interesting to consider the limit case $\alpha \to 0$. In that case, the calibration error and bias artefacts act directly on the QoI, i.e. the measured bottom force. The dynamic response of the numerical substructure is insignificant, and its anisotropic character does not play a role anymore. According to (4.5), and omitting the "*bottom*" in the indices, we have

$$\begin{aligned}
\gamma^2_{F_x}(\theta)\int_0^T \bar{F}_x(t)^2 dt &= \int_0^T \left[F_x(t|\theta) - \bar{F}_x(t)\right]^2 dt \\
&\underset{\alpha\to 0}{=} \int_0^T \left[\theta_1\bar{F}_x(t) + \theta_3 - \bar{F}_x(t)\right]^2 dt \\
&\underset{\alpha\to 0}{=} (\theta_1 - 1)^2 \int_0^T \bar{F}_x(t)^2 dt + 2(\theta_1 - 1)\theta_3 \int_0^T \bar{F}_x(t) dt + \theta_3^2
\end{aligned}$$

so

$$\gamma^2_{F_x}(\theta) \underset{\alpha\to 0}{=} (\theta_1-1)^2 + 2(\theta_1-1)\theta_3\frac{\int_0^T \bar{F}_x(t)dt}{\int_0^T \bar{F}_x(t)^2dt} + \frac{\theta_3^2}{\int_0^T \bar{F}_x(t)^2dt} \tag{5.8}$$

In our case, it can be checked numerically that the last term is negligible compared to the two first ones. Denoting $r_x = \frac{\int_0^T \bar{F}_x(t)dt}{\int_0^T \bar{F}_x(t)^2dt}$, $r_z = \frac{\int_0^T \bar{F}_z(t)dt}{\int_0^T \bar{F}_z(t)^2dt}$, and reasoning similarly for $\gamma^2_{F_z}$, we get

$$\gamma^2_{F_x}(\theta)+\gamma^2_{F_z}(\theta) \underset{\alpha\to 0}{\simeq} (\theta_1-1)^2+(\theta_2-1)^2+2(\theta_1-1)\theta_3 r_x+2(\theta_2-1)\theta_4 r_z \tag{5.9}$$

The fidelity φ_2 is found by taking minus half the logarithm of (5.9). Since the x- and z- components of the measured force play a similar role in the calculation of φ_2, and since the sensors exhibit the same calibration errors and biases, it is expected that the first-order Sobol' indices for θ_1 and θ_2 will be equal for $\alpha \to 0$. The biases influence φ_2 in interaction with the gains for all truncation ratios, and their Sobol' indices will converge to a limit that depends on r_x and r_z, and thus on $\tau(t)$.

Influence of α on φ_3 We recall that φ_3 is not a fidelity indicator, and as such, it will not be commented in details. It is however interesting to observe that $\mathrm{E}[\varphi_3(\Theta)]$ decreases dramatically when α decreases. This is mainly due to the fact that the power transferred to the physical substructure at the truncation point tends to zero when $\alpha \to 0$. Hence, the normalizing factor in (5.6) decreases much faster than the power mismatch at the numerator. Furthermore, it is seen in Figure 5.9 that the time delay and signal loss on the velocity actuation play an important role, and are in general much more important than their counterparts acting on the force measurement. This is due to the fact that the former artefacts modify (directly) v_p, while the latter ones acts on f_n. The multiplying factors of these two terms in the power mismatch equation $f_n \cdot v_n - f_p \cdot v_p$ are f_p and v_n, the former being several orders of magnitude than the latter. So, in the sense of variance decomposition, φ_3 is therefore more sensitive to artefacts acting on the velocity actuation than on the one acting on the force measurement.

We can conclude this study by noting that the influence of force measurement noise was insignificant for all cases, for the reasons outlined in Section 5.1.3. Note however that a noisy inputs can lead to stability issues with other numerical substructures, and might as such need some consideration.

5.3 Conclusion

In this section, we have applied the method presented in Chapter 3 to study the fidelity of the active truncation of a taut polyester mooring line. The initial truncation ratio α was equal to 0.8, meaning that a setup that would have required a 20 m deep basin can be tested in 4 m water depth. The control system connecting the substructures was modeled by a total of ten artefacts, described by twelve parameters. Two fidelity indicators were considered, φ_1, focusing on the interaction between the slender structure and the floater, and φ_2, on its interaction with the seabed. The dynamics of the polyester line was described by a non-closed form model. The co-simulations including the artefacts were performed as described in Chapter 4.

This study enabled us gain insight in the complex interaction between the two substructures and the control system. The sensitivity analysis put in evidence the importance of calibration errors on the force sensors and, for φ_1, signal loss in the force measurement. The effect of noise on the fidelity indicators was found to be insignificant. The analysis also indicated that artefacts of different nature were interacting, and could jointly influence the fidelity.

In a first variation of our problem, we studied a local performance indicator, that quantified the power mismatch between the substructures. We showed that it was possible to achieve an high level of fidelity, even when the control system was not consistently transferring the mechanical power between the substructures. The local performance indicator was very sensitive to the time delay on the actuation side, parametrized by θ_{10}, while this parameter was of limited importance for the fidelity indicators φ_1 and φ_2. This "mitigating" effect was due to the mechanical properties and dynamic behaviour of polyester line.

In the second variation of our problem, we showed that for a given control system, it was beneficial to decrease the truncation ratio α to achieve high-fidelity. Indeed the expected value of φ_1 increased then significantly, while the expected value of φ_2 remained undisturbed. For both fidelity indicators, α did not influence much the variance of the fidelity indicators, but reducing α increased the probabilistic robustness of the setup (based on φ_1). It was shown that the sensitivity to given artefacts was strongly dependent on α.

These results are of practical interest for the development of active truncation. While the developed fidelity analysis method is generic, it must be emphasized that the conclusions presented here are valid for the present system and set of artefacts only.

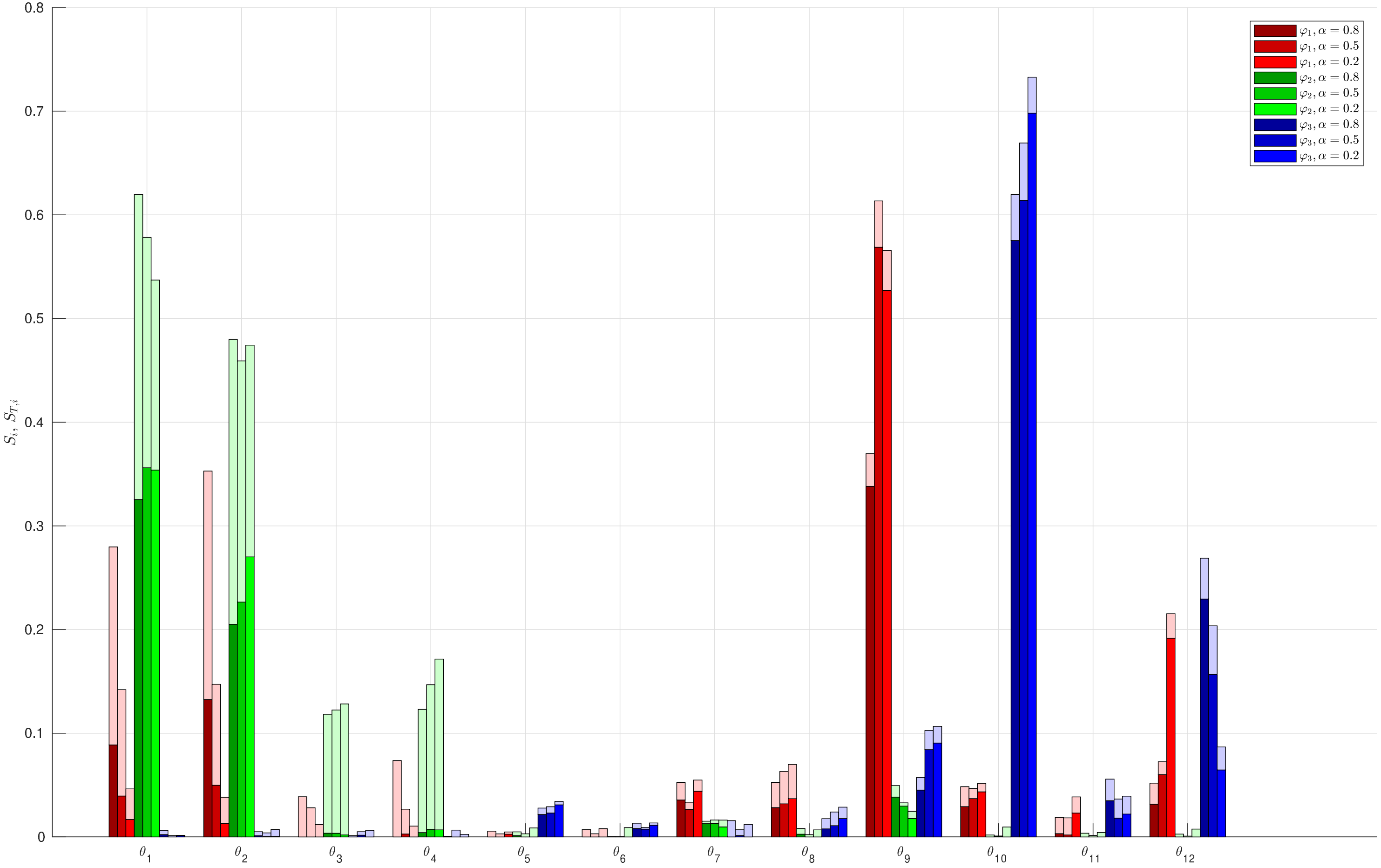

Figure 5.9: Comparison of the outcomes of the sensitivity analyses for three truncation ratios $\alpha \in \{0.2, 0.5, 0.8\}$.

Chapter 6

Conclusion and suggested further work

6.1 Conclusion

In this thesis we studied the fidelity of cyber-physical empirical methods (CPEM), with a focus on the control system that interconnects the substructures. An imperfect control system prevents the dynamic equilibrium between the substructures to be fulfilled, hereby influencing the properties of the dynamical system under study, and jeopardizing the validity of the CPEM as an empirical method.

We formulated a generic model for CPEMs. In this model, the interconnections between the substructures were subjected to multiple, random and heterogeneous *artefacts*, modeling the imperfect control system, and described by a parameter θ. The effect of the artefacts *on the quantities of interest* for the experimentalist was quantified by a performance indicator, denoted the *fidelity*. It was assumed that a *probabilistic* description of θ was available, based on previous experience or on a dedicated survey.

Based on this problem formulation, we developed a pragmatic method that enables the designer of a CPEM to identify artefacts that play a significant role for the fidelity (RQ1). We also showed how absolute bounds on θ could be established, which guarantee sufficiently high fidelity (RQ3). Associating this result with the probabilistic description of θ enabled us to conclude whether probabilistic robust fidelity of a given CPEM was achieved (RQ2). An overview of the method was given in Figure 3.4.

In our work, the orthogonality properties of Polynomial Chaos Exapansions was used to efficiently propagate the uncertainty, and perform the sensitivity analysis. Adaptive (Polynomial-Chaos-based) Kriging was used to model the local uncertainty on the fidelity in the regions where it was close to its minimum admissible value.

The developed method was illustrated by a first example in Chapter 3, in which a coupled linear oscillator was substructured into two simple oscillators. The interconnection was subjected to simple artefacts (namely gains and time delays), which allowed to verify the data-based results against analytical ones. In Chapter 5, we used the method to study the active truncation of slender marine structures. In this problem, the substructures had to be described by *non-closed form* models, and the setup was subjected to a larger number of heterogeneous artefacts (gains, biases, noise, signal losses and time delays), parametrized in a twelve-dimensional space. Strong assumptions would have been required to make this problem tractable with classical analytical methods, which would have weakened the obtained conclusions about fidelity.

The computational efficiency of the method for higher-dimensional and high-reliability problems was put in evidence through this second example. Global sensitivity results could be obtained with a few hundred simulations, and probability of failures of the order of $10^{-5} - 10^{-4}$ could be estimated with less than 100 enrichment steps, even if θ was taking values in a twelve-dimensional space.

Through this case study, we also showed the importance of assessing the considered CPEM *through its fidelity*, based on the the Quantities of Interest for the experimentalist, rather than through *local* performance criteria, such as the ability of the control system to transfer the mechanical power between the substructures.

This case study highlighted some useful points, when it comes to active truncation, which have been summarized in the conclusion of Chapter 5. In addition to these results, our method provides a solid basis to discard some artefacts, with a view to performing an analytical study, and an indication of which type of artefacts such a study must include.

6.2 Suggested further work

We will, in the following paragraphs, outline possible directions of research, which may emerge from the present work.

The proposed method enables us to include a complex set of artefacts and substructure models in the fidelity analysis. The quality of results of such an analysis is, however, strongly dependent on the quality of the probabilistic description of the artefacts, and of the validity of the substructures' models. As a consequence, a rigorous survey on the components of the control system is crucial, and guidelines are probably needed in this respect. When it comes to the modeling of the substructures, all simplifications should be made with a critical eye. For the active truncation problem considered here, we neglected the presence of the bottom chain segment and its interaction with the seabed. This is believed to be a good first approximation, and enabled us to illustrate the developed method within the time frame available for this study. It constitutes however a source of uncertainty regarding the present results. It is expected that nonlinear FE analysis programs, including beam elements, a realistic modeling of soil-structure interaction, and, in the future, time-domain VIV models, should be the standard way to model the slender marine structures. There should always be a reflection on the employed drag and added-mass coefficients, as well as structural damping models.

The present method does not provide a way of assessing whether the fidelity (may it be its expected value, or its minimum admissible value) are sufficiently high *for the intended use of the data generated with the CPEM*. Further work is needed to support the decision on the choice of a fidelity indicator, excitation τ, and level of fidelity that is necessary for a given application. Replacing the deterministic excitation τ by a set of scenarios, as classically done in probabilistic robust control (Tempo et al., 2013), is a possibility to consider.

In the developed method, the control system was represented by a set of artefacts. Further work should address how *unicity* of the decomposition of an artefact into elementary artefacts can be achieved, and how artefacts parameters can reliably be estimated from measured signals when operating a CPEM.

We have, in our examples, focused mostly on the *analysis* of CPEMs, even if the obtained sensitivity results constitute a major help to the designer for improving the fidelity. It should however be explored, through a case study, how the surrogate models developed in the present work could be used in a control system *design* context. The optimal control system can be found as the one minimizing some cost function $c(\theta)$, while maximizing the fidelity, and ensuring high-enough fidelity, as formulated in (3.12). Once the optimal artefact's parameters are determined, the next step would be to establish a method to synthesize a control system satisfying these requirements.

It is expected that the combination of surrogate modelling and active learning techniques, applied here to the analysis of CPEM, can contribute to solve, in an efficient and pragmatic manner, a much wider class of probabilistic robust control problems. The versatility of the method makes it especially suitable to address the design and analysis of complex cyber-physical systems.

Bibliography

Abbiati, G., Marelli, S., Bursi, O. S., Sudret, B., and Stojadinovic, B. (2015). Uncertainty Propagation and Global Sensitivity Analysis in Hybrid Simulation using Polynomial Chaos Expansion. In *Proceedings of the Fourth International Conference on Soft Computing Technology in Civil, Structural and Environmental Engineering.*

Ahmadizadeh, M. and Mosqueda, G. (2009). Online energy-based error indicator for the assessment of numerical and experimental errors in a hybrid simulation. *Engineering Structures*, 31(9):1987–1996.

Akaike, H. (1974). A new look at the statistical model identification. *IEEE transactions on automatic control*, 19(6):716–723.

Aksnes, V., Berthelsen, P. A., and Da Fonseca, N. M. M. D. (2015). On the need for calibration of numerical models of large floating units against experimental data. In *The Twenty-Fifth International Ocean and Polar Engineering Conference.* International Society of Offshore and Polar Engineers.

Alamo, T., Tempo, R., Luque, A., and Ramirez, D. R. (2015). Randomized methods for design of uncertain systems: Sample complexity and sequential algorithms. *Automatica*, 52:160–172.

Allen, C. K. and Goupee, A. J. (2017). Assessment of Wind/wave basin capability for emulating active blade pitch and generator control influence on floating wind turbine response. In *Proceedings of the 27th International Offshore and Polar Engineering Conference (ISOPE 2017)*, San Fransisco.

Argyros, A. (2011). *Efficient Dynamic Modelling of Deepwater Moorings.* PhD Thesis, University of Cambridge.

ASME (ed.) (2016). Guide for Verification and Validation in Computational Solid Mechanics. Technical Report ASME V&V 10-2006 (R2016).

Azcona, J., Bouchotrouch, F., González, M., Garciandía, J., Munduate, X., Kelberlau, F., and Nygaard, T. A. (2014). Aerodynamic Thrust Modelling in Wave Tank Tests of Offshore Floating Wind Turbines Using a Ducted Fan. *Journal of Physics: Conference Series*, 524:012089.

Baarholm, R., Fylling, I., Stansberg, C. T., and Oritsland, O. (2006). Model testing of ultra-deepwater floater systems: Truncation and software verification methodology. In *ASME 2006 25th International Conference on Ocean, Offshore and Arctic Engineering*.

Bachynski, E. E., Chabaud, V., and Sauder, T. (2015). Real-time Hybrid Model Testing of Floating Wind Turbines: Sensitivity to Limited Actuation. *Energy Procedia*, 80:2–12.

Bachynski, E. E., Thys, M., Chabaud, V., Sauder, T., and Sæther, L. O. (2016). Real-time Hybrid Model Testing of a Braceless Semi-submersible Wind turbine. Part II: Experimental Results. In *ASME 2016 35th International Conference on Ocean, Offshore and Arctic Engineering, No OMAE2016-54437*.

Bayati, I., Belloli, M., Bernini, L., and Zasso, A. (2017). Aerodynamic design methodology for wind tunnel tests of wind turbine rotors. *Journal of Wind Engineering and Industrial Aerodynamics*, 167:217–227.

Bayati, I., Belloli, M., Ferrari, D., Fossati, F., and Giberti, H. (2014). Design of a 6-DoF Robotic Platform for Wind Tunnel Tests of Floating Wind Turbines. *Energy Procedia*, 53:313–323.

Blatman, G. and Sudret, B. (2010). An adaptive algorithm to build up sparse polynomial chaos expansions for stochastic finite element analysis. *Probabilistic Engineering Mechanics*, 25(2):183–197.

Blatman, G. and Sudret, B. (2011). Adaptive sparse polynomial chaos expansion based on least angle regression. *Journal of Computational Physics*, 230(6):2345–2367.

Botelho, R. M. and Christenson, R. E. (2014). Mathematical Framework for Real-Time Hybrid Substructuring of Marine Structural Systems. In *Dynamics of Civil Structures, Volume 4*, pages 175–185. Springer.

Bousias, S. N. (2014). Seismic Hybrid Simulation of Stiff Structures: Overview and Current Advances. *Journal of Structures*, 2014:1–8.

Bowers, S. (2016). Shell begins production at world's deepest underwater oilfield. *The Guardian, September 11th, 2016*.

Box, G. E. and Wilson, K. B. (1951). On the experimental attainment of optimum conditions. *Journal of the Royal Statistical Society*, 13(1):1–45.

Bridon (2013). Oil and gas wire and fibre rope catalog.

Buchner, B., Wichers, J. E. W., De Wilde, J. J., and others (1999). Features of the State-of-the-art Deepwater Offshore Basin. In *Offshore Technology Conference*. Offshore Technology Conference.

Bursi, O. S., Wang, Z., Jia, C., and Wu, B. (2013). Monolithic and partitioned time integration methods for real-time heterogeneous simulations. *Computational Mechanics*, 52(1):99–119.

Calafiore, G. C., Dabbene, F., and Tempo, R. (2011). Research on probabilistic methods for control system design. *Automatica*, 47(7):1279–1293.

Cameron, R. H. and Martin, W. T. (1947). The Orthogonal Development of Non-Linear Functionals in Series of Fourier-Hermite Functionals. *The Annals of Mathematics*, 48(2):385.

Cao, Y. and Tahchiev, G. (2013). A Study on an Active Hybrid Decomposed Mooring System for Model Testing in Ocean Basin for Offshore Platforms. In *ASME 2013 32nd International Conference on Ocean, Offshore and Arctic Engineering*. American Society of Mechanical Engineers.

Carrion, J. E. (2007). *Model-Based Strategies for Real-Time Hybrid Testing*. ProQuest.

Chabaud, V. (2016). *Real-Time Hybrid Model Testing of Floating Wind Turbines*. PhD Thesis, Norwegian University of Science and Technology.

Chabaud, V., Eliassen, L., Thys, M., and Sauder, T. (2018). Multiple-degree-of-freedom actuation of rotor loads in model testing of floating wind turbines using cable-driven parallel robots. *Journal of Physics: Conference Series*.

Chakrabarti, S. K., editor (2005). *Handbook of Offshore Engineering*. Elsevier. OCLC: 835766876.

Chen, X., Aravena, J. L., and Zhou, K. (2005). Risk analysis in robust control-making the case for probabilistic robust control. In *Proceedings of the American Control Conference*, pages 1533–1538.

Chernoff, H. (1952). A measure of asymptotic efficiency for tests of a hypothesis based on the sum of observations. *Annals of Mathematical Statistics*, 23(4):493–507.

Christiansen, N. H. (2014). *Hybrid Method Simulation of Slender Marine Structures*. PhD thesis, DTU Mechanical Engineering : DCAMM, Lyngby.

Cook, R. D. (2002). *Concepts and Applications of Finite Element Analysis*. Wiley, New York, 4th ed. edition.

Cressie, N. (1990). The origins of kriging. *Mathematical geology*, 22(3):239–252.

De Klerk, D., Rixen, D. J., and Voormeeren, S. N. (2008). General Framework for Dynamic Substructuring: History, Review and Classification of Techniques. *AIAA Journal*, 46(5):1169–1181.

de Ridder, E.-J., Otto, W., Zondervan, G.-J., Huijs, F., and Vaz, G. (2014). Development of a Scaled-Down Floating Wind Turbine for Offshore Basin Testing. In *ASME 2014 33rd International Conference on Ocean, Offshore and Arctic Engineering*. American Society of Mechanical Engineers.

DNV GL (2014). Recommended Practice - Environmental Conditions and Environmental Loads.

DNV GL (2015). Offshore Standard - Position mooring (DNVGL-OS-E301).

DNV GL (2017). Recommended Practice - Design, testing and analysis of offshore fibre ropes. Technical Report DNVGL-RP-E305.

Drazin, P. L., Govindjee, S., and Mosalam, K. M. (2015). Hybrid Simulation Theory for Continuous Beams. *Journal of Engineering Mechanics*, 141(7):04015005.

Dubourg, V. (2011). *Adaptive Surrogate Models for Reliability Analysis and Reliability-Based Design Optimization.* PhD thesis, Université Blaise Pascal-Clermont-Ferrand II.

Eaton, M. L. (2007). Multivariate Statistics: A Vector Space Approach. *Lecture Notes, Monograph Series, Institute of Mathematical Statistics*, 53.

Echard, B., Gayton, N., and Lemaire, M. (2011). AK-MCS: An active learning reliability method combining Kriging and Monte Carlo Simulation. *Structural Safety*, 33(2):145–154.

Echard, B., Gayton, N., Lemaire, M., and Relun, N. (2013). A combined Importance Sampling and Kriging reliability method for small failure probabilities with time-demanding numerical models. *Reliability Engineering & System Safety*, 111:232–240.

Edrington, C. S., Steurer, M., Langston, J., El-Mezyani, T., and Schoder, K. (2015). Role of Power Hardware in the Loop in Modeling and Simulation for Experimentation in Power and Energy Systems. *Proceedings of the IEEE*, 103(12):2401–2409.

Embrechts, P., Lindskog, F., and Mcneil, A. (2003). Modelling Dependence with Copulas and Applications to Risk Management. In *Handbook of Heavy Tailed Distributions in Finance*, pages 329–384. Elsevier.

Fahy, F. and Gardonio, P. (2007). *Sound and Structural Vibration.* Academic Press, 2 edition.

Faltinsen, O. M. and Timokha, A. N. (2009). *Sloshing.* Cambridge University Press.

Fawzi, H., Tabuada, P., and Diggavi, S. (2014). Secure Estimation and Control for Cyber-Physical Systems Under Adversarial Attacks. *IEEE Transactions on Automatic Control*, 59(6):1454–1467.

Felix-Gonzalez, I. and Mercier, R. S. (2016). Optimized design of statically equivalent mooring systems. *Ocean Engineering*, 111:384–397.

Fergestad, D. and Løtveit, S. A. (2015). *Handbook on Design and Operations of Flexible Pipes.* Joint industry project "safe and cost effective operations of flexible pipes" edition.

Ferreira, F. M., Lages, E. N., Afonso, S. M., and Lyra, P. R. (2016). Dynamic design optimization of an equivalent truncated mooring system. *Ocean Engineering*, 122:186–201.

Filipi, Z., Fathy, H., Hagena, J., Knafl, A., Ahlawat, R., Liu, J., Jung, D., Assanis, D. N., Peng, H., and Stein, J. (2006). Engine-in-the-loop testing for evaluating hybrid propulsion concepts and transient emissions-HMMWV case study. Technical report, SAE Technical Paper.

Friedman, J. H. (1991). Multivariate Adaptive Regression Splines. *The Annals of Statistics*, 19(1):1–67.

Fylling, I. and Stansberg, C. T. (2005). Model Testing of Deepwater Floating Production Systems: Strategy for Truncation of Moorings and Risers. In *DOT Brazil.*

Gao, X., Castaneda, N., and Dyke, S. J. (2013). Real time hybrid simulation: From dynamic system, motion control to experimental error. *Earthquake Engineering & Structural Dynamics*, 42(6):815–832.

Gawthrop, P., Neild, S., Gonzalez-Buelga, A., and Wagg, D. (2009). Causality in real-time dynamic substructure testing. *Mechatronics*, 19(7):1105–1115.

Gawthrop, P. J., Wallace, M. I., and Wagg, D. J. (2005). Bond-graph based substructuring of dynamical systems. *Earthquake Engineering & Structural Dynamics.*

Goebel, R., Sanfelice, R. G., and Teel, A. R. (2012). *Hybrid Dynamical Systems: Modeling, Stability, and Robustness.* Princeton University Press, Princeton, N.J.

Goldberg, D. E. (1989). *Genetic Algorithms in Search, Optimization, and Machine Learning.* Addison-Wesley.

Goupee, A. J., Koo, B. J., Kimball, R. W., Lambrakos, K. F., and Dagher, H. J. (2014). Experimental comparison of three floating wind turbine concepts. *Journal of Offshore Mechanics and Arctic Engineering*, 136(2):020906.

Gross, D. C. (1999). Report from the Fidelity Implementation Study Group. In *Simulation Interoperability Workshop*, Orlando, Florida.

Hall, M. (2016). *Hybrid Modeling of Floating Wind Turbines.* PhD Thesis, University of Maine.

Hall, M., Goupee, A., and Jonkman, J. (2017). Development of performance specifications for hybrid modeling of floating wind turbines in wave basin tests. *Journal of Ocean Engineering and Marine Energy*.

Hespanha, J. P., Naghshtabrizi, P., and Xu, Y. (2007). A survey of recent results in networked control systems. *Proceedings of IEEE*, 95(1):138.

Hills, R. G., Maniaci, D. C., and Naughton, J. W. (2015). V&V Framework. Sandia Report SAND2015-7455, Sandia National Laboratories.

Homma, T. and Saltelli, A. (1996). Importance measures in global sensitivity analysis of nonlinear models. *Reliability Engineering & System Safety*, 52(1):1–17.

Horiuchi, T., Inoue, M., Konno, T., and Namita, Y. (1999). Real-Time Hybrid Experimental System With Actuator Delay Compensation And Its Application to a Piping System With Energy Absorber. *Earthquake Engineering & Structural Dynamics*, 28:1121–1141.

Hover, F. S., Miller, S. N., and Triantafyllou, M. S. (1997). Vortex-induced vibration of marine cables: Experiments using force feedback. *Journal of fluids and structures*, 11(3):307–326.

Hover, F. S., Techet, A. H., and Triantafyllou, M. S. (1998). Forces on oscillating uniform and tapered cylinders in cross flow. *Journal of Fluid Mechanics*, 363:97–114.

Howell, C. T. (1992). Investigation of the dynamics of low-tension cables. Technical report, DTIC Document.

Humayed, A., Lin, J., Li, F., and Luo, B. (2017). Cyber-Physical Systems Security—A Survey. *IEEE Internet of Things Journal*, 4(6):1802–1831.

Huse, E. (1986). Influence of mooring line damping upon rig motions. In *Offshore Technology Conference*. Offshore Technology Conference.

IEEE CPS (2018). Scope and Mission. http://www.ieee-cps.org/.

ITTC (1999). The Specialist Committee on Deep Water Mooring Final Report and Recommendations to the 22nd ITTC. Technical report.

ITTC (2005). Testing and Extrapolation Methods Loads and Responses, Ocean Engineering, Truncation of Test Models and Integration with Numerical Simulations.

ITTC (2017). Recommended Procedures and Guidelines - Active Hybrid Model Tests of Floating Offshore Structures with Mooring Lines.

Jaulin, L., Kieffer, M., Didrit, O., and Walter, E. (2001). *Applied Interval Analysis: With Examples in Parameter and State Estimation, Robust Control and Robotics*. Springer-Verlag, London.

Jaynes, E. T. (1957). Information Theory and Statistical Mechanics. *The Physical Review*, 106(4):620–630.

Johansen, V. (2007). *Modelling of Flexible Slender Systems for Real-Time Simulation and Control Applications*. PhD thesis, Norwegian University of Science and Technology.

Journée, J. and Massie, W. (2001). *Offshore Hydromechanics*. Delft University of Technology.

Jung, R.-Y. and Benson Shing, P. (2006). Performance evaluation of a real-time pseudodynamic test system. *Earthquake Engineering & Structural Dynamics*, 35(7):789–810.

Kapur, J. N. (1989). *Maximum-Entropy Models in Science and Engineering*. John Wiley & Sons.

Kendon, T. E., Oritsland, O., Baarholm, R. J., Karlsen, S. I., Stansberg, C.-T., Rossi, R. R., Barreira, R. A., Matos, V. L., and Sales, J. S. (2008). Ultra-deepwater model testing of a semisubmersible and hybrid verification. In *ASME 2008 27th International Conference on Offshore Mechanics and Arctic Engineering*, pages 277–290. American Society of Mechanical Engineers.

Khalil, H. K. (2014). *Nonlinear Control*. Pearson.

Kim, M., Koo, B., Mercier, R., and Ward, E. (2005). Vessel/mooring/riser coupled dynamic analysis of a turret-moored FPSO compared with OTRC experiment. *Ocean Engineering*, 32(14-15):1780–1802.

Kyrychko, Y., Blyuss, K., Gonzalez-Buelga, A., Hogan, S., and Wagg, D. (2006). Real-time dynamic substructuring in a coupled oscillator–pendulum system. *Proceedings of the Royal Society A: Mathematical, Physical and Engineering Sciences*, 462(2068):1271–1294.

Kyrychko, Y. N. and Hogan, S. J. (2010). On the Use of Delay Equations in Engineering Applications. *Journal of Vibration and Control*, 16(7-8):943–960.

Le Gratiet, L., Marelli, S., and Sudret, B. (2015). Metamodel-Based Sensitivity Analysis: Polynomial Chaos Expansions and Gaussian Processes. In Ghanem, R., Higdon, D., and Owhadi, H., editors, *Handbook of Uncertainty Quantification*, pages 1–37. Springer International Publishing, Cham.

Lemaire, M. (2009). *Structural Reliability*. ISTE ; Wiley, London : Hoboken, NJ.

Loysel, T., Chollet, S., Gervaise, E., Brosset, L., De Seze, P.-E., and others (2012). Results of the first sloshing model test benchmark. In *The Twenty-Second International Offshore and Polar Engineering Conference*. International Society of Offshore and Polar Engineers.

MacDiarmid, M. and Bacic, M. (2007). Quantifying the accuracy of hardware-in-the-loop simulations. In *American Control Conference, 2007. ACC'07*, pages 5147–5152. IEEE.

MacDiarmid, M., Bacic, M., and Daniel, R. (2008). Extension and application of a novel hardware-in-the-loop simulator design methodology. In *Decision and Control, 2008. CDC 2008. 47th IEEE Conference On*, pages 5054–5061. IEEE.

Magee, A. R. (2018). The Role of Model Testing in the Execution of Deepwater Projects. In *Proceedings of the Offshore Technology Conference*, Kuala Lumpur, Malaysia.

Maghareh, A., Dyke, S. J., Prakash, A., and Bunting, G. B. (2014). Establishing a predictive performance indicator for real-time hybrid simulation. *Earthquake Engineering & Structural Dynamics*, 43(15):2299–2318.

Mainçon, P. (2011). A Wiener-Laguerre Model of VIV Forces Given Recent Cylinder Velocities. *Mathematical Problems in Engineering*, 2011:1–43.

Manwell, J. F., McGowan, J. G., and Rogers, A. L. (2009). *Wind Energy Explained: Theory, Design and Application.* Wiley, Chichester, U.K, 2nd ed edition. OCLC: ocn431936159.

Marelli, S., Lamas, C., Sudret, B., and Konakli, K. (2017a). UQLab User Manual – Sensitivity Analysis. Technical Report UQLab-V1.0-106, Chair of Risk, Safety & Uncertainty Quantification, ETH Zürich.

Marelli, S., Schobi, R., and Sudret, B. (2017b). UQLab user manual – Structural Reliability. Technical Report UQLab-V1.0-107, Chair of Risk, Safety & Uncertainty Quantification, ETH Zürich.

Marelli, S. and Sudret, B. (2014). UQLAB : A framework for Uncertainty Quantification in MATLAB. SIAM Conference on Uncertainty Quantification (ICVRAM), USA, 2014.

Marelli, S. and Sudret, B. (2017). UQLab Manual – Polynomial chaos expansions. Technical Report UQLab-V1.0-104, Chair of Risk, Safety & Uncertainty Quantification, ETH Zürich.

Martin, H. R., Kimball, R. W., Viselli, A. M., and Goupee, A. J. (2014). Methodology for wind/wave basin testing of floating offshore wind turbines. *Journal of Offshore Mechanics and Arctic Engineering*, 136(2):020905.

Martin, S., Day, S., and Gilmour, C. B. (2015). Rotor scaling methodologies for small scale testing of floating wind turbines. In *Proceedings of the ASME 2015 34th International Conference on Ocean, Offshore and Arctic Engineering.*

McCrum, D. and Williams, M. (2016). An overview of seismic hybrid testing of engineering structures. *Engineering Structures*, 118:240–261.

McCulloch, W. S. and Pitts, W. (1943). A logical calculus of the ideas immanent in nervous activity. *The bulletin of mathematical biophysics*, 5(4):115–133.

Melchers, R. E. (1990). Radial importance sampling for structural reliability. *Journal of engineering mechanics*, 116(1):189–203.

Misselhorn, W. E., Theron, N. J., and Els, P. S. (2006). Investigation of hardware-in-the-loop for use in suspension development. *Vehicle System Dynamics*, 44(1):65–81.

Molin, B. (2002). *Hydrodynamique des structures offshore*. Editions Technip, Paris.

Molins, C., Trubat, P., Gironella, X., and Campos, A. (2015). Design Optimization for a Truncated Catenary Mooring System for Scale Model Test. *Journal of Marine Science and Engineering*, 3(4):1362–1381.

Montgomery, D. C. (2013). *Design and Analysis of Experiments (8th Edition)*. John Wiley & Sons.

Mosqueda, G., Bozidar Stojadinovic, and Stephen A. Mahin (2007a). Real-Time Error Monitoring for Hybrid Simulation. Part I: Methodology and Experimental Verification. *Journal of Structural Engineering*, 133(8).

Mosqueda, G., Bozidar Stojadinovic, and Stephen A. Mahin (2007b). Real-Time Error Monitoring for Hybrid Simulation. Part II: Structural Response Modification due to Errors. *Journal of Structural Engineering*, 133(8).

Mosqueda, G., Stojadinovic, B., and Mahin, S. (2005). Implementation and Accuracy of Continuous Hybrid Simulation with Geographically Distributed Substructures. Technical report, Earthquake Engineering Research Center University of California, Berkeley.

Muthanna, C. (2014). Model testing of offshore structures, Lecture in Experimental Methods in Marine Hydrodynamics, NTNU.

Naeckel, O., Langston, J., Steurer, M., Fleming, F., Paran, S., Edrington, C., and Noe, M. (2015). Power Hardware-in-the-Loop Testing of an Air Coil Superconducting Fault Current Limiter Demonstrator. *IEEE Transactions on Applied Superconductivity*, 25(3):1–7.

Nakashima, M., Kato, M., and Takaoka, E. (1992). Development of real-time pseudo dynamic testing. *Earthquake Engineering and Structural Dynamics, Wiley*, 21(1):79–92.

Nakata, N., Dyke, S. J., Zhang, J., Mosqueda, G., Shao, X., Mahmoud, H., Hite Head, M., Bletzinger, M., Marshall, G. A., Ou, G., and Song, C. (2014a). Hybrid Simulation Primer and Dictionary.

Nakata, N., Laplace, P., Song, W., Chae, Y., Marshall, G. A., Ou, G., Gonzales, C. A. R., and Song, C. (2014b). Hybrid Simulation: A Discussion of Current Assessment Measures.

Newman, J. N. (1977). *Marine Hydrodynamics*. MIT Press.

Oguz, E., Clelland, D., Day, A. H., Incecik, A., López, J. A., Sánchez, G., and Almeria, G. G. (2018). Experimental and numerical analysis of a TLP floating offshore wind turbine. *Ocean Engineering*, 147:591–605.

Øksendal, B. (2003). *Stochastic Differential Equations*. Universitext. Springer Berlin Heidelberg, Berlin, Heidelberg.

Owen, N. E., Challenor, P., Menon, P. P., and Bennani, S. (2015). Comparison of surrogate-based uncertainty quantification methods for computationally expensive simulators. *arXiv preprint arXiv:1511.00926*.

Papazoglou, V. J. and Mavrakos, S. A. (1990). Non-linear Cable Response and Model Testing in Water. *Journal of Sound and Vibration*, 140(1):103–105.

Pasqualetti, F., Dorfler, F., and Bullo, F. (2013). Attack Detection and Identification in Cyber-Physical Systems. *IEEE Transactions on Automatic Control*, 58(11):2715–2729.

Plummer, A. R. (2006). Model-in-the-Loop Testing. *Proceedings of the Institution of Mechanical Engineers, Part I: Journal of Systems and Control Engineering*, 220(3):183–199.

Pott, A. and Bruckmann, T., editors (2015). *Cable-Driven Parallel Robots*, volume 32 of *Mechanisms and Machine Science*. Springer International Publishing, Cham.

Qiu, W., Sales Junior, J., Lee, D., Lie, H., Magarovskii, V., Mikami, T., Rousset, J.-M., Sphaier, S., Tao, L., and Wang, X. (2014). Uncertainties related to predictions of loads and responses for ocean and offshore structures. *Ocean Engineering*, 86:58–67.

Ren, W. (2007). *Accuracy Evaluation of Power Hardware-in- the-Loop (PHIL) Simulation*. PhD Thesis, Florida State University.

Ren, W., Steurer, M., and Baldwin, T. (2009). An Effective Method for Evaluating the Accuracy of Power Hardware-in-the-Loop Simulations. *IEEE Transactions on Industry Applications*, 45(4):1484–1490.

Rognebakke, O. F. and Faltinsen, O. M. (2003). Coupling of sloshing and ship motions. *Journal of Ship Research*, 47(3):208–221.

Rustad, A. M. (2007). *Modeling and Control of Top Tensioned Risers*. PhD Thesis, Norwegian University of Science and Technology, Trondheim.

Rustad, A. M., Larsen, C. M., and Sørensen, A. J. (2008). FEM modelling and automatic control for collision prevention of top tensioned risers. *Marine Structures*, 21(1):80–112.

Sadjina, S., Kyllingstad, L. T., Rindarøy, M., Skjong, S., Æsøy, V., Fathi, D. E., Hassani, V., Johnsen, T., Nielsen, J. B., and Pedersen, E. (2017). Distributed Co-Simulation of Maritime Systems and Operations. *arXiv preprint arXiv:1701.00997*.

Saltelli, A., editor (2008). *Global Sensitivity Analysis: The Primer*. John Wiley, Chichester, England ; Hoboken, NJ. OCLC: ocn180852094.

Santner, T. J., Williams, B. J., and Notz, W. I. (2003). *The Design and Analysis of Computer Experiments*. Springer New York, New York, NY. OCLC: 851741845.

Saporta, G. (2006). *Probabilités, analyse des données et statistique*. Editions TECHNIP.

Sauder, T., Chabaud, V., Thys, M., Bachynski, E. E., and Sæther, L. O. (2016). Real-time Hybrid Model Testing of a Braceless Semi-submersible Wind turbine. Part I: The Hybrid Approach. In *ASME 2016 35th International Conference on Ocean, Offshore and Arctic Engineering, No OMAE2016-54435*.

Sauder, T., Marelli, S., Larsen, K., and Sørensen, A. J. (2018). Active truncation of slender marine structures: Influence of the control system on fidelity. *Applied Ocean Research*, 74:154–169.

Sauder, T., Marelli, S., and Sørensen, A. J. (2019). Probabilistic Robust Design of Control Systems for High-Fidelity Cyber-Physical Testing. *Automatica (accepted for publication)*.

Sauder, T., Sørensen, A. J., and Larsen, K. (2017). Real-Time Hybrid Model Testing of a Top Tensioned Riser: A Numerical Case Study On Interface Time-Delay and Truncation Ratio. In *ASME 2017 36th International Conference on Ocean, Offshore and Arctic Engineering*, Trondheim, Norway.

Savin, e. and Faverjon, B. (2017). Computation of higher-order moments of generalized polynomial chaos expansions. *International Journal for Numerical Methods in Engineering*, 111(12):1192–1200.

Schöbi, R., Marelli, S., and Sudret, B. (2017). UQLab user manual – PC-Kriging. Technical Report UQLab-V1.0-109, Chair of Risk, Safety & Uncertainty Quantification, ETH Zürich.

Schöbi, R., Sudret, B., and Marelli, S. (2016). Rare Event Estimation Using Polynomial-Chaos Kriging. *ASCE-ASME Journal of Risk and Uncertainty in Engineering Systems, Part A: Civil Engineering*, page D4016002.

Schöbi, R., Sudret, B., and Wiart, J. (2015). Polynomial-chaos-based Kriging. *International Journal for Uncertainty Quantification*, 5(2).

Schwarz, G. (1978). Estimating the Dimension of a Model. *Annals of Statistics*, 6(2):461–464.

Shafer, G. (1976). *A Mathematical Theory of Evidence.* Princeton University Press.

Shampine, L. F. and Reichelt, M. W. (1997). The MATLAB ODE Suite. *SIAM Journal on Scientific Computing*, 18(1):1–22.

Shao, X. and Griffith, C. (2013). An overview of hybrid simulation implementations in NEES projects. *Engineering Structures*, 56:1439–1451.

Sharma, R., editor (2017). *Deep-Sea Mining.* Springer International Publishing, Cham.

SINTEF Ocean (2015). SIMA 3.2 User Guide. Technical report.

Skjetne, R. and Egeland, O. (2006). Hardware-in-the-loop testing of marine control system. *Modeling, Identification and Control: A Norwegian Research Bulletin*, 27(4):239–258.

Skjong, S. (2017). *Modeling and Simulation of Maritime Systems and Operations for Virtual Prototyping Using Co-Simulations.* PhD Thesis, Norwegian University of Science and Technology, Trondheim, Norway.

Smogeli, O. N., Hover, F. S., and Triantafyllou, M. S. (2003). Force-feedback control in VIV experiments. In *ASME 2003 22nd International Conference on Offshore Mechanics and Arctic Engineering*, pages 685–695. American Society of Mechanical Engineers.

Sobol, I. M. (1993). Sensitivity estimates for nonlinear mathematical models. *Mathematical Modelling and Computational Experiments*, 1(4):407–414.

Sobol', I. M. (2001). Global sensitivity indices for nonlinear mathematical models and their Monte Carlo estimates. *Mathematics and computers in simulation*, 55(1):271–280.

Sørensen, A. J. (2011). A survey of dynamic positioning control systems. *Annual Reviews in Control*, 35(1):123–136.

Stansberg, C. T., Ormberg, H., and Oritsland, O. (2002). Challenges in Deep Water Experiments: Hybrid Approach. *Journal of Offshore Mechanics and Arctic Engineering*, 124(2):90.

Steen, S. (2014). *Experimental Methods in Marine Hydrodynamics.* Department of Marine Technology, NTNU.

Stein, M. (1987). Large Sample Properties of Simulations Using Latin Hypercube Sampling. *Technometrics*, 29(2):143.

Stoten, D. P. (2017). A comparative study and unification of two methods for controlling dynamically substructured systems: A Unified Approach for Control of Dynamically Substructured Systems. *Earthquake Engineering & Structural Dynamics*, 46(2):317–339.

Sudret, B. (2007). *Uncertainty Propagation and Sensitivity Analysis in Mechanical Models. Contributions to Structural Reliability and Stochastic Spectral Methods.* Rapport d'activité scientifique en vue de l'obtention de l'Habilitation à Diriger des Recherches, Université Blaise Pascal - Clermont II.

Sudret, B. (2008). Global sensitivity analysis using polynomial chaos expansions. *Reliability Engineering & System Safety*, 93(7):964–979.

Sudret, B. and Marelli, S. (2017). Lecture Notes in Uncertainty Quantification and Rare Event Estimation in Engineering. Technical report, ETH, Zurich.

Tabuada, P., Caliskan, S. Y., Rungger, M., and Majumdar, R. (2014). Towards Robustness for Cyber-Physical Systems. *IEEE Transactions on Automatic Control*, 59(12):3151–3163.

Takanashi, K., Udagawa, K., Seki, M., Okada, T., and Tanaka, H. (1975). Nonlinear Earthquake Response Analysis of Structures by A Computer-Actuator On-line System. *Bulletin of Earthquake Resistant Structure Research Center, Japan Institute of Industrial Science, University of Tokyo*, 8.

Takaya, Y., Yasukawa, K., Kawasaki, T., Fujinaga, K., Ohta, J., Usui, Y., Nakamura, K., Kimura, J.-I., Chang, Q., Hamada, M., Dodbiba, G., Nozaki, T., Iijima, K., Morisawa, T., Kuwahara, T., Ishida, Y., Ichimura, T., Kitazume, M., Fujita, T., and Kato, Y. (2018). The tremendous potential of deep-sea mud as a source of rare-earth elements. *Nature, Scientific Reports*, 8(1).

Tempo, R., Calafiore, G., and Dabbene, F. (2013). *Randomized Algorithms for Analysis and Control of Uncertain Systems: With Applications.* Communications and control engineering. Springer, London, second edition edition.

The Maritime Executive (2018). World's First Deepsea Mining Support Vessel Launched. https://www.maritime-executive.com/article/world-s-first-deepsea-mining-support-vessel-launched.

Thorsen, M. J. (2016). *Time Domain Analysis of Vortex-Induced Vibrations.* PhD Thesis, Norwegian University of Science and Technology, Trondheim, Norway.

Thys, M., Chabaud, V., Sauder, T., Eliassen, L., Sæther, L. O., and Magnussen, O. B. (2018). Real-time hybrid model testing of a semi-submersible 10 MW floating wind turbine, and advances in the test method. In *ASME 2018 1st International Offshore Wind Technical Conference*, San Fransisco.

Triantafyllou, M. S. and Howell, C. T. (1994). Dynamic Response of Cables Under Negative Tension: An Ill-Posed Problem. *Journal of Sound and Vibration*, 173(4):433–447.

Vandiver, J. K. and Li, L. (2005). SHEAR7 V4. 4 PROGRAM THEORETICAL MANUAL March 25, 2005.

Vapnik, V. N. (1995). *The Nature of Statistical Learning Theory*. Springer-Verlag New York, Inc., New York, NY, USA.

Vilsen, S., Sauder, T., Føre, M., and Sørensen, A. J. (2018). Controller analysis in real-time hybrid model testing of an offshore floating system. In *ASME 2018 37th International Conference on Offshore Mechanics and Arctic Engineering*, Madrid, Spain.

Vilsen, S., Sauder, T., and Sørensen, A. J. (2017). Real-time hybrid model testing of moored floating structures using nonlinear finite element simulations. In *Dynamics of Coupled Structures*, volume 4 of *Conference Proceedings of the Society for Experimental Mechanics Series*, pages 79–92. Springer International Publishing.

Vilsen, S., Sauder, T., Sørensen, A. J., and Føre, M. (2019). Method for Real-Time Hybrid Model Testing of Ocean Structures: Case Study on Horizontal Mooring Systems. *Ocean Engineering (accepted for publication)*.

Voormeeren, S. N. (2007). *Coupling Procedure Improvement & Uncertainty Quantification in Experimental Dynamic Substructuring*. Master's thesis, TU Delft, Delft University of Technology.

Wagg, D., Neild, S., and Gawthrop, P. (2008). Real-Time Testing With Dynamic Substructuring. In Bursi, O. S. and Wagg, D., editors, *Modern Testing Techniques for Structural Systems*, number 502 in CISM International Centre for Mechanical Sciences, pages 293–342. Springer Vienna.

Wallace, M. I., Wagg, D. J., Neild, S. A., Bunniss, P., Lieven, N. A. J., and Crewe, A. J. (2007). Testing coupled rotor blade–lag damper vibration using real-time dynamic substructuring. *Journal of Sound and Vibration*, 307(3):737–754.

Watts, S. (1999). Hybrid Hydrodynamic Modelling. *J. Offshore Tech.*, pages 13–17.

Webster, W. C. (1995). Mooring-induced damping. *Ocean Engineering*, 22(6):571–591.

Wei, H., Xiao, L., Tian, X., and Kou, Y. (2017). Four-level screening method for multi-variable truncation design of deepwater mooring system. *Marine Structures*, 51:40–64.

Wendt, F. F., Robertson, A. N., and Jonkman, J. M. (2017). FAST Model Calibration and Validation of the OC5-DeepCwind Floating Offshore Wind System Against Wave Tank Test Data. In *The 27th International Ocean and Polar Engineering Conference*. International Society of Offshore and Polar Engineers.

Whyte, C. A., Mackie, K. R., and Stojadinovic, B. (2015). Hybrid Simulation of Thermomechanical Structural Response. *Journal of Structural Engineering*, 142(2):04015107.

Xiu, D. and Karniadakis, G. E. (2002). The Wiener–Askey polynomial chaos for stochastic differential equations. *SIAM journal on scientific computing*, 24(2):619–644.

Ye, M., Duan, M., Li, M., Chen, J., Tian, K., Han, F., and Hu, Z. (2014). An active truncation method for simulating deep-water riser installation. *Ships and Offshore Structures*, 9(6):619–632.

Yum, K. K. (2017). Real-Time Hybrid Model (ReaTHM®) Testing of the Hybrid Power Plant: Concept and Feasibility Test. In *ASME 2017 36th International Conference on Ocean, Offshore and Arctic Engineering*, pages V010T09A010–V010T09A010. American Society of Mechanical Engineers.

Zadeh, L. A. (1965). Fuzzy sets. *Information and Control*, 8(3):338–353.

Zaki, M. J. and Meira, W. (2014). *Data Mining and Analysis: Fundamental Concepts and Algorithms*. Cambridge University Press, New York, NY.

Zhan, J. P. (2010). *Review and Verification of Marine Riser Analysis Programs: Global Response Analysis*. Master thesis, Norwegian University of Science and Technology, Trondheim, Norway.

Zhang, Z., Staino, A., Basu, B., and Nielsen, S. R. (2016). Performance evaluation of full-scale tuned liquid dampers (TLDs) for vibration control of large wind turbines using real-time hybrid testing. *Engineering Structures*, 126:417–431.

Zhou, K., Doyle, J. C., and Glover, K. (1996). *Robust and Optimal Control*. Prentice Hall.

Zhu, W., Pekarek, S., Jatskevich, J., Wasynczuk, O., and Delisle, D. (2005). A Model-in-the-Loop Interface to Emulate Source Dynamics in a Zonal DC Distribution System. *IEEE Transactions on Power Electronics*, 20(2):438–445.

List of Tables

List of Figures

Appendix A

Mathematical background and proofs

A.1 Gaussian random vectors

This section is a short introduction to Gaussian random vectors.

Definition 23. *Let $k \in \mathbb{N}^*$. A random vector $Z = (Z_1, ..., Z_k)^\top$ is said to be multivariate normally distributed if it admits the following joint PDF.*

$$f_Z(z_1, \ldots, z_k) = \frac{1}{\sqrt{(2\pi)^k |\Sigma|}} e^{-\frac{1}{2}(z-\mu)^\top \Sigma^{-1} (z-\mu)} \tag{A.1}$$

where $\mu \in \mathbb{R}^k$ is the mean *of Z, and $\Sigma \in \mathbb{R}^{k \times k}$ is a symmetric definite positive matrix, called the* covariance matrix *of Z, satisfying*

$$\forall i, j \in \mathbb{N}_k^*, \mathrm{E}[(Z_i - \mu_i)(Z_j - \mu_j)] = \Sigma_{ij} \tag{A.2}$$

Example 14. *Let $k = 2$. A bivariate normally distributed random vector with mean $\mu = (\mu_1, \mu_2)^\top$ and covariance $\Sigma = \begin{pmatrix} \sigma_1^2 & \rho\sigma_1\sigma_2 \\ \rho\sigma_1\sigma_2 & \sigma_2^2 \end{pmatrix}$ admits the following distribution:*

$$f_Z(z_1, z_2) = \frac{1}{2\pi\sigma_1\sigma_2\sqrt{1-\rho^2}} e^{-\frac{1}{2(1-\rho^2)}\left(\frac{(z_1-\mu_1)^2}{\sigma_1^2} + \frac{(z_2-\mu_2)^2}{\sigma_2^2} - \frac{2\rho(z_1-\mu_1)(z_2-\mu_2)}{\sigma_1\sigma_2}\right)} \tag{A.3}$$

Figure A.1 shows contour plots of f_Z for various ratios σ_1/σ_2 and various values of the correlation coefficient ρ. If $\rho = 0$, then z_1 and z_2 are uncorrelated and independent. The principal axes of the ellipses presented in Figure A.1 are the eigenvectors of the covariance matrix.

Arbitrary random vectors whose covariance matrix is zero in every entry outside the main diagonal are called *uncorrelated.* Note that for Gaussian random vectors, this implies that the joint PDF f_Z can be factorized as $\prod_{i\in\mathbb{N}_k^*} f_{Z_i}(z_i)$, which in turns implies that the components of Z also are independent.

A.2 Equivalence between the regression and projection approaches

See Section 2.2.3.

Proposition 1. *The regression approach and projection approaches, used to identify PCE coefficients, are equivalent.*

Proof. The square of $\epsilon(X)$, used in the regression approach, can be written as

$$\epsilon^2(X) = \mathcal{M}^2(X) - 2\sum_{\alpha\in\mathcal{A}} a_\alpha \mathcal{M}(X)\psi_\alpha(X) + \sum_{(\alpha,\beta)\in\mathcal{A}^2} a_\alpha a_\beta \psi_\alpha(X)\psi_\beta(X) \quad (A.4)$$

Then taking the expectation of this expression, and exploiting the fact that the polynomial basis is orthonormal, yields

$$\mathrm{E}[\epsilon^2(X)] = \mathrm{E}[\mathcal{M}^2(X)] - 2\sum_{\alpha\in\mathcal{A}} a_\alpha \mathrm{E}[\mathcal{M}(X)\psi_\alpha(X)] + \sum_{\alpha\in\mathcal{A}} a_\alpha^2 \quad (A.5)$$

A necessary condition for the a_α coefficients to minimize $\mathrm{E}[\epsilon^2(X)]$ is to satisfy the following first-order optimality condition:

$$\forall\alpha \in \mathcal{A}, \frac{\partial \mathrm{E}[\epsilon^2(X)]}{\partial a_\alpha} = 0 \quad (A.6)$$

which leads to

$$\forall\alpha \in \mathcal{A}, -2\mathrm{E}[\mathcal{M}(X)\psi_\alpha(X)] + 2a_\alpha = 0 \quad (A.7)$$

which is equivalent to equation (2.13) □

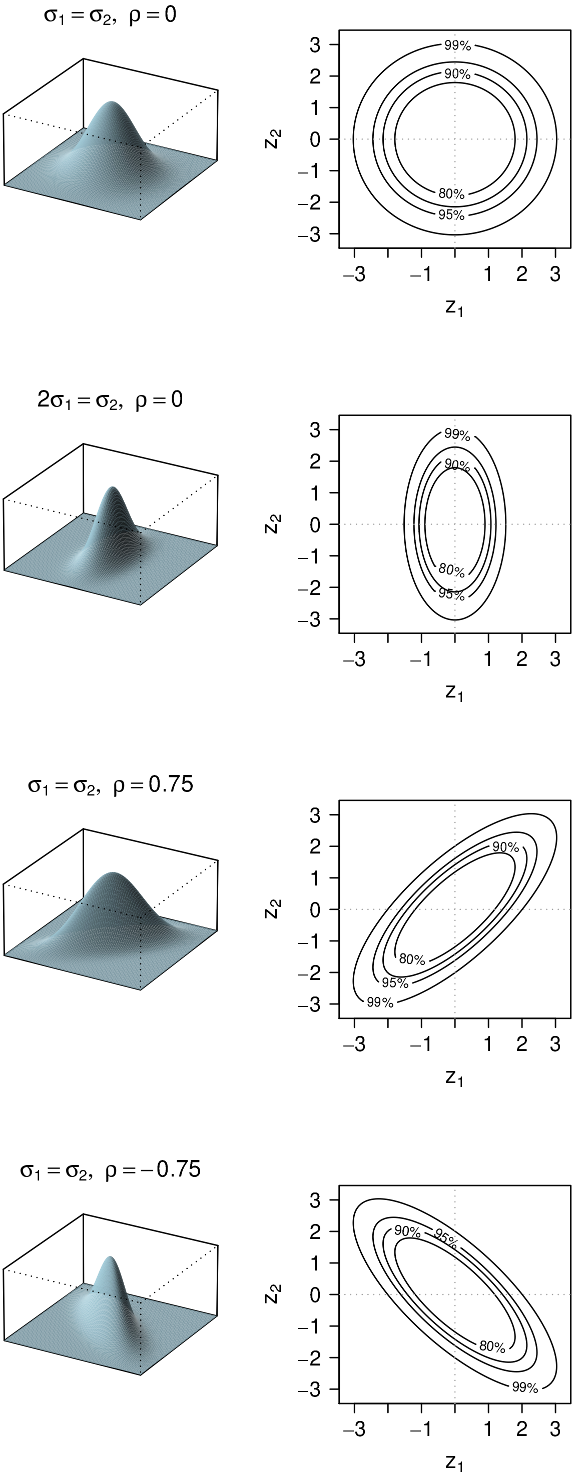

Figure A.1: Joint PDF of a bivariate normally distributed random vector with zero mean, and various variance and correlations values. Three-dimensional plot (left hand side) and contour plots representing the 80th, 90th, 95th and 99th percentiles (r.h.s.).

Appendix B

Additional figures

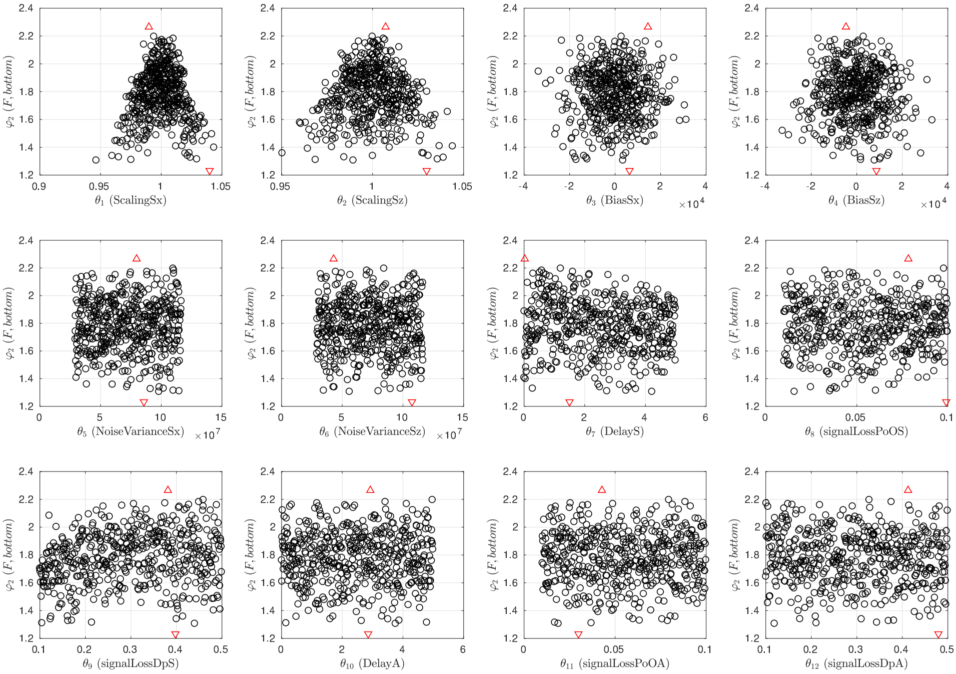

Figure B.1: Scatter diagrams showing the value of φ_2 (fidelity indicator based on line force transferred to the bottom), as a function of the twelve parameters describing the artefacts. The dots correspond to 512 samples of Θ obtained by Latin Hypercube Sampling (set denoted $\mathcal{E}_5$ in the text).

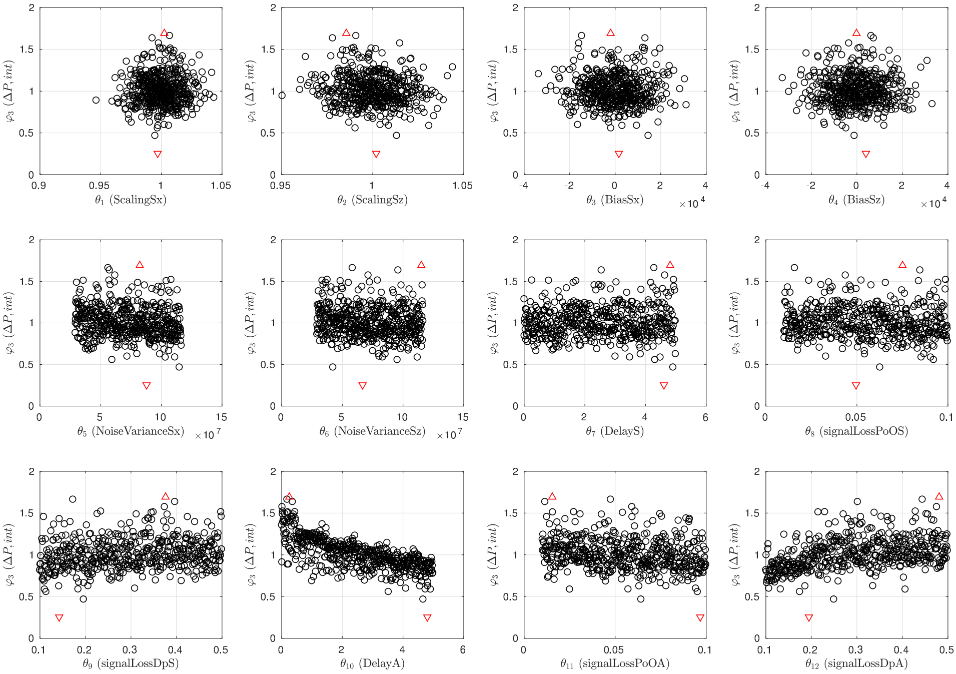

Figure B.2: Scatter diagrams showing the value of φ_3 (pseudo-fidelity indicator based on power transfer mismatch at the truncation point), as a function of the twelve parameters describing the artefacts. The dots correspond to 512 samples of Θ obtained by Latin Hypercube Sampling (set denoted $\mathcal{E}_5$ in the text).

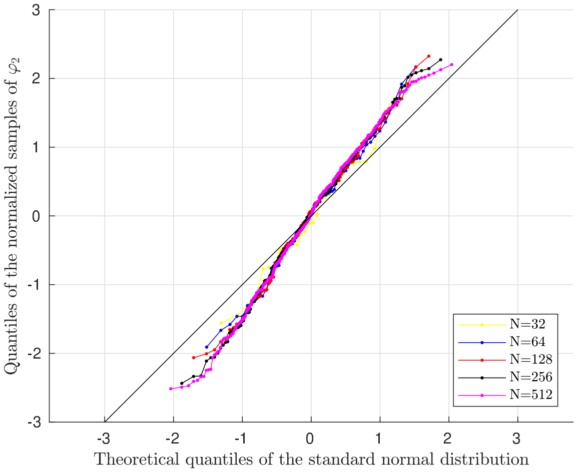

Figure B.3: Quantile-quantile (QQ) plots comparing the distribution of φ_2 to a normal distribution, for various sizes of $\mathcal{E}$.

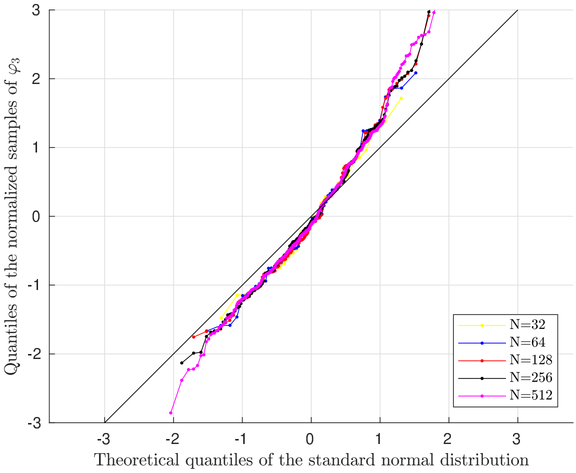

Figure B.4: Quantile-quantile (QQ) plots comparing the distribution of φ_3 to a normal distribution, for various sizes of $\mathcal{E}$.

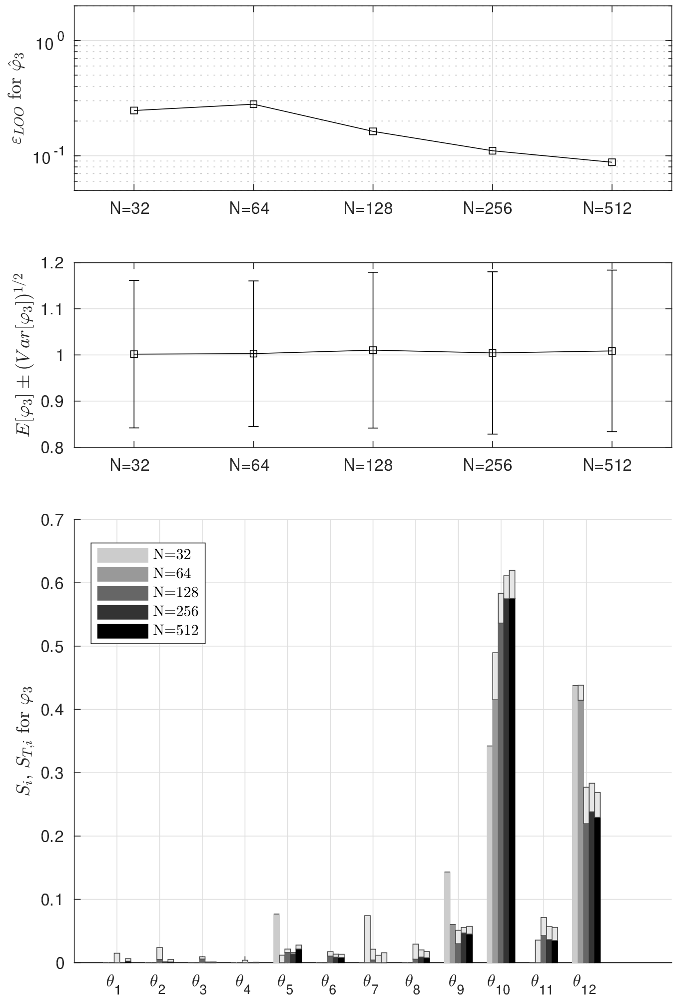

Figure B.5: Similar results as in 5.5 but for φ_3.

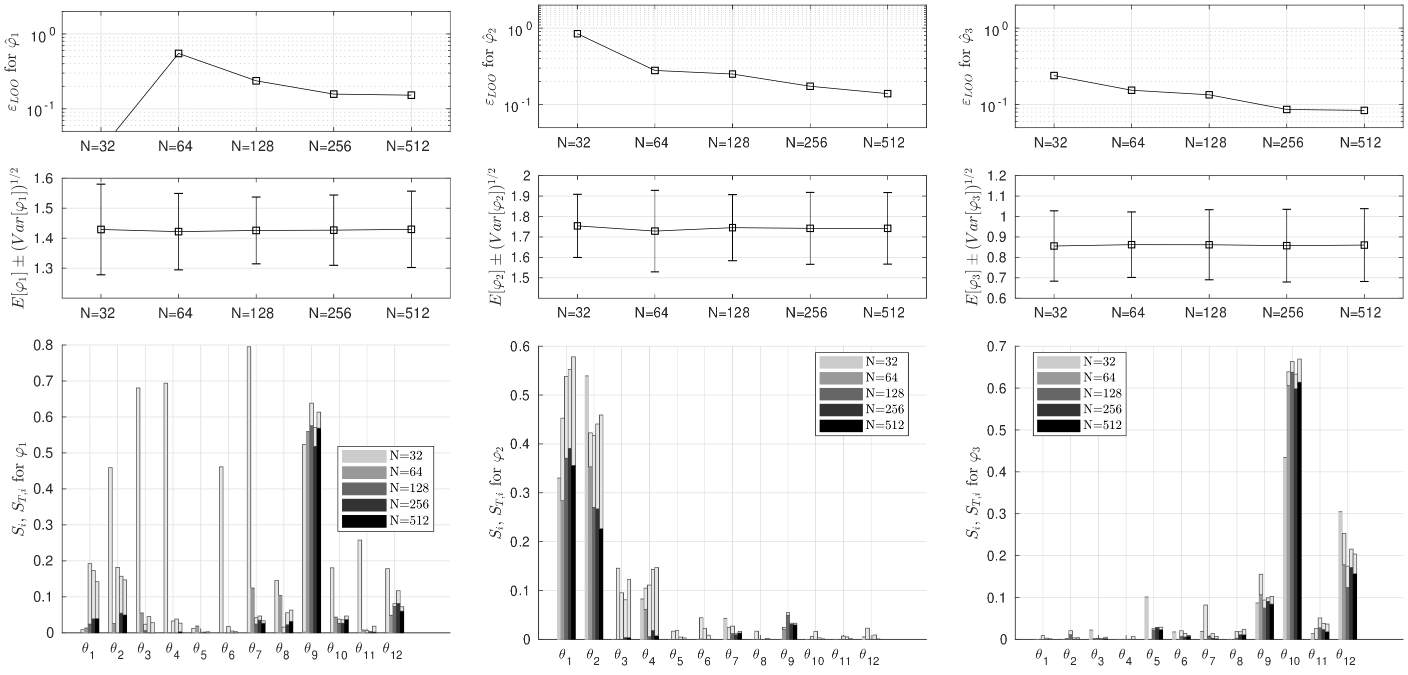

(a) φ_1 (b) φ_2 (c) φ_3

Figure B.6: Similar figure as Figure 5.5 and B.5, but for $\alpha = 0.5$.

Previous PhD theses published at the Department of Marine Technology
(earlier: Faculty of Marine Technology)
NORWEGIAN UNIVERSITY OF SCIENCE AND TECHNOLOGY

Report No.	Author	Title
	Kavlie, Dag	Optimization of Plane Elastic Grillages, 1967
	Hansen, Hans R.	Man-Machine Communication and Data-Storage Methods in Ship Structural Design, 1971
	Gisvold, Kaare M.	A Method for non-linear mixed -integer programming and its Application to Design Problems, 1971
	Lund, Sverre	Tanker Frame Optimalization by means of SUMT-Transformation and Behaviour Models, 1971
	Vinje, Tor	On Vibration of Spherical Shells Interacting with Fluid, 1972
	Lorentz, Jan D.	Tank Arrangement for Crude Oil Carriers in Accordance with the new Anti-Pollution Regulations, 1975
	Carlsen, Carl A.	Computer-Aided Design of Tanker Structures, 1975
	Larsen, Carl M.	Static and Dynamic Analysis of Offshore Pipelines during Installation, 1976
UR-79-01	Brigt Hatlestad, MK	The finite element method used in a fatigue evaluation of fixed offshore platforms. (Dr.Ing. Thesis)
UR-79-02	Erik Pettersen, MK	Analysis and design of cellular structures. (Dr.Ing. Thesis)
UR-79-03	Sverre Valsgård, MK	Finite difference and finite element methods applied to nonlinear analysis of plated structures. (Dr.Ing. Thesis)
UR-79-04	Nils T. Nordsve, MK	Finite element collapse analysis of structural members considering imperfections and stresses due to fabrication. (Dr.Ing. Thesis)
UR-79-05	Ivar J. Fylling, MK	Analysis of towline forces in ocean towing systems. (Dr.Ing. Thesis)
UR-80-06	Nils Sandsmark, MM	Analysis of Stationary and Transient Heat Conduction by the Use of the Finite Element Method. (Dr.Ing. Thesis)
UR-80-09	Sverre Haver, MK	Analysis of uncertainties related to the stochastic modeling of ocean waves. (Dr.Ing. Thesis)
UR-81-15	Odland, Jonas	On the Strength of welded Ring stiffened cylindrical Shells primarily subjected to axial Compression
UR-82-17	Engesvik, Knut	Analysis of Uncertainties in the fatigue Capacity of

		Welded Joints
UR-82-18	Rye, Henrik	Ocean wave groups
UR-83-30	Eide, Oddvar Inge	On Cumulative Fatigue Damage in Steel Welded Joints
UR-83-33	Mo, Olav	Stochastic Time Domain Analysis of Slender Offshore Structures
UR-83-34	Amdahl, Jørgen	Energy absorption in Ship-platform impacts
UR-84-37	Mørch, Morten	Motions and mooring forces of semi submersibles as determined by full-scale measurements and theoretical analysis
UR-84-38	Soares, C. Guedes	Probabilistic models for load effects in ship structures
UR-84-39	Aarsnes, Jan V.	Current forces on ships
UR-84-40	Czujko, Jerzy	Collapse Analysis of Plates subjected to Biaxial Compression and Lateral Load
UR-85-46	Alf G. Engseth, MK	Finite element collapse analysis of tubular steel offshore structures. (Dr.Ing. Thesis)
UR-86-47	Dengody Sheshappa, MP	A Computer Design Model for Optimizing Fishing Vessel Designs Based on Techno-Economic Analysis. (Dr.Ing. Thesis)
UR-86-48	Vidar Aanesland, MH	A Theoretical and Numerical Study of Ship Wave Resistance. (Dr.Ing. Thesis)
UR-86-49	Heinz-Joachim Wessel, MK	Fracture Mechanics Analysis of Crack Growth in Plate Girders. (Dr.Ing. Thesis)
UR-86-50	Jon Taby, MK	Ultimate and Post-ultimate Strength of Dented Tubular Members. (Dr.Ing. Thesis)
UR-86-51	Walter Lian, MH	A Numerical Study of Two-Dimensional Separated Flow Past Bluff Bodies at Moderate KC-Numbers. (Dr.Ing. Thesis)
UR-86-52	Bjørn Sortland, MH	Force Measurements in Oscillating Flow on Ship Sections and Circular Cylinders in a U-Tube Water Tank. (Dr.Ing. Thesis)
UR-86-53	Kurt Strand, MM	A System Dynamic Approach to One-dimensional Fluid Flow. (Dr.Ing. Thesis)
UR-86-54	Arne Edvin Løken, MH	Three Dimensional Second Order Hydrodynamic Effects on Ocean Structures in Waves. (Dr.Ing. Thesis)
UR-86-55	Sigurd Falch, MH	A Numerical Study of Slamming of Two-Dimensional Bodies. (Dr.Ing. Thesis)
UR-87-56	Arne Braathen, MH	Application of a Vortex Tracking Method to the Prediction of Roll Damping of a Two-Dimension Floating Body. (Dr.Ing. Thesis)

UR-87-57	Bernt Leira, MK	Gaussian Vector Processes for Reliability Analysis involving Wave-Induced Load Effects. (Dr.Ing. Thesis)
UR-87-58	Magnus Småvik, MM	Thermal Load and Process Characteristics in a Two-Stroke Diesel Engine with Thermal Barriers (in Norwegian). (Dr.Ing. Thesis)
MTA-88-59	Bernt Arild Bremdal, MP	An Investigation of Marine Installation Processes – A Knowledge - Based Planning Approach. (Dr.Ing. Thesis)
MTA-88-60	Xu Jun, MK	Non-linear Dynamic Analysis of Space-framed Offshore Structures. (Dr.Ing. Thesis)
MTA-89-61	Gang Miao, MH	Hydrodynamic Forces and Dynamic Responses of Circular Cylinders in Wave Zones. (Dr.Ing. Thesis)
MTA-89-62	Martin Greenhow, MH	Linear and Non-Linear Studies of Waves and Floating Bodies. Part I and Part II. (Dr.Techn. Thesis)
MTA-89-63	Chang Li, MH	Force Coefficients of Spheres and Cubes in Oscillatory Flow with and without Current. (Dr.Ing. Thesis
MTA-89-64	Hu Ying, MP	A Study of Marketing and Design in Development of Marine Transport Systems. (Dr.Ing. Thesis)
MTA-89-65	Arild Jæger, MH	Seakeeping, Dynamic Stability and Performance of a Wedge Shaped Planing Hull. (Dr.Ing. Thesis)
MTA-89-66	Chan Siu Hung, MM	The dynamic characteristics of tilting-pad bearings
MTA-89-67	Kim Wikstrøm, MP	Analysis av projekteringen for ett offshore projekt. (Licenciat-avhandling)
MTA-89-68	Jiao Guoyang, MK	Reliability Analysis of Crack Growth under Random Loading, considering Model Updating. (Dr.Ing. Thesis)
MTA-89-69	Arnt Olufsen, MK	Uncertainty and Reliability Analysis of Fixed Offshore Structures. (Dr.Ing. Thesis)
MTA-89-70	Wu Yu-Lin, MR	System Reliability Analyses of Offshore Structures using improved Truss and Beam Models. (Dr.Ing. Thesis)
MTA-90-71	Jan Roger Hoff, MH	Three-dimensional Green function of a vessel with forward speed in waves. (Dr.Ing. Thesis)
MTA-90-72	Rong Zhao, MH	Slow-Drift Motions of a Moored Two-Dimensional Body in Irregular Waves. (Dr.Ing. Thesis)
MTA-90-73	Atle Minsaas, MP	Economical Risk Analysis. (Dr.Ing. Thesis)
MTA-90-74	Knut-Aril Farnes, MK	Long-term Statistics of Response in Non-linear Marine Structures. (Dr.Ing. Thesis)
MTA-90-75	Torbjørn Sotberg, MK	Application of Reliability Methods for Safety Assessment of Submarine Pipelines. (Dr.Ing.

		Thesis)
MTA-90-76	Zeuthen, Steffen, MP	SEAMAID. A computational model of the design process in a constraint-based logic programming environment. An example from the offshore domain. (Dr.Ing. Thesis)
MTA-91-77	Haagensen, Sven, MM	Fuel Dependant Cyclic Variability in a Spark Ignition Engine - An Optical Approach. (Dr.Ing. Thesis)
MTA-91-78	Løland, Geir, MH	Current forces on and flow through fish farms. (Dr.Ing. Thesis)
MTA-91-79	Hoen, Christopher, MK	System Identification of Structures Excited by Stochastic Load Processes. (Dr.Ing. Thesis)
MTA-91-80	Haugen, Stein, MK	Probabilistic Evaluation of Frequency of Collision between Ships and Offshore Platforms. (Dr.Ing. Thesis)
MTA-91-81	Sødahl, Nils, MK	Methods for Design and Analysis of Flexible Risers. (Dr.Ing. Thesis)
MTA-91-82	Ormberg, Harald, MK	Non-linear Response Analysis of Floating Fish Farm Systems. (Dr.Ing. Thesis)
MTA-91-83	Marley, Mark J., MK	Time Variant Reliability under Fatigue Degradation. (Dr.Ing. Thesis)
MTA-91-84	Krokstad, Jørgen R., MH	Second-order Loads in Multidirectional Seas. (Dr.Ing. Thesis)
MTA-91-85	Molteberg, Gunnar A., MM	The Application of System Identification Techniques to Performance Monitoring of Four Stroke Turbocharged Diesel Engines. (Dr.Ing. Thesis)
MTA-92-86	Mørch, Hans Jørgen Bjelke, MH	Aspects of Hydrofoil Design: with Emphasis on Hydrofoil Interaction in Calm Water. (Dr.Ing. Thesis)
MTA-92-87	Chan Siu Hung, MM	Nonlinear Analysis of Rotordynamic Instabilities in Highspeed Turbomachinery. (Dr.Ing. Thesis)
MTA-92-88	Bessason, Bjarni, MK	Assessment of Earthquake Loading and Response of Seismically Isolated Bridges. (Dr.Ing. Thesis)
MTA-92-89	Langli, Geir, MP	Improving Operational Safety through exploitation of Design Knowledge - an investigation of offshore platform safety. (Dr.Ing. Thesis)
MTA-92-90	Sævik, Svein, MK	On Stresses and Fatigue in Flexible Pipes. (Dr.Ing. Thesis)
MTA-92-91	Ask, Tor Ø., MM	Ignition and Flame Growth in Lean Gas-Air Mixtures. An Experimental Study with a Schlieren System. (Dr.Ing. Thesis)
MTA-86-92	Hessen, Gunnar, MK	Fracture Mechanics Analysis of Stiffened Tubular Members. (Dr.Ing. Thesis)

MTA-93-93	Steinebach, Christian, MM	Knowledge Based Systems for Diagnosis of Rotating Machinery. (Dr.Ing. Thesis)
MTA-93-94	Dalane, Jan Inge, MK	System Reliability in Design and Maintenance of Fixed Offshore Structures. (Dr.Ing. Thesis)
MTA-93-95	Steen, Sverre, MH	Cobblestone Effect on SES. (Dr.Ing. Thesis)
MTA-93-96	Karunakaran, Daniel, MK	Nonlinear Dynamic Response and Reliability Analysis of Drag-dominated Offshore Platforms. (Dr.Ing. Thesis)
MTA-93-97	Hagen, Arnulf, MP	The Framework of a Design Process Language. (Dr.Ing. Thesis)
MTA-93-98	Nordrik, Rune, MM	Investigation of Spark Ignition and Autoignition in Methane and Air Using Computational Fluid Dynamics and Chemical Reaction Kinetics. A Numerical Study of Ignition Processes in Internal Combustion Engines. (Dr.Ing. Thesis)
MTA-94-99	Passano, Elizabeth, MK	Efficient Analysis of Nonlinear Slender Marine Structures. (Dr.Ing. Thesis)
MTA-94-100	Kvålsvold, Jan, MH	Hydroelastic Modelling of Wetdeck Slamming on Multihull Vessels. (Dr.Ing. Thesis)
MTA-94-102	Bech, Sidsel M., MK	Experimental and Numerical Determination of Stiffness and Strength of GRP/PVC Sandwich Structures. (Dr.Ing. Thesis)
MTA-95-103	Paulsen, Hallvard, MM	A Study of Transient Jet and Spray using a Schlieren Method and Digital Image Processing. (Dr.Ing. Thesis)
MTA-95-104	Hovde, Geir Olav, MK	Fatigue and Overload Reliability of Offshore Structural Systems, Considering the Effect of Inspection and Repair. (Dr.Ing. Thesis)
MTA-95-105	Wang, Xiaozhi, MK	Reliability Analysis of Production Ships with Emphasis on Load Combination and Ultimate Strength. (Dr.Ing. Thesis)
MTA-95-106	Ulstein, Tore, MH	Nonlinear Effects of a Flexible Stern Seal Bag on Cobblestone Oscillations of an SES. (Dr.Ing. Thesis)
MTA-95-107	Solaas, Frøydis, MH	Analytical and Numerical Studies of Sloshing in Tanks. (Dr.Ing. Thesis)
MTA-95-108	Hellan, Øyvind, MK	Nonlinear Pushover and Cyclic Analyses in Ultimate Limit State Design and Reassessment of Tubular Steel Offshore Structures. (Dr.Ing. Thesis)
MTA-95-109	Hermundstad, Ole A., MK	Theoretical and Experimental Hydroelastic Analysis of High Speed Vessels. (Dr.Ing. Thesis)
MTA-96-110	Bratland, Anne K., MH	Wave-Current Interaction Effects on Large-Volume Bodies in Water of Finite Depth. (Dr.Ing. Thesis)
MTA-96-111	Herfjord, Kjell, MH	A Study of Two-dimensional Separated Flow by a Combination of the Finite Element Method and

		Navier-Stokes Equations. (Dr.Ing. Thesis)
MTA-96-112	Æsøy, Vilmar, MM	Hot Surface Assisted Compression Ignition in a Direct Injection Natural Gas Engine. (Dr.Ing. Thesis)
MTA-96-113	Eknes, Monika L., MK	Escalation Scenarios Initiated by Gas Explosions on Offshore Installations. (Dr.Ing. Thesis)
MTA-96-114	Erikstad, Stein O., MP	A Decision Support Model for Preliminary Ship Design. (Dr.Ing. Thesis)
MTA-96-115	Pedersen, Egil, MH	A Nautical Study of Towed Marine Seismic Streamer Cable Configurations. (Dr.Ing. Thesis)
MTA-97-116	Moksnes, Paul O., MM	Modelling Two-Phase Thermo-Fluid Systems Using Bond Graphs. (Dr.Ing. Thesis)
MTA-97-117	Halse, Karl H., MK	On Vortex Shedding and Prediction of Vortex-Induced Vibrations of Circular Cylinders. (Dr.Ing. Thesis)
MTA-97-118	Igland, Ragnar T., MK	Reliability Analysis of Pipelines during Laying, considering Ultimate Strength under Combined Loads. (Dr.Ing. Thesis)
MTA-97-119	Pedersen, Hans-P., MP	Levendefiskteknologi for fiskefartøy. (Dr.Ing. Thesis)
MTA-98-120	Vikestad, Kyrre, MK	Multi-Frequency Response of a Cylinder Subjected to Vortex Shedding and Support Motions. (Dr.Ing. Thesis)
MTA-98-121	Azadi, Mohammad R. E., MK	Analysis of Static and Dynamic Pile-Soil-Jacket Behaviour. (Dr.Ing. Thesis)
MTA-98-122	Ulltang, Terje, MP	A Communication Model for Product Information. (Dr.Ing. Thesis)
MTA-98-123	Torbergsen, Erik, MM	Impeller/Diffuser Interaction Forces in Centrifugal Pumps. (Dr.Ing. Thesis)
MTA-98-124	Hansen, Edmond, MH	A Discrete Element Model to Study Marginal Ice Zone Dynamics and the Behaviour of Vessels Moored in Broken Ice. (Dr.Ing. Thesis)
MTA-98-125	Videiro, Paulo M., MK	Reliability Based Design of Marine Structures. (Dr.Ing. Thesis)
MTA-99-126	Mainçon, Philippe, MK	Fatigue Reliability of Long Welds Application to Titanium Risers. (Dr.Ing. Thesis)
MTA-99-127	Haugen, Elin M., MH	Hydroelastic Analysis of Slamming on Stiffened Plates with Application to Catamaran Wetdecks. (Dr.Ing. Thesis)
MTA-99-128	Langhelle, Nina K., MK	Experimental Validation and Calibration of Nonlinear Finite Element Models for Use in Design of Aluminium Structures Exposed to Fire. (Dr.Ing. Thesis)
MTA-99-	Berstad, Are J., MK	Calculation of Fatigue Damage in Ship Structures.

129		(Dr.Ing. Thesis)
MTA-99-130	Andersen, Trond M., MM	Short Term Maintenance Planning. (Dr.Ing. Thesis)
MTA-99-131	Tveiten, Bård Wathne, MK	Fatigue Assessment of Welded Aluminium Ship Details. (Dr.Ing. Thesis)
MTA-99-132	Søreide, Fredrik, MP	Applications of underwater technology in deep water archaeology. Principles and practice. (Dr.Ing. Thesis)
MTA-99-133	Tønnessen, Rune, MH	A Finite Element Method Applied to Unsteady Viscous Flow Around 2D Blunt Bodies With Sharp Corners. (Dr.Ing. Thesis)
MTA-99-134	Elvekrok, Dag R., MP	Engineering Integration in Field Development Projects in the Norwegian Oil and Gas Industry. The Supplier Management of Norne. (Dr.Ing. Thesis)
MTA-99-135	Fagerholt, Kjetil, MP	Optimeringsbaserte Metoder for Ruteplanlegging innen skipsfart. (Dr.Ing. Thesis)
MTA-99-136	Bysveen, Marie, MM	Visualization in Two Directions on a Dynamic Combustion Rig for Studies of Fuel Quality. (Dr.Ing. Thesis)
MTA-2000-137	Storteig, Eskild, MM	Dynamic characteristics and leakage performance of liquid annular seals in centrifugal pumps. (Dr.Ing. Thesis)
MTA-2000-138	Sagli, Gro, MK	Model uncertainty and simplified estimates of long term extremes of hull girder loads in ships. (Dr.Ing. Thesis)
MTA-2000-139	Tronstad, Harald, MK	Nonlinear analysis and design of cable net structures like fishing gear based on the finite element method. (Dr.Ing. Thesis)
MTA-2000-140	Kroneberg, André, MP	Innovation in shipping by using scenarios. (Dr.Ing. Thesis)
MTA-2000-141	Haslum, Herbjørn Alf, MH	Simplified methods applied to nonlinear motion of spar platforms. (Dr.Ing. Thesis)
MTA-2001-142	Samdal, Ole Johan, MM	Modelling of Degradation Mechanisms and Stressor Interaction on Static Mechanical Equipment Residual Lifetime. (Dr.Ing. Thesis)
MTA-2001-143	Baarholm, Rolf Jarle, MH	Theoretical and experimental studies of wave impact underneath decks of offshore platforms. (Dr.Ing. Thesis)
MTA-2001-144	Wang, Lihua, MK	Probabilistic Analysis of Nonlinear Wave-induced Loads on Ships. (Dr.Ing. Thesis)
MTA-2001-145	Kristensen, Odd H. Holt, MK	Ultimate Capacity of Aluminium Plates under Multiple Loads, Considering HAZ Properties. (Dr.Ing. Thesis)
MTA-2001-146	Greco, Marilena, MH	A Two-Dimensional Study of Green-Water

		Loading. (Dr.Ing. Thesis)
MTA-2001-147	Heggelund, Svein E., MK	Calculation of Global Design Loads and Load Effects in Large High Speed Catamarans. (Dr.Ing. Thesis)
MTA-2001-148	Babalola, Olusegun T., MK	Fatigue Strength of Titanium Risers – Defect Sensitivity. (Dr.Ing. Thesis)
MTA-2001-149	Mohammed, Abuu K., MK	Nonlinear Shell Finite Elements for Ultimate Strength and Collapse Analysis of Ship Structures. (Dr.Ing. Thesis)
MTA-2002-150	Holmedal, Lars E., MH	Wave-current interactions in the vicinity of the sea bed. (Dr.Ing. Thesis)
MTA-2002-151	Rognebakke, Olav F., MH	Sloshing in rectangular tanks and interaction with ship motions. (Dr.Ing. Thesis)
MTA-2002-152	Lader, Pål Furset, MH	Geometry and Kinematics of Breaking Waves. (Dr.Ing. Thesis)
MTA-2002-153	Yang, Qinzheng, MH	Wash and wave resistance of ships in finite water depth. (Dr.Ing. Thesis)
MTA-2002-154	Melhus, Øyvin, MM	Utilization of VOC in Diesel Engines. Ignition and combustion of VOC released by crude oil tankers. (Dr.Ing. Thesis)
MTA-2002-155	Ronæss, Marit, MH	Wave Induced Motions of Two Ships Advancing on Parallel Course. (Dr.Ing. Thesis)
MTA-2002-156	Økland, Ole D., MK	Numerical and experimental investigation of whipping in twin hull vessels exposed to severe wet deck slamming. (Dr.Ing. Thesis)
MTA-2002-157	Ge, Chunhua, MK	Global Hydroelastic Response of Catamarans due to Wet Deck Slamming. (Dr.Ing. Thesis)
MTA-2002-158	Byklum, Eirik, MK	Nonlinear Shell Finite Elements for Ultimate Strength and Collapse Analysis of Ship Structures. (Dr.Ing. Thesis)
IMT-2003-1	Chen, Haibo, MK	Probabilistic Evaluation of FPSO-Tanker Collision in Tandem Offloading Operation. (Dr.Ing. Thesis)
IMT-2003-2	Skaugset, Kjetil Bjørn, MK	On the Suppression of Vortex Induced Vibrations of Circular Cylinders by Radial Water Jets. (Dr.Ing. Thesis)
IMT-2003-3	Chezhian, Muthu	Three-Dimensional Analysis of Slamming. (Dr.Ing. Thesis)
IMT-2003-4	Buhaug, Øyvind	Deposit Formation on Cylinder Liner Surfaces in Medium Speed Engines. (Dr.Ing. Thesis)
IMT-2003-5	Tregde, Vidar	Aspects of Ship Design: Optimization of Aft Hull with Inverse Geometry Design. (Dr.Ing. Thesis)
IMT-	Wist, Hanne Therese	Statistical Properties of Successive Ocean Wave

2003-6		Parameters. (Dr.Ing. Thesis)
IMT-2004-7	Ransau, Samuel	Numerical Methods for Flows with Evolving Interfaces. (Dr.Ing. Thesis)
IMT-2004-8	Soma, Torkel	Blue-Chip or Sub-Standard. A data interrogation approach of identity safety characteristics of shipping organization. (Dr.Ing. Thesis)
IMT-2004-9	Ersdal, Svein	An experimental study of hydrodynamic forces on cylinders and cables in near axial flow. (Dr.Ing. Thesis)
IMT-2005-10	Brodtkorb, Per Andreas	The Probability of Occurrence of Dangerous Wave Situations at Sea. (Dr.Ing. Thesis)
IMT-2005-11	Yttervik, Rune	Ocean current variability in relation to offshore engineering. (Dr.Ing. Thesis)
IMT-2005-12	Fredheim, Arne	Current Forces on Net-Structures. (Dr.Ing. Thesis)
IMT-2005-13	Heggernes, Kjetil	Flow around marine structures. (Dr.Ing. Thesis
IMT-2005-14	Fouques, Sebastien	Lagrangian Modelling of Ocean Surface Waves and Synthetic Aperture Radar Wave Measurements. (Dr.Ing. Thesis)
IMT-2006-15	Holm, Håvard	Numerical calculation of viscous free surface flow around marine structures. (Dr.Ing. Thesis)
IMT-2006-16	Bjørheim, Lars G.	Failure Assessment of Long Through Thickness Fatigue Cracks in Ship Hulls. (Dr.Ing. Thesis)
IMT-2006-17	Hansson, Lisbeth	Safety Management for Prevention of Occupational Accidents. (Dr.Ing. Thesis)
IMT-2006-18	Zhu, Xinying	Application of the CIP Method to Strongly Nonlinear Wave-Body Interaction Problems. (Dr.Ing. Thesis)
IMT-2006-19	Reite, Karl Johan	Modelling and Control of Trawl Systems. (Dr.Ing. Thesis)
IMT-2006-20	Smogeli, Øyvind Notland	Control of Marine Propellers. From Normal to Extreme Conditions. (Dr.Ing. Thesis)
IMT-2007-21	Storhaug, Gaute	Experimental Investigation of Wave Induced Vibrations and Their Effect on the Fatigue Loading of Ships. (Dr.Ing. Thesis)
IMT-2007-22	Sun, Hui	A Boundary Element Method Applied to Strongly Nonlinear Wave-Body Interaction Problems. (PhD Thesis, CeSOS)
IMT-2007-23	Rustad, Anne Marthine	Modelling and Control of Top Tensioned Risers. (PhD Thesis, CeSOS)
IMT-2007-24	Johansen, Vegar	Modelling flexible slender system for real-time simulations and control applications
IMT-2007-25	Wroldsen, Anders Sunde	Modelling and control of tensegrity structures.

		(PhD Thesis, CeSOS)
IMT-2007-26	Aronsen, Kristoffer Høye	An experimental investigation of in-line and combined inline and cross flow vortex induced vibrations. (Dr. avhandling, IMT)
IMT-2007-27	Gao, Zhen	Stochastic Response Analysis of Mooring Systems with Emphasis on Frequency-domain Analysis of Fatigue due to Wide-band Response Processes (PhD Thesis, CeSOS)
IMT-2007-28	Thorstensen, Tom Anders	Lifetime Profit Modelling of Ageing Systems Utilizing Information about Technical Condition. (Dr.ing. thesis, IMT)
IMT-2008-29	Refsnes, Jon Erling Gorset	Nonlinear Model-Based Control of Slender Body AUVs (PhD Thesis, IMT)
IMT-2008-30	Berntsen, Per Ivar B.	Structural Reliability Based Position Mooring. (PhD-Thesis, IMT)
IMT-2008-31	Ye, Naiquan	Fatigue Assessment of Aluminium Welded Box-stiffener Joints in Ships (Dr.ing. thesis, IMT)
IMT-2008-32	Radan, Damir	Integrated Control of Marine Electrical Power Systems. (PhD-Thesis, IMT)
IMT-2008-33	Thomassen, Paul	Methods for Dynamic Response Analysis and Fatigue Life Estimation of Floating Fish Cages. (Dr.ing. thesis, IMT)
IMT-2008-34	Pákozdi, Csaba	A Smoothed Particle Hydrodynamics Study of Two-dimensional Nonlinear Sloshing in Rectangular Tanks. (Dr.ing.thesis, IMT/ CeSOS)
IMT-2007-35	Grytøyr, Guttorm	A Higher-Order Boundary Element Method and Applications to Marine Hydrodynamics. (Dr.ing.thesis, IMT)
IMT-2008-36	Drummen, Ingo	Experimental and Numerical Investigation of Nonlinear Wave-Induced Load Effects in Containerships considering Hydroelasticity. (PhD thesis, CeSOS)
IMT-2008-37	Skejic, Renato	Maneuvering and Seakeeping of a Singel Ship and of Two Ships in Interaction. (PhD-Thesis, CeSOS)
IMT-2008-38	Harlem, Alf	An Age-Based Replacement Model for Repairable Systems with Attention to High-Speed Marine Diesel Engines. (PhD-Thesis, IMT)
IMT-2008-39	Alsos, Hagbart S.	Ship Grounding. Analysis of Ductile Fracture, Bottom Damage and Hull Girder Response. (PhD-thesis, IMT)
IMT-2008-40	Graczyk, Mateusz	Experimental Investigation of Sloshing Loading and Load Effects in Membrane LNG Tanks Subjected to Random Excitation. (PhD-thesis, CeSOS)
IMT-2008-41	Taghipour, Reza	Efficient Prediction of Dynamic Response for Flexible amd Multi-body Marine Structures. (PhD-

		thesis, CeSOS)
IMT-2008-42	Ruth, Eivind	Propulsion control and thrust allocation on marine vessels. (PhD thesis, CeSOS)
IMT-2008-43	Nystad, Bent Helge	Technical Condition Indexes and Remaining Useful Life of Aggregated Systems. PhD thesis, IMT
IMT-2008-44	Soni, Prashant Kumar	Hydrodynamic Coefficients for Vortex Induced Vibrations of Flexible Beams, PhD thesis, CeSOS
IMT-2009-45	Amlashi, Hadi K.K.	Ultimate Strength and Reliability-based Design of Ship Hulls with Emphasis on Combined Global and Local Loads. PhD Thesis, IMT
IMT-2009-46	Pedersen, Tom Arne	Bond Graph Modelling of Marine Power Systems. PhD Thesis, IMT
IMT-2009-47	Kristiansen, Trygve	Two-Dimensional Numerical and Experimental Studies of Piston-Mode Resonance. PhD-Thesis, CeSOS
IMT-2009-48	Ong, Muk Chen	Applications of a Standard High Reynolds Number Model and a Stochastic Scour Prediction Model for Marine Structures. PhD-thesis, IMT
IMT-2009-49	Hong, Lin	Simplified Analysis and Design of Ships subjected to Collision and Grounding. PhD-thesis, IMT
IMT-2009-50	Koushan, Kamran	Vortex Induced Vibrations of Free Span Pipelines, PhD thesis, IMT
IMT-2009-51	Korsvik, Jarl Eirik	Heuristic Methods for Ship Routing and Scheduling. PhD-thesis, IMT
IMT-2009-52	Lee, Jihoon	Experimental Investigation and Numerical in Analyzing the Ocean Current Displacement of Longlines. Ph.d.-Thesis, IMT.
IMT-2009-53	Vestbøstad, Tone Gran	A Numerical Study of Wave-in-Deck Impact usin a Two-Dimensional Constrained Interpolation Profile Method, Ph.d.thesis, CeSOS.
IMT-2009-54	Bruun, Kristine	Bond Graph Modelling of Fuel Cells for Marine Power Plants. Ph.d.-thesis, IMT
IMT 2009-55	Holstad, Anders	Numerical Investigation of Turbulence in a Sekwed Three-Dimensional Channel Flow, Ph.d.-thesis, IMT.
IMT 2009-56	Ayala-Uraga, Efren	Reliability-Based Assessment of Deteriorating Ship-shaped Offshore Structures, Ph.d.-thesis, IMT
IMT 2009-57	Kong, Xiangjun	A Numerical Study of a Damaged Ship in Beam Sea Waves. Ph.d.-thesis, IMT/CeSOS.
IMT 2010-58	Kristiansen, David	Wave Induced Effects on Floaters of Aquaculture Plants, Ph.d.-thesis, CeSOS.

IMT 2010-59	Ludvigsen, Martin	An ROV-Toolbox for Optical and Acoustic Scientific Seabed Investigation. Ph.d.-thesis IMT.
IMT 2010-60	Hals, Jørgen	Modelling and Phase Control of Wave-Energy Converters. Ph.d.thesis, CeSOS.
IMT 2010- 61	Shu, Zhi	Uncertainty Assessment of Wave Loads and Ultimate Strength of Tankers and Bulk Carriers in a Reliability Framework. Ph.d. Thesis, IMT/ CeSOS
IMT 2010-62	Shao, Yanlin	Numerical Potential-Flow Studies on Weakly-Nonlinear Wave-Body Interactions with/without Small Forward Speed, Ph.d.thesis,CeSOS.
IMT 2010-63	Califano, Andrea	Dynamic Loads on Marine Propellers due to Intermittent Ventilation. Ph.d.thesis, IMT.
IMT 2010-64	El Khoury, George	Numerical Simulations of Massively Separated Turbulent Flows, Ph.d.-thesis, IMT
IMT 2010-65	Seim, Knut Sponheim	Mixing Process in Dense Overflows with Emphasis on the Faroe Bank Channel Overflow. Ph.d.thesis, IMT
IMT 2010-66	Jia, Huirong	Structural Analysis of Intect and Damaged Ships in a Collission Risk Analysis Perspective. Ph.d.thesis CeSoS.
IMT 2010-67	Jiao, Linlin	Wave-Induced Effects on a Pontoon-type Very Large Floating Structures (VLFS). Ph.D.-thesis, CeSOS.
IMT 2010-68	Abrahamsen, Bjørn Christian	Sloshing Induced Tank Roof with Entrapped Air Pocket. Ph.d.thesis, CeSOS.
IMT 2011-69	Karimirad, Madjid	Stochastic Dynamic Response Analysis of Spar-Type Wind Turbines with Catenary or Taut Mooring Systems. Ph.d.-thesis, CeSOS.
IMT - 2011-70	Erlend Meland	Condition Monitoring of Safety Critical Valves. Ph.d.-thesis, IMT.
IMT – 2011-71	Yang, Limin	Stochastic Dynamic System Analysis of Wave Energy Converter with Hydraulic Power Take-Off, with Particular Reference to Wear Damage Analysis, Ph.d. Thesis, CeSOS.
IMT – 2011-72	Visscher, Jan	Application of Particla Image Velocimetry on Turbulent Marine Flows, Ph.d.Thesis, IMT.
IMT – 2011-73	Su, Biao	Numerical Predictions of Global and Local Ice Loads on Ships. Ph.d.Thesis, CeSOS.
IMT – 2011-74	Liu, Zhenhui	Analytical and Numerical Analysis of Iceberg Collision with Ship Structures. Ph.d.Thesis, IMT.
IMT – 2011-75	Aarsæther, Karl Gunnar	Modeling and Analysis of Ship Traffic by Observation and Numerical Simulation. Ph.d.Thesis, IMT.

Imt – 2011-76	Wu, Jie	Hydrodynamic Force Identification from Stochastic Vortex Induced Vibration Experiments with Slender Beams. Ph.d.Thesis, IMT.
Imt – 2011-77	Amini, Hamid	Azimuth Propulsors in Off-design Conditions. Ph.d.Thesis, IMT.
IMT – 2011-78	Nguyen, Tan-Hoi	Toward a System of Real-Time Prediction and Monitoring of Bottom Damage Conditions During Ship Grounding. Ph.d.thesis, IMT.
IMT-2011-79	Tavakoli, Mohammad T.	Assessment of Oil Spill in Ship Collision and Grounding, Ph.d.thesis, IMT.
IMT-2011-80	Guo, Bingjie	Numerical and Experimental Investigation of Added Resistance in Waves. Ph.d.Thesis, IMT.
IMT-2011-81	Chen, Qiaofeng	Ultimate Strength of Aluminium Panels, considering HAZ Effects, IMT
IMT-2012-82	Kota, Ravikiran S.	Wave Loads on Decks of Offshore Structures in Random Seas, CeSOS.
IMT-2012-83	Sten, Ronny	Dynamic Simulation of Deep Water Drilling Risers with Heave Compensating System, IMT.
IMT-2012-84	Berle, Øyvind	Risk and resilience in global maritime supply chains, IMT.
IMT-2012-85	Fang, Shaoji	Fault Tolerant Position Mooring Control Based on Structural Reliability, CeSOS.
IMT-2012-86	You, Jikun	Numerical studies on wave forces and moored ship motions in intermediate and shallow water, CeSOS.
IMT-2012-87	Xiang ,Xu	Maneuvering of two interacting ships in waves, CeSOS
IMT-2012-88	Dong, Wenbin	Time-domain fatigue response and reliability analysis of offshore wind turbines with emphasis on welded tubular joints and gear components, CeSOS
IMT-2012-89	Zhu, Suji	Investigation of Wave-Induced Nonlinear Load Effects in Open Ships considering Hull Girder Vibrations in Bending and Torsion, CeSOS
IMT-2012-90	Zhou, Li	Numerical and Experimental Investigation of Station-keeping in Level Ice, CeSOS
IMT-2012-91	Ushakov, Sergey	Particulate matter emission characteristics from diesel enignes operating on conventional and alternative marine fuels, IMT
IMT-2013-1	Yin, Decao	Experimental and Numerical Analysis of Combined In-line and Cross-flow Vortex Induced Vibrations, CeSOS

IMT-2013-2	Kurniawan, Adi	Modelling and geometry optimisation of wave energy converters, CeSOS
IMT-2013-3	Al Ryati, Nabil	Technical condition indexes doe auxiliary marine diesel engines, IMT
IMT-2013-4	Firoozkoohi, Reza	Experimental, numerical and analytical investigation of the effect of screens on sloshing, CeSOS
IMT-2013-5	Ommani, Babak	Potential-Flow Predictions of a Semi-Displacement Vessel Including Applications to Calm Water Broaching, CeSOS
IMT-2013-6	Xing, Yihan	Modelling and analysis of the gearbox in a floating spar-type wind turbine, CeSOS
IMT-7-2013	Balland, Océane	Optimization models for reducing air emissions from ships, IMT
IMT-8-2013	Yang, Dan	Transitional wake flow behind an inclined flat plate-----Computation and analysis, IMT
IMT-9-2013	Abdillah, Suyuthi	Prediction of Extreme Loads and Fatigue Damage for a Ship Hull due to Ice Action, IMT
IMT-10-2013	Ramìrez, Pedro Agustìn Pèrez	Ageing management and life extension of technical systems- Concepts and methods applied to oil and gas facilities, IMT
IMT-11-2013	Chuang, Zhenju	Experimental and Numerical Investigation of Speed Loss due to Seakeeping and Maneuvering. IMT
IMT-12-2013	Etemaddar, Mahmoud	Load and Response Analysis of Wind Turbines under Atmospheric Icing and Controller System Faults with Emphasis on Spar Type Floating Wind Turbines, IMT
IMT-13-2013	Lindstad, Haakon	Strategies and measures for reducing maritime CO2 emissons, IMT
IMT-14-2013	Haris, Sabril	Damage interaction analysis of ship collisions, IMT
IMT-15-2013	Shainee, Mohamed	Conceptual Design, Numerical and Experimental Investigation of a SPM Cage Concept for Offshore Mariculture, IMT
IMT-16-2013	Gansel, Lars	Flow past porous cylinders and effects of biofouling and fish behavior on the flow in and around Atlantic salmon net cages, IMT
IMT-17-2013	Gaspar, Henrique	Handling Aspects of Complexity in Conceptual Ship Design, IMT
IMT-18-2013	Thys, Maxime	Theoretical and Experimental Investigation of a Free Running Fishing Vessel at Small Frequency of Encounter, CeSOS
IMT-19-2013	Aglen, Ida	VIV in Free Spanning Pipelines, CeSOS

IMT-1-2014	Song, An	Theoretical and experimental studies of wave diffraction and radiation loads on a horizontally submerged perforated plate, CeSOS
IMT-2-2014	Rogne, Øyvind Ygre	Numerical and Experimental Investigation of a Hinged 5-body Wave Energy Converter, CeSOS
IMT-3-2014	Dai, Lijuan	Safe and efficient operation and maintenance of offshore wind farms ,IMT
IMT-4-2014	Bachynski, Erin Elizabeth	Design and Dynamic Analysis of Tension Leg Platform Wind Turbines, CeSOS
IMT-5-2014	Wang, Jingbo	Water Entry of Freefall Wedged – Wedge motions and Cavity Dynamics, CeSOS
IMT-6-2014	Kim, Ekaterina	Experimental and numerical studies related to the coupled behavior of ice mass and steel structures during accidental collisions, IMT
IMT-7-2014	Tan, Xiang	Numerical investigation of ship's continuous- mode icebreaking in leverl ice, CeSOS
IMT-8-2014	Muliawan, Made Jaya	Design and Analysis of Combined Floating Wave and Wind Power Facilities, with Emphasis on Extreme Load Effects of the Mooring System, CeSOS
IMT-9-2014	Jiang, Zhiyu	Long-term response analysis of wind turbines with an emphasis on fault and shutdown conditions, IMT
IMT-10-2014	Dukan, Fredrik	ROV Motion Control Systems, IMT
IMT-11-2014	Grimsmo, Nils I.	Dynamic simulations of hydraulic cylinder for heave compensation of deep water drilling risers, IMT
IMT-12-2014	Kvittem, Marit I.	Modelling and response analysis for fatigue design of a semisubmersible wind turbine, CeSOS
IMT-13-2014	Akhtar, Juned	The Effects of Human Fatigue on Risk at Sea, IMT
IMT-14-2014	Syahroni, Nur	Fatigue Assessment of Welded Joints Taking into Account Effects of Residual Stress, IMT
IMT-1-2015	Bøckmann, Eirik	Wave Propulsion of ships, IMT
IMT-2-2015	Wang, Kai	Modelling and dynamic analysis of a semi-submersible floating vertical axis wind turbine, CeSOS
IMT-3-2015	Fredriksen, Arnt Gunvald	A numerical and experimental study of a two-dimensional body with moonpool in waves and current, CeSOS
IMT-4-2015	Jose Patricio Gallardo Canabes	Numerical studies of viscous flow around bluff bodies, IMT

IMT-5-2015	Vegard Longva	Formulation and application of finite element techniques for slender marine structures subjected to contact interactions, IMT
IMT-6-2015	Jacobus De Vaal	Aerodynamic modelling of floating wind turbines, CeSOS
IMT-7-2015	Fachri Nasution	Fatigue Performance of Copper Power Conductors, IMT
IMT-8-2015	Oleh I Karpa	Development of bivariate extreme value distributions for applications in marine technology,CeSOS
IMT-9-2015	Daniel de Almeida Fernandes	An output feedback motion control system for ROVs, AMOS
IMT-10-2015	Bo Zhao	Particle Filter for Fault Diagnosis: Application to Dynamic Positioning Vessel and Underwater Robotics, CeSOS
IMT-11-2015	Wenting Zhu	Impact of emission allocation in maritime transportation, IMT
IMT-12-2015	Amir Rasekhi Nejad	Dynamic Analysis and Design of Gearboxes in Offshore Wind Turbines in a Structural Reliability Perspective, CeSOS
IMT-13-2015	Arturo Jesùs Ortega Malca	Dynamic Response of Flexibles Risers due to Unsteady Slug Flow, CeSOS
IMT-14-2015	Dagfinn Husjord	Guidance and decision-support system for safe navigation of ships operating in close proximity, IMT
IMT-15-2015	Anirban Bhattacharyya	Ducted Propellers: Behaviour in Waves and Scale Effects, IMT
IMT-16-2015	Qin Zhang	Image Processing for Ice Parameter Identification in Ice Management, IMT
IMT-1-2016	Vincentius Rumawas	Human Factors in Ship Design and Operation: An Experiential Learning, IMT
IMT-2-2016	Martin Storheim	Structural response in ship-platform and ship-ice collisions, IMT
IMT-3-2016	Mia Abrahamsen Prsic	Numerical Simulations of the Flow around single and Tandem Circular Cylinders Close to a Plane Wall, IMT
IMT-4-2016	Tufan Arslan	Large-eddy simulations of cross-flow around ship sections, IMT

IMT-5-2016	Pierre Yves-Henry	Parametrisation of aquatic vegetation in hydraulic and coastal research,IMT
IMT-6-2016	Lin Li	Dynamic Analysis of the Instalation of Monopiles for Offshore Wind Turbines, CeSOS
IMT-7-2016	Øivind Kåre Kjerstad	Dynamic Positioning of Marine Vessels in Ice, IMT
IMT-8-2016	Xiaopeng Wu	Numerical Analysis of Anchor Handling and Fish Trawling Operations in a Safety Perspective, CeSOS
IMT-9-2016	Zhengshun Cheng	Integrated Dynamic Analysis of Floating Vertical Axis Wind Turbines, CeSOS
IMT-10-2016	Ling Wan	Experimental and Numerical Study of a Combined Offshore Wind and Wave Energy Converter Concept
IMT-11-2016	Wei Chai	Stochastic dynamic analysis and reliability evaluation of the roll motion for ships in random seas, CeSOS
IMT-12-2016	Øyvind Selnes Patricksson	Decision support for conceptual ship design with focus on a changing life cycle and future uncertainty, IMT
IMT-13-2016	Mats Jørgen Thorsen	Time domain analysis of vortex-induced vibrations, IMT
IMT-14-2016	Edgar McGuinness	Safety in the Norwegian Fishing Fleet – Analysis and measures for improvement, IMT
IMT-15-2016	Sepideh Jafarzadeh	Energy effiency and emission abatement in the fishing fleet, IMT
IMT-16-2016	Wilson Ivan Guachamin Acero	Assessment of marine operations for offshore wind turbine installation with emphasis on response-based operational limits, IMT
IMT-17-2016	Mauro Candeloro	Tools and Methods for Autonomous Operations on Seabed and Water Coumn using Underwater Vehicles, IMT
IMT-18-2016	Valentin Chabaud	Real-Time Hybrid Model Testing of Floating Wind Tubines, IMT
IMT-1-2017	Mohammad Saud Afzal	Three-dimensional streaming in a sea bed boundary layer
IMT-2-2017	Peng Li	A Theoretical and Experimental Study of Wave-induced Hydroelastic Response of a Circular Floating Collar
IMT-3-2017	Martin Bergström	A simulation-based design method for arctic maritime transport systems

IMT-4-2017	Bhushan Taskar	The effect of waves on marine propellers and propulsion
IMT-5-2017	Mohsen Bardestani	A two-dimensional numerical and experimental study of a floater with net and sinker tube in waves and current
IMT-6-2017	Fatemeh Hoseini Dadmarzi	Direct Numerical Simualtion of turbulent wakes behind different plate configurations
IMT-7-2017	Michel R. Miyazaki	Modeling and control of hybrid marine power plants
IMT-8-2017	Giri Rajasekhar Gunnu	Safety and effiency enhancement of anchor handling operations with particular emphasis on the stability of anchor handling vessels
IMT-9-2017	Kevin Koosup Yum	Transient Performance and Emissions of a Turbocharged Diesel Engine for Marine Power Plants
IMT-10-2017	Zhaolong Yu	Hydrodynamic and structural aspects of ship collisions
IMT-11-2017	Martin Hassel	Risk Analysis and Modelling of Allisions between Passing Vessels and Offshore Installations
IMT-12-2017	Astrid H. Brodtkorb	Hybrid Control of Marine Vessels – Dynamic Positioning in Varying Conditions
IMT-13-2017	Kjersti Bruserud	Simultaneous stochastic model of waves and current for prediction of structural design loads
IMT-14-2017	Finn-Idar Grøtta Giske	Long-Term Extreme Response Analysis of Marine Structures Using Inverse Reliability Methods
IMT-15-2017	Stian Skjong	Modeling and Simulation of Maritime Systems and Operations for Virtual Prototyping using co-Simulations
IMT-1-2018	Yingguang Chu	Virtual Prototyping for Marine Crane Design and Operations
IMT-2-2018	Sergey Gavrilin	Validation of ship manoeuvring simulation models
IMT-3-2018	Jeevith Hegde	Tools and methods to manage risk in autonomous subsea inspection,maintenance and repair operations
IMT-4-2018	Ida M. Strand	Sea Loads on Closed Flexible Fish Cages
IMT-5-2018	Erlend Kvinge Jørgensen	Navigation and Control of Underwater Robotic Vehicles

IMT-6-2018	Bård Stovner	Aided Intertial Navigation of Underwater Vehicles
IMT-7-2018	Erlend Liavåg Grotle	Thermodynamic Response Enhanced by Sloshing in Marine LNG Fuel Tanks
IMT-8-2018	Børge Rokseth	Safety and Verification of Advanced Maritime Vessels
IMT-9-2018	Jan Vidar Ulveseter	Advances in Semi-Empirical Time Domain Modelling of Vortex-Induced Vibrations
IMT-10-2018	Chenyu Luan	Design and analysis for a steel braceless semi-submersible hull for supporting a 5-MW horizontal axis wind turbine
IMT-11-2018	Carl Fredrik Rehn	Ship Design under Uncertainty
IMT-12-2018	Øyvind Ødegård	Towards Autonomous Operations and Systems in Marine Archaeology
IMT-13-2018	Stein Melvær Nornes	Guidance and Control of Marine Robotics for Ocean Mapping and Monitoring
IMT-14-2018	Petter Norgren	Autonomous Underwater Vehicles in Arctic Marine Operations: Arctic marine research and ice monitoring
IMT-15-2018	Minjoo Choi	Modular Adaptable Ship Design for Handling Uncertainty in the Future Operating Context
MT-16-2018	Ole Alexander Eidsvik	Dynamics of Remotely Operated Underwater Vehicle Systems
IMT-17-2018	Mahdi Ghane	Fault Diagnosis of Floating Wind Turbine Drivetrain- Methodologies and Applications
IMT-18-2018	Christoph Alexander Thieme	Risk Analysis and Modelling of Autonomous Marine Systems
IMT-19-2018	Yugao Shen	Operational limits for floating-collar fish farms in waves and current, without and with well-boat presence
IMT-20-2018	Tianjiao Dai	Investigations of shear interaction and stresses in flexible pipes and umbilicals
IMT-21-2018	Sigurd Solheim Pettersen	Resilience by Latent Capabilities in Marine Systems
IMT-22-2018	Thomas Sauder	Fidelity of cyber-physical empirical methods. Application to the active truncation of slender marine structures